Scale-Down Characterisation of Post-Centrifuge Flocculation Processes and the Study of its Impact upon Downstream Processing during Mammalian Cell Antibody Production

A thesis submitted to University College London

for the degree of Doctor of Engineering

by

Georgina Espuny Garcia del Real

December 2016

Department of Biochemical Engineering
University College London
Bernard Katz Building
Gordon Street
London WC1H 0AH

Declaration

I, Georgina Espuny Garcia del Real, confirm that the work presented in this thesis is my own. Where information had been derived from other sources, I confirm that this has been indicated in the thesis.

Signature: 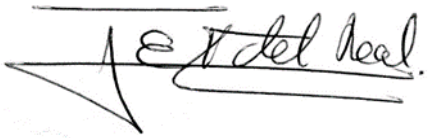 **Date:** 09/12/2016

Abstract

The high demand for biopharmaceuticals has been met thanks to improved upstream productivity. Downstream, which has not advanced at the same pace, calls for new clarification strategies to cope with the increased process-related impurities associated with upstream improvements.

This thesis has focused on the implementation of polyelectrolyte flocculation between centrifugation and depth filtration during the primary recovery of a monoclonal antibody Chinese hamster ovary (CHO) cell process. A high-throughput, automated ultra scale-down (USD) flocculation methodology was developed with industrial relevance in mind for process development activities. The impact flocculation had on depth filtration and protein A chromatography performance was subsequently investigated and supported by analytical assays and techniques to assess impurity removal.

Cell densities at time of harvest > $20x10^6$ cells.mL^{-1} were critical for flocculation to occur on centrifuged CHO cell cultures. Flocculant addition time limited the flocculation scale-up success between two vessels with different geometrical ratios and working volumes (1.5 L and 800 µL). The influence of mixing time scales (macromixing, mesomixing and micromixing) on this variable defined the USD flocculation scale-up basis, which was: predominance of micromixing in the vessels (flocculant addition time scale-up) and constant power input per unit volume (impeller speed scale-up).

The implementation of constant pressure, single-layer USD filtration methods with flocculated feeds was precluded due to the low filter capacity values obtained (< 35 $L.m^{-2}$). In contrast, constant flux filtration with multi-layer depth filters at laboratory scale reached manufacturing-scale filter capacity values (> 490 $L.m^{-2}$). Flocculation achieved larger depth filtration capacities and lower process-related impurities before protein A chromatography when compared to the current manufacturing processing option. Post-protein A chromatography, the clear eluate obtained with flocculation contrasted with the turbid eluate of the current processing option. Mass spectrometry data confirmed the turbid eluate was mainly constituted of negatively charged CHO cell protein precipitates.

Acknowledgements

There are many people to whom I would like to express my gratitude for helping me bring this thesis to fruition. I would like to thank my academic supervisor Dr Daniel Bracewell and my industrial supervisor Dr Jim Davies for their guidance, help and support that have undoubtedly contributed to keeping my work on track. I would also like to thank Dr Lee Allen and Dr Evi Dimitriadou, both from Lonza Biologics (Slough, UK), for their input and help during the early stages of this project, Dr Katherine Lintern for sharing her expertise in mass spectrometry analytical studies, and Prof Nigel Titchener-Hooker for the invaluable opportunity given. I would also like to thank the Engineering and Physical Sciences Research Council (EPSRC) and Technology Strategy Board (TSB) for funding this project.

On a more personal note, I would like to thank my late grandmother for her unlimited patience and love, and for teaching me everything she knew from a very early age; my parents for their constant support, for always being by my side and for the sacrifices made, particularly during the past decade; Eduardo for always being the best version of himself, for his help and care, for the laughter and for the amazing travels together. Finally, I also want to thank my Catalan and Basque friends, particularly Alba, Anna and Hasier, with whom I have been able to share the ups and downs of our doctoral lives.

In the loving memory of my *yaya*,

the strongest, most loving and hard-working woman

I will ever encounter

Table of Contents

List of Figures

List of Tables

Nomenclature

A	Effective filtration area (m^2)
Abs_λ	Absorbance at λ nm wavelength (A.U.)
a	Constant for the minimum asymptote in a four parameter logistic non-linear regression model
b	Constant for the steepness of the curve in a four parameter logistic non-linear regression model
C	Clearance from the vessel bottom to the impeller (m)
C_{Hx}	Constant domain on the heavy chain of an immunoglobulin G where x = 1, 2 or 3
C_L	Constant domain on the light chain of an immunoglobulin G
c	Correction factor to account for non-ideal flow inside the centrifuge
D_b	Baffle diameter (m)
D_i	Impeller diameter (m)
D_m	Diameter of the magnetic disc (m)
D_T	Tank or vessel diameter (m)
D_t	Turbulent diffusivity ($m^2.s^{-1}$)
d	Constant for the inflection point of the curve in a four parameter logistic non-linear regression model
d_i	Internal diameter of the pipe/tip used for reagent addition (m)
d_x	Particle size characteristic descriptor where x = 10, 50 or 90 (μm)
dV/dt	Instantaneous volumetric flow rate ($m^3.s^{-1}$)
E	Correction factor to account for the deceleration time in a bench-top centrifuge

e	Constant for the maximum asymptote in a four parameter logistic non-linear regression model
F	Correction factor to account for the acceleration time in a bench-top centrifuge
Fc	Effector part of an immunoglobulin G
F_V	Variable region of an immunoglobulin G responsible for selectivity in antigen binding
$F_{v,i}$	Percentage volume frequency particle size distribution in the *i* particle size interval
$\bar{G}$	Average shear rate (s^{-1})
g	Gravitational acceleration ($m.s^{-2}$)
H_b	Distance between the baffle and the vessel's wall (m)
H_{ib}	Height of the impeller blade (m)
H_L	Height of the liquid level in a vessel (m)
I	Intensity of the emerging radiation (cd)
I_0	Intensity of the incident radiation (cd)
J	Filter flux rate ($L.m^{-2}.h^{-1}$)
K	Constant for the theoretical calculation of the characteristic large eddy disintegration mesomixing time
K_B	Equilibrium constant of the reaction between iodine and iodide ions to form triiodide ($m^3.mol^{-1}$)
l	Path length of the beam of light through the sample or path length of the cuvette (m)
N	Impeller speed (s^{-1})
n	Number of separation discs in the stack of a disc-stack centrifuge

n_f	Number of feed points in a vessel
n_x	Number of moles of species x (mol)
OD_{600}	Optical density at 600 nm wavelength (A.U.)
OD_f	Optical density of the feed material prior to centrifugation (A.U.)
OD_s	Optical density of the centrifuge supernatant (A.U.)
OD_{ws}	Optical density of the best possibly clarified centrifuge supernatant or well-spun (A.U.)
P	Power input (W)
P_0	Impeller power number
P_i	Inlet pressure during constant flux filtration (bar)
pH*	Iodine dismutation pH
Q	Volumetric filtrate flow rate ($m^3.s^{-1}$)
Q_0	Initial volumetric filtrate flow rate ($m^3.s^{-1}$)
Q_0^*	Initial volumetric filtrate flow rate per unit filter area ($L.m^{-2}.s^{-1}$)
Q_b	Feed rate at which an external fluid is added into a mixing vessel in semibatch operation mode ($m^3.s^{-1}$)
Q_x	Centrifuge volumetric flow rate ($m.s^{-1}$) where x = lab (bench-top centrifuge), ds (disc-stack centrifuge), tub (tubular bowl centrifuge)
Re	Reynolds number
R_f	Filter resistance (m^{-1})
r*	Ratio between the distance from the vessel's central vertical axis to the feed point and the vessel radius
r_1	Bench-top centrifuge inner radius (m)

r_2	Bench-top centrifuge outer radius (m)
r_i	Disc-stack centrifuge separation disc inner radius (m)
r_o	Disc-stack centrifuge separation disc outer radius (m)
S	Correction factor for the area occupied by the caulks in a disc-stack centrifuge
T	Temperature (K or °C)
t	Filtration time (s)
t_0	Filtration time when the star-up phase is completed during ultra scale-down constant pressure filtration (s)
t_c	Circulation time (s)
t_{crit}	Critical addition time (s)
t_d	Characteristic turbulent dispersion mesomixing time (s)
t_e	Characteristic micromixing time (s)
t_f	Feed or reagent addition time (s)
t_m	Characteristic macromixing time (s)
t_s	Characteristic large eddy disintegration mesomixing time (s)
$\bar{u}$	External fluid velocity in the vicinity of the feed pipe through which the reagent is added into the mixing vessel ($m.s^{-1}$)
$\bar{u}_r$	Mean radial velocity component of $\bar{u}$ ($m.s^{-1}$)
$\bar{u}_t$	Mean tangential velocity component of $\bar{u}$ ($m.s^{-1}$)
u_r	Radial component of the fluid velocity relative to the tip speed
u_t	Tangential component of the fluid velocity relative to the tip speed
V	Filtrate volume (m^3)
V^*	Cumulative filtrate volume per unit filter area ($L.m^{-2}$)

V_0^*	Cumulative filtrate volume per unit filter area when the start-up phase is completed during ultra scale-down constant pressure filtration ($L.m^{-2}$)
$V_{\%,i}$	Percentage volume particle size distribution in the *i* particle size interval
V_B	Volume of reagent added into the flocculation mixing vessel (m^3)
V_H	Variable domain on the heavy chain of an immunoglobulin G
V_L	Variable domain on the light chain of an immunoglobulin G
V_l	Vessel's liquid working volume (m^3)
V_{lab}	Volume of material in a centrifuge tube when using a bench-top centrifuge (m^3)
V_{max}^*	Maximum predicted filtration throughput before complete filter plugging ($L.m^{-2}$)
v_g	Speed of a small spherical particle suspended in a viscous fluid and under a gravitational field ($m.s^{-1}$)
v_{tip}	Impeller tip speed ($m.s^{-1}$)
W_i	Width of the *i* particle size interval
W_{ib}	Width of the impeller blade (m)
X_1	Extent of the reaction between borate ions and acid to form boric acid
X_2	Extent of the Dushman reaction
X_S	Fluid segregation index
[x]	Molar concentration of species x ($mol.m^{-3}$)
$[x]_0$	Initial molar concentration of species x ($mol.m^{-3}$)

Y_S Yield of the Dushman reaction under imperfect micromixing conditions

Y_{ST} Yield of the Dushman reaction under perfect micromixing conditions

Greek letters

Γ Torque force (N)

ΔP Pressure drop across the filter (Pa)

Λ_c Macroscale concentration (m)

Σ Equivalent settling area of a centrifuge (m^2)

Φ Relative local energy dissipation rate

α Constant in the linearised filtration models for constant pressure and constant flux filtration

β Constant in the linearised filtration models for constant pressure and constant flux filtration

δ Constant in the linearised filtration models for constant pressure and constant flux filtration

ε Local turbulent energy dissipation rate per unit mass of fluid ($W.kg^{-1}$)

ε_λ Molar extinction coefficient at λ nm wavelength of the species being quantified in the sample ($m^2.mol^{-1}$)

ε_{avg} Average turbulent energy dissipation rate per unit mass of fluid ($W.kg^{-1}$)

ε_{max} Maximum turbulent energy dissipation rate per unit mass of fluid ($W.kg^{-1}$)

θ Separation disc half angle in a disc-stack centrifuge (radians)

μ Fluid dynamic viscosity (Pa.s)

ν	Fluid kinematic viscosity ($m^2.s^{-1}$)
ρ	Liquid density ($kg.m^{-3}$)
ω	Radial velocity in a centrifuge (s^{-1})

Abbreviations

ACN	Acetonitrile
ADC	Antibody Drug Conjugate
ATPS	Aqueous Two-Phase System
BCA	Bicinchoninic Acid
CFD	Computational Fluid Dynamics
CGMPs	Current Good Manufacuring Practices
CHO	Chinese Hamster Ovary
CMO	Contract Manufacturing Organisation
CV	Column Volume
dAb	domain Antibody
DNA	Deoxyribonucleic Acid
DSP	Downstream Processing
EBA	Expanded Bed Adsorption chromatography
EDD	Engulfment-Deformation-Diffusion mechanistic model for micromixing time
EMA	European Medicines Agency
Fab	Fragment of antibody
FDA	Food and Drug Administration
G3PDH	Glyceraldehyde-3-Phosphate Dehydrogenase
GRP78	78 kDa Glucose-Regulated Protein or Chaperone BiP
GS	Glutamine Synthetase
HCD	High Cell Density

HCP	Host Cell Protein
HPLC	High Performance Liquid Chromatography
HTP	High-Throughput
IEM	Interaction by Exchange with the Mean mechanistic model for micromixing time
IgG	Immunoglobulin G
LCD	Low Cell Density
LC-MS/MS	Liquid Chromatography – Mass Spectrometry/Mass Spectrometry
mAb	monoclonal Antibody
MALDI-TOF/TOF	Matrix-Assisted Laser Desorption/Ionisation - Time Of Flight - Time Of Flight
MES	2-(N-morpholino)ethanesulfonic acid
MW	Molecular Weight
MWCO	Molecular Weight Cut-Off
NFF	Normal Flow Filtration
NTU	Nephelometric Turbidity Units
PBS	Phosphate Buffered Saline
pDADMAC	poly-(Diallyldimethylammonium) Chloride
PEG	Polyethylene Glycol
PEI	Polyethylenimine
ppm	parts per million
PSD	Particle Size Distribution
PTFE	Polytetrafluoroethylene

QbD	Quality by Design
sdAb	single domain Antibody
SDS-PAGE	Sodium Dodecyl Sulphate - Polyacrylamide Gel Electrophoresis
STR	Stirred Tank Reactor
TFA	Trifluoroacetic Acid
TFF	Tangential Flow Filtration
TMP	Transmembrane Pressure
UF/DF	Ultrafiltration/Diafiltration
USD	Ultra Scale-Down
USP30	Ubiquitin carboxyl-terminal hydrolase 30

1. Introduction

1.1. Antibodies for Therapeutic Use

Therapeutic monoclonal antibodies (mAbs) have demonstrated a considerable level of success in the pharmaceutical market (see Section 1.1.3). Their success as drugs relies upon the robust and flexible nature of immunoglobulins (IgGs) (Chames et al., 2009; Elvin et al., 2013). Therapeutic mAbs were made possible when in 1975 Georges Köhler and César Milstein immortalised hybridoma cells that were secreting antibody of a predefined specificity (Chames et al., 2009; Salemi et al., 2015). The early therapeutic mAbs faced immunogenicity and efficacy problems due to their murine nature (Chames et al., 2009). However, advancements in molecular biology in the early 90s resulted in optimised mAbs of improved immunogenicity, efficacy and potency; cloning the IgG genes in eukaryotic expression vectors, molecular evolution procedures and *in vitro* selection methods were key to mAb evolution (Chames et al., 2009; Hoogenboom and Chames, 2000). Further improvements in molecular and genetic engineering allowed mAbs to evolve from murine molecules to chimeric (i.e. 70 % human with a fully human Fc portion), humanised (i.e. 85-90 % human) and fully human antibodies (Chames et al., 2009).

1.1.1. Monoclonal Antibody (mAb) Structure

Therapeutic mAbs are IgG molecules with a molecular weight (MW) around 150 kDa composed of two identical heavy and light chains linked by disulphide bonds and carrying post-translational modifications such as glycosylations (see Figure 1.1) (Chames et al., 2009; Chan and Carter, 2010). There are four subclasses or isotypes of IgG (IgG_1 to IgG_4), which differ in the number and position of the disulphide bonds (Seiler et al., 1985). Each heavy chain (MW ~ 50 kDa) contains a variable domain (V_H) and three constant domains (C_{H1}, C_{H2} and C_{H3}). Each light chain (MW ~ 25 kDa) is constituted of a variable domain (V_L) and a single constant domain (C_L) (Chan and Carter, 2010; Sommerfeld and Strube, 2005). According to their functions, the mAb can be further divided into the Fc and Fv regions (see Figure 1.1). The Fv region is in charge of selectively binding to the

antigen by the variable domains. The Fc region is the effector part of the antibody and interacts either with the Fc receptors for IgG on effector cells or with the complement component C1q triggering different immunological responses inside the patient's body (Brekke and Sandlie, 2003; Chan and Carter, 2010; Elvin et al., 2013). For in-depth descriptions of the mechanisms of action used by therapeutic mAbs the reader is referred to Chames et al. (2009) and Chan and Carter (2010).

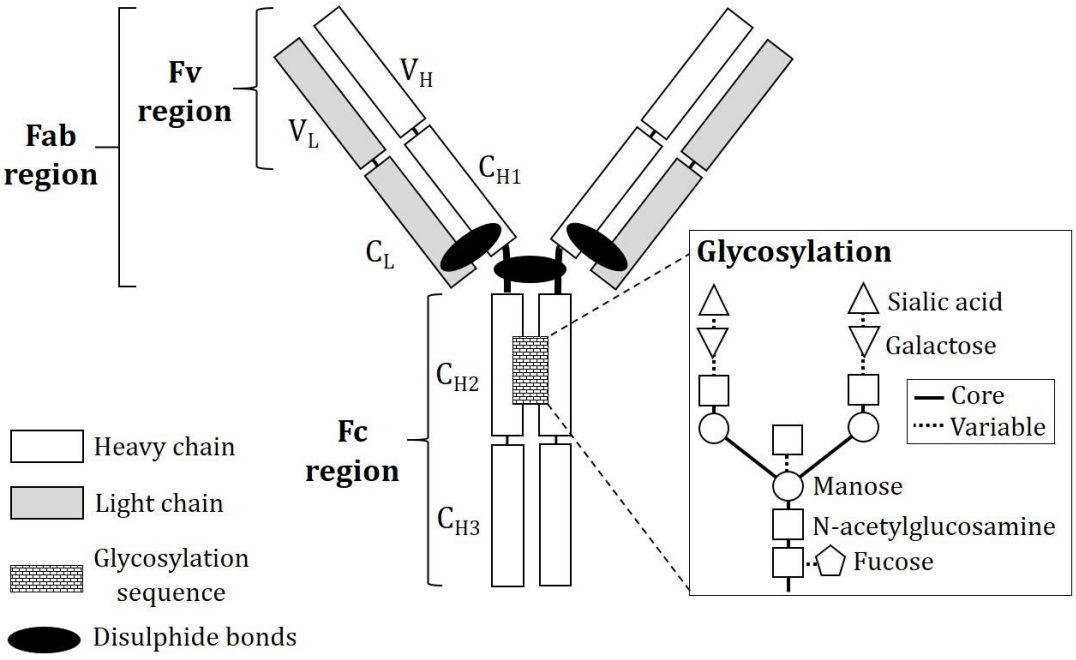

Figure 1.1. Structure and key features of an IgG molecule.
All IgG molecules consist of two identical light chains and two identical heavy chains. The heavy chains, which are constituted of one variable domain (V_H) and three constant domains (C_{H1}, C_{H2} and C_{H3}) each, are covalently linked in the hinge (i.e. flexible) region. The light chains, which contain one variable domain (V_L) and a single constant domain (C_L), are covalently linked to the heavy chain via their constant domain. Antigen recognition and binding is effectuated by the complementarity determining regions (CDR) of the light and heavy chain variable domains. The Fc region, which carries the post-translational glycosylation, is in charge of effectuating the cellular immunological responses. Figure adapted from Brekke and Sandie (2003) and Chan and Carter (2010).

1.1.2. Therapeutic mAbs and Antibody-Related Molecules

1.1.2.1. Therapeutic mAbs

The molecular structure of mAbs has been described in Section 1.1.1. Therapeutic mAbs are large proteins derived either from immunisation of unmodified or transgenic animals, or from display technologies that use libraries of IgG nucleic acid sequences from a variety of sources (Chan and Carter, 2010; Elvin et al., 2013).

Most clinical studies have shown that large amounts of therapeutic mAb need to be injected into the patients to achieve clinical efficacy (Chames et al., 2009). To improve their therapeutic action, the Fc region or the carbohydrate composition of the glycosylation post-translational modification (see Figure 1.1) is engineered resulting in the 'next generation mAbs' (Chames et al., 2009; Chan and Carter, 2010).

1.1.2.2. IgG-Based Bispecific Antibodies

Another strategy to further increase the clinical potential of mAbs is the generation of bispecific antibodies, where monospecific mAbs are engineered to bind a second antigen while maintaining high affinity for the first antigen (Chan and Carter, 2010). To obtain these IgGs the V_L and V_H domains (see Figure 1.1) are modified with variable domains of a second antigen-binding specificity, or by linking a single variable domain with a second specificity to the IgG (Chan and Carter, 2010).

1.1.2.3. Antibody Fragments (Fabs)

Fragments of antibody are mAb fragments that lack the effector function (i.e. Fc region) but retain the binding activity of a full-size IgG (Chames et al., 2009; Chan and Carter, 2010). They are constituted by the entire IgG light chain (V_L and C_L) and the variable (V_H) and C_{H1} constant domains of the IgG heavy chain (see Figure 1.1). Antibody fragments do not carry any post-translational modification and can be functionally expressed in *Escherichia coli* (Brekke and Sandlie, 2003). Because of their reduced size, these therapeutic molecules overcome the limitations of full-size mAbs to penetrate the target tumors (Chames et al., 2009).

However, their serum half-life is shorter than that of full-size mAbs and they are rapidly eliminated by renal clearance (Chames et al., 2009; Chan and Carter, 2010). Nonetheless, their small size makes Fabs suitable for radioimmunotherapy and imaging applications (Chames et al., 2009).

1.1.2.4. Domain Antibodies (dAbs)

Single domain antibodies (sdAb), also referred to as scFv (single chain Fv region), are monovalent molecules comprising the variable domains of the IgG heavy and light chains (i.e. the Fv region; see Figure 1.1) linked by a short peptide linker (Chan and Carter, 2010). These molecules can be efficiently expressed in bacteria, and due to their small size and single-domain nature they can access epitopes on the target surface that larger antibody fragments cannot reach (Saerens et al., 2008). However, their very short half-life in serum (~2 hours) stops them from being used as therapeutic antibodies (Chames et al., 2009). Instead, they are used in serotherapy to neturalise toxins and as binding moieties when integrated into more complex molecules (Chames et al., 2009; Saerens et al., 2008).

Multimerisation of dAbs has resulted in the creation of diabodies, triabodies and tetrabodies. These multivalent molecules have increased serum half-life (Chames et al., 2009), they can have different antigen specificities (Brekke and Sandlie, 2003; Chames et al., 2009; Elvin et al., 2013; Saerens et al., 2008), and they can be combined with other antibody domains to allow specific Fc-mediated effector functions in the immunological response (Chan and Carter, 2010; Saerens et al., 2008).

1.1.2.5. Fc-Fusion Proteins

Fc-fusion proteins are molecules in which the IgG Fc region has been genetically linked to a protein of interest (e.g. enzyme, extracellular domain of a receptor or protein ligand). The Fc region confers (i) increased serum life-time of the molecule; (ii) easier heterelogous expression and purification; and (iii) the ability to interact with the Fc-receptors found on immune cells to trigger an immunological response (Carter, 2011; Huang, 2009).

1.1.2.6. Antibody-Drug Conjugates (ADCs)

Antibody-drug conjugates are mAbs that have been covalently linked to small drug molecules of particularly high cytotoxicity. Each antibody will typically carry more than one drug molecule. Antibody-drug conjugates specifically bind to the target cancer cells where the drug is delivered. Therefore, ADCs offer lower systemic toxicity when compared to cancer chemotherapy treatments. Also, different linker chemistries can be used to attach the drug molecules to the antibody to allow control over the pharmacokinetics and delivery of the cytotoxic drug (Hamilton, 2015).

1.1.3. Market Analysis for Therapeutical mAbs

Since the approval of the first therapeutic mAb in 1986 (immunosuppressant Orthoclone OKT3), mAbs and antibody-related molecules have grown to become the dominant product class within the biopharmaceutical market (Ecker et al., 2015). Forty-seven antibody products (i.e. mAbs and antibody-related molecules) have been approved in the USA and/or Europe for the treatment of diverse diseases, though they mainly target cancer, inflammatory and immunological disorders (Chan and Carter, 2010; Ecker et al., 2015; Elvin et al., 2013; Reichert, 2012). The majority of the commercialised antibody products are full-length mAbs expressed in mammalian cell lines. Only three antibody products are expressed in *Escherichia coli* i.e. two Fabs and one Fc-fusion protein (Ecker et al., 2015; Reichert, 2012). A comprehensive list of the therapeutic antibody products currently marketed in the USA and Europe can be found in the review by Ecker and co-workers (2015).

The sales from all antibody products grew by 90 % from 2008 to 2013, with global sales revenue of almost $75 billion (Ecker et al., 2015). However, the majority of sales are generated by five therapeutic mAbs with blockbuster status, i.e. bevacizumab/Avastin®; rituximab/Rituxan®; adalimumab/Humira®; infliximab/Remicade®; and trastuzumab/Herceptin® (Elvin et al., 2013). It is expected that the global sales of therapeutic antibody products will continue growing to reach world-wide sales of more than $94 billion by 2017 and nearly $125 billion by 2020 (Ecker et al., 2015). Sales will be driven by the predicted

increase in demand for the antibody products commercialised at the present time and also by new approved products given that over 300 antibody product candidates are currently in different phases of clinical trials (Ecker et al., 2015; Elvin et al., 2013; Reichert, 2012). The introduction of biosimilars, and new markets thereof, are expected to be other factors driving sales growth for antibody products in the future (Ecker et al., 2015)

The increase in global demand for therapeutic antibody products will require an even further increase in the manufacturing capability of these products, which has justified the implementation of mAb manufacturing platforms (see Section 1.2).

1.2. Current Manufacturing Process for mAbs

The biochemical similarities between different therapeutic mAbs has resulted in the emergence of templated recovery and purification schemes (Low et al., 2007; Shukla et al., 2007). A 'platform' unit operation is described as "one that can be used without much optimisation in a wide range of feed conditions" (Low et al., 2007). Established production platforms offer advantages over individualised production processes because they increase speed to market (reduce time and investment during process development), and harmonise practises and information across different manufacturing sites (Low et al., 2007). Nonetheless, significant biochemical differences between therapeutic mAbs may exist, thus causing downstream purification challenges that require the departure from established mAb production platforms (Shukla et al., 2007).

This subsection gives an overview of the unit operations that have become part of a typical therapeutic mAb production platform. Figure 1.2 sums up the manufacturing process flow.

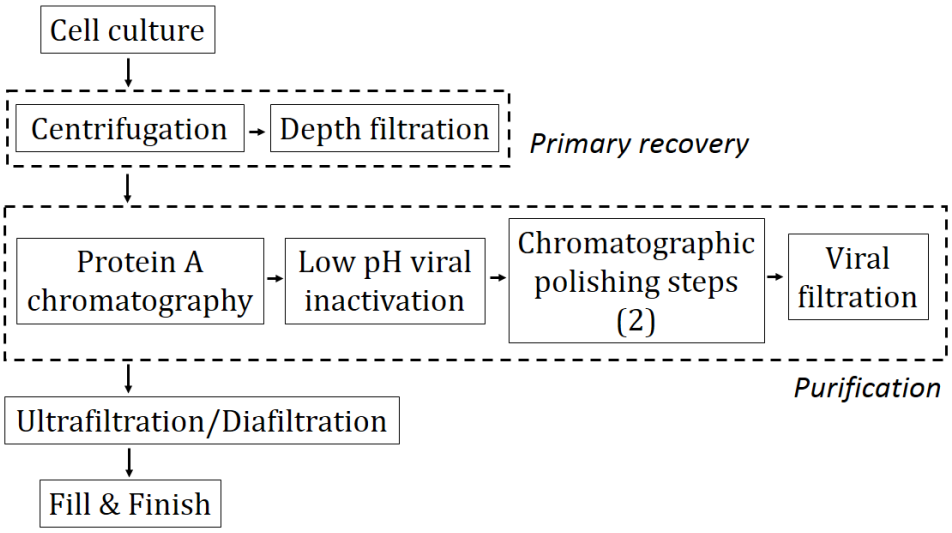

Figure 1.2. Manufacturing platform process for therapeutic monoclonal antibodies.
Figure adapted from Low et al. (2007) and Shukla et al. (2007).

1.2.1. Cell Hosts

The choice of cell host will be dictated by the antibody structure, the importance of glycosylation as a post-translational modification, the required productivity, ease of purification and production costs (Chadd and Chamow, 2001; Li et al., 2010). Bacterial and mammalian producing cell lines constitute the cell hosts for commercialised mAb products, although the expression of mAb products in yeast cells, transgenic animals, insect cells and plants has also been reported (Chadd and Chamow, 2001; Li et al., 2010; Reichert, 2012). Bacterial systems (i.e. *Escherichia coli*), which lack the cellular machinery to glycosylate proteins, are suitable for the expression of Fabs and dAbs (Chadd and Chamow, 2001). Therapeutic mAbs and antibody-related molecules that require glycosylation (e.g. Fc-fusion proteins) are expressed in mammalian cell systems (Chadd and Chamow, 2001; Shukla et al., 2007). These cell hosts include Chinese Hamster Ovary (CHO) cells, NS0 or SP2/0 murine myeloma cells and PER.C6® human cells (Chadd and Chamow, 2001; Elvin et al., 2013; Li et al., 2010; Reichert, 2012). Nonetheless, the preferred expression system for commercialised therapeutic mAbs are CHO cells (Low et al., 2007; Reichert, 2012).

1.2.2. Cell Culture

Different types of bioreactor have been employed at industrial scale for mammalian cell culture. These include stirred tank bioreactors, hollow filter bioreactors, airlift bioreactors and rotary cell culture systems. Nonetheless, suspension cell culture in stainless steel stirred tank bioreactors has become the cell culture platform of choice for large scale production of commercially available therapeutic mAbs. Stirred tank bioreactors provide: a homogeneous environment for cell growth; convenient control of process parameters; and facile scale up. Fed-batch is the most successfully used feeding strategy at large production scale, although repeated batch and perfusion are other feeding strategies also favoured at industrial scale. Different cell lines have shown to more easily adapt to fed-batch cell cultures, and provide higher cell density, viability and antibody titres (Jain and Kumar, 2008).

1.2.3. Primary Recovery

The aim of primary recovery is to remove the solids (i.e. cells and cell debris) present in the cell culture broth from the liquid phase where the mAb is in soluble form as they are secreted by the cells. Continuous disc-stack centrifugation coupled with depth filtration has become the industry standard for primary recovery (Low et al., 2007; Shukla et al., 2007). This combination has shown to be robust enough to provide satisfactory clarification performance despite existing variations in cell density and viability between different mAb production processes (Shukla et al., 2007). High cell densities and low shear centrifuges have relegated cross-flow microfiltration to small scale or low capital cost mAb production, given that it cannot offer the scalability and process performance robustness that centrifugation can (Low et al., 2007). Depth filtration is used as a secondary clarification step to remove cells and cell debris still present in the centrifuge supernatant, which must be removed prior to chromatography (Low et al., 2007; Shukla et al., 2007). However, direct depth filtration can also be used for whole cell broth removal, although it is only common for bench, pilot or smaller commercial-scale applications (Liu et al., 2010). Charged depth filters are preferred over uncharged depth filters due to the combined action of mechanical

sieving and zeta potential to remove impurities (Low et al., 2007). An absolute filter with pore size rating of 0.45 μm or 0.20 μm follows depth filtration to ensure the removal of solid particulates and bacteria before chromatography; bacteria are only removed when using 0.20 μm filters (Shukla et al., 2007).

1.2.4. Purification

The main consideration when designing the purification strategy is purity, although other key considerations include overall yield, process throughput, robustness, reliability and scalability (Shukla et al., 2007). The following are classified as impurities: host cell proteins (HCPs), deoxyribonucleic acid (DNA), endotoxins and some cell culture media additives (process-related impurities), and high MW mAb aggregates (product-related impurities). Viruses are also regarded as impurities, and must be cleared during mAb purification (Liu et al., 2010; Shukla and Thömmes, 2010; Shukla et al., 2007).

Chromatographic steps have become the backbone of current biopharmaceutical purification processes due to their high selectivity and resolution (Liu et al., 2010; Shukla and Thömmes, 2010). Protein A chromatography is the capture step of choice in mAb platform processes (Low et al., 2007; Shukla and Hinckley, 2008; Shukla et al., 2007). Protein A chromatography offers a high degree of clearance for HCPs due to the specific affinity of the protein A ligand for the Fc region of mAbs. Protein A chromatography has been shown to reduce >90 % the HCP content in clarified CHO cell broths (Shukla and Hinckley, 2008; Shukla et al., 2007). Protein A chromatography consists of the following steps: (i) loading of clarified cell culture broth at neutral pH (pH 6-8); (ii) one or more washes at intermediate pH (pH 4-6) to remove HCPs and other impurities; (iii) mAb elution at low pH (pH 2.5-4); (iv) stripping the column at pH ~ 2 to remove any remaining impurities; (v) cleaning the column at alkaline pHs; and (vi) regenerating the column with equilibration buffer (if subsequently used) or storing the column in storage buffer, typically containing ethanol (Liu et al., 2010; Shukla and Hinckley, 2008; Shukla et al., 2007).

As detailed in Figure 1.2, a viral inactivation step typically follows capture protein A chromatography. The Food and Drug Administration (FDA) regulatory

guidelines for the production of biopharmaceutical products derived from human or animal cell lines require the use of two dedicated orthogonal steps for viral reduction (U.S. Department of Health and Human Services, Food and Drug Administration, 1998). A low pH incubation step (pH ≤ 3.8) is typically included post-protein A chromatography as elution is performed at low pH. Following acid inactivation, the solution is then neutralised to ensure mAb stability (Shukla et al., 2007).

At least two chromatography steps, referred to as polishing steps, follow protein A chromatography to achieve the required purity levels to ensure patient safety (see Figure 1.2). Orthogonal chromatographic modes of interaction are selected to effectively separate the impurities still present in the protein A chromatography eluate (i.e. HCPs, mAb aggregates, DNA and leached protein A ligands). Cation exchange chromatography and anion exchange chromatography operated in flow-through mode has been the post-protein A purification sequence adopted by a number of commercialised therapeutic mAbs. While cation exchange chromatography removes HCPs, aggregates and leached protein A ligands, anion exchange chromatography clears DNA and further HCPs. Other chromatographic modes such as hydrophobic interaction chromatography, size exclusion chromatography, hydroxyapatite and immobilised metal affinity chromatography have also been successfully implemented. However, the chromatographic mode chosen will depend upon the nature of the impurities present and its ability to reduce the viral load (Shukla et al., 2007).

Viral filtration is typically performed after one of the polishing chromatographic steps as the second viral inactivation step (see Figure 1.2). The placement of the viral filters in the process will depend upon the volume to be filtered. Therefore, the type of viral filter employed can be standardised, but the placement and size of the filters will be specific to the mAb process (Shukla et al., 2007).

1.2.5. Ultrafiltration/Diafiltration (UF/DF)

Upon completing downstream purification, the mAb is concentrated while the product buffer is exchanged for the formulation buffer (see Figure 1.2) employing an UF/DF unit (van Reis and Zydney, 2007; Shukla et al., 2007). Standardised

specifications for the type of membrane, transmembrane pressure (TMP) and cross-flow rate employed, as well as the concentration factor at which diafiltration is performed can be used for all mAbs. Nonetheless, fluid viscosity and mAb aggregation concerns need to be solved on a case-by-case basis (Shukla et al., 2007).

1.3. Current Manufacturing Challenges in mAb Production and Proposed Solutions

1.3.1. Challenges

1.3.1.1. Increasing Cell Densities

In the past two decades the intensive optimisation work in cell line selection, growth media, feeding strategies and bioreactor conditions has led to increased product titre and cell density values; some biopharmaceutical companies have reported 5-10 $g.L^{-1}$ of mAb and cell densities of $>20x10^6$ $cells.mL^{-1}$ for a 14-day fed-batch mammalian cell process (Huang et al., 2010; Kelley, 2009; Li et al., 2010; Shukla and Thömmes, 2010). The high cell densities achieved have introduced elevated levels of process-related impurities that have placed increased demands upon traditional primary recovery and purification operations (Low et al., 2007; Singh et al., 2013; Westoby et al., 2011). As a consequence, process bottlenecks have shifted from upstream to downstream, which accounts for ~80 % of the total mAb production costs (Hogwood et al., 2013a; Kelley, 2009; Shukla and Thömmes, 2010).

1.3.1.2. Precipitation and Non-Specific Binding during Protein A Chromatography

Low pH elution during protein A chromatography has been shown to induce product aggregation for some mAbs or precipitate HCPs that are non-specifically interacting with either the product or the resin (Liu et al., 2010; Shukla and Thömmes, 2010; Shukla et al., 2007; Tarrant et al., 2012). Low pH elution can therefore result in: (i) reduced product yield; (ii) reduced column lifetime if precipitation occurs during elution; (iii) increased process costs and complexity if an additional solid-liquid separation step post-protein A chromatography is

needed; and (iv) a more challenging fluid for the chromatographic polishing steps (Kandula et al., 2009; Shukla and Thömmes, 2010; Shukla et al., 2007).

1.3.1.3. Ultra-High Protein Concentrations during UF/DF

The high mAb doses (>100 $mg.mL^{-1}$) of some blockbuster mAb therapies have turned UF/DF into a challenging unit operation considering the large volumes and ultra-high protein concentrations processed during buffer exchange. Protein aggregation can occur during pumping or during exposure to stainless steel surfaces for long periods of time. Aggregation this late into the process can have a detrimental effect and poses serious patient safety risks (Shukla and Thömmes, 2010).

1.3.2. Potential Solutions during Primary Recovery

The development of novel bioprocess technologies for both upstream and downstream unit operations has been pursued in response to: (i) the burden on the primary recovery and purification steps arising from increased cell densities and productivities (see Section 1.3.1); (ii) the need to increase production capacity; and (iii) the pressure to further reduce cost of goods (Kelley, 2009; Singh et al., 2016). Primary recovery is gaining importance in production since reduced levels of impurities and adventitious agents such as endotoxins and viruses can be achieved with thoughtful primary recovery designs (Shukla and Thömmes, 2010; Singh et al., 2016; Yigzaw et al., 2006). Reduced burden on primary recovery and purification unit operations has resulted into: (i) reduced depth filter area requirements; (ii) increased protein A resin lifetime; and (iii) less precipitates during the pH adjustment of the protein A chromatography pool (Hogwood et al., 2013b; Liu et al., 2010; Yigzaw et al., 2006). The following primary recovery technologies are being revisited as viable solutions to address the current downstream bottleneck in mAb processes.

1.3.2.1. Expanded Bed Adsorption (EBA) Chromatography

Expanded bed adsorption chromatography integrates solid-liquid separation, volume reduction and partial purification in one unit operation by capturing the product with resins of high specificity and capacity while processing crude

feedstock (Anspach et al., 1999; Shukla and Thömmes, 2010; Xu et al., 2014). For a review on the principles of EBA chromatography and its theoretical considerations the reader is referred to Anspach and co-workers (1999).

Expanded bed chromatography has been applied for the product capture and clarification of mammalian, *Escherichia coli* and yeast systems as well as cell homogenates (Anspach et al., 1999; Xu et al., 2014). However, the implementation of EBA is not without limitations (Anspach et al., 1999), i.e. the (i) requirement of a minimal bed height for efficient protein adsorption; (ii) low flow rates and long processing times can affect the feedstock quality and product stability; (iii) presence of cells and impurities adsorbing to the resin can hinder the diffusion of proteins into the beads thereby lowering protein binding capacity; (iv) dependence on the feedstock's viscosity and density values compromises chromatographic bed stability; and (v) cells or cell aggregates can foul and block the fluid distribution system. Nonetheless, improved resins and flow distribution systems have been recently introduced to allow large-scale processing and to increase process robustness (Shukla and Thömmes, 2010).

1.3.2.2. Aqueous Two-Phase Systems (ATPS)

Aqueous two-phase systems are regarded as downstream purification strategies, although they have also been used for the extraction of cells, viruses and plasmid DNA (Albertsson et al., 1970; Benavides et al., 2006; Bradley and Scott, 2004; Frerix et al., 2005; Kumar et al., 2001; Singh et al., 2016). This technology consists of two immiscible aqueous phases normally created by two polymers (e.g. polyethylene glycol (PEG) and dextran) or one polymer (e.g. PEG) and one salt (e.g. phosphates, sulfates and citrates) mixed in water (Shukla and Thömmes, 2010; Singh et al., 2016). The target product and the impurities will dissolve in one or the other liquid phase depending on the composition of the two-phase system and their own properties (Singh et al., 2016). This technology does not degrade or denature the product, and has shown to achieve 90 % product recovery as well as significantly reduce process impurities in mAb processes (Singh et al., 2016). Nonetheless, the high salt concentrations required to achieve high product yields hinder the implementation of ATPS at manufacturing scale; the high salt concentrations required at large scale can potentially shorten the life

of the equipment and precipitate the target product (Singh et al., 2016). Multi-staging the ATPS extraction process has been proposed as a solution (Singh et al., 2016).

1.3.2.3. Crystallisation

Crystallisation is the process by which a specific solute comes out of solution when approaching its supersaturation point, which can be achieved by solution cooling, solvent addition, chemical reaction, pH change or solvent evaporation (Hekmat, 2015). Crystallisation processes have been reported to be highly variable thus they need to be designed and developed on a case-by-case basis (Hekmat, 2015). They have also been described as time consuming, result in low process yields and be of particular difficulty in the context of crystallisation of full-length mAbs (Hebel et al., 2013). Although crystallisation has been proposed as an alternative primary recovery strategy, preparative crystallisation from impure protein solutions requires feed pre-conditioning methods such as precipitation or extraction to be successful (Hekmat, 2015).

1.3.2.4. Precipitation

Precipitation is an established technology in other industries (e.g. plasma protein industry). Precipitation consists in lowering the solubility of target soluble molecules (either the product or process impurities) to create solid particles that can be removed or recovered employing a solid-liquid separation step (Roush and Lu, 2008; Singh et al., 2016). Precipitation is achieved by (i) pH or conductivity changes; or (ii) adding precipitants like ethanol, PEG, polyethersulfone or capryilic acid (Lydersen et al., 1994; Shpritzer et al., 2006; Shukla and Thömmes, 2010; Singh et al., 2016; Westoby et al., 2011). Precipitation can also be achieved by polymers carrying affinity tags that respond to changes in temperature, ionic strength or pH. This technology is referred to as affinity precipitation, and the targets in this case are recombinant proteins linked to small peptides or domains (Singh et al., 2016).

Precipitation in mammalian cell mAb processes has achieved lower levels of DNA, HCPs and cellular debris, inactivated viruses and improved the filtration throughput and filter capacity of subsequent filtration steps (Brodsky et al., 2012;

Lydersen et al., 1994; Westoby et al., 2011). Nonetheless, process selectivity, scalability, robustness, costs as well as precipitant clearance need to be evaluated and guaranteed before implementing precipitation at manufacturing scale (Shukla and Thömmes, 2010; Singh et al., 2016).

1.3.2.5. Flocculation

Flocculation is extensively implemented in the waste water treatment, food, beverage and cosmetic industries (Roush and Lu, 2008; Singh et al., 2016). Flocculation has also been used in the biopharmaceutical industry for bacterial, yeast and mammalian cell processes to improve primary recovery clarification efficiency, yield and robustness as well as to reduce the impurity levels (Barany and Szepesszentgyörgyi, 2004; Cordes et al., 1990; Kim et al., 2001; Liu et al., 2010; McDonald et al., 2009; Milburn et al., 1990; Peram et al., 2010; Riske et al., 2007; Salt et al., 1995, 1996; Singh et al., 2013). When used as a primary recovery strategy in mammalian cell processes, flocculation has been shown to minimise the post-centrifugation depth filter requirements in high cell density processes (Liu et al., 2010; Low et al., 2007) and enhance the clarification throughput of subsequent filtration operations (Riske et al., 2007). A detailed description of the fundamentals of flocculation follows in Section 1.3.3.

1.3.3. The Fundamentals of Polyelectrolyte Flocculation

For the purpose of this thesis, this section only discusses the fundamentals of flocculation when charged polymers (i.e. polyelectrolytes) are used as flocculating agents or flocculants.

1.3.3.1. Flocculation Mechanisms of Action

Flocculation consists in the destabilisation of colloidal suspensions upon the addition of a flocculant; the flocculant adheres to dispersed particulates present in the suspension and generates larger-sized particles as a result (Singh et al., 2016). The flocculation process can be broken down in the following steps (see Figure 1.3) (Bratby, 1980; Gregory, 1986):

(i) *Dispersion of the flocculant in the solution*. Mixing is required to avoid local flocculant overdosage and re-stabilisation of the particles.

(ii) *Adsorption of the flocculant onto the particles*. This is a transport-limited step which relies on Brownian motion for the polymer to become progressively attached to the surface of the particles. Adsorption will occur via hydrogen bonds, electrostatic or hydrophobic interactions.

(iii) *Re-conformation of the adsorbed flocculant to give a configuration in equilibrium*. Little is known about the rate at which re-configuration is achieved, and it is questioned whether a temporary configuration is reached before the next destabilisation step.

(iv) *Collision between destabilised particles to form aggregates*. Aggregates will be formed via the 'electrostatic patch' and/or the 'bridging' mechanisms (see Figure 1.3.B and Figure 1.3.C).

(v) *Floc break-up*. The nature of the break-up process depends on the size of the flocs relative to the microscale of turbulence (see Section 1.5.2). Rupture due to fluctuating dynamic pressure will occur on flocs with a diameter larger than 100 μm.

Providing further insight into the flocculation mechanisms of action, flocculation by the 'electrostatic patch' mechanism describes the agglomeration of small particles, whose charges have been neutralised by the polyelectrolyte molecules, due to electrostatic attraction (see Figure 1.3.B) (Bratby, 1980; Roush and Lu, 2008). Flocculation by 'bridging' refers to the collision of adjacent polyelectrolyte-coated particles that result in the formation of bridges and increasingly larger flocs thereof (see Figure 1.3.C) (Bratby, 1980; Roush and Lu, 2008). Each flocculation mechanism will be favoured under certain flocculation conditions, although they are not exclusive and can happen at the same time. Electrostatic patch neutralisation will occur when strong ionic attraction between the flocculant and the particle surface exists; this situation will be given when using high charge density flocculants, and at low particle concentration and low ionic strength conditions (Bratby, 1980). The bridging mechanism will occur when using low charge density or high MW flocculants, and/or at high particle concentration and high ionic strength conditions (Bratby, 1980). The flocculation mechanism of action will determine floc strength. The bridging mechanism

generates strong flocs, yet floc disruption is irreversible when exposed to shear stress (Bratby, 1980; Singh et al., 2016). On the contrary, flocs obtained by the electrostatic patch mechanism are weaker, but re-flocculation can occur after floc breakage (Bratby, 1980; Singh et al., 2016).

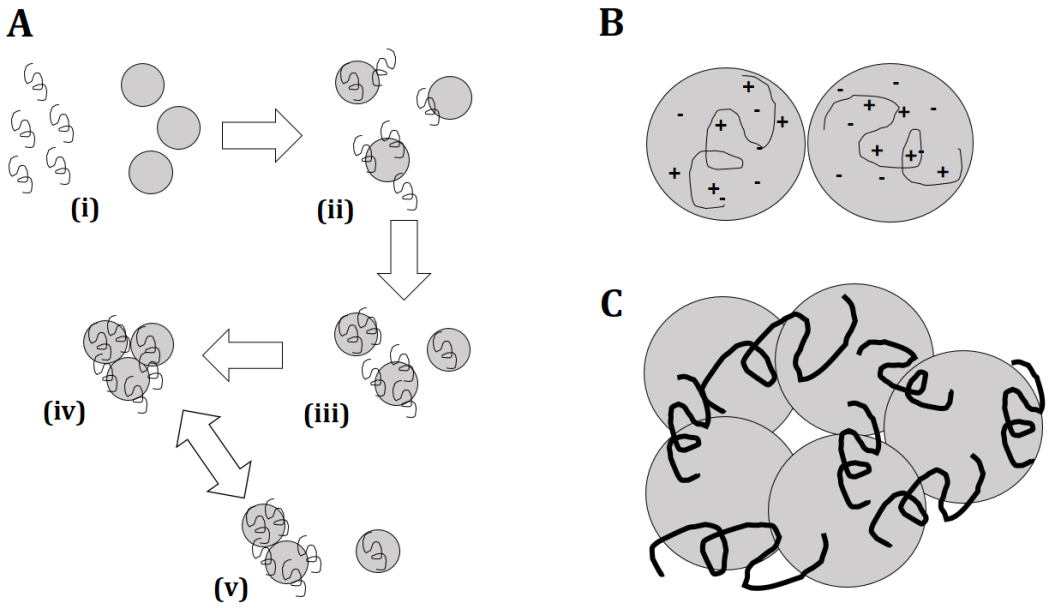

Figure 1.3. Steps during polyelectrolyte flocculation (A) and flocculation mechanisms of action (B and C).
A*. Steps describing the destabilisation of a colloidal suspension upon the addition of a flocculant. These are: (i) dispersion of the flocculant in the solution*; *(ii) adsorption of the flocculant onto the particles; (iii) re-conformation of the adsorbed flocculant to give a configuration in equilibrium*; *(iv) collision between destabilised particles to form aggregates; and (v) floc break-up.* ***B****. Flocculation by the 'electrostatic patch' mechanism.* ***C****. Flocculation by the 'bridging' mechanism. Refer to the text for a detailed description of the steps involving the destabilisation of colloidal suspensions and the flocculation mechanisms involved. Diagram adapted from Bolto and Gregory (2007).*

1.3.3.2. Flocculation Kinetics

The collision between destabilised particles leading to the formation of flocs is a two-stage process. Perikinetic and orthokinetic flocculation (first and second stage, respectively) are governed by the forces whereby the particles come together and agglomerate, which in turn are determined by the size of the flocs (Bratby, 1980). Table 1.1 summarises the key aspects of perikinetic and orthokinetic flocculation.

Mathematical models describing both perikinetic and orthokinetic flocculation can be found in Bratby (1980). An in-depth review of these mathematical models is out of the scope of this thesis thus an overview of these follows. Von Smoluchoswski proposed a mathematical model describing perikinetic flocculation for spherical particles diffusing in a radial direction that has not been further developed. Contrary, many different models have been proposed for orthokinetic flocculation. From the first orthokinetic models, which assumed laminar flow conditions, others have been developed to account for turbulent regimes, floc break-up and the random motion of the flocculated particles (Bratby, 1980).

Table 1.1. Key aspects of perikinetic and orthokinetic flocculation.
Summary from Bratby (1980).

	Driving force	Step	Performance variables
Perikinetic flocculation	Brownian motion/ Thermal agitation	Immediately after destabilisation of the colloidal suspension	Particle diameter (diameter < 1 μm)
Orthokinetic flocculation	Induced velocity gradients in the liquid (i.e. liquid mixing)	After perikinetic flocculation is completed	Fluid velocity gradients Flocculation time

1.3.3.3. Types of Flocculant

Flocculants can be classified as cationic, anionic or multimodal (see Table 1.2). The choice of flocculant will be dictated by the charge of the target molecules, which will in turn depend upon the pH of the solution and the pI of the target molecules (Singh et al., 2016).

1.3.3.3.1. Cationic Flocculants

Poly-diallyldimethylammonium chloride (pDADMAC) is a water-soluble quaternary ammonium polymer that has been used to flocculate cell culture fluids in order to provide a clarification alternative to centrifugation in high cell density cell culture harvests (McNerney et al., 2015; Singh et al., 2016; Tomic et al., 2015).

The group of polyamines consists of polymers with multiple amine functional groups that are protonated (i.e. positively charged) over a wide pH range due to the basic nature of the amine groups (Singh et al., 2016). This group of cationic polymers includes polyethylenimine (PEI), polyvinylamine, poly-N-methylvinylamine and polyallylamine (Singh et al., 2016). Polyamines have been used in the flocculation of yeast (Cordes et al., 1990; Milburn et al., 1990; Salt et al., 1995, 1996), bacterial (Barany and Szepesszentgyörgyi, 2004; Salt et al., 1995) and mammalian cell processes (Ma et al., 2010; Peram et al., 2010).

Polyaminoacids have been employed in mammalian cell culture processes to flocculate clarified and non-clarified cell culture broths. Flocculation with polyaminoacids (e.g. polyarginine and polylysine) has been assessed as a replacement for one or more chromatographic steps (Peram et al., 2010).

Chitosan is a linear polymer of beta-(1-4) linked D-glucosamine monomers generated by the chemical deacetylation of chitin, which is typically obtained from arthropod shells (Liu et al., 2010). Chitosan is a promising flocculant since it is inexpensively produced from non-mammalian sources and can be currently obtained with high purity and low monomer levels (Liu et al., 2010). Nonetheless, potential allergies from patients to arthropods (i.e. shellfish) is a concern. Chitosan has been used to flocculate yeast (Liu et al., 2010), bacterial (Barany and Szepesszentgyörgyi, 2004; Strand et al., 2003) and mammalian cell feed streams (Riske et al., 2007).

1.3.3.3.2. Anionic Flocculants

Anionic polyelectrolytes were used by McDonald et al. (2009) to selectively flocculate mAbs from CHO cell harvests with the aim to replace the capture and intermediate chromatographic steps during downstream purification. This study showed the limited application of anionic flocculants with high titre and high conductivity CHO cell broths; feed dilution was required to selectively flocculate the mAb.

Table 1.2. Characteristics of polyelectrolyte flocculants used in biopharmaceutical processes.

Summary from Felo et al. (2015), Liu et al. (2010), *Roush and Lu* (2008), *and Singh et al.* (2016).

Flocculant type	Flocculant examples	Flocculant charge	Mode of action	Target molecules	Technical challenges
Cationic	Polyamines (PEI, pDADMAC, etc.) Polyaminoacids Polyacrylamides Chitosan	Positive	Electrostatic interactions	Negatively charged compounds Process impurities	Scalability Variability Toxicology concerns
Anionic	Polymethacrylic acid Polyacrylic acid Carboxymethylcellulose Polyvinylsulfonate Polyacrylamidomethyl Propane sulfonate	Negative	Electrostatic & Hydrophobic interactions Hydrogen bonds	Positively charged compounds Product	Product stability Toxicology concerns
Multimodal	AMPS-ABZ copolymer Modified benzyl poly(allylamine)	Smart polymer responding to changes in the solution	Electrostatic & Hydrophobic interactions Hydrogen bonds	Product	Product stability Toxicology concerns

1.3.3.3.3. Multimodal Ionic Flocculants

Multimodal ionic flocculants respond to the limitations of cationic and ionic flocculants with regards to: feed dilution before flocculant addition, difficulty re-dissolving the flocs after anionic flocculation, excess residual polymer and operating at very specific flocculation conditions. Multimodal ionic flocculants can successfully flocculate over wide pH and conductivity ranges. They also easily re-dissolve after floc formation as they come out of solution upon changing the environmental conditions (e.g. presence of multivalent ions) (Kang et al., 2013; Singh et al., 2016).

1.3.3.4. Flocculation Process Variables

Flocculation performance has been reported to depend upon a large number of physico-chemical variables that relate to the characteristics of both the flocculant and the fluid being flocculated. Therefore, careful consideration should be given to optimise the flocculation step in order to yield a process with high product recovery and maximum impurity removal. The flocculation variables described to significantly impact process performance and robustness are the following (Bratby, 1980; Kim et al., 2001; Salt et al., 1995; Singh et al., 2016):

(i) Flocculant physico-chemical characteristics: MW, charge in reference to the particle's surface charge, charge density, rigidity, linear or branched.

(ii) Flocculant concentration.

(iii) Mode of flocculant addition.

(iv) Hydrophobic-hydrophilic balance within the floc.

(vi) Fluid characteristics: nature and amount of insoluble particulates, pH, ionic strength, properties of the target molecules.

(vii) Mixing regime or shear stress encountered in the flocculation vessel.

(viii) Duration of flocculation.

1.3.3.5. Evaluation of Flocculation Performance

The first approach towards evaluating flocculation performance is analysing product yield and impurity removal (Cordes et al., 1990; Milburn et al., 1990; Peram et al., 2010). Floc diameter is also a key parameter, as particle size will significantly impact upon the performance of the subsequent centrifugation and/or filtration steps (Kim et al., 2001; Riske et al., 2007; Shpritzer et al., 2006). Floc strength is another important factor, particularly when the flocs are processed via centrifugation, due to the shear forces encountered in the centrifuge feed zone (Riske et al., 2007; Shpritzer et al., 2006). Finally, the amount of residual flocculant must be quantified to ensure the flocculating agents are removed to acceptable levels in the final drug product (Liu et al., 2010).

Different methods exist to evaluate product yield and impurity removal. These range from commercially available kits to analytical techniques developed in-house; the preference will vary from manufacturer to manufacturer. Floc diameter can be determined via light scattering measurements (Kim et al., 2001; Salt et al., 1996; Strand et al., 2003) or using the Coulter counter device (Cordes et al., 1990). Nonetheless, optical density and turbidity measurements (Bonnerjea et al., 1988; Kim et al., 2001; Milburn et al., 1990; Peram et al., 2010; Riske et al., 2007; Salt et al., 1995, 1996; Strand et al., 2003), zeta potential measurements (Cordes et al., 1990; Salt et al., 1996; Strand et al., 2003; Treweek et al., 1979), sedimentation velocity measurements under gravitational or centrifugal forces (Bratby, 1980) and filtration rate measurements (Kim et al., 2001) are other widespread techniques used to empirically evaluate flocculation performance. With regards to floc strength, macroscopic and microscopic methodologies can be applied (Jarvis et al., 2005). Bell and Dunnill (1982a, 1982b) exemplify the use of macroscopic methodologies to study floc strength: evaluating the average velocity gradient to which particles are exposed inside the flocculation vessel. Finally, residual flocculant concentration in the process feed can be measured with the following techniques: spectrophotometry (Treweek et al., 1979), zeta potential measurements (Barany and Szepesszentgyörgyi, 2004), surface plasmon resonance spectroscopy, quantitative polymerase chain

reaction, high performance liquid chromatography, enzyme-linked immunosorbent assay and fluorescent tags (Singh et al., 2016).

1.3.3.6. Dosage Curves in Polyelectrolyte Flocculation

Flocculant dosage curves are generated by plotting increasing flocculant concentrations against the residual turbidity (or spectrophotometric absorbance at λ nm) in the supernatant liquid after a given settling period (Hughes et al., 1990; Roussy et al., 2005; Tenney et al., 1969). Flocculation performance in flocculant dosage curves can also be expressed by filtration rate of the flocs (Adin and Rebhun, 1974; Slater and Kitchener, 1966), chemical oxygen demand reduction and colour removal in wastewater treatment experiments (Guibal and Roussy, 2007; Lee et al., 2011; Tenney and Stumm, 1965) or number of cells left in the supernatant (Busch and Stumm, 1968; Strand et al., 2001). However, supernatant turbidity and absorbance measurements are regarded as simpler and quicker approaches that result in equivalent information (Busch and Stumm, 1968; Slater and Kitchener, 1966).

Figure 1.4 shows an example of a flocculant dosage curve. When flocculant concentration is less than optimum, insufficient bridging to withstand the shearing forces imposed by the mixing conditions will occur and no flocs will be formed ('No flocculation' region in Figure 1.4). Flocculation will commence when enough flocculant is added to bring neighbouring solid particles together and form aggregates ('Gradual flocculation' region in Figure 1.4). Furthermore, no significant amounts of flocculant will be detected in the supernatant in this region since all flocculant added is adsorbed to the solid particles. Optimal flocculant dose corresponds to that where supernatant turbidity is at its minimum ('Optimal' in Figure 1.4). A complete reduction in medium turbidity will never be achieved, and the optimum flocculant dose will be that at wich an increase in dose results in an insignificant improvement of supernatant turbidity. Finally, at flocculant concentrations larger than the optimum flocculant dose, re-stabilisation of the solid particles takes place ('Re-stabilisation' in Figure 1.4). When the surface of the solid particles become covered with flocculant, they start to repel each other because of electrostatic or static hinderance, or both. At this point, excess flocculant will be detected in the supernatant (Busch and Stumm,

1968; Hughes et al., 1990; Qian et al., 2004; Strand et al., 2003; Tenney and Stumm, 1965; Tenney et al., 1969).

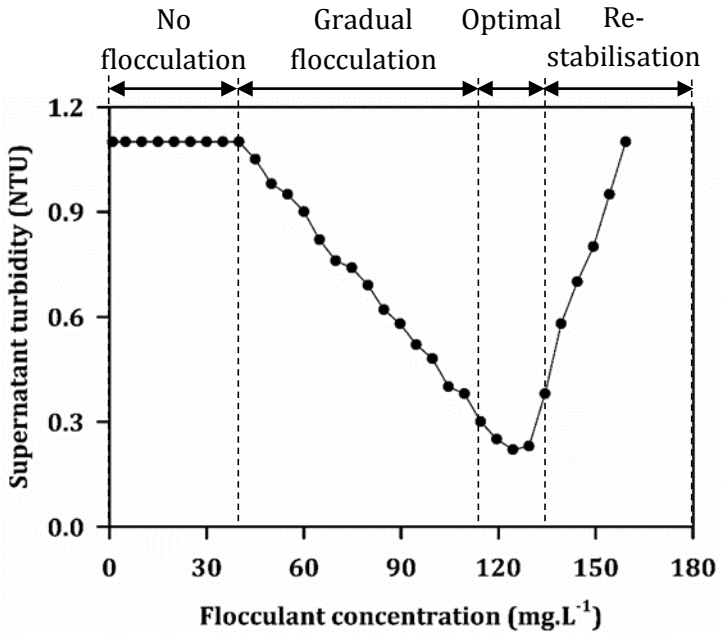

Figure 1.4. Example of flocculant dosage curve in polyelectrolyte flocculation.

Flocculant dosage curves are employed to investigate the optimal flocculant concentration for a given test condition (Gasner and Wang, 1970; Guibal and Roussy, 2007; Lee et al., 2011). However, they can also be plotted for various test conditions to evaluate the effect of the following parameters on flocculation performance: pH, ionic strength, viscosity and composition of the medium, solids concentration, concentration and age of the flocculant stock solution, mode of flocculant addition, type of flocculant and its molecular weight (Barany and Szepesszentgyörgyi, 2004; Hughes et al., 1990; Owen et al., 2002; Qian et al., 2004; Roussy et al., 2005; Strand et al., 2003; Sukenik et al., 1988; Tenney et al., 1969). The information obtained not only helps select the right flocculant dosage for a given set of conditions but also sheds some light into the governing flocculation mechanisms (Gasner and Wang, 1970; Narkis and Rebhun, 1983; Roussy et al., 2005; Strand et al., 2003). For instance, very sharp optimum flocculant dosage curves when using strong cationic or anionic polyelectrolytes indicate flocculation via the bridging mechanism (see Section 1.3.3.1) (Gasner and Wang, 1970). In contrast, the electrostatic patch flocculation mechanism (see

Section 1.3.3.1) generates curves where the slope of the re-stabilisation region (see Figure 1.4) is much steeper than that of the charge neutralisation segment ('Gradual flocculation' in Figure 1.4) (Guibal and Roussy, 2007).

1.3.4. Considerations for Implementing Flocculation at Manufacturing Scale

The cytoxicity of residual monomers and additives present in commercially available flocculants converts them into critical process variables during the selection of flocculating agents. Biopharmaceutical grade flocculants, which guarantee limited polymer variability to comply with the requirements of current good manufacturing practices (CGMPs), exist but are few in number. Therefore, a judicious risk analysis with regards to the cytotoxicity of the flocculants used must be conducted considering most approved mAbs are administered via the parenteral route. In addition to this, effective flocculant clearance to an acceptable residual level in the final drug product must be demonstrated (Aunins and Wang, 1989; Singh et al., 2016; Thömmes and Etzel, 2007). The methodologies used for the detection of residual quantities of polymer in the process feed are listed in Section 1.3.3.

Finally, other important factors to be considered before the implementation of flocculation at manufacturing scale are: (i) the effect that the flocculant chosen has upon the product quality attributes and the lifetime of the chromatographic resins; and (ii) the scalability of this unit operation from laboratory to pilot and manufacturing scale (Singh et al., 2016).

1.4. Scale-Down Technologies for the Study of Primary Recovery

The initial scale-down studies aimed at modelling process performance using traditional engineering principles. The first scale-down studies were pilot-scale models that reduced the amount of material required down to the litre scale. Smaller scale-down models were further developed, ultimately leading to the creation of ultra scale-down (USD) devices. Ultra scale-down models work within

the millilitre scale and they are used to determine the key dominating effects during scale-up of bioprocesses (Tait et al., 2009; Titchener-Hooker et al., 2008).

1.4.1. Centrifugation

1.4.1.1. Small Scale Centrifugation Mimics

The first attempts to scale down centrifugation were pursued by Mannweiler and Hoare (1992). In their initial approach they reduced the centrifuge separation area by removing some of the separation discs of a small disc stack centrifuge. Nonetheless, the amount of material required to operate the centrifuge was not significantly reduced since the centrifuge solids holding space remained unchanged. Subsequently, the next attempt by Maybury et al. (1998) consisted in decreasing both the centrifuge separation area and volume process material requirements by placing different solid inserts inside the centrifuge bowl.

The development towards the USD centrifugation approach started with protein precipitation scale-down studies (Boychyn et al., 2000). Based upon the use of Sigma theory (see Section 1.4.1.2), the authors mimicked the clarification performance of a multichamber bowl industrial-scale centrifuge with a bench-top centrifuge. However, the extent of solids removal was over-predicted by 50 % because the shear stress encountered in the feed zone of the continuous flow centrifuge used was not accounted for. The USD centrifugation model was further optimised including the Sigma value (seeSection 1.4.1.2) and the contributory effect that the acceleration and deceleration stages have upon centrifugation performance (Maybury et al., 2000).

Following these USD centrifugation studies, Boychyn et al. (2001) used the high-speed shearing device first described by Levy et al. (1999) to reproduce the energy dissipation rates encountered in the feed zone of a multichamber centrifuge. The performance of a large-scale multichamber centrifuge was mimicked by first pre-shearing the feed with the high-speed shearing device described and then using a bench-top centrifuge. The shear forces encountered in the feed zones of other large-scale continuous centrifuges were subsequently investigated (Boychyn et al., 2003). The USD centrifugation model has been verified with *Saccharomyces cerevisiae* (Boychyn et al., 2003; Tustian et al., 2007),

Escherichia coli (Berrill et al., 2008; Chatel et al., 2014; Tustian et al., 2007) and mammalian (Hutchinson et al., 2006; Lau et al., 2013) cell suspensions.

Centrifugation was further scaled down to 96-well plates, thus allowing the study of centrifugation in a high-throughput mode (Tait et al., 2009). The methodology consisted in using a 96-well plate filled with different volumes of pre-sheared bioprocessing material to obtain varying equivalent flow rates on a single microplate. Centrifugation performance was predicted within a ±10 % error margin when compared to the previous bench-top USD centrifugation methodology.

1.4.1.2. Sigma Theory

Sigma theory was first described by Ambler (1959). This theory allows describing centrifugation performance in terms of separation area independently of the process parameters. It is out of the scope of this thesis to include the derivation of Sigma theory, for which the reader is referred to Ambler (1959).

The Sigma theory is based on Stokes' law, which describes the drag force exerted on a small spherical particle suspended in a viscous fluid. Considering that (i) the speed of a small spherical particle suspended in a viscous fluid and under a gravitational field (v_g, $m.s^{-1}$) will be constant under identical process conditions independently of the size and geometry of the centrifuge; and that (ii) two times v_g is equal to the ratio of volumetric flow rate (Q, $m^3.s^{-1}$) to equivalent settling area ($\sum$, m^2), it is possible to compare different centrifuges with gravity settling systems on the basis that (Ambler, 1959; Maybury et al., 2000):

$$\left(\frac{V}{t\sum c}\right)_{lab} = \left(\frac{Q}{\sum c}\right)_{ds} = \left(\frac{Q}{\sum c}\right)_{tub} = \cdots \qquad \text{(Equation 1.1)}$$

where V_{lab} is the volume of material in a centrifugal tube for a bench-top centrifuge (m^3), t_{lab} is the centrifugation time of a batch centrifuge (s), $\sum$ is the equivalent settling area of the centrifuge (m^2), c is the correction factor to account for the deviation from the ideal flow patterns used to define particle dynamics in the centrifuge (Maybury et al., 2000), Q is the volumetric flow rate to the centrifuge ($m^3.s^{-1}$), and the suffixes refer to different centrifuge geometries (*lab*

is bench-top centrifuge, *ds* is disc stack centrifuge and *tub* is tubular bowl centrifuge). The value of $\sum$ is specific to the centrifuge geometry used and to the centrifugation conditions at which it is operated. The equations for the calculation of the $\sum$ value of widely used centrifuge designs can be found in Ambler (1959) and Maybury et al. (2000). The values of c are also specific to each centrifuge design, and while it is generally accepted that the correction factor for a bench-top centrifuge is equal to 1, different c values have been reported for the same large-scale centrifuge design (Boychyn et al., 2003; Maybury et al., 2000).

1.4.2. Normal Flow Filtration (NFF)

Normal flow filtration, also referred to as dead-end filtration, is the filtration mode where the direction of fluid flow is perpendicular to the filter; NFF differs from tangential flow filtration (TFF) in that fluid flows parallel to the filter in the latter. In addition to the direction of the fluid flow, filtration can also be classified in constant pressure or constant flux rate depending upon the driving force used. Constant pressure filtration can be further divided into positive and negative pressure filtration (van Reis and Zydney, 2007).

1.4.2.1. Membrane Filtration vs. Depth Filtration

In bioprocesses membrane filtration is used for pressure-driven separations such as microfiltration, virus filtration and ultrafiltration (van Reis and Zydney, 2007). Membrane pore size varies depending upon its application; microfiltration (pore size 0.05 – 10 μm) uses membrane filtration to retain cells and cell debris thus allowing proteins and smaller solutes into the filtrate, virus filtration (pore size 20 – 70 nm) uses membrane filtration to retain viruses, and ultrafiltration (pore size 1 - 20 nm) uses membrane filtration to retain proteins and other macromolecules (van Reis and Zydney, 2007). Microfiltration is the only membrane filtration step applied during primary recovery, and it is usually operated in TFF mode to minimise membrane fouling and increase product yield and throughput (Liu et al., 2010). Membrane filters can generate a particle-free harvest solution that requires no secondary clarification before capture chromatography if a 0.2 μm-rated membrane is used (van Reis and Zydney, 2001). However, the trend towards high cell density cell cultures limits the

implementation of membrane filtration processes during primary recovery (van Reis and Zydney, 2001).

Depth filtration operates in NFF mode and uses porous filter material to retain particles inside the tortous filter matrix (see Figure 1.5) rather than just on the filter surface (van Reis and Zydney, 2007; Shukla and Kandula, 2009). This mechanism allows for the retention of more particles than surface retention can achieve (Shukla and Kandula, 2009). Consequently, depth filtration is used when the feedstream contains high particle loads (i.e. during primary recovery operations, though not exclusively) (Liu et al., 2010; Shukla and Kandula, 2009). The depth filters used in the biopharmaceutical industry cover pore size ranges from <0.1 to 15 μm. However, the rise of commercially available multi-layer depth filters has extended particle size retention up to 100 μm by layering multiple depth filter sheets of different pore size ranges (Singh et al., 2016). Multi-layer depth filters retain large particles inside the filter matrix as opposed to on the filter surface, which normally results in fast fouling rates as the result of cake layer formation (Singh et al., 2016). Furthermore, more compacted depth filtration processes are obtained with multi-layer depth filters. Depth filters are typically composed of cellulose or polypropylene fibers, a porous filter aid such as diatomaceous earth to increase the surface area, and a binder (Liu et al., 2010; Shukla and Kandula, 2009; Shukla et al., 2007; Singh et al., 2016). The binder can be charged to confer the depth filter media a positive charge; otherwise, an additional charged polymer may be added (Liu et al., 2010; Shukla and Kandula, 2009). Therefore, the structure and composition of depth filters allow solids removal to be accomplished via both adsorptive (i.e. hydrophobic, electrostatic and multi-modal interactions) and size exclusion-sieving mechanisms (Liu et al., 2010; van Reis and Zydney, 2007; Singh et al., 2016; Yigzaw et al., 2006). Finally, depth filters can incorporate a filter membrane with an absolute pore size at the bottom-most layer to protect the subsequent guard filter (Shukla and Kandula, 2009).

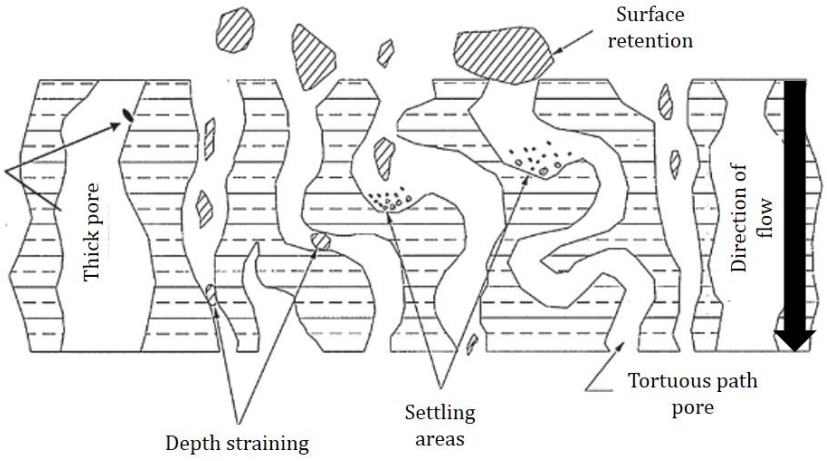

Figure 1.5. Schematic representation of the cross-section area and particle retention in a depth filter.
A single depth filter layer is approximately 2-4 mm thick and is defined by its nominal pore rating and charge (Liu et al., 2010). The figure shown describes the different modes by which particles are removed via depth filtration. While small particles are retained within the filter matrix via size-based retention mechanisms and/or adsorptive mechanisms, particles larger than the porous opening are retained on the filter surface. Figure adapted from Shukla and Kandula (2009).

1.4.2.2. Small Scale Filtration Mimics

Early scale-down filtration studies investigated ultrafiltration of protein solutions to assess the effect of membrane polarisation (Porter, 1972), pH and ionic strength (Fane et al., 1983) on filtration performance. Commercially available laboratory-scale filters have since been developed; these enable the study of different types of membranes, depth filters and operational variables. Despite all this progress, the feed volume requirements of laboratory-scale filters limit the number of studies that can be performed during early process development. To counteract these limitations, scale-down and ultra scale-down NFF systems have been developed in the past two decades (see Table 1.3). Reynolds (2003) described a modified Nutsche filter (i.e. a laboratory batch filtration vessel) with an active filtration area of 10 cm^2 that was used to mimic the continuous filtration performance of a production-scale rotary vertical leaf filter of 24 m^2. Different commercially available small-scale and high-throughput membrane filtration devices were investigated by Chandler and Zydney (2004) (see Table 1.3). The authors concluded that while 96-well filtration plates could be used for scalability purposes, care must be taken: (i) when scaling filtration

results from small systems employing flat sheet membranes to larger-scale systems with more complex patterns, such as pleated membranes; and (ii) to ensure the membrane resistance values of the small-scale systems are consistent with these of the larger filtration systems. Vandezande et al. (2005) published another attempt to scale down NFF filtration. In this case the authors successfully scaled down a nanofiltration step (i.e. membrane filtration) from 12.6 to 4.52 cm^2 using a custom-made NFF device (see Table 1.3). A significant improvement was achieved by Jackson et al. (2006) with the automation of 96-well filter plate experiments. The authors also presented two custom-made filtration systems of 8 and 24 wells that could be automated. The custom-made filtration systems showed: (i) good scalability results with a conventional laboratory-scale membrane cell (3.8 cm^2); (ii) reduced errors associated with 96-well filter plates; and (iii) that simultaneous evaluation of different filter types was possible. Furthermore, automation enabled time-point measurements of the permeate. The active filtration area of Jackson's et al. (2006) custom-made 8-well filtration module was further reduced to 0.28 cm^2 by Kong et al. (2010) (see Table 1.3), which was used along with the automated platform for the study of plasmid DNA sterile filtration. The scalability of this 0.28 cm^2 filter module has been confirmed in membrane filtration experiments (Kong et al., 2010), and in depth filtration studies using mammalian cell culture broths (Hogwood et al., 2013b; Lau et al., 2013).

Table 1.3. Normal flow filtration scale-down methods.

Scale-down system	Filtration mode	Feed volume	Active filtration area
Modified laboratory Nutsche filter (Reynolds et al., 2003)	Continuous, constant flux or constant pressure	Not specified	10 cm^2
96-well filter plate and Syringe filters (Chandler and Zydney, 2004)	Batch, constant positive pressure	Not specified	0.28 cm^2 (96-well plate) 2.7, 3.6, 4.3 cm^2 (syringe filters)
Custom-made filtration module with 16 separate stirred cells (Vandezande et al., 2005)	Batch, constant positive pressure	25 mL	4.5 cm^2
Automated 96-well filter plate and Custom-made 8 & 24-well filter module (Jackson et al., 2006)	Batch, constant negative pressure	0.30 mL (96-well) 0.83 mL (8-well) 2.5 mL (24-well)	0.28 cm^2 (96-well) 0.79 cm^2 (8 & 24-well)
Automated custom-made 8-well filter module (Hogwood et al., 2013b; Kong et al., 2010; Lau et al., 2013)	Batch, constant negative pressure	5 mL	0.28 cm^2

1.4.2.3. Normal Flow Filtration Performance Analysis

During filtration process development, NFF performance is judged on two mechanical performance criteria (capacity and retention) and the quality of the filter effluent. Capacity is defined as the volume of fluid that can be processed per filter unit area before a maximum differential pressure is reached; capacity is generally expressed in litres per square meter ($L.m^{-2}$). Capacity measurements can be acquired in constant flux rate or constant pressure filtration mode; in the former filter capacity will correspond to a maximum pressure limit, and in the latter filter capacity will correspond to a maximum flux limit. However, filtration end-point can occur before the established pressure or flux limits in the event of

solids breakthrough (i.e. abrupt increase in filtrate turbidity). Filter retention is traditionally determined by the trailing sterilising-grade filter (typically 0.22 μm pore size), and corresponds to this last filter's filtration capacity when operated in constant flux rate mode. Finally, filtrate quality is assessed by measuring (i) filtrate turbidity or optical density to evaluate solids content; and (ii) impurities (i.e. DNA, HCPs, etc.) and product yield (van Reis and Zydney, 2007; Yavorsky et al., 2003).

Capacity measurements acquired in constant pressure filtration mode allow for a variable flux rate over time. As a consequence, filter capacity predictions might be underestimated; the high initial flux rates that can occur under contant pressure filtration can inefficiently load the filter and cause premature filter clogging as a result. Therefore, constant flux filtration capacity measurements are recommended for a more accurate filtration performance profile (Yavorsky et al., 2003).

Filter capacity values, obtained either in contant pressure or contant flux rate mode, are used for filter sizing purposes and to evaluate the filter fouling mechanism. Filter sizing methods include the flow decay method, V_{max} analysis and P_{max} analysis. The flow decay method, which consists in measuring the cumulative filtrate volume until flux rate drops to 10-20 % its initial value, requires large volumes of process fluid. In contrast, in the V_{max} and P_{max} analyses data is obtained over a short period of time; filtration is performed at constant pressure and constant flux mode, respectively. The V_{max} and P_{max} data is later extrapolated to longer filtration times to calculate the maximum fluid volume the filter can process; the linearised form of the corresponding filtration fouling model is used for this purpose (van Reis et al., 1991; Yavorsky et al., 2003).

Filter fouling can occur on the filter surface by pore blockage or cake layer formation, as well as within the filter porous structure (see Figure 1.5 and Figure 1.6). Filter fouling causes a decay in flux rate during constant pressure operation and increases pressure drop during constant flux operation. Four classical filtration fouling models exist for Newtonian solid-liquid suspensions. These models are standard pore blockage, intermediate pore blockage, pore constriction, and cake filtration (see Figure 1.6). Each filter fouling model is

described by a mathematical equation specific to each filtration mode (i.e. constant flux and constant pressure). These models assume that: (i) there is no back-transport or detachment; and (ii) all filter pores are of equal diameter and length and are parallel one another. Each filtration fouling model has a linearised form of the equation, which is used during data analysis and model indentification (van Reis and Zydney, 2007).

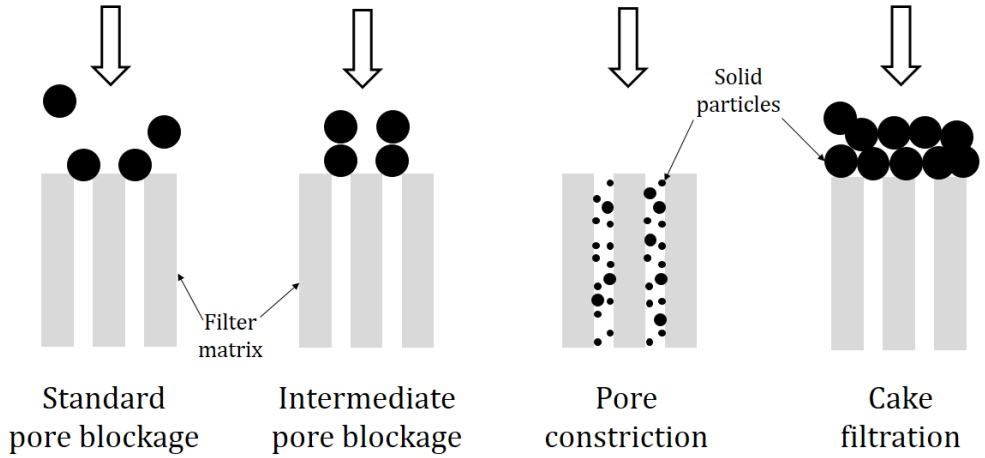

Figure 1.6. Schematic representation of the four classic filter fouling mechanisms.
Standard pore blockage assumes the fouling particles completely obstruct the filter pores without the superimposition of other particles; this model is typically observed when the fouling particles are larger than the filter pore size. Intermediate pore blockage occurs when the filter pores are obstructed by the foulant, although this model allows for particle superimposition on the filter surface. Pore constriction occurs when the foulant leads to a reduction in the effective filter pore size due to the deposition of fouling particles along the walls of the filter pores; the pore column volume will decrease as filtration progresses until complete pore blockage. Cake filtration is the result of fouling particles depositing on the filter surface; the cake layer provides additional resistance to fluid flow, which increases as filtration progresses (Iritani, 2013; van Reis and Zydney, 2007).

1.4.3. Flocculation

Few small-scale flocculation studies have been carried out to date. Some of the flocculation studies published in the literature have used laboratory-scale working volumes, e.g. 8 mL (Strand et al., 2003) and 15 mL (Bonnerjea et al., 1988; Milburn et al., 1990). However, none of the flocculation work published has aimed at developing a small-scale mimic of larger scale flocculation processes. The closest study to this approach was that of Berrill and co-workers (2008), in

which the authors investigated, at laboratory-scale (~100 mL), the interactions between flocculation and centrifugation in order to develop a flocculation step that enhanced subsequent centrifugation performance.

1.5. Mixing for Microscale Process Development

1.5.1. Mixing in Microplates

The use of microplates in process development studies requires a detailed understanding of the hydrodynamic phenomena taking place inside the wells (Micheletti and Lye, 2006). Several publications on fluid dynamics (Weiss et al., 2002; Zhang et al., 2008) and gas-liquid mass transfer (Barrett et al., 2010; Doig et al., 2005; Hermann et al., 2003) in microtitre plates can be found in the literature. This subsection describes the effect that the mixing method and well geometry have upon the fluid dynamics inside microplate wells.

1.5.1.1. Mixing Methods in Microplates

1.5.1.1.1. Orbital Shaking

Orbital shaking is described as "the simplest and most efficient way of promoting liquid mixing when considering multiple wells or plates" (Micheletti and Lye, 2006). Orbital mixing has been the mixing method of choice for several microscale process development (Barrett et al., 2010; Hermann et al., 2003; Lye et al., 2003) and gas-liquid mass transfer (Doig et al., 2005; Lye et al., 2003) investigations. Many authors (Barrett et al., 2010; Duetz and Witholt, 2001; Weiss et al., 2002; Zhang et al., 2008) have used the mixing model developed by Büchs et al. (2001) to describe fluid motion in orbitally shaken microwells. Büchs' mixing model describes orbitally shaken systems as a fluid being 'in-phase' (fluid follows the rotating movement of the shaker) or 'out-of-phase' (fluid does not follow the rotating movement of the shaker). Reynolds number is also commonly used to describe fluid motion in microwells (Micheletti and Lye, 2006).

Fluid motion in orbitally shaken microplates has been shown to be influenced by: (i) the shaking frequency and amplitude of the orbit; (ii) the diameter and geometry of the microwell; (iii) the liquid fill volume; and (iv) the properties of

the fluid, such as density and viscosity (Barrett et al., 2010; Doig et al., 2005). Orbital frequency and amplitude have been shown to greatly impact upon the gas-liquid mass transfer rates in microplates (Duetz and Witholt, 2001; Hermann et al., 2003). However, fluid motion in microwells has been shown to be more strongly dependent on the orbital amplitude than on frequency (Zhang et al., 2008).

1.5.1.1.2. Jet Mixing

In this case fluid motion is created by the liquid flow originated when liquid is added into a well. If liquid addition into a well is performed in a single jet, mixing solely occurs during the lifespan of the jet. Thereby, it is common to repeat this operation more than once to achieve a homogeneous solution inside the well. Jet mixing performance has been shown to depend upon the following variables: (i) jet nozzle position; (ii) relative size of the well/vessel to the jet flow; (iii) volumetric flow rate at which the liquid is added; (iv) liquid volume added; and (v) the shape of the well (Nealon et al., 2006).

1.5.1.1.3. Magnetic Mixers

Magnetic stirrers have been long used at laboratory-scale to mix solutions. Different magnetic stirrer designs fit for mixing in microwells are currently commercially available (e.g. V&P Scientific Inc., CA, USA), although no studies have been performed to date on characterising fluid motion in magnetically mixed microwells.

1.5.1.1.4. Other Methods

Surface acoustic waves (Beckman Coulter Life Sciences, IN, USA) and adaptative focused acoustics (Covaris Inc., MA, USA) are two commercially-available mixing technologies that can be applied during high-throughput screening in microwells. Both technologies resort to the use of acoustic energy to develop a non-contact mixing methodology that accelerates mass transport-limited diffusion processes at the micro- and nanolitre scale. Other commercially-available mixing systems rely on sonication (e.g. SonicMan™, Brooks Automation Inc., MA, USA), although

the generation of heat and the typically-large dimensions of these mixing systems have hindered their widespread implementation.

1.5.1.2. Impact of Microwell Geometry on Mixing

Zhang and co-authors (2008) studied orbital mixing in microwells with two different commercially-available microplate configurations (96- and 24-well microplates). Their studies using computational fluid dynamics (CFD) showed that the fluid velocity profiles in each microplate geometry was different. This difference stemmed from an axial component to the fluid velocity (in addition to the radial fluid motion) present in the 96-well but not in the 24-well microplates that resulted in a greater mixing performance. The authors' CFD results were confirmed by measurements of power consumption and energy dissipation rate values indicating considerably greater energy dissipation rates in the 96-well microplate. However, these findings cannot be extrapolated to all microplate systems given that power consumption and energy dissipation rate estimations strongly depend upon the size of the microwell, the fill volume and the frequency and amplitude in orbitally shaken systems (Zhang et al., 2008).

The shape of the microwell itself has also been found to impact upon the fluid dynamics. Nealon et al. (2006) studied the effect that different well dimensions had on macromixing time (see Section 1.5.3) when employing the jet mixing method (see Section 1.5.1.1.2). Macromixing time differed up to one order of magnitude. Furthermore, the liquid volume required to ensure complete macromixing was also subject to the dimensions of the microwell. Nealon et al. (2006) also suggested that using microwells with a V-shaped bottom could result in decreased macromixing times and increased mixing efficiency. Finally, Hermann et al. (2003) showed that square-shaped microwells acted as baffles inside the well, which resulted in increased turbulence and gas-liquid transfer rates.

1.5.2. Turbulent Mixing and Scale-Up Correlations in Stirred Tank Reactors (STRs)

Turbulence is a flow regime characterised by fluid moving erratically in the form of cross-currents. Turbulent flow then contrasts with laminar flow, where fluid flow is characteristically streamlined (Doran, 1995).

1.5.2.1. Kolmogorov's Theory of Isotropic Turbulence

Kolmogorov's theory of isotropic turbulence has been extensively and successfully used to describe turbulent flows in stirred tanks, which are described by the values of energy dissipation rate per unit mass of fluid (ε, $W.kg^{-1}$). This theory is only valid at high turbulent conditions, i.e. high Reynolds numbers (Kawase and Moo-Young, 1990).

The kinetic energy contained in a turbulent fluid is directed into rotational flows called eddies. Eddies of different sizes co-exist inside the reactor for as long as turbulence lasts. The largest eddies (i.e. primary eddies) have a length scale of similar magnitude to that of the main flow stream, and in a stirred vessel they are produced by mechanical and/or pneumatic agitation. Primary eddies are anisotropic as well as unstable, and disintegrate into smaller eddies of intermediate size. Eventually, the intermediate eddies break up into smaller eddies that will in turn break up into smaller ones until the smallest size of isotropic eddies, also called microeddies, is reached (Doran, 1995; Kawase and Moo-Young, 1990; Kresta, 1998).

Mixing is achieved by dispersion during the turbulent disintegration of eddies into smaller ones. However, below the size of the microeddies mixing relies on molecular diffusion. During fluid flow dispersion, the kinetic energy contained in the primary eddies is transmitted to eddies of decreasing size. But when the eddies become microeddies, their kinetic energy is dissipated as heat (see Figure 1.7). Therefore, fluid flow dispersion is limited by the size of the microeddies formed in a particular system, which is given by the Kolmogorov scale of mixing. According to Kolmogorov's theory of isotropic turbulence, the size of the microeddies depends upon the power supplied by the stirrer providing

liquid motion, and the kinematic viscosity of the fluid (Bałdyga and Bourne, 1999; Doran, 1995; Kawase and Moo-Young, 1990; Kresta, 1998).

At infinitely large Reynolds numbers energy dissipation by viscous effects is unimportant, and the energy spectrum is only determined by ε (i.e. by the power supplied by the stirrer). Kolmogorov referred to this energy spectrum as 'inertial subrange' (see Figure 1.7). However, as the size of the eddies decrease, energy dissipation is affected by fluid viscosity (Bałdyga and Bourne, 1999; Kawase and Moo-Young, 1990; Kresta, 1998).

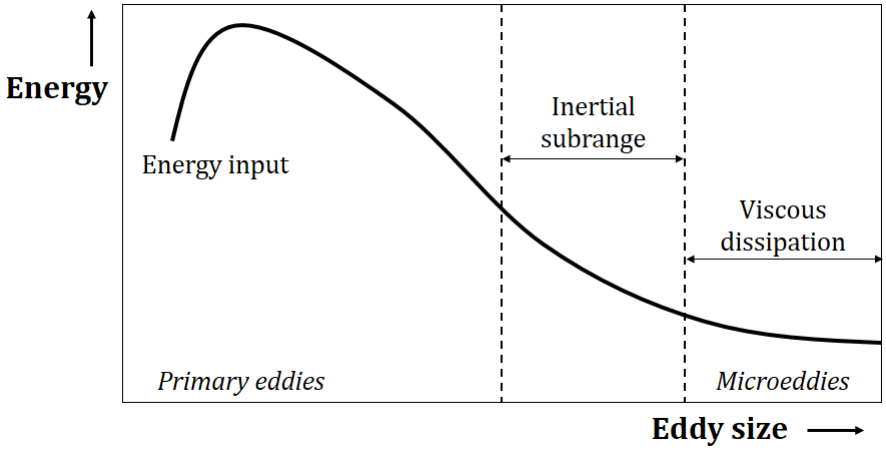

Figure 1.7. Schematic representation of the energy spectrum of turbulence according to Kolmogorov's theory of isotropic turbulence.
Primary eddies are produced by mechanical and/or pneumatic agitation and are the highest energy-containing eddies. The primary eddies eventually break up into smaller ones until the smallest-size eddies (i.e. microeddies) are reached. At large Reynolds numbers (i.e. within the inertial subrange), energy dissipation during eddy break-up is independent of fluid viscosity. However, as the size of the eddies decreases, the viscous forces increasingly affect energy dissipation (i.e. viscous dissipation). Figure adapted from Kawase and Moo-Young (1990).

Local isotropic turbulence in stirred turbulent vessels is an idealised situation since the local rate of energy dissipation has been shown to vary by several orders of magnitude throughout a stirred vessel. Compared to other models, Kolmogorov's theory of isotropic turbulence simplifies the complex hydrodynamics encountered in mixing vessels, which include gas-liquid interfaces that are difficult to rigorously characterise with a simple model. Nonetheless, turbulent fluid flow inside a mixing vessel can be reasonably represented by energy dissipation rate values. Finally, different authors have shown that Kolmogorov's theory of isotropic turbulence can be also used with

non-Newtonian fluids, such as non-Newtonian fermentation broths (Kawase and Moo-Young, 1990; Kresta, 1998).

1.5.2.2. Turbulent Fluid Flow in STRs

Turbulent energy dissipation is not homogeneously distributed inside a STR, where the highest turbulent regimes are found in the impeller region. The fluid currents converge in the impeller region and it is here where exchange of material occurs. Fluid flow is slower and mainly streamlined away from the impeller blade tips and the impeller discharge stream. Consequently, mixing in these regions is much less intense than in the impeller region. In addition to this, fluid in STRs is recirculated due to the periodic pumping action of the impeller. Besides turbulent dispersion (see Section 1.5.2.1), fluid flow recirculation is the main reason for mixing in STRs. Fluid flow follows a specific pattern inside STRs, which is determined by the: (i) impeller design; (ii) properties of the fluid; and (iii) size and geometric proportions of the vessel, baffles and impeller. Nonetheless, fluid flow patterns inside STRs can be broadly classified into axial and radial flows depending on the direction of the liquid leaving the impeller (the impeller design used will determine the direction of the flow). Radial-flow impellers (see Figure 1.8, left), such as the six-blade disc turbine, drive liquid flow radially from the impeller against the walls of the tank, where the flow divides into two streams: one flows up to the top of the tank, and the other to the bottom; the flow recirculates and eventually returns back to the impeller region. Axial-flow impellers (see Figure 1.8, right), such as pitched-blade turbines, drive liquid flow downwards from the impeller against the floor of the tank, where it then spreads out over the floor and flows up along the tank wall before being drawn back to the impeller (Bourne and Yu, 1994; Doran, 1995; Ng and Yianneskis, 2000).

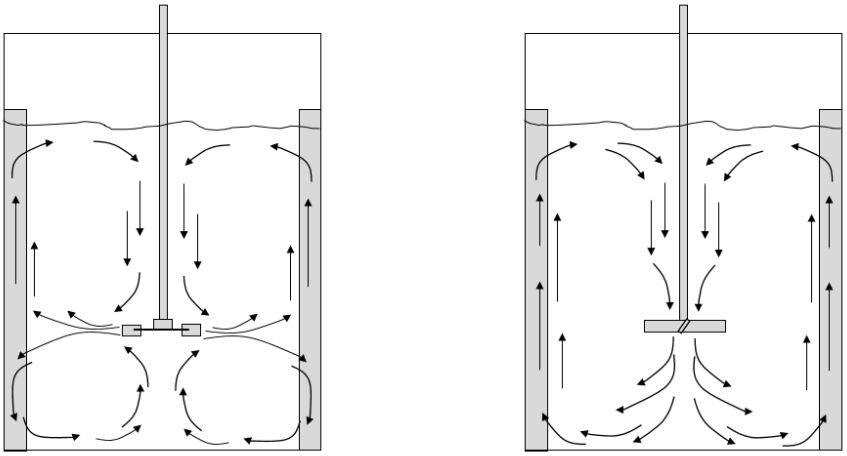

Figure 1.8. Fluid flow patterns produced by radial-flow and axial-flow impellers in a tank equipped with baffles.
The figure schematically describes the fluid flow patterns generated by radial-flow and axial-flow impellers in a tank equipped with baffles as observed from the side of the stirred tank. The following impellers have been represented in the figure: six-blade disc turbine (radial flow) and three-pitched blade turbine (axial flow). Figure adapted from Doran (1995).

1.5.2.3. Scale-Up Correlations in STRs for Turbulent Conditions

Local turbulent energy dissipation rate per unit mass of fluid (ε) is used to describe the hydrodynamic stresses encountered in STRs (Henzler, 2000; Hortsch and Weuster-Botz, 2010; Zhou and Kresta, 1996). However, established "rules of thumb" such as constant power input per unit volume (P/V_l) and constant torque per unit volume (Γ/V_l) are traditionally used to size mixing vessels during the scale-up process.

1.5.2.3.1. Constant Power Input Per Unit Volume

Constant power input per unit volume has been used as a scale-up basis with considerable success in some areas (Ho et al., 1987; Kresta, 1998; Uhl and Von Essen, 1986). The P/V_l ratio is also expressed as the average energy dissipation rate per unit mass of fluid (ε_{avg}) in a vessel (Hortsch and Weuster-Botz, 2010; McCabe et al., 2001):

$$\varepsilon_{avg} = \frac{P}{\rho V_l} = \frac{P_o \rho N^3 D_i^5}{\rho V_l} = P_o \frac{N^3 D_i^5}{V_l} \qquad \text{(Equation 1.2)}$$

where ε_{avg} is the average turbulent energy dissipation rate per unit mass of fluid ($W.kg^{-1}$), P is the power input (W), ρ is the liquid density ($kg.m^{-3}$), V_l is the vessel's liquid working volume (m^3), P_o is the impeller power number, N is the impeller speed (s^{-1}) and D_i is the impeller diameter (m). Scaling up based on constant P/V_l has been reported to require exact geometric similarity since P/V_l averages the largely different values of ε encountered in a STR; values of ε near the impeller are at least 10 times larger than in the bulk of the tank (Kresta, 1998; Zhou and Kresta, 1996). Constant $N^3D_i^2$ ($W.kg^{-1}$) (Kresta, 1998; Zhou and Kresta, 1996) and constant average shear rate ($\overline{G}$, s^{-1}) (Camp and Stein, 1943; Koh et al., 1984) have been described as alternative scale-up correlations to more closely match the maximum ε values encountered in the vessel. Nonetheless, $N^3D_i^2$ and $\overline{G}$ are both proportional to ε_{avg}.

1.5.2.3.2. Constant Torque Per Unit Volume

Constant torque per unit volume is described by constant impeller tip speed (Ho et al., 1987; Uhl and Von Essen, 1986). This is calculated as follows (Doran, 1995):

$$v_{tip} = \pi N D_i \qquad \text{(Equation 1.3)}$$

where v_{tip} is the impeller tip speed ($m.s^{-1}$), N is the impeller speed (s^{-1}) and D_i is the impeller diameter (m).

Both these two scale-up "rules of thumb" require geometric similarity between the stirred tanks used for the scale-down or scale-up process. However, process performance can be replicated at a different scale if the key process variables that determine the scale-up success are reproduced (Titchener-Hooker et al., 2008; Zlokarnik, 2002).

1.5.3. Mixing Time Scales and their Effect on Kinetic Processes

When putting two miscible and reactive fluids in contact, mixing directly influences the chemical reaction if the reaction kinetics are faster or are of the same order as the characteristic time for the mixing steps leading to homogenisation (Bałdyga and Bourne, 1990, 1999; Fournier et al., 1996a; Marcant and David, 1991; Schaer et al., 1999; Villermaux and Falk, 1994). Mixing has been shown to determine product quality in industrially relevant processes

such as precipitation, polymerisation and crystallisation. The following product quality attributes were affected by mixing: MW distribution (polymerisation), size distribution and average particle size (crystallisation and precipitation) (Bałdyga and Bourne, 1999; Bałdyga and Pohorecki, 1995; Fournier et al., 1996b; Marcant and David, 1991; Pohorecki and Bałdyga, 1988; Villermaux and Falk, 1994).

To investigate if a chemical process is affected by mixing, the characteristic time of the three main mixing mechanisms needs to be calculated. These mixing mechanisms are classified according to the scale of the vessel (i.e. characteristic length scale) at which they are relevant, and occur in both turbulent and laminar conditions. These mixing time scales are classified as macromixing, mesomixing and micromixing (see Figure 1.9) (Bałdyga and Bourne, 1992, 1999; Bałdyga and Pohorecki, 1995; Vicum et al., 2004).

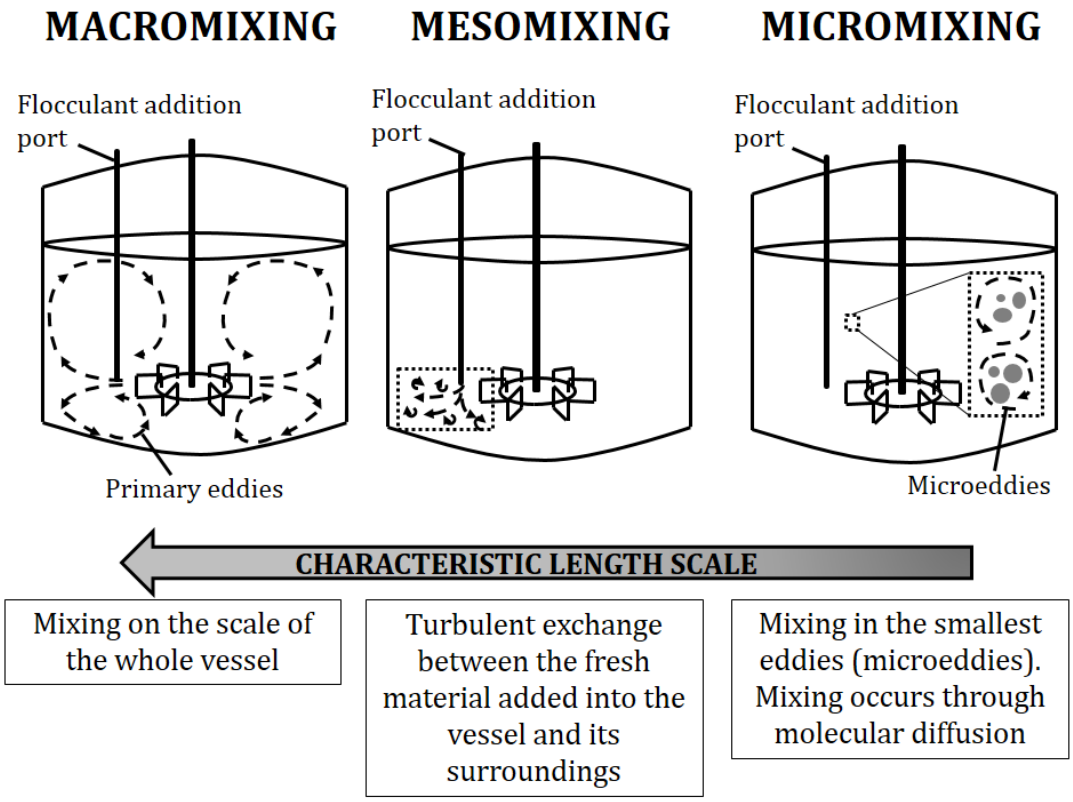

Figure 1.9. Schematic diagram of the characteristic length scales of mixing in a standard stirred tank reactor equipped with a six-bladed disc turbine. *Figure adapted from Espuny Garcia del Real et al. (2014).*

Macromixing refers to the mixing on the scale of the whole vessel (Bałdyga and Bourne, 1999; Bałdyga and Pohorecki, 1995; Bourne et al., 1989), i.e. macromixing refers to the large-scale flow processes that cause the realisation of large-scale distributions (Bałdyga and Pohorecki, 1995). Macromixing, which is independent of fluid viscosity under turbulent conditions (Bourne et al., 1989), controls the mean reactant concentration for the other two smaller mixing time scales (meso- and micromixing), and moves fluids that are undergoing meso- and micromixing through environments where the turbulent properties vary (Bałdyga and Bourne, 1992, 1999; Bałdyga and Pohorecki, 1995). Macromixing can be well characterised by the macroscopic flow patterns; in STRs macromixing is characterised by the circulation time (Bałdyga and Pohorecki, 1995). Macromixing models are only physically meaningful for slow reactions only, as they employ the average concentration of reactants in the whole mixing tank. Mixing and kinetic models for fast or instantaneous reactions need to consider smaller mixing time scales (Bałdyga and Bourne, 1999).

Mesomixing considers the inhomogeneity appearing around the feeding point when fresh material is added into a vessel at high feed rates, whether in batch (i.e. single addition), semibatch (i.e. continued but limited addition) or continuous modes (Bałdyga and Pohorecki, 1995). Fast chemical reactions will occur near the feeding point, where a plume of fresh feed is formed after the addition of fresh material. This plume will be of coarse scale relative to the micromixing time scale, but of fine scale relative to the scale of the vessel (see Figure 1.9). The turbulent exchange between the fresh material and its surroundings occurs via two mesomixing mechanisms: (i) turbulent dispersion; and (ii) large eddy disintegration. First, the fresh plume will diffuse into the turbulent environment (i.e. turbulent dispersion), where the large eddies carrying the fresh material will subsequently disintegrate into small spots containing the fresh material (i.e. large eddy disintegration). While mixing by inertial disintegration of large eddies (see Section 1.5.2) proceeds without any direct effect on molecular mixing, the structure of the large eddies and the small spots of fresh material will determine the environment for micromixing (Bałdyga and Bourne, 1999; Bałdyga and Pohorecki, 1995).

Micromixing, the smallest of the mixing time scales, refers to the viscous deformation of fluid elements (see Section 1.5.2) followed by molecular diffusion (see Figure 1.9) (Bałdyga and Bourne, 1999; Bałdyga and Pohorecki, 1995). Micromixing has been described to be the mixing time scale responsible for influencing the selectivity, yield and product quality of several industrial processes such as polymerisation, crystallisation and precipitation (Assirelli et al., 2002; Bałdyga and Pohorecki, 1995; Fournier et al., 1996b; Guichardon and Falk, 2000; Marcant and David, 1991; Pohorecki and Bałdyga, 1988). Micromixing is also responsible for product distribution in fast parallel and competitive-consecutive chemical reactions, where reagents are initially present in separate feed streams (Bałdyga and Bourne, 1990; Bałdyga and Pohorecki, 1995; Bourne and Yu, 1994; Bourne et al., 1989; Rousseaux et al., 1999). Many publications have demonstrated the dependence of micromixing time on impeller speed, location of the feeding point, feeding time, diameter of the feeding pipe and viscosity of the fluid (Bałdyga et al., 1993; Bourne et al., 1989, 1995; Fournier et al., 1996b; Gholap et al., 1994; Marcant and David, 1991). Therefore, process performance, including that of subsequent solid-liquid separation steps for particle-inducing processes such as precipitation, can be improved by characterising micromixing efficiency (Guichardon and Falk, 2000; Pohorecki and Bałdyga, 1988; Rousseaux et al., 1999).

Unlike macromixing, micromixing is measured through indirect methods (Rice and Baud, 1990). Physical (e.g. conductometric and optical) and chemical methods can be used to experimentally characterise micromixing; the reader is referred to to Fournier et al. (1996b) for a detailed description of these methods. Different micromixing models can also be employed to predict micromixing time; these models are classified as mechanistic and analytical (Bałdyga and Bourne, 1999; Villermaux and Falk, 1994). Mechanistic models are based on simple and idealised mechanisms that simulate the mixing process (Bałdyga and Bourne, 1999). Although mechanistic models do not properly describe the physics of mixing, it is possible to fit the model parameters to theories of turbulence. The mechanistic models for micromixing time are (Bałdyga and Bourne, 1999): (i) the three-environment or interdiffusion model; (ii) the coalescence and redispersion model; (iii) the interaction by exchange with the mean (IEM) model; (iv) diffusion

models; and (v) both the discrete and continuous engulfment-deformation-diffusion (EDD) models. Both discrete and continuous EDD models are based on the same theory, which relate to the relevant aspects of turbulence; for this reason, EDD models give reasonable results when compared to experimental data (Bałdyga and Bourne, 1999). With regards to the analytical models for micromixing time, these are based on a comprehensive description of the fluid dynamics in the mixing region, and are possible thanks to the development of CFD (Villermaux and Falk, 1994). Refer to Bałdyga and Bourne (1999) for a detailed description of the micromixing models covered in this subsection.

Micromixing models are of interest to successfully predict the course of fast complex reactions such as competitive-consecutive and parallel reactions. For instance, in polymerisation processes micromixing models can be employed to predict the consumption of the initiator compound or the effects of mixing upon the degree of polymerisation; in precipitation and crystallisation processes, micromixing models have been used to predict particle size distribution and explain the effect of mixing on particle morphology as well as on protein solubility (Bałdyga and Pohorecki, 1995).

1.6. Aims of the Research

The primary focus of this project was to evaluate the use of flocculation as a feed conditioning strategy to assist in the clarification and impurity reduction performed by primary recovery unit operations during mAb production, using an industrially relevant mammalian glutamine synthetase (GS) CHO cell line. The objectives listed in Section 1.7 are used to define the different goals of the project and lay out the content of the subsequent thesis results chapters.

1.7. Objectives of the Research

The objective throughout the project was to obtain process-relevant data useful for the biopharmaceutical industry. Consequently, industrially relevant process materials, operational settings and equipment that mimicked the conditions encountered at manufacturing scale during mAb production with GS-CHO cell

lines were used in this thesis. The research objectives of the project, which relate to the thesis results chapters, are summarised below:

Objective 1: Assess the possibility to use flocculation as a post-centrifugation feed conditioning strategy, identify a successful flocculant and establish the analytical methods and protocols to characterise flocculation performance.

The absence of literature describing flocculation processes on post-centrifuged mammalian cell broths suggested the importance of an evaluation into whether such process materials could indeed be successfully flocculated. Reference in the literature to flocculating agents interfering with analytical methods commonly used to analyse flocculation performance required an investigation into such incidences with the flocculant used in this thesis. Chapter 3 describes the evaluation of different GS-CHO cell lines to validate the flocculation of post-centrifuged mammalian cell broths. This chapter also characterises the implementation, development and optimisation, when necessary, of analytical methods and protocols to evaluate flocculation performance, which are later used in subsequent thesis chapters.

Objective 2: Develop and validate an ultra scale-down flocculation methodology for the rapid evaluation of flocculation conditions during early process development.

The extended flocculation literature demonstrates flocculation performance is determined by numerous process variables. This required the development of a scaled-down, high-throughput, automated methodology to evaluate multiple flocculation conditions. Such a platform was particularly required to enhance the understanding of how cell culture and centrifugation conditions would impact upon flocculation performance. Chapter 4 describes the development of this methodology which was validated with clarified Baker's yeast homogenate, used as an example of high-solid content biological material. This methodology was subsequently validated with centrifuged mammalian cell process material in Chapter 5, which also includes an overview of high-throughput and automated

approaches for the rapid evaluation of flocculation performance in mammalian cell processes.

Objective 3: Evaluate the capacity of post-centrifuge flocculation to assist depth filtration in the removal of solids and process-related impurities during mAb production with GS-CHO cell lines.

The introduction of flocculation requires a subsequent solid-liquid separation step to remove the flocs formed upon the addition of the flocculating agent. Depth filtration post-centrifugation was the solid-liquid separation step chosen to make use of the primary recovery process currently implemented by Lonza Biologics during mAb production. Chapter 6 describes the integrated study of flocculation and depth filtration with ultra scale-down methodologies. This chapter includes an overview on how flocculation and depth filtration affected filtration performance and discusses options to minimise their negative effect. The evaluation of flocculation's capacity to assist in the removal of solids and process-related impurities is described in Chapter 7. The studies were carried out at laboratory scale by comparing the clarification and purification performances achieved by current and proposed flocculated primary recovery strategies. This comparative evaluation is extended in Chapter 8 to protein A chromatography, which constituted the first chromatographic step of the mAb production process, by identifying the process-related impurities co-eluting with the product. This chapter concludes the investigation of the impact that post-centrifuge flocculation had upon subsequent primary recovery and purification unit operations.

2. Materials and Methods

This chapter describes the materials and methods for the experimental work presented in this thesis. Each results chapter will then summarise the experimental set-up and the experimental conditions of the studies included in the chapter. All chemicals used were of AnalaR (or equivalent) grade and, unless otherwise stated, purchased from Sigma-Aldrich (Gillingham, UK). All buffers and reagents were prepared using laboratory deionised water (Milli-Q, Merck-Millipore, MA, USA). Data analysis was performed, unless otherwise stated, in Microsoft Excel and graphical presentation in Sigma Plot (version 11.0, Systat Software Inc., Chicago, IL, USA).

2.1. Preparation of Mammalian Cell Centrate

Two different glutamine synthetase Chinese hamster ovary (GS-CHO) cell lines stably expressing an IgG_4 monoclonal antibody (mAb) were used. These were the CY01 and the Xceed™ cell lines. Each cell line expressed a different IgG_4 monoclonal antibody, but the pI of both ranged between 6.8 and 7.2 as determined by isoelectric focusing (Lonza Biologics, personal communication). The CY01 GS-CHO cell line, which was generously provided by Lonza Biologics (Slough, UK), reached maximum cell densities during cell culture of $9.7x10^6$ cells.mL^{-1} and product titres of 0.8 g.L^{-1}; this cell line will be referred to as low cell density (LCD) cell line in this thesis. Higher maximum cell densities during cell culture ($47x10^6$ cells.mL^{-1}) and product titres (6.5 g.L^{-1}) were achieved with the Xceed™ GS-CHO cell line; this cell line will be referred to as high cell density (HCD) cell line in this thesis. High cell density cell culture broths were employed in all mammalian cell experiments unless otherwise stated.

2.1.1. Low Cell Density Mammalian Cell Line

2.1.1.1. Cell Storage and Recovery

A working cell bank, made up by 1 mL vials ($1x10^8$ cells.mL^{-1}), had been created from the master cell bank vials provided by Lonza Biologics (Slough, UK). The cells were stored in liquid nitrogen in chemically defined medium (CD-CHO

medium, Life Technologies, Paisley, UK) containing 10 % v/v dimethyl sulfoxide. During cell recovery one working cell bank vial was placed in a 37°C unstirred water bath (SUB14, Grant Instruments, Royston, UK) for 2 minutes before decanting its contents into a 15 mL, sterile conical bottom centrifuge tube (ThermoFisher Scientific, Waltham, USA) containing 9 mL of CD-CHO medium at 37°C. The tube was centrifuged at 450g for 5 minutes (Eppendorf 5180R, Hamburg, Germany), after which the supernatant was discarded. The cell pellet was re-suspended in 5 mL of CD-CHO medium at 37°C and then transferred into a 125 mL un-baffled shake flask with vent caps (Corning Incorporated Life Sciences, MA, USA) containing 20 mL of CD-CHO medium at 37°C. Flasks were incubated overnight (SANYO CO_2 Incubator MC0-181C, Watford, UK) at 37°C and 5 % CO_2 on an orbital shaker set at 2.5 rps (IKA® 260, Wolf Laboratories, York, UK). Cell viability was checked the following day as described in the Section 2.1.1.5.

2.1.1.2. Cell Maintenance

Cells were cultured in 250 mL disposable, un-baffled shake flasks with vent caps (Corning Incorporated Life Sciences, MA, USA) containing 100 mL of CD-CHO medium (Life Technologies, Paisley, UK). Incubation conditions were those used during cell line recovery. Cells were sub-cultured every 3 or 4 days (i.e. during the exponential growth phase) for up to 25 passages. Post-inoculation viable cell density was kept at $0.2x10^6$ cells.mL^{-1}. The cell culture medium contained 25 µM L-methionine sulphoximine at a final concentration of 0.1 % v/v to maintain the selective pressure on the cells containing the glutamine synthetase plasmid. When larger cell culture volumes were required (e.g. for the 5 L STR cell culture seeding train), 1 L disposable, un-baffled shake flasks with vent caps (Corning Incorporated Life Sciences, MA, USA) containing 300 mL of CD-CHO medium at 37°C were used.

2.1.1.3. Cell Culture – Shake Flask

Cells were cultured in CD-CHO medium (Life Technologies, Paisley, UK) for 9 days at the same cell culture conditions and post-inoculation viable cell density used during cell line maintenance. Samples with a volume of 1.5 mL were taken in

aseptic conditions for cell viability, product titre and total protein concentration measurements as described in the Section 2.1.1.5, 2.10.2 and 2.10.1, respectively.

2.1.1.4. Cell Culture – Stirred Tank Reactor

Cell culture broth was obtained from a third party, but using the CY01 (i.e. LCD) cell line. Cells were cultured for 12 days in two 5 L stirred tank reactors (STRs) of 3.5 L working volume run in parallel with an in-built control system (BIOSTAT® B-DCU control unit, Sartorius Stedim, Göttingen, Germany) and operated at the following set-points: 37.0 ± 0.1°C, pH 7.10 ± 1.0 and dissolved oxygen tension of 30.0 ± 1.0 % air saturation. The set pH was maintained using CO_2 sparging and sodium carbonate buffer (100 mM $NaHCO_3$ and 100 mM Na_2CO_3). The set dissolved oxygen tension was kept constant using air and oxygen pumped at 100 $cm^3.min^{-1}$ via a horse-shoe sparger. Mixing was achieved with a single three-pitched blade impeller (45° angle) operated at 4.3 rps and aligned to generate a down-pumping flow. Cell culture was carried out in fed-batch mode using CD-CHO medium (Life Technologies, Paisley, UK). Glucose concentration was measured daily with the BioProfile 400 Automated Analyser (Nova Biomedical, Deeside, UK) and maintained at 2 $g.L^{-1}$ by bolus addition of a 10-times concentrated CD-CHO medium feed (Life Technologies, Paisley, UK), supplemented with glucose up to 150 $g.L^{-1}$; bolus addition was performed using a tube welder (Terumo SCD IIB Sterile tubing Welder, Terumo Medical Corporation, Elkton, USA) or a septum. Cell culture sample volumes of 500 µL were centrifuged (Microcentrifuge 5424 R, Eppendorf, Hamburg, Germany) for 1 minute at 216.7 rps and 20°C to recover the supernatant prior to glucose analysis. Harvesting occurred during the cell culture decline phase.

2.1.1.5. Cell Viability and Cell Count

Cell viability and cell count were measured using an automated cell viability analyser (Vi-Cell™ XR Cell Viability Analyser, Beckman Coulter, High Wycombe, UK) based on trypan blue exclusion (Strober, 2001). Samples were either non-diluted or diluted 1 in 2 using phosphate buffered saline (PBS). Each cell count and viability value was the average of 50 separate measurements taken using the instrument's pre-defined CHO cell settings.

2.1.1.6. Cell Clarification

Limited volumes of LCD cell culture were available, thus the implementation of ultra scale-down techniques to clarify the cell culture broth was required. The LCD cell culture broth was clarified via USD centrifugation, for which a high-speed rotating shear device was used in combination with a bench-top centrifuge to mimic the process-scale centrifugation conditions, including the shear forces encountered in the feed zone of an industrial centrifuge. The shear device, which was developed and constructed by the Mechanical workshop at UCL (Levy et al., 1999), consists of a 40 mm diameter and 1 mm thick stainless steel rotating disc contained in a chamber of 50 mm diameter and 10 mm height (Hutchinson et al., 2006). A custom-built power unit controls the rotational speed of the disc, which ranges from 0 to 333.3 rps (Chatel et al., 2014). The chamber has a total volume of 20 mL, although 50 mL disposable syringes were used to dispense the liquid into the chamber ensuring any air within it was displaced.

Low cell density cell culture broth was sheared for 20 seconds at 100 rps with the shearing device to mimic the conditions encountered in the Westfalia CSA-1 disc-stack centrifuge (Westfalia Separator GmbH, Oelde, Germany), which was the hydro-hermetically sealed (i.e. low shear stress) centrifuge used to clarify HCD cell culture broth (see Section 2.1.2). These shearing conditions, which are equivalent to exposing the material to a maximum energy dissipation rate per unit mass of fluid, ε_{max}, of 0.045×10^6 $W.Kg^{-1}$ (Chatel et al., 2014), have been shown to be sufficient for all material to be subjected to the energy dissipation present in the chamber (Hutchinson et al., 2006). The target disc speed was set with 20 mL of deionised water before shearing the cell culture broth. The sheared samples were transferred to 50 mL sterile conical bottom centrifuge tubes, and then centrifuged (Eppendorf 5810R, Eppendorf, Hamburg, Germany) for 18 minutes at 66.7 rps to mimic the centrifugation conditions (i.e. $Q/\sum = V/(t\sum)$) used to clarify HCD mammalian cell culture broth (Westfalia CSA-1 disc stack centrifuge, 163.3 rps, 70 $L.h^{-1}$; see Section 2.1.2). The $\sum$ value for the bench-top centrifuge used was equal to 1.60 m^2 and was calculated as follows:

$$\Sigma_{lab} = c_{lab}\frac{V_{lab}\omega^2(3-2E-2F)}{6g\ln\left(\frac{2r_2}{r_1+r_2}\right)} \quad \text{(Equation 2.1)}$$

where $\sum_{lab}$ is the equivalent settling area of a batch bench-top centrifuge (m^2), c_{lab} is the calibration factor for a batch centrifuge (c_{lab} = 1; Hutchinson et al., 2006), V_{lab} is the volume of material in the centrifuge tube (V_{lab} = 5x10^{-5} m^3), ω is the radial velocity (s^{-1}), E is the correction factor (E = 0.018) to account for deceleration and is equal to the fraction of overall centrifugation time for deceleration assuming a linear deceleration rate (Maybury et al., 2000), F is the correction factor (F = 0.027) to account for acceleration and is equal to the fraction of overall centrifugation time for acceleration assuming a linear acceleration rate (Maybury et al., 2000), g is the gravitational acceleration ($m.s^{-2}$), r_1 is the centrifuge inner radius (r_1 = 0.100 m) and r_2 is the outer radius of the suspension in the centrifuge tube (r_2 = 0.191 m).

Only the upper 50 % volume of centrifuged supernatant inside the centrifuge tubes was recovered in order to avoid disturbing the pellet. The recovered supernatant was pooled before measuring its particle size distribution (PSD) by laser light diffraction (see Section 2.11.4) as well as its optical density at 600 nm wavelength (OD_{600}) to calculate the percentage solids remaining (see Section 2.11.3). The clarified LCD cell culture was then flocculated within a period of one hour. A 2 mL supernatant sample was always set apart and stored at -80°C for future analysis.

2.1.2. High Cell Density Mammalian Cell Line

High cell density mammalian cell broth was provided by Lonza Biologics (Slough, UK) and either clarified at UCL or in Lonza Biologics' premises via pilot-scale centrifugation. Different batches of HCD cell culture broth were used in this thesis.

2.1.2.1. Cell Culture

Cells were cultured at Lonza Biologics' premises in a 15 L STR (10 L working volume) with an in-built control system and fed-batch mode for 14 days.

Table 2.1 summarises the cell culture data of the different batches of HCD cell culture broth used in this thesis.

2.1.2.2. Cell Clarification

High cell density cell culture was clarified via disc-stack centrifugation within minutes of harvesting the bioreactor when clarification was performed at Lonza Biologics (Slough, UK). Centrifugation was performed within 3 hours of harvesting the bioreactor when performed at the Advanced Centre for Biochemical Engineering (UCL, London, UK). Table 2.2 summarises the centrifugation conditions and the clarification performance achieved for each batch of HCD cell culture used.

Centrifugation at Lonza Biologics (Slough, UK) was performed with an Alfa Laval MBPX-404 disc-stack centrifuge (Alfa Laval Corporate AB, Lund, Sweden) equipped with a hydro-hermetically sealed feed zone. Solid-liquid separation was performed inside 89 conical stacked discs (at 45° angle) with 0.5 mm gap between each disc. The total separating bowl volume was 2.2 L with a solids holding capacity of 1.1 L. The centrifuge operated at a bowl speed of 158.3 rps and unknown flow rate (60 – 400 $L.h^{-1}$). The calculated Sigma value, $\sum$, for this centrifuge at the operating conditions used was 5276 m^2.

At UCL cell culture clarification was performed with a Westfalia CSA-1 disc-stack centrifuge (Westfalia Separator GmbH, Oelde, Germany) equipped with a hydro-hermetically sealed feed zone. In this centrifuge solid-liquid separation was performed inside 45 conical stacked discs (at 38.5° angle) with 0.5 mm gap between each disc. The centrifuge bowl volume was equal to 0.6 L and the solids holing capacity to 0.25 L. The Westfalia CSA-1 disc-stack centrifuge was operated to mimic the clarification performance achieved by the centrifugation step of one of Lonza Biologics' mAb cell culture processes. Ten litres of well-mixed HCD cell culture broth were pumped (605 Di peristaltic pump, Watson-Marlow Pumps Group, Wilmington, US) at a constant flow rate of 70 $L.h^{-1}$ into the centrifuge, which was operated at a bowl speed of 163.3 rps and temperature of 23°C. The resultant Q/Σ value was 2.85×10^{-8} $m.s^{-1}$; the calculated $\sum$ value at the operating conditions used was 681.2 m^2. The $\sum$ value was calculated as follows:

$$\Sigma_{ds} = c_{ds}\frac{2\pi S}{3} \times \frac{n}{g} \times \frac{\omega^2\left(r_o^3 - r_i^3\right)}{\tan\theta} \qquad \text{(Equation 2.2)}$$

where $\sum_{ds}$ is the equivalent settling area of a disc-stack centrifuge (m^2), c_{ds} is the calibration factor to account for non-ideal flow in a disc-stack centrifuge (c_{ds} = 0.4 - 0.5; Hutchinson et al., 2006), n is the number of centrifuge separation discs in the stack, S is the correction factor for the area occupied by the caulks (S = 0.9), ω is the radial velocity (s^{-1}), r_0 is the centrifuge separation disc outer radius (r_0 = 0.055 m), r_i is the centrifuge separation disc inner radius (r_i = 0.026 m), g is the gravitational acceleration ($m.s^{-2}$) and θ is the centrifuge separation disc half angle (radians). Centrifugal separation was performed at a backpressure of ~ 1.5 bar to ensure the centrifuge feed zone stayed fully flooded (i.e. hydro-hermetically sealed). The supernatant was recovered in fractions of 0.6 L, which were then analysed via OD_{600} measurements. The supernatant fractions that did not correspond to the centrifugation steady state were discarded while the rest were pooled. The OD_{600} of the final pooled centrate was then measured to calculate the percentage solids remaining (see Section 2.11.3). The PSD of the HCD mammalian cell centrate was studied by laser light diffraction (see Section 2.11.4) before being stored. Storage conditions differed depending on the batch number (see Table 2.2). The HCD mammalian cell centrate from batch number 1 (see Table 2.2) was stored in 0.5 L fractions at 5°C for a period of up to 94 days and at -80°C in one 200 mL fraction. Sodium azide to a final concentration of 0.05 % w/v was added to the centrate kept at 5°C to prevent bacterial growth (Lichstein and Soule, 1944). The HCD mammalian cell centrate batch number 2 (see Table 2.2) was stored in Lonza Biologics' premises at -20°C and in 1.6 L fractions; the centrate was later shipped to UCL stored on dry ice. The HCD centrate from batch number 3 and 4 (see Table 2.2) were stored at -80°C in 0.5 L and 50 mL fractions.

Table 2.1. Cell culture data of the high cell density cell culture material.
Cells (Xceed™ cell line) were cultured in a 15 L STR and in fed-batch mode for 14 days at Lonza Biologics' premises (Slough, UK). Peak cell density refers to the maximum cell density value achieved during cell culture. Product titre was measured on day 14 of cell culture before harvesting. Cell culture and product titre data were supplied by Lonza Biologics (Slough, UK).

		Cell culture			
Batch	**Thesis chapter**	**Peak total cell density (cells.mL^{-1})**	**Total cell density at harvest (cells.mL^{-1})**	**Viability at harvest (%)**	**Product titre (g.L^{-1})**
1	3	29.0x10^{6}	19.5x10^{6}	65	3.8
2	5	28.0x10^{6}	20.0x10^{6}	78	4.7
3	6	29.0x10^{6}	23.0x10^{6}	72	0.8
4	7 & 8	46.6x10^{6}	30.0x10^{6}	80	6.5

Table 2.2. Centrifugation conditions and clarification performance data of the high cell density cell culture material.
Cells (Xceed™ cell line) were cultured in a 15 L STR and in fed-batch mode for 14 days at Lonza Biologics' premises (Slough, UK). Cell culture clarification at pilot scale using a low-shear disc-stack centrifuge. Centrifugation performance was assessed by the percentage solids remaining in the clarified supernatant calculated as described in Section 2.11.3.

	Clarification			
Batch	**Location**	**Centrifuge**	**Q/∑ (m.s^{-1})**	**Solids remaining (%)**
1	UCL	Westfalia CSA-1	2.85x10^{-8}	2.2
2	Lonza Biologics	Alfa Laval MBPX-404	Unknown	Unknown
3	UCL	Westfalia CSA-1	2.85x10^{-8}	3.5
4	UCL	Westfalia CSA-1	2.85x10^{-8}	1.6

2.2. Preparation of Clarified Yeast Homogenate

High activity Baker's yeast (*Saccharomyces cerevisiae*) provided by DCL London (London, UK) was suspended to 28 % w/v in phosphate buffer (0.1 M NaH_2PO_4, adjusted to pH 6.5 using 3 M NaOH). The yeast suspension was next homogenised with a Lab60 continuous flow high-pressure homogeniser (APV UK Ltd., Crawley, UK); homogenisation conditions were: five discrete passes, 500 bar pressure and constant temperature of 4°C. The homogenate was then centrifuged (Beckam Avanti J-E centrifuge fitted with a JA-10 rotor; Beckam Coulter Ltd., High Wycombe, UK) for 45 minutes at 105 rps and 4°C. The supernatant was recovered and stored at -20°C in aliquots of 45 mL for future use while the cell debris sediment was discarded. The PSD of the clarified yeast homogenate was measured prior to freezing by laser light diffraction as described in Section 2.11.4. The fresh Baker's yeast supplied was processed within one to two days from the delivery date. The supernatant was stored for a maximum of three weeks.

2.3. Configuration and Operational Characterisation of the Flocculation Systems

The flocculation mixing systems used were classified in three different scales depending on their volumetric dimensions as follows: pilot scale (above 1 L working volume), laboratory scale (1 mL to 1 L working volume), and USD scale (below 1 mL working volume).

2.3.1. Pilot Scale

2.3.1.1. Configuration

An LH fermentation reactor and corresponding stirrer driving unit (Model 500 Series II, L.H. Engineering Co Ltd, Stoke Poges, Buckinghamshire, UK) was used. The reactor consisted of a 2 L vessel of 124.5 mm diameter (D_T) and 1.5 L working volume, equipped with a 41.5 mm diameter (D_i) six-bladed disc turbine positioned at 1/3 the vessel diameter from the bottom, also referred to as clearance (C) (see Figure 2.1 and Figure 2.2). To achieve a turbulent regime the reactor had four baffles of 12.5 mm diameter (D_b) located 1.3 mm (H_b) away from

the vessel's wall. Reagent additions were via a 3.0 mm internal diameter pipe (d_i) positioned 13 mm away from the centre of the impeller blade and controlled with a calibrated syringe pump (Ultra programmable PHD Ultra, Harvard Apparatus Ltd., Kent, UK) equipped with two disposable 100 mL syringes filled with reagent. The pipe was only submerged in the liquid vessel during reagent addition. See Figure 2.1 for a schematic diagram of the reactor and Figure 2.2 for impeller dimensions.

2.3.1.2. Operational Characterisation

A calibrated stroboscope (RS Components Ltd, Birchington Road, Corby, Northants, UK) was used to confirm the coupling between the reactor's shaft rotational speed and the driving unit rotational speed display, which indicated speeds ranging from 1.7 to 18.3 rps in 0.83 rps intervals. The coupling was studied across a total range of 21 rotational speeds. A reflective paper stuck on the impeller shaft was used as the reference point. Triplicate readings were made at different speeds and at a fixed distance of 3 cm from the reference point.

Controlled reagent additions by the syringe pump were calibrated at nine different flow rates (184, 150, 120, 90.0, 60.0, 30.0, 15.0, 6.00 and 3.00 $mL.min^{-1}$) using a 0.5 M sulphuric acid solution (98 % v/v concentrate, Merck KGaA, Darmstadt, Germany) and a 4 % w/v PEI stock solution (linear, molecular weight (MW) = 50,000 - 100,000 Da; MP Biomedicals LLC, Illkirch-Graffenstaden, France). The weight of the reagent displaced by the syringe pump (6 mL when using sulphuric acid and 37.5 mL when using PEI) was measured with an analytical balance (Ohaus Pioneer™ PA413, Ohaus Corporation, USA). Volume was calculated with their corresponding density values, which were 1050 $kg.m^{-3}$ (0.5 M sulphuric acid) and 1030 $kg.m^{-3}$ (4 % w/v PEI). Measurements were performed in triplicate.

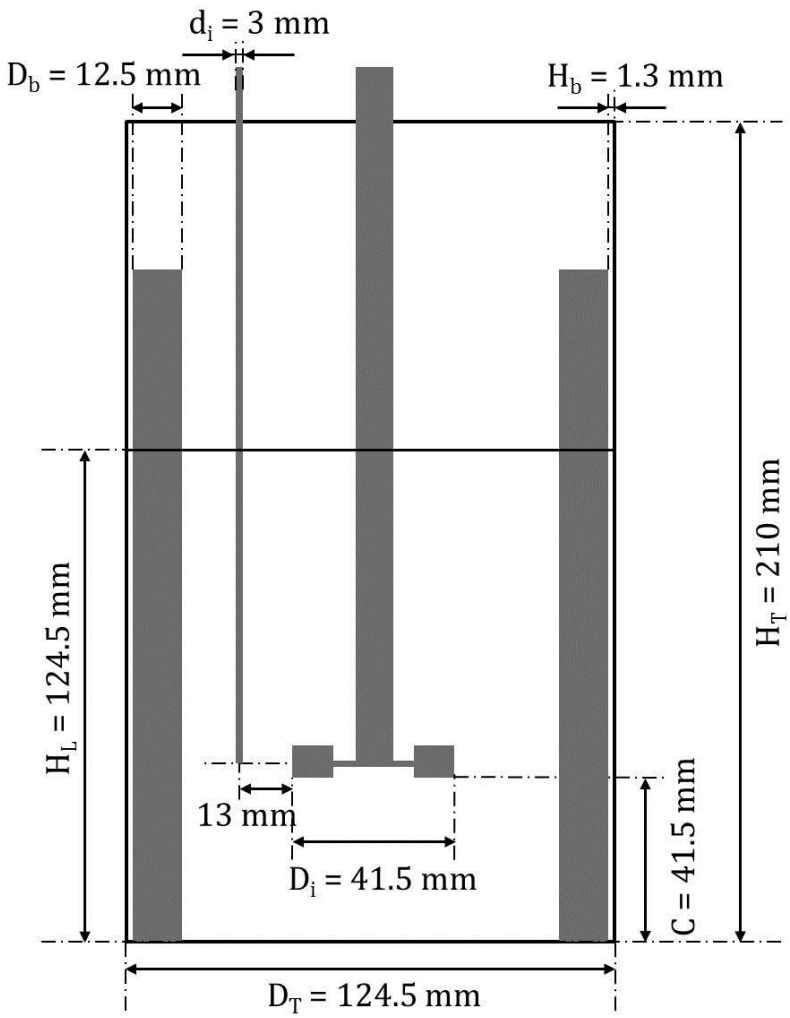

Figure 2.1. Diagram to scale of the pilot-scale flocculation system.
A 2 L stirred tank reactor of standard geometrical configuration equipped with a six-bladed disc turbine (as detailed in Figure 2.2) was used during the flocculation experiments at pilot scale. The vessel's dimensional specifications are detailed in the diagram. Key geometrical ratios were as follows: $H_L:D_T = 1:1$; $D_i:D_T = 1:3$; $D_i:C = 1:1$; $D_T:D_b = 1:10$; $D_T:H_b = 1:100$, *where* H_L *is the height of the liquid level,* D_T *is the diameter of the tank,* D_i *is the impeller diameter, C is the clearance between the tank bottom and the impeller,* D_b *is the diameter of the baffle,* H_b *is the distance between the baffle and the tank's wall and* d_i *is the internal diameter of the pipe used for reagent addition.*

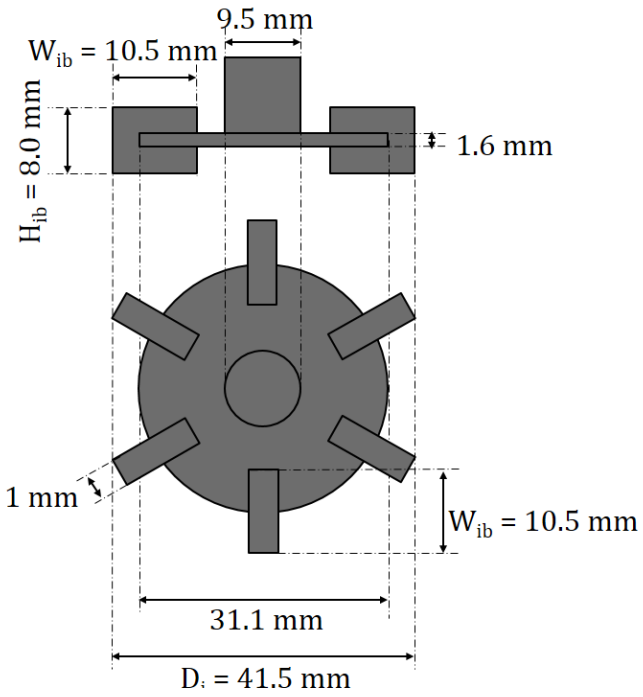

Figure 2.2. Diagram to scale of the six-bladed disc turbine used in the pilot-scale flocculation system.
The impeller's dimensional specifications are detailed in the diagram. Key geometrical ratios were as follows: H_{ib}:D_i = 1:4; W_{ib}:D_i = 1:5, where H_{ib} is the height of the impeller blade, D_i is the impeller diameter and W_{ib} is the width of the impeller blade.

2.3.2. Laboratory Scale

A custom made (UCL Mechanical workshop) glass vessel with a total volume of 100 mL and 70 mL working volume was used. The vessel, of 44.4 mm diameter (D_T), was equipped with four 5 mm stainless steel baffles (D_b) and either a 20 mm diameter (D_i) stainless steel six-bladed disc impeller (UCL Mechanical workshop) or a 20 mm diameter (D_i) plastic three-pitched blade impeller (Cornwall Model Boats Ltd., Cornwall, UK). Mixing motion was provided by an overhead motor with rotational speeds ranging from 0 to 33.3 rps to which the impellers were attached. Impeller clearance (C) was equal to $1/3D_i$ (six-bladed disc impeller) or $1/2D_i$ (three-pitched blade impeller). Reagent additions were performed manually by accurately pipetting the required volume of reagent near the impeller blade without disturbing its rotational motion.

2.3.3. Ultra Scale-Down Scale

2.3.3.1. Configuration

A microwell-based mixing system of 800 µL working volume was used. This system consisted of a 1.2 mL 96-well microplate (square round-bottom microplate, ABGene, Epsom, UK) and a custom-made perforated Perspex lid with 96 magnetic impellers fixed to it (see Figure 2.3.A). Each impeller consisted of two neodymium magnetic discs of 3.4 mm diameter (D_m) coated in a 0.05 mm thick layer of parylene and encapsulated in a 5.5 mm diameter (D_i) polytetrafluoroethylene (PTFE) seal (V&P Scientific, San Diego, USA). The PTFE seal had been perforated through its horizontal axis to fix the impeller to the lid by a 0.5 mm metallic wire. The impeller freely rotated through its horizontal axis at a clearance, C, of 5 mm from the liquid level as well as from the bottom of the plate when located on a magnetic stirrer (Model 75CI, V&P Scientific). The magnetic motor rotational speed could be adjusted by a unit controller within a scale of 0 to 100 % relative speed with an accuracy of 5 %. The magnetic stirrer was mounted on the deck of a liquid handling robot (Freedom EVO® 150, Tecan, Männedorf, Switzerland) via a custom-made Perspex platform (Figure 2.3.B). Controlled reagent additions were via PTFE-coated stainless steel tips of 1 mm internal diameter (d_i) located in the centre of the microwell with the outlet 1 mm above the tip of the impeller disc. These tips were located above the microwell mixing system and were only submerged in the liquid vessel during reagent addition (see Figure 2.3.B). Refer to Figure 2.4 for the schematic diagram of the mixing device.

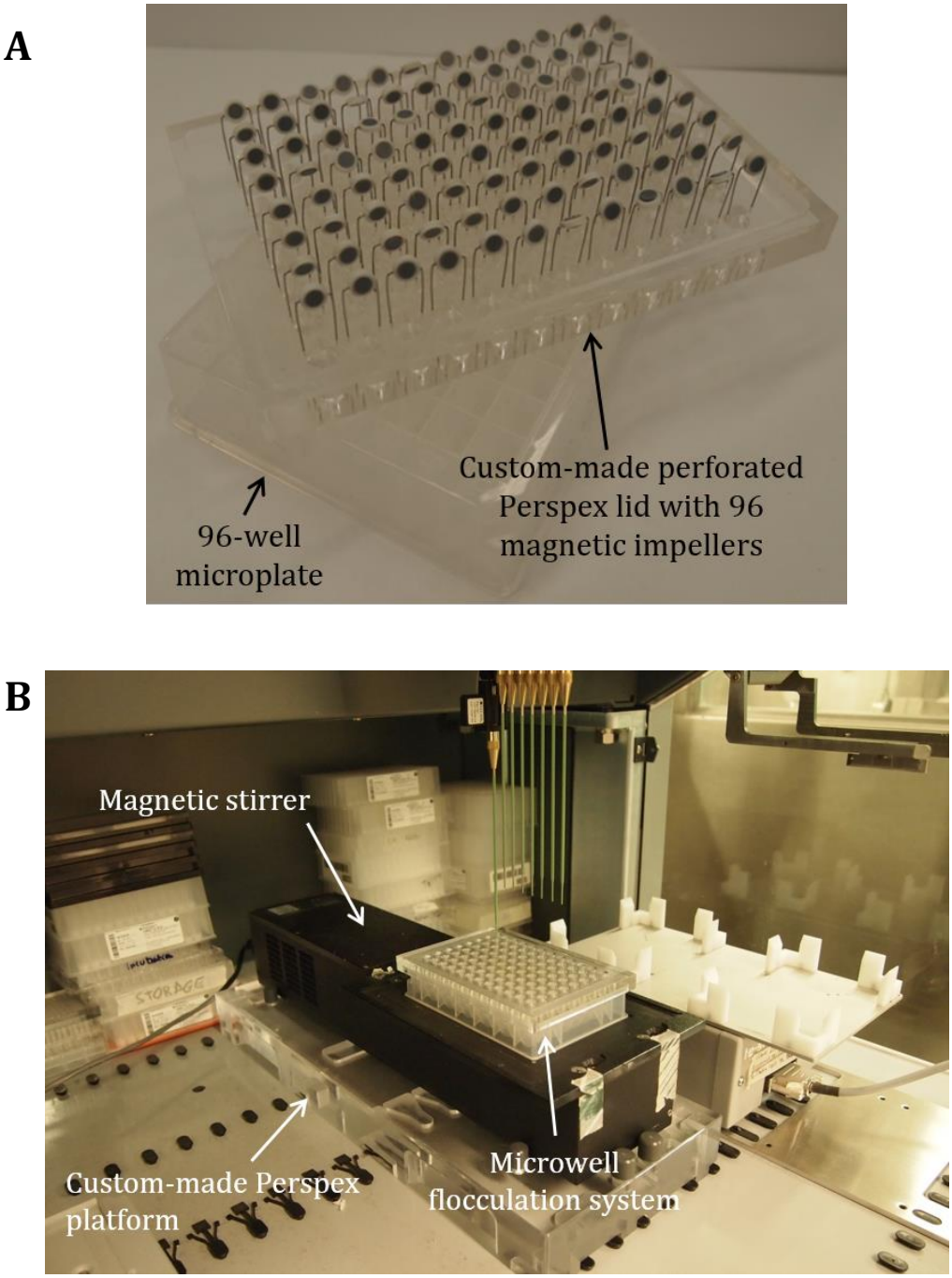

Figure 2.3. Picture of the ultra scale-down flocculation system (A) and its operating set-up (B).
A. *The ultra scale-down flocculation system consisted of a 1.2 mL 96-well microplate and a custom-made perforated Perspex lid with 96 magnetic impellers attached to it. The lid is inverted in the picture to reveal the impellers that would remain inside the wells during normal operating conditions.* ***B.*** *The ultra scale-down flocculation system was located on a magnetic stirrer mounted on the deck of a Tecan liquid handling robot thanks to a custom-made Perspex platform. The picture shows the controlled addition of reagent into one of the microplate wells.*

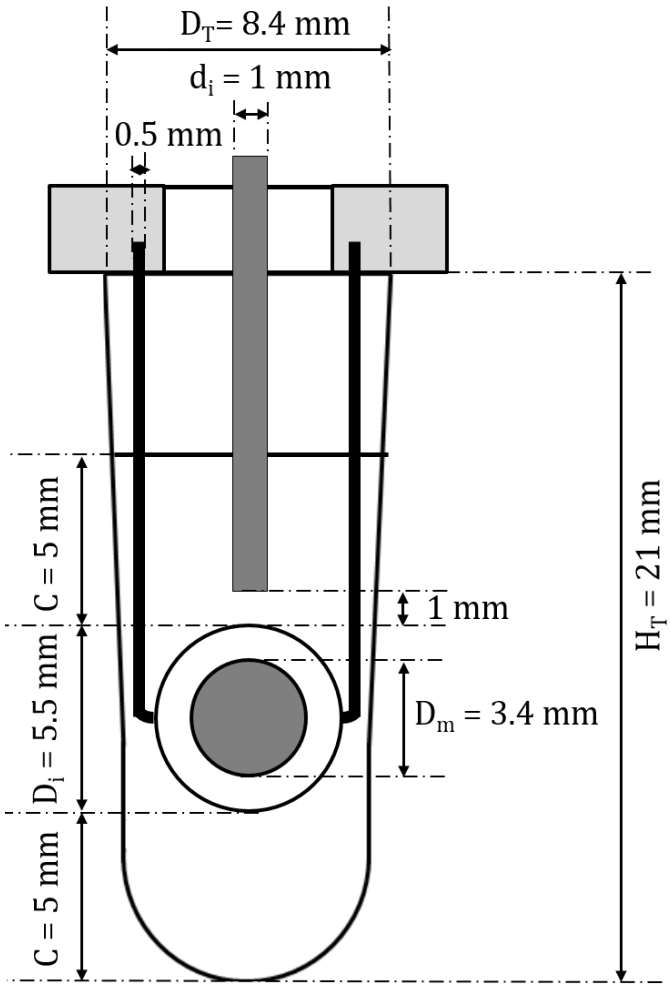

Figure 2.4. Diagram to scale of the ultra scale-down flocculation system. *The diagram describes the dimensional specifications of one of the 96 wells the microplate-based ultra scale-down flocculation system consisted of. In each well there was one magnetic impeller that rotated through its horizontal axis; each magnetic impeller was constituted of two magnetic discs coated in a PTFE seal. Reagent additions were performed at 1 mm from the impeller via a stainless-steel, PTFE-coated tip of 1 mm internal diameter. The tip for reagent additions accessed the centre of the well vertically through the perforated Perspex lid to which the impellers were fixed to. The system's working volume was 800 µL per well.*

2.3.3.2. Operational Characterisation

A calibrated stroboscope (RS Components Ltd, Birchington Road, Corby, Northants, UK) was used to determine the equivalence of the unit controller percentage speed scale in revolutions per second, and confirm the coupling between the magnetic discs and the magnetic drive. A reflective paper stuck on the magnetic spinning drive as well as on the impellers selected was used as a reference point. To ensure impeller speed was constant across the microplate,

19 different impellers were assessed. These were located in the following wells: A1, A6, A12, B3, B9, D3, D4, D5, D6, D7, D8, E1, E12, F4, F7, F10, H1, H7 and H12. Twenty one different speeds were studied; these ranged from the 0 % to the 100 % speed of the unit controller, and were separated in 5 % speed intervals. Measurements were done in triplicate and at a fixed distance of 3 cm from the reference point.

In order to ensure accurate liquid handling by the Freedom EVO® 150 robotic platform, new liquid classes were created using the Freedom EVOware® software (Tecan, Männedorf, Switzerland). New liquid classes were created for the following solutions: 12, 6, 4, 3 and 1 % w/v PEI (linear, MW from 50,000 to 100,000 Da; MP Biomedicals LLC, Illkirch-Graffenstaden, France), and 0.5 M sulphuric acid (98 % v/v concentrate, Merck KGaA, Darmstadt, Germany). The liquid handling of water-based solutions was performed with the default 'Water' liquid class provided by the software. The new liquid classes were calibrated at four different volumes (100, 50, 20 and 10 µL) and for all eight tips of the liquid handling arm. The liquid dispensed by each tip was weighed using an analytical balance (Ohaus Pioneer™ PA413, Ohaus Corporation, USA) and converted into volume with the solution's density value, which was determined as described in Section 2.11.6. The dispensed volume data was plotted against the diluent volume; diluent volume refers to the volume specified in the software to be dispensed by the liquid handling robot (see Figure 2.5 for an example). The linear regression between the dispensed and the diluent volumes was calculated to determine the offset and the slope values of the linear regression equation. The calibration of the new liquid classes was completed by introducing the average of the offset and slope (i.e. factor) values of the linear regression equations calculated in the Freedom EVOware® software.

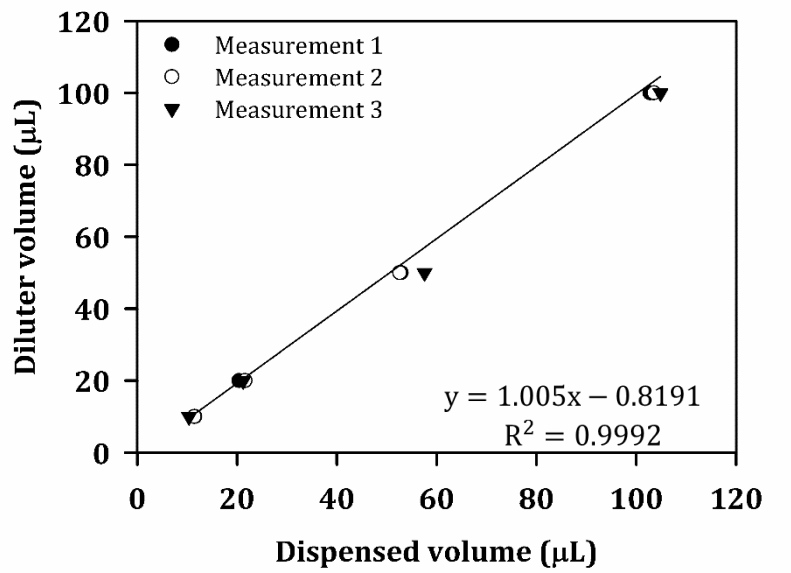

Figure 2.5. Example of calibration of a new liquid class in the liquid handling robot.
This example of calibration shows the four-point calibration curve of tip number 1 with a 4 % w/v PEI solution between 10 and 100 µL. The volume dispensed by the tip was weighted and the equivalent volume calculated with the solution's density value (4 % w/v PEI density = 1030 kg.m^{-3}). Measurements were done in triplicate. To obtain the calibration curve, the experimental dispensed volume data was plotted against the diluter volume (i.e. desired volume) data. The linear regression equation between these two variables was then calculated to obtain the offset and the slope values, which were then introduced into the software's liquid handling robot for accurate liquid handling.

2.4. Mixing Time Scale Studies

2.4.1. Theoretical Calculation of Mixing Time Constants

The theoretical values of the different characteristic mixing times were calculated for the pilot scale flocculation system only since they apply to baffled tanks with fully developed turbulence (Bałdyga and Bourne, 1992, 1999; Vicum et al., 2004). For the calculation of mesomixing time (both mesomixing turbulent dispersion and mesomixing turbulent disintegration) a stationary, homogeneous and isotropic turbulent environment was assumed to exist inside the pilot scale mixing system.

2.4.1.1. Macromixing

Macromixing characteristic time was calculated as described by Bałdyga and Bourne (1999):

$$t_m \approx 3 - 5t_c \qquad \text{(Equation 2.3)}$$

where t_m is the macromixing time (s) and t_c is the circulation time (s). For a six-bladed disc impeller t_c was calculated as below (Bałdyga and Bourne, 1999):

$$Nt_c = 0.85\left(\frac{D_T}{D_i}\right)^2 \qquad \text{(Equation 2.4)}$$

where N is the impeller speed (s^{-1}), D_T is the vessel diameter (m) and D_i is the impeller diameter (m). This equation was assumed to be valid for impeller clearances (C) equal to 1/2 and 1/3 the liquid height (H_L). Refer to Section 2.3.1 for the geometrical specifications of the flocculation vessel and impeller used at pilot scale.

2.4.1.2. Mesomixing

The characteristic time for mesomixing turbulent dispersion was calculated as described by Bałdyga and Bourne (1999):

$$t_d = \frac{Q_b}{\bar{u}D_t} \qquad \text{(Equation 2.5)}$$

where t_d is the dispersive mesomixing time (s), Q_b is the feed rate at which an external fluid is added into the mixing vessel ($m^3.s^{-1}$), ū is the external fluid velocity in the vicinity of the feed pipe through which the liquid is added into the mixing system ($m.s^{-1}$) and D_t is the turbulent diffusivity ($m^2.s^{-1}$). The value of Q_b was calculated as the ratio of flocculant volume added to addition time. The value of ū was approximated by the fluid's mean radial and mean tangential velocities as follows (Bałdyga and Bourne, 1999):

$$\bar{u} = \sqrt{(\bar{u_r})^2 + (\bar{u_t})^2} = \sqrt{(u_r \pi N D_i)^2 + (u_t \pi N D_i)^2} \qquad \text{(Equation 2.6)}$$

where ū is the external fluid velocity in the vicinity of the feed pipe ($m.s^{-1}$), $\bar{u}_r$ is the mean radial velocity ($m.s^{-1}$), $\bar{u}_t$ is the mean tangential velocity ($m.s^{-1}$), u_r is the

radial component of the fluid velocity relative to the tip speed, u_t is the tangential component of the fluid velocity relative to the tip speed, N is the impeller speed (s^{-1}) and D_i is the impeller diameter (m). The radial and tangential components of the fluid velocity relative to the tip speed (u_r and u_t, respectively) were determined from the turbulent flow studies of Wu and Patterson (1989). While the configuration of the vessel used by these authors was the same as the pilot-scale flocculation system used (see Figure 2.1), the dimensions were different. Ratios instead of distances were considered to account for this variation; in particular, the ratio between the radial component (i.e. distance from the vessel central vertical axis to the feed point) and the vessel radius was considered for the calculations of u_r and u_t. The feed point located perpendicularly to the impeller blade at 7.7 cm from the vessel central vertical axis in Wu and Patterson's (1989) work was used to calculate ū. At these conditions u_r and u_t were 0.42 and 0.27, respectively. Turbulent diffusivity was calculated according to Bałdyga and Bourne (1999) as follows:

$$D_t = 5.84 \times 10^{-3} \varepsilon^{1/3} D_i^{4/3} \qquad \text{(Equation 2.7)}$$

where D_t is the turbulent diffusivity ($m^2.s^{-1}$), ε is the local turbulent energy dissipation rate per unit mass of fluid ($W.kg^{-1}$) and D_i is the impeller diameter (m). Local turbulent energy dissipation was calculated applying the experimental flow model described by Bourne and Yu (1994). This model divides the flow generated in a STR by a six-bladed disc turbine in six characteristic flow regions, and offers an estimate of the value of ε in each one of them. The feed point in the pilot-scale flocculation system was located in region 2 of Bourne and Yu's (1994) experimental flow model, and at a relative distance to the tank radius between 0.46 and 0.8 (refer Section 2.3.1 for the detailed configuration of the pilot scale system). At these conditions the experimental flow model stated that:

$$\phi = \frac{\varepsilon}{\varepsilon_{avg}} = 268.7 e^{-4.98 r^*} \qquad \text{(Equation 2.8)}$$

where Φ is the relative local energy dissipation rate, ε is the local turbulent energy dissipation rate per unit mass of fluid ($W.kg^{-1}$), ε_{avg} is the average turbulent energy dissipation rate per unit mass of fluid ($W.kg^{-1}$), r* is the ratio

between the distance from the vessel's central vertical axis to the feed point and the vessel radius. Equation 2.8 was used in all the local turbulent energy dissipation calculations.

The characteristic time for mesomixing turbulent disintegration was calculated as described by Bałdyga and Bourne (1999):

$$t_s = K\left(\frac{\Lambda_c^2}{\varepsilon}\right)^{1/3} \qquad \text{(Equation 2.9)}$$

where t_s is the characteristic time for turbulent disintegration mesomixing (s), K is a constant equal to 2, Λ_c is the macroscale concentration (m) and ε is the local turbulent energy dissipation rate per unit mass of fluid ($W.kg^{-1}$). The value of Λ_c was calculated according to Bałdyga and Bourne (1999) as follows:

$$\Lambda_c = \sqrt{\frac{V_B}{\pi \bar{u} n_f t_f}} \qquad \text{(Equation 2.10)}$$

where Λ_c is the macroscale concentration (m), V_B is the volume of reagent added into the mixing vessel (m^3), ū is the external fluid velocity in the vicinity of the feed pipe ($m.s^{-1}$), n_f is the number of feed points in the mixing vessel and t_f is the feed addition time (s). The value of ū was calculated according to Equation 2.6. Only one feed point was used at pilot scale during the flocculation studies (see Figure 2.1).

2.4.1.3. Micromixing

Micromixing characteristic time was calculated as follows (Bałdyga and Bourne, 1999):

$$t_e = 17.3\left(\frac{\nu}{\varepsilon}\right)^{1/2} \qquad \text{(Equation 2.11)}$$

where t_e is the micromixing time (s), *v* is the kinematic viscosity of the fluid inside the vessel ($m^2.s^{-1}$) and ε is the local turbulent energy dissipation rate per unit mass of fluid ($W.kg^{-1}$).

2.4.2. Experimental Characterisation of Micromixing Time

Micromixing time inside the USD and pilot-scale flocculation vessels was experimentally characterised by a system of fast parallel competing reactions developed by Fournier et al. (1996b) whose yield is sensitive to micromixing.

2.4.2.1. Theoretical Considerations

The experimental method used to calculate micromixing time consists in determining the segregation state of the fluid, which is quantified by the segregation index (X_S). The segregation index is a function of the characteristic reaction time and micromixing time. The reaction time is given by the experimental conditions. The micromixing time is a function of the hydrodynamic conditions encountered inside the reactor; that is, micromixing time depends upon the feed addition time, the feed addition point and the mixing intensity (Fournier et al., 1996a, 1996b). This allows the study of the effect of feed addition time upon the value of X_S to characterise the conditions where micromixing are free from the influence of macromixing and mesomixing time in a semibatch reactor. For a particular vessel and fixed hydrodynamic conditions, the value of X_S gradually decreases as feed addition time increases until its value equals that of the critical addition time (t_{crit}), beyond which the value of X_S remains constant. The value of t_{crit} is not a precise quantity. Instead, t_{crit} designates the transition from a situation where product distribution is inhomogeneous and both meso- and micromixing controlled ($t_f < t_{crit}$), to a situation where reaction rate and product distribution are micromixing controlled ($t_f > t_{crit}$) (Bałdyga and Bourne, 1992; Guichardon and Falk, 2000). At t_f values smaller than t_{crit}, product distribution can also be controlled by macromixing time; macromixing time will be the controlling mechanism when the product concentration gradients develop at the scale of the entire vessel instead of in the vicinity of the feed point, which can occur at very high feed addition rates (Bałdyga et al., 1993).

The segregation state of the fluid is measured by the formation of iodine (I_2) under the influence of an acid (H^+) in an alkaline medium. The formation of iodine is subjected to two fast, parallel competing chemical reactions. These are:

an acid-base neutralisation (Reaction 1) and an oxidation reaction called the Dushman reaction (Reaction 2).

$$H_2BO_3^- + H^+ \leftrightarrow H_2BO_3 \quad \text{(Reaction 1)}$$

$$\frac{5}{6}I^- + \frac{1}{6}IO_3^- + H^+ \leftrightarrow \frac{1}{2}I_2 + \frac{1}{2}H_20 \quad \text{(Reaction 2)}$$

Reaction 1 is instantaneous, whereas Reaction 2 is fast but of the same order of magnitude as the micromixing process. Under perfect micromixing conditions the acid is instantaneously dispersed in the reactive medium and totally consumed by Reaction 1 as it is in stoichiometric defect with respect to the borate ions ($H_2BO_3^-$). In these conditions iodine is not produced since Reaction 2 is comparatively slower. In contrast, if mixing of the acid is not achieved down to molecular scale iodine is produced. That is, when micromixing time is in the same range or larger than the reaction time of Reaction 2, the acid remains inside segregated acid clouds. Following complete consumption of borate ions, the acid can react with iodide (I^-) and iodate (IO_3^-) to produce iodine. Therefore, the formation of iodine is a measure of the segregration state of the fluid. Iodine may further react with the excess iodide to form triiodide (I_3^-) according to Reaction 3.

$$I_2 + I^- \leftrightarrow I_3^- \quad \text{(Reaction 3)}$$

Triiodide has absorption maxima at wavelengths of 288 and 353 nm, although the latter offers less interference with iodide and solvent adsorption. The concentration of triiodide in the fluid can therefore be quantified by the Beer-Lambert law, which states that (Hollas, 2004):

$$Abs_\lambda = \log_{10}\left(\frac{I_0}{I}\right) = \varepsilon_\lambda[x]l \quad \text{(Equation 2.12)}$$

where Abs_λ is the absorbance value obtained at λ nm wavelength (A.U.), I_0 is the intensity of the incident radiation (cd), I is the intensity of the emerging radiation (cd), ε_λ is the molar extinction coefficient at λ nm wavelength of the species being quantified in the sample ($m^2.mol^{-1}$), [x] is the concentration of the species being quantified in the sample ($mol.m^{-3}$) and l is the path length of the beam of light through the sample (m). Substituting the variables for the concentration of triiodide ions at λ equal to 353 nm:

$$[I_3^-] = \frac{Abs_{353}}{l * \varepsilon_{353}}$$ (Equation 2.13)

where $[I_3^-]$ is the concentration of triiodide ions (mol.m^{-3}), Abs_{353} is the absorbance of the bulk measured at the end of the acid injection at 353 nm wavelength (A.U.), l is the path length of the cuvette (m) and ε_{353} is the molar extinction coefficient of triiodide at 353 nm, which for a double-beam spectrophotometer is 2606 m^2.mol^{-1} (Guichardon and Falk, 2000).

The values of the segregation index (X_S) range between 0 and 1. When the value of X_S is equal to 0, the system is perfectly micromixed. And when X_S is equal to 1, the system is completely segregated. Any value between 0 and 1 describes partial segregation, which is calculated as the ratio of the yields for the Dushman reaction (i.e. Reaction 2 or formation of iodine) obtained under imperfect and perfect micromixing (Fournier et al., 1996b; Guichardon and Falk, 2000):

$$X_S = \frac{Y_S}{Y_{ST}}$$ (Equation 2.14)

where X_S is the segregation index, Y_S is the yield of the Dushman reaction under imperfect micromixing conditions, or actual iodine yield, and Y_{ST} is the value of Y_S when micromixing is infinitely slow, or maximum iodine yield.

Under imperfect micromixing conditions, the actual yield of iodine will be the ratio between the moles of acid consumed by the reaction to produce iodine and the total moles of acid injected. At iodide concentrations lower than 1.4x10^{-1} mol.L^{-1}, which is the case in the experimental mixing time studies performed in this thesis (see Table 2.3), the number of acid moles consumed is stoichiometrically proportional to the sum of the final iodine and triiodide concentrations (Fournier et al., 1996b). Thus, the yield of the Dushman reaction under imperfect micromixing conditions (Y_S) is calculated as follows (Guichardon and Falk, 2000):

$$Y_S = \frac{2\left(n_{I_2} + n_{I_3^-}\right)}{n_{H_0^+}} = \frac{2V_l([I_2] + [I_3^-])}{V_B[H^+]_0}$$ (Equation 2.15)

where n_{I_2} is the number of moles of iodine produced (mol), $n_{I_3^-}$ is the number of moles of triiodide produced (mol), $n_{H_0^+}$ is the number of moles of acid

injected (mol), V_l is the working volume of the flocculation vessel (m^3), $[I_2]$ is the final molar concentration of iodine ($mol.m^{-3}$), $[I_3^-]$ is the final molar concentration of triiodide ($mol.m^{-3}$), V_B is the volume of acid injected into the flocculation vessel (m^3) and $[H^+]_0$ is the initial molar concentration of acid or molar concentration of acid in the solution injected ($mol.m^{-3}$). The molar concentration of triiodide achieved after the completion of the fast parallel competing reactions was calculated applying Equation 2.13. The final molar concentration of iodine was determined by combining the mass balance equation for iodide and the equilibrium constant for Reaction 3. The mass balance equation for iodide states that (Guichardon and Falk, 2000):

$$[I^-] = [I^-]_0 - \frac{5}{3}([I_2] + [I_3^-]) - [I_3^-] \quad \text{(Equation 2.16)}$$

where $[I^-]$ is the final molar concentration of iodide ($mol.m^{-3}$), $[I^-]_0$ is the initial molar concentration of iodide ($mol.m^{-3}$), $[I_2]$ is the final molar concentration of iodine ($mol.m^{-3}$) and $[I_3^-]$ is the final molar concentration of triiodide ($mol.m^{-3}$). The equilibrium constant of Reaction 3 is calculated as follows (Guichardon and Falk, 2000):

$$K_B = \frac{[I_3^-]}{[I_2][I^-]} \quad \text{(Equation 2.17)}$$

where the equilibrium constant K_B ($m^3.mol^{-1}$) is a function of the temperature, or T (K). The equilibrium constant of Reaction 3 is calculated as follows (Palmer et al., 1984):

$$\log_{10} K_B = \frac{555}{T} + 7.355 - 2.575 \log_{10} T \quad \text{(Equation 2.18)}$$

where K_B is the equilibrium constant of the reaction ($m^3.mol^{-1}$) and T is the temperature at which the reaction takes place (K). When Equation 2.16 and Equation 2.17 are combined, a second-order algebraic equation where iodine concentration is the unknown variable is obtained:

$$-\frac{5}{3}[I_2]^2 + \left([I^-]_0 - \frac{8}{3}[I_3^-]\right)[I_2] - \frac{[I_3^-]}{K_B} = 0 \quad \text{(Equation 2.19)}$$

where $[I_2]$ is the final molar concentration of iodine (mol.m^{-3}), $[I^-]_0$ is the initial molar concentration of iodide (mol.m^{-3}), $[I_3^-]$ is the final molar concentration of triiodide (mol.m^{-3}) and K_B is the equilibrium constant of Reaction 3 (m^3.mol^{-1}).

When micromixing is infinitely slow, Reaction 1 and Reaction 2 are considered quasi-instantaneous compared to the mixing process. Under these conditions, the acid ions are consumed in proportion to the local concentration of borate and iodate ions, and the formation of iodine only relates to the stoichiometric ratio of the reactants (Fournier et al., 1996b; Guichardon and Falk, 2000). The selectivity between Reaction 1 and Reaction 2 in these conditions is written as (Fournier et al., 1996b):

$$\frac{X_2}{X_1} = \frac{6[IO_3^-]_0}{[H_2BO_3^-]_0} \qquad \text{(Equation 2.20)}$$

where X_1 and X_2 are the respective extents of Reaction 1 and Reaction 2. Therefore, the maximum iodine yield, or $Y_{ST,}$ is calculated as below (Fournier et al., 1996b; Guichardon and Falk, 2000):

$$Y_{ST} = \frac{X_2}{X_1 + X_2} = \frac{6[IO_3^-]_0}{[H_2BO_3^-]_0 + 6[IO_3^-]_0} \qquad \text{(Equation 2.21)}$$

where X_2 is the extent of Reaction 2, X_1 is the extent of Reaction 1, $[IO_3^-]_0$ is the initial molar concentration of iodate ions (mol.m^{-3}) and $[H_2BO_3^-]_0$ is the initial molar concentration of borate ions (mol.m^{-3}). The initial concentration of borate ions is known because when boric acid (H_3BO_3) reacts with a strong base such as sodium hydroxide (NaOH), both used in the experimental method employed in this thesis to calculate micromixing time (see Table 2.3), the following three reaction products are generated (Fournier et al., 1996b):

$$H_3BO_3 + OH^- \leftrightarrow H_2BO_3^- + H_2O \qquad \text{(Reaction 4.a)}$$

$$H_2BO_3^- + OH^- \leftrightarrow HBO_3^{2-} + H_2O \qquad \text{(Reaction 4.b)}$$

$$HBO_3^{2-} + OH^- \leftrightarrow BO_3^{3-} + H_2O \qquad \text{(Reaction 4.c)}$$

The concentration of borate ions at equilibrium is pH dependent. The molar concentrations of sodium hydroxide and boric acid employed in the experimental method used in this thesis to calculated micromixing time (see Table 2.3) led to a

buffer pH of 9.14. Since the pKa value of Reaction 4.a is also 9.14 (Guichardon and Falk, 2000), sodium hydroxide and boric acid are assumed to have totally reacted to form an equimolecular mixture of boric acid and borate ions (Fournier et al., 1996b; Guichardon and Falk, 2000). Therefore, the initial concentration of boric acid was equal to the initial concentration of borate ions.

Finally, borate ions have a twofold role. They are the reactants in Reaction 1, and they act as buffering species to keep the pH of the solution constant. The control of the pH is of utmost importance because iodine formation is thermodynamically possible in the absence of acid aggregates when the mean pH value is lower than pH*, where pH* is iodine dismutation pH. When pH < pH*, the iodide and iodate ions, which are present in excess at the experimental conditions employed to calculate micromixing time (see Table 2.3), can react with the acid released by Reaction 4.a to form iodine and shift the equilibrium of Reaction 4.a to the left. To ensure that the formation of iodine is only due to bad micromixing, the buffer composition used in the experiments has to guarantee pH working values between 8.5 and 9.5 since the value of pH* is close to 7. The dissociation of iodine at extreme alkaline pHs also needs to be avoided by not working at high pH values (Fournier et al., 1996b; Guichardon and Falk, 2000).

2.4.2.2. Experimental Conditions

The experiments to calculate micromixing time were performed at room temperature (i.e. 22°C) with the following reactant concentrations, which were adopted from the work of Guichardon and Falk (2000). First, stock solutions of boric acid, sodium hydroxide (VWR International, BDH Prolabo, Leuven, Belgium), potassium iodide (KI) and potassium iodate (KIO_3) were prepared as described in Table 2.3. All stock solutions were prepared with laboratory deionised water as a diluent and just before use to avoid the oxidation of the reagents. The volumes of stock solution described in Table 2.3 were carefully pipetted into the flocculation systems in the following sequence to guarantee that the iodide and iodate ions coexisted in a basic solution with the aim to prevent the thermodynamic formation of iodine. Boric acid and sodium hydroxide were first mixed to obtain an alkaline buffer solution. Potassium iodide was then added, followed by potassium iodate and deionised water to the final working

volume of the flocculation system. The molar composition of the bulk solution before acid addition is detailed in Table 2.3. At this point, the pH of the bulk solution was 9.14. After setting the impeller to the required speed, a volume equal to $8x10^{-3}$ times the vessel's working volume of 0.5 M sulphuric acid (98 % v/v concentrate, Merck KGaA, Darmstadt, Germany) was added to the bulk solution. Two minutes after the end of the acid injection, the absorbance of the resultant solution was measured at 353 nm wavelength (BioMate™ 3S Spectrophotometer, Eppendorf, Hamburg, Germany) using disposable UVette® cuvettes (Eppendorf, Hamburg, Germany).

Published literature (Bałdyga and Bourne, 1999; Bourne et al., 1989, 1995; Gholap et al., 1994) shows that fourfold to sevenfold increases in the viscosity of the bulk solution cause significant changes in the micromixing time. However, the differences in viscosity between the flocculant stock solutions, the clarified cell culture material used during the flocculation experiments (see Section 4.3.2 and Section 5.3.1) and the water-based solutions used to characterise micromixing time (see Table 2.3) were found to be modest in comparison. Thus, no viscosity-raising additives were added to the buffering solution during the micromixing time experiments.

Table 2.3. Composition and stock solution volumes used in the experimental characterisation of micromixing.
Laboratory deionised water was used as the diluent. Reactants were weighted on an analytical scale (Ohaus Pioneer™ PA413, Ohaus Corporation, USA) and volumetric quantities were measured by calibrated pipettes. The table details the composition of the stock solutions prepared for the micromixing time studies performed (Stock solution), the volume of each stock solution used to prepare the final buffering solution in each flocculation system before acid addition (Micromixing time studies), and the final composition of the bulk fluid before acid addition (Final molar concentration).

		H_3BO_3	NaOH	KI	KIO_3	H_2O
Stock solution	*Weight (g)*	22.5	7.27	3.87	0.99	-
	Water volume (mL)	600	200	20.0	200	-
Micromixing time studies	*Pilot scale (mL)*	450	150	15.0	150	735
	Microwell (µL)	240	77.0	8.00	80.0	395
Final molar concentration *($x10^{-3}$ mol.L^{-1})*		182	90.9	11.7	2.31	-

2.5. Scale-Up Correlations for Flocculation Studies

Average turbulent energy dissipation rate per unit mass of fluid (ε_{avg}) and impeller tip speed (v_{tip}) are the scale-up "rules of thumb" employed during flocculation scale-up. Refer to Section 1.5.2 for the equations used to calculate ε_{avg} and v_{tip}.

At pilot scale P_o was determined from the literature. When Reynolds number (Re) is larger than $3x10^3$, the P_o of a six-bladed disc turbine is 5.8 (McCabe et al., 2005); the change from a turbulent to a transitional flow regime was considered to take place at $Re < 10^3$ (Norwood and Metzner, 1960). A reduction of 5.6 % in the value of P_o at pilot scale was considered when $Re < 3x10^3$ (Bates et al., 1963). The Reynolds number of the pilot-scale flocculation system was calculated as described in Section 2.6. The P_0 of the magnetic impeller from the USD flocculation system was empirically estimated as described in Section 4.3.1.

2.6. Reynolds Number for Stirred Tank Reactors

The Reynolds number for the pilot-scale flocculation vessel (see Section 2.3.1) was calculated as follows (Doran, 1995):

$$Re = \frac{ND_i^2\rho}{\mu} \qquad \text{(Equation 2.22)}$$

where Re is the impeller Reynolds number, N is the impeller speed (s^{-1}), D_i is the impeller diameter (m), ρ is the fluid density ($kg.m^{-3}$) and μ is the fluid dynamic viscosity (Pa.s). In a baffled stirred tank reactor of standard geometrical configuration (i.e. H_L:D_T = 1:1; D_i:D_T = 1:3; D_T:D_b = 1:10) equipped with a six-bladed disc turbine of standard geometrical ratios (i.e. H_{ib}:D_i = 1:4; W_{ib}:D_i = 1:5) and positioned at 1/3 the tank diameter from the bottom of the vessel, the change from a turbulent to a transitional flow regime was considered to take place at $Re < 10^3$ (Norwood and Metzner, 1960).

2.7. Flocculation Studies

Flocculation experiments were always performed at room temperature (i.e. 22°C) and using PEI (linear, MW = 50,000 - 100,000 Da; MP Biomedicals LLC, Illkirch-Graffenstaden, France) as the flocculating reagent. The volume of flocculant stock solution added into the flocculation vessel was always 5 % of the vessel's liquid working volume. Different PEI stock solutions were used depending on the final PEI concentration. Flocculant stock solutions were prepared by mixing the required amount of PEI with a buffer of the same pH and ionic strength conditions as these of the flocculation experiment. The effect that PEI, a weak base (Shepherd and Kitchener, 1956), had on the final pH was assumed to be negligible due to the stronger buffering capacity of the buffers used. Flocculant stock solutions were prepared the day before the experiment and allowed to mix overnight to ensure the flocculant was well mixed.

2.7.1. Mammalian Cell Centrate

2.7.1.1. Pilot Scale

Flocculation was performed in a 1.5 L STR of standard geometrical configuration at pH 7 with controlled flocculant additions at 13 mm from the impeller blade using a calibrated syringe pump. The volume of PEI stock solution added into the vessel was always equal to 75 mL. Refer to Section 2.3.1 for a description of the pilot-scale flocculation system and its experimental set-up. Flocculant concentration, impeller speed and flocculant addition rate varied depending on the flocculation study. After the addition of PEI into the vessel, the flocs were allowed to mature for 10 minutes. Phosphate buffered saline (obtained from PBS tablets) was the diluent used to prepare the PEI stock solutions employed at this scale.

2.7.1.2. Laboratory Scale

Flocculation was performed in a 70 mL working volume glass vessel (see Section 2.3.2) by manually pipetting 3.5 mL of PEI stock solution as close to the impeller blade as possible but without disturbing its rotation. The flocculant was added into the vessel in a single addition. Flocculation was performed at different

pHs, PEI concentrations and with different impeller designs. At this scale, flocs were allowed to mature for 15 minutes. The flocculant stock solutions and the buffers used for their preparation varied depending on the pH and the PEI concentration conditions of the experiment.

2.7.1.3. Ultra Scale-Down Scale

Flocculation was performed at pH 7 in the 96-well mixing system described in Section 2.3.3 with controlled flocculant additions at 1 mm from the magnetic impeller using a Freedom EVO® 150 Tecan (Männedorf, Switzerland) liquid handling platform. The volume of PEI stock solution added into each well was always equal to 40 μL. Flocculant concentration, impeller speed and flocculant addition rate varied depending on the flocculation study. To accurately aspirate and dispense the PEI stock solutions, new liquid classes were created for the liquid handling robot (see Section 2.3.3). Flocculation was performed in four microwells (D4, D5, D6, D7) or in the entire 96-well microplate depending on the flocculation study. After flocculant injection, the flocs were allowed to mature for 10 minutes. Phosphate buffered saline (obtained from PBS tablets) was the diluent used to prepare the PEI stock solutions employed at this scale.

2.7.2. Clarified Yeast Homogenate

Flocculation was performed at pH 6.5 by adding a 4 % w/v PEI stock solution to a final flocculant concentration of 0.2 % v/v. Impeller speed and flocculant addition rate varied depending on the flocculation study. An aging time of 10 minutes was allowed for the flocs to mature; shorter ageing times have successfully flocculated centrifuged yeast homogenates when using PEI (Milburn et al., 1990). At USD scale, flocculation was performed in four different wells (D4, D5, D6, D7). Refer to Section 2.3.1 and Section 2.3.3 for a detailed description of the set-up and the configuration of the flocculation systems used at pilot and USD scale, respectively.

2.8. Depth Filtration Studies

2.8.1. Ultra Scale-Down Constant Pressure Filtration

Ultra scale-down filtration was performed using a robotic liquid handling platform (Freedom EVO® 100, Tecan, Männedorf, Switzerland) equipped with a two-position high-throughput vacuum separation module (TeVacS, Tecan, Männedorf, Switzerland). This module allowed operating at constant vacuum pressures between 100 and 700 mbar. Filter discs (6.4 mm diameter, 0.32 cm^2 surface area) were cut in-house from 60 x 60 cm filter sheets (DE45 grade Millistak+® DE media series, EMD Millipore, MA, USA) or 50 mm filter discs (05SP grade Zeta Plus™ SP series, 3M Purification Inc., St Paul, USA) using a drill and a hardened carbon steel hollow punch of ¼" diameter (Cromwell Group Ltd, Leicester, UK). Refer to Table 2.4 for the filter specifications. The cut-out discs were then placed in the correct orientation into the lower part of the custom-made filter housings (Mechanical workshop, UCL) (Figure 2.6.A). The upper part of the filter housing, which works as a reservoir of up to 5 mL for the process material, was screwed onto the bottom part. The effective filtration area was reduced to 0.28 cm^2 as a consequence. The assembled filter housings were then placed within the filtration block (Mechanical workshop, UCL), which was fitted onto the vacuum separation module (Figure 2.6.B) with filtrate collection containers located underneath each housing. Filtration was performed at room temperature, normal flow filtration mode (i.e. flow perpendicular to the filter surface) and constant pressure. Filtration was monitored in real-time (3 - 9 seconds interval) in an associated Microsoft Excel spreadsheet thanks to the robot's liquid level detection system. The output data obtained was cumulative filtrate volume *versus* filtration time. Prior to filtration with process material, 15 mL of deionised water were passed through the filter (536 $L.m^{-2}$) at the same operating pressure the filtration experiment was performed in order to wet the filter and calculate the filter water flux. Filter water flux rates were calculated to ensure correct filter orientation within the filter housing and satisfactory filter performance, as well as to calculate filter resistance according to the following equations (Doran, 1995):

$$J = \frac{1}{A} * \frac{dV}{dt} = \frac{\Delta P}{\mu R_f} \quad \text{(Equation 2.23)}$$

$$R_f = \frac{A\,\Delta P}{\mu \frac{dV}{dt}} \quad \text{(Equation 2.24)}$$

where J is the filter flux rate ($L.m^{-2}.h^{-1}$), A is the effective filtration area (m^2), dV/dt is the instantaneous volumetric flow rate ($m^3.s^{-1}$), ΔP is the pressure drop across the filter (Pa), μ is the dynamic viscosity of the fluid (Pa.s) and R_f is the filter resistance (m^{-1}). While the dV/dt values were calculated from the first derivative of the linear regression obtained for the water flux *versus* the pressure drop data, μ was constant and equal to the dynamic viscosity of water at 22°C, which is $9.7x10^{-4}$ Pa.s (Perry and Green, 2008). After the water flux measurements, the process material was filtered until the initial flux value had dropped by 90 %. Filter loading was kept constant in all filtration experiments.

Table 2.4. Specifications and operating conditions of the depth filters used in the ultra scale-down, constant pressure filtration experiments.

Thesis chapter	Filter	Specifications	ΔP (mbar)
6	Millistak+® DE45	1-0.50 µm; 1 layer; Positively charged; Max ΔP 2.1 bar; Flushing 50 $L.m^{-2}$ EMD Millipore	100 400 700
6	ZetaPlus™ 05SP grade	10-1.50 µm; 1 layer; Positively charged; Max ΔP 2.4 bar; Flushing 54 $L.m^{-2}$ 3M Purification Inc.	100 400 700

The data from the constant pressure, normal flow filtration experiments (i.e. flux decline data) was analysed using the four classical filtration models: pore blockage, intermediate pore blockage, pore constriction, and cake filtration (van Reis and Zydney, 2007). The governing equations describing these four filtration models when operating at constant pressure are summarised in Table 2.5. These equations assume that the filter fouling rate is proportional to the rate at which the fouling material is brought onto the filter by the filtration flow, thus neglecting any back-transport or detachment mechanisms (van Reis and Zydney,

2007). The linearised forms of the four constant pressure filtration models were used to analyse the filtration data and for filtration model identification purposes.

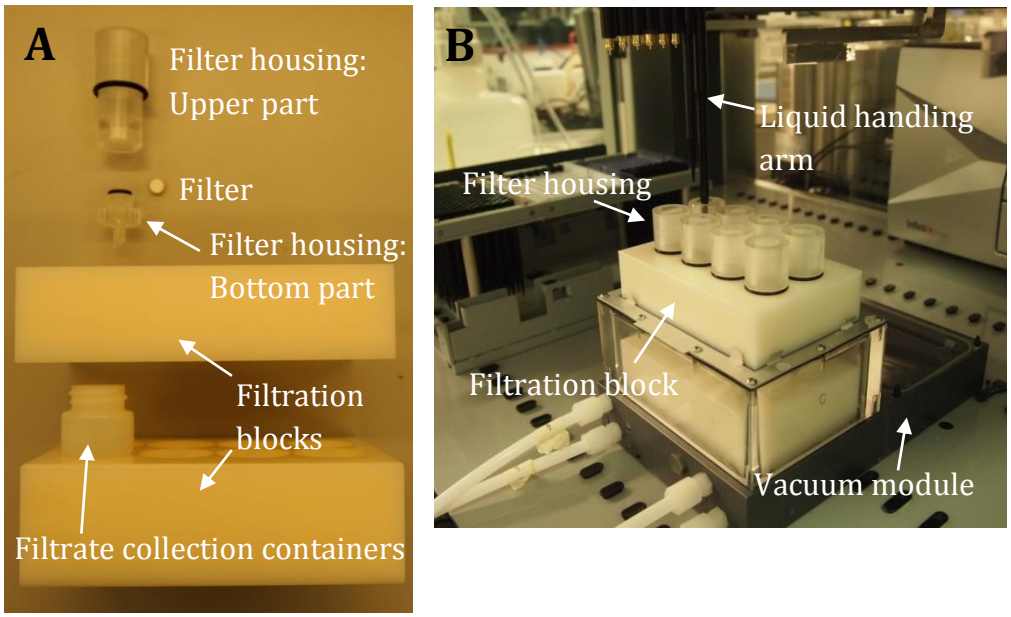

Figure 2.6. Detailed experimental set-up of the ultra scale-down, constant pressure normal flow filtration methodology.
A*. Custom-made (Mechanical Workshop, UCL) ultra scale-down normal flow filtration set-up.* ***B****. Ultra scale-down filtration set-up fitted onto the high-throughput vacuum separation module (TeVacS, Tecan) located on the deck of the robotic liquid handling platform (Freedom EVO® 100, Tecan).*

Table 2.5. Governing equations for the four classic filter fouling models during constant pressure filtration.
The equations were adapted from van Reis and Zydney (2007). The variables are as follows: Q is the filtrate flow rate ($m^3.s^{-1}$), Q_0 is the initial filtrate flow rate ($m^3.s^{-1}$), V is the filtrate volume (m^3), t is the filtration time (t), β, α, and δ are constants.

Constant pressure	Flow rate (Q)	Linearised form
Pore blockage	$\frac{Q}{Q_0} = e^{-\beta t}$	$\ln Q = \alpha t + \delta$
Intermediate blockage	$\frac{Q}{Q_0} = (1+\beta t)^{-1}$	$\frac{1}{Q} = \alpha t + \delta$
Pore constriction	$\frac{Q}{Q_0} = (1+\beta t)^{-2}$	$\frac{t}{V} = \alpha t + \delta$
Cake filtration	$\frac{Q}{Q_0} = (1+\beta t)^{-1/2}$	$\frac{t}{V} = \alpha V + \delta$

2.8.1.1. Modified Pore Constriction Model

Lau and co-workers (2013) re-wrote the linearised equation for the pore constriction constant pressure filtration model to account for the significant filtration changes occurring in timescales of the order of 1 to 60 seconds when employing the USD constant pressure filtration methodology. The modified pore constriction model can identify the filtration start-up phase, that is, the moment when the depth filter discs placed in the USD filtration housings are operating as designed (i.e. when the filters are compressed and filled with process fluid). The linearised modified pore constriction model is written as (Lau et al., 2013):

$$\frac{(t - t_0)}{(V^* - V_0^*)} = \frac{1}{(V_{max}^* - V_0^*)}(t - t_0) + \frac{1}{Q_0^*} \qquad \text{(Equation 2.25)}$$

where t is the filtration time (s), t_0 is the filtration time value when the start-up phase is completed (s), V^* is the cumulative filtrate volume per filter area ($L.m^{-2}$), V_0^* is the value of cumulative filtrate volume per filter area when the start-up phase is completed ($L.m^{-2}$), V_{max}^* is the maximum predicted filtration throughput before complete filter plugging ($L.m^{-2}$) and Q_0^* is the initial filtrate flow rate per filter area ($L.m^{-2}.s^{-1}$).

Equation 2.25 was applied when the pore constriction model was the filtration model that best fitted the USD constant pressure depth filtration data. The values of t_0 and V_0^* were identified for each filtration run. The calculated t_0 values ranged from 4.5 to 8.3 seconds. The methodology used to identify t_0 and V_0^* is described in Figure 2.7 to Figure 2.9 with an example of calculation. First, the normalised cumulative filtrate volume (V^*) was plotted against filtration time (t) (Figure 2.7). The line of best fit was determined, making sure there was a good fit for the early filtration period (i.e. t < 20 seconds). A fourth order polynomial fit was obtained for all the filtration runs. The modified pore constriction model (Equation 2.25) was then plotted for different theoretical values of t_0 (i.e. t_0 = 1, t_0 = 2, etc.) (Figure 2.8). The intercepts of the linear best fit equations obtained for each value of t_0, that is, the values of Q_0^*, were recorded. The line of best fit obtained from plotting V^* over t (fourth order polynomial) (Figure 2.7) was used to provide the first derivative dV^*/dt values for filtration times (t) ranging from 0 to 11 seconds. The resultant values are plotted in Figure 2.9. In this plot the Q_0^* values recorded from Figure 2.8

were also graphically represented to determine the start-up filtration time (t_0). The value of t_0 for the filtration run was that of the filtration time (t) in Figure 2.9 where dV^*/dt was equal to Q_0^*. Finally, the value of V_0^* was calculated substituting t for t_0 in the experimental line of best fit (fourth order polynomial) obtained in Figure 2.7.

Ultra scale-down depth filtration performance was assessed based upon (i) the maximum predicted filtration throughput before complete filter plugging (V_{max}^*) and (ii) filtrate clarification as described by the filtrate OD_{600} measurements performed as described in Section 2.11.1.

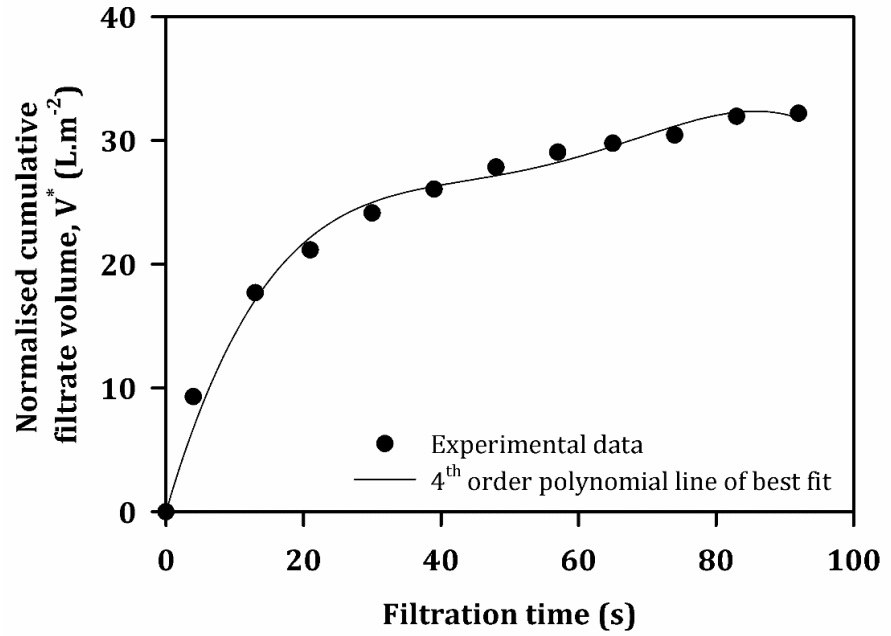

Figure 2.7. Example of calculation of the filtration start-up phase during ultra scale-down constant pressure filtration – Step 1.
The figure represents the normalised cumulative filtrate volume data against filtration time. This example data set was obtained when using the ultra scale-down constant pressure filtration system to depth filter HCD mammalian cell centrate flocculated using the ultra scale-down flocculation device described in Section 2.3.3. Flocculation conditions were: 0.30 % w/v PEI and 1 µL.s^{-1} flocculant addition rate. Filtration conditions were: 700 mbar constant vacuum pressure, DE45 depth filter media (EMD Millipore). The R^2 value of the line of best fit was 0.99.

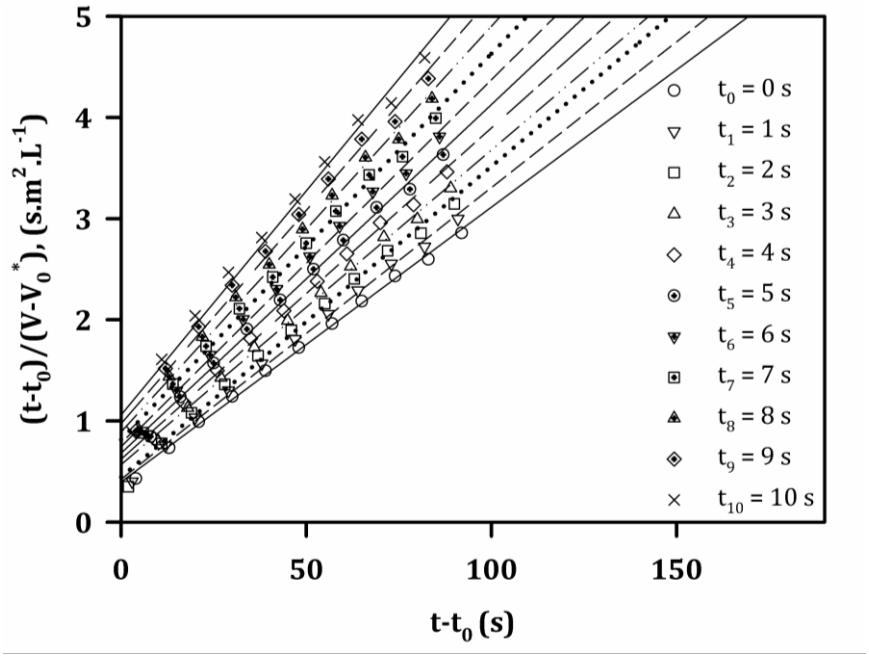

Figure 2.8. Example of calculation of the filtration start-up phase during ultra scale-down constant pressure filtration – Step 2.

The data plotted in Figure 2.7 was transformed using the modified pore constriction model (Equation 2.25) with t_0 values ranging from 0 to 10 seconds. Linear lines of best fit ($R^2 > 0.99$) were calculated for each data set and are plotted in the figure. The y-axis intercept of the lines of best fit corresponded to $1/Q_0^*$, and the slope to $1/V_{max}^*$.

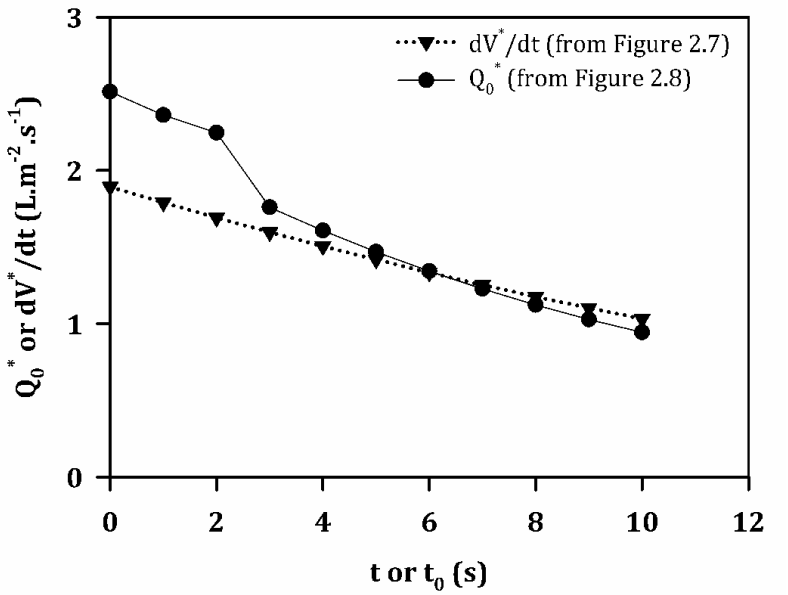

Figure 2.9. Example of calculation of the filtration start-up phase during ultra scale-down constant pressure filtration – Step 3.

The dV^*/dt values at different filtration times (t) were obtained from the first derivative of the line of best fit for the experimental filtration data plotted in Figure 2.7. The Q_0^* values were the y-axis intercept of the lines of best fit obtained for the transformed data at different t_0 (Figure 2.8). The intercept between the dV^*/dt and Q_0^* curves plotted in the figure corresponds to the value of t_0, that is, the value of filtration time when the start-up phase is completed. In this example t_0 = 6 s and Q_0^* = 1.34 $L.m^{-2}.s^{-1}$ or 4824 $L.m^{-2}.h^{-1}$.

2.8.2. Laboratory-Scale Constant Flux Filtration

Constant flux filtration was performed at laboratory scale with an ÄKTAcrossflow filtration system controlled by Unicorn version 4.0 software (GE Healthcare, Uppsala, Sweden) that monitored the cumulative filtrate volume, filtrate absorbance at 280 nm wavelength (Abs_{280}), filtrate pH, inlet pressure (P_i), pressure drop (ΔP) and flux. The system was primed with 0.2 litres of process material before every filtration run. Constant flux filtration was performed at room temperature and normal flow filtration mode. Filtration was stopped when the maximum P_i specified by the manufacturer of the filter was reached, or when all the process material was filtered. Filtrate was manually collected in 10 mL fractions allowing the off-line measurement of filtrate OD_{600} and filtrate Abs_{280} with a spectrophotometer according to Section 2.11.1. The first five 10 mL fractions were always discarded to avoid filtrate dilution due to the presence in the system of buffer used to flush the filters. The remaining filtrate fractions were pooled and either (i) aliquoted in 50 mL tubes and stored at -80°C for future analysis and/or processing; (ii) stored at 4°C for next-day processing; or (iii) immediately processed through another filter.

Different depth filter capsules from different manufacturers were employed depending upon the aim of the study. Sterile filtration was always performed with the same filter type. Table 2.6 describes the filters used and their specifications, as well as the operating conditions employed. Phosphate buffered saline (obtained from PBS tablets) filtered through an absolute 0.22 µm polyethersulfone filter (Stericup® filter units, Millipore, MA, USA) was used to flush the filters. Connection adapters were purchased from Cole-Parmer International (Court Vernon Hills, IL, USA).

The data from the constant flux, normal flow filtration experiments was analysed using the four classical models: pore blockage, intermediate pore blockage, pore constriction, and cake filtration (van Reis and Zydney, 2007). The governing equations describing these four filtration models when operating at constant flux are summarised in Table 2.7. These equations assume that the filter fouling rate is proportional to the rate at which the fouling material is brought onto the filter

by the filtration flow, thus neglecting any back-transport or detachment mechanisms (van Reis and Zydney, 2007). The linearised forms of the four constant flux filtration models were used to analyse the filtration data and for filtration model identification purposes.

Table 2.6. Specifications and operating conditions of the filter capsules used in the laboratory scale, constant flux filtration experiments.

Thesis chapter	Filter	Specifications	Flux (LMH)
6 - 7	Clarisolve® 40MS µPod® (CS40MS01L3)	40 µm particles; 23 cm^2; 8 layers; Positively charged; Max P_i 2.1 bar; Flushing 36 min at 3.8 $mL.min^{-1}$ EMD Millipore	100
7	ZetaPlus™ BC25 capsule EXT grade 60ZA05A (BC0025S60ZA05A)	3-0.30 µm; 25 cm^2; 2 layers; Positively charged; Max P_i 2.75 bar; Flushing 2.7 min at 50 $mL.min^{-1}$ 3M Purification Inc.	130
7	ZetaPlus™ BC25 capsule EXT grade 90ZA05A (BC0025S90ZA05A)	3-0.20 µm; 25 cm^2; 2 layers; Positively charged; Max P_i 2.75 bar; Flushing 2.7 min at 50 $mL.min^{-1}$ 3M Purification Inc.	130
7	SartoScale Disposable Sartopore® 2 0.45/0.2 µm (5445307HS--FF)	0.45/0.2 µm; 17.3 cm^2; 1 layer; No charge; Max P_i 4 bar; Flushing 2.7 min at 50 $mL.min^{-1}$ Sartorius (Epsom, Surrey, UK)	100 130

Table 2.7. Governing equations for the four classic filter fouling models during constant flux filtration.
The equations were adapted from van Reis and Zydney (2007). The variables are as follows: P is the pressure across the filter (Pa), P_0 is the pressure across the filter at the start of the filtration process (Pa), V is the filtrate volume (m^3), t is the filtration time (t), β, α, and δ are constants.

Constant flux	Pressure (P)	Linearised form
Pore blockage	$\frac{P}{P_0} = (1 - \beta t)^{-1/2}$	$\frac{1}{P^2} = \alpha - \delta V$
Intermediate blockage	$\frac{P}{P_0} = (1 - \beta t)^{-1}$	$\frac{1}{P} = \alpha - \delta V$
Pore constriction	$\frac{P}{P_0} = (1 - \beta t)^{-2}$	$\frac{1}{P^{1/2}} = \alpha - \delta V$
Cake filtration	$\frac{P}{P_0} = 1 + \beta t$	$P = \alpha + \delta V$

2.9. Affinity Chromatography

Affinity chromatography was performed with a 4.7 mL MabSelect SuRe pre-packed chromatography column (HiScreen MabSelect SuRe, GE Heathcare, Uppsala, Sweden) with 30 $mg.mL^{-1}$ theoretical dynamic binding capacity. The protocol consisted of a pre-rinse step followed by equilibration, loading, three post-load washing steps, elution, strip, regeneration and neutralisation. Table 2.8 describes the buffer column volumes (CVs), buffer composition and the volumetric and linear velocities used in each chromatographic step. The column was stored at 4°C in 20 % ethanol. All buffers used were filtered through an absolute 0.22 µm polyethersulfone filter (Stericup® filter units, Millipore, MA, USA).

An ÄKTA avant chromatographic system (GE Healthcare, Uppsala, Sweden) that allowed in-line Abs_{280}, pH and conductivity measurements was used. The built-in cooling fraction collector enabled the collection of 2 mL fractions during the run as well as the storage of samples at 5°C. Unicorn 6.1 software (GE Healthcare, Uppsala, Sweden) was used for system control, data collection and data analysis. Sample injection was automatic.

2.10. Analytical Methods

2.10.1. Quantification of Total Protein Concentration

Samples were centrifuged (Eppendorf 5415R, Eppendorf, Hamburg, Germany) at 216.7 rps and 4°C for 30 minutes in 1 mL tubes to remove the solid particulates before protein quantification analysis. Total protein concentration was determined using a bicinchoninic acid (BCA) kit (Pierce™ BCA protein assay, Thermo Scientific, Rockford, USA) and following the manufacturer's protocol for the microplate procedure. Absorbance measurements at 562 nm wavelength were performed with a microplate reader (Safire$^{2™}$, Tecan Group Ltd., Maännedorf, Switzerland) as described in Section 2.11.1. Measurements were performed in triplicate in flat bottom transparent 96-well microplates (Sarstedt AG & Co, Nümbrecht, Germany).

Table 2.8. Affinity chromatography protocol.

Step	Buffer composition	CVs	Volumetric & linear velocity (mL.min^{-1} & cm.h^{-1})
Pre-rinse	0.1 M sodium hydroxide	3	3.13 / 400
Equilibration	50 mM sodium phosphate, 250 mM sodium chloride pH 7.0	6	3.13 / 400
Load	Sample	N/A	1.57 / 200
Wash 1	50 mM sodium phosphate, 250 mM sodium chloride pH 7.0	2	1.57 / 200
Wash 2	50 mM sodium phosphate, 2.0 M sodium chloride pH 7.0	4	3.13 / 400
Wash 3	50 mM sodium phosphate, 250 mM sodium chloride pH 7.0	2	3.13 / 400
Elution	10 mM sodium formate pH 3.5	5	3.13 / 400
Strip	100 mM citric acid pH 2.1	2 - 6	3.13 / 400
Regeneration	0.1 M sodium hydroxide	3	3.13 / 400
Neutralisation	50 mM sodium phosphate, 250 mM sodium chloride pH 7.0	6	3.13 / 400

2.10.2. Quantification of Monoclonal Antibody Concentration

Quantification of the mAb expressed by the GS-CHO mammalian cell lines used was performed via high performance liquid chromatography (HPLC) using an Agilent 1200 Series HPLC system (Agilent Technologies LDA UK Ltd, Stockport, UK) and a 1 mL HiTrap Protein G HP pre-packed chromatography column (GE Healthcare Life Sciences, Little Chalfont, UK). All samples were centrifuged (Eppendorf 5415R, Eppendorf, Hamburg, Germany) at 216.7 rps and 4°C for 30 minutes to remove any particulates present in them. To determine the unknown mAb concentration in the tested samples, a standard curve was prepared from serial dilutions of a reference standard which was cell-line specific. All dilutions were performed using the equilibration buffer. Samples and reference standard dilutions were loaded into a 0.5 mL HPLC round bottom microplate (CrossLab 96-well plate, Agilent Technologies LDA UK Ltd, Stockport, UK) by pipetting 300 µL per well. The microplate was then covered with a silicone plate seal (Pre-Slit Well Cap, ThermoFisher Scientific Inc., Rockford, USA) to minimise liquid losses through evaporation. Reference standards were measured in duplicate and samples in triplicate. Protein was detected by UV absorbance at 280 nm wavelength. The elution peak areas of both the reference standards and the samples were recorded, and the unknown mAb concentration was determined by interpolation from the reference standard curves generated.

Different HPLC methods were employed depending on the cell line used. For the LCD mammalian cell culture (i.e. CY01 cell line), the column was equilibrated for 4.0 minutes at 1 $mL.min^{-1}$ with 20 mM sodium phosphate, pH 7.0, and then loaded with 100 µL of sample at 2 $mL.min^{-1}$. The column was then washed for 8 minutes with equilibration buffer pumped at 2 $mL.min^{-1}$. Elution was performed with 20 mM glycine, pH 2.8 pumped at 2 $mL.min^{-1}$ for 3 minutes. A post-elution wash with equilibration buffer pumped at 2 $mL.min^{-1}$ for 4 minutes followed. Finally, the column was stripped for 1 minute with elution buffer pumped at 2 $mL.min^{-1}$ before regenerating the column by gradually reducing the elution buffer to 0 % v/v and increasing the equilibration buffer to 100 % v/v. The reference

standard for the LCD mammalian cell culture samples was purified IgG_4 expressed in the CY01 cell line present at a concentration of 2.8 $g.L^{-1}$.

In the HPLC method used with HCD mammalian cell samples (i.e. Xceed™ cell line), the column was first equilibrated for 2.0 minutes at 2.0 $mL.min^{-1}$ with 20 mM sodium phosphate, 110 mM sodium chloride, pH 7.0, and then loaded with 100 µL of sample at 2 $mL.min^{-1}$. The column was then washed with equilibration buffer for 2.5 minutes at 2 $mL.min^{-1}$. A second wash with 20 mM sodium phosphate, 500 mM sodium chloride, pH 7.0 pumped at 2 $mL.min^{-1}$ for 4.0 minutes was introduced to elute the interfering flocculant. The column was next re-equilibrated for 4.0 minutes with equilibration buffer at 2 $mL.min^{-1}$ before eluting with 20 mM glycine, pH 2.8 pumped at 2 $mL.min^{-1}$ for 5.0 minutes. A post-elution wash with equilibration buffer pumped at 2 $mL.min^{-1}$ for 2.0 minutes followed before stripping the column with elution buffer at 2 $mL.min^{-1}$ for 1.5 minutes. Finally, the column was regenerated for 2 minutes by gradually increasing at 2 $mL.min^{-1}$ the equilibration buffer from 0 to 100 % v/v. The reference standard used with the HCD mammalian cell samples was donated by Lonza Biologics (Slough, UK) and consisted of a purified IgG_4 expressed in the Xceed™ cell line present at a concentration of 8.2 $g.L^{-1}$.

2.10.3. Quantification of DNA Concentration

The content of DNA in the samples was quantified using a commercially available fluorometric assay (Quant-iT™ PicoGreen® dsDNA assay kit, Invitrogen, Paisley, UK). The method was carried out according to the manufacturer's protocol using a 96-well, flat bottom black microplate (Nunc™ Microplate, 96 well plate non-treated non-sterile without lid black, ThermoFisher Scientific, MA, USA). Samples were diluted in 1 x Tris-EDTA buffer prepared with UltraPure DNase/RNase-Free distilled water (ThermoFisher Scientific, MA, USA) and the 20-times concentrated Tris-EDTA buffer supplied in the kit. Fluorescence measurements were performed at standard fluorescein wavelengths (excitation at 480 nm and emission at 520 nm) with a microplate reader as described in Section 2.11.1. To ensure that the sample readings remained within the instrument's detection range, the microplate reader gain was optimised so that

the sample containing the highest DNA concentration yielded a fluorescence intensity near to the fluorometer's maximum. Sample DNA measurements were performed in triplicate.

2.10.4. Quantification of Chinese Hamster Ovary Host Cell Proteins

A commercially available immunoassay kit consisting of a chemiluminescent homogeneous bead-based technology was used for the detection of CHO host cell proteins (HCPs) (AlphaLISA® CHO HCP broad reactivity kit, PerkinElmer, MA, USA). The quick, two-incubation step protocol described in the manufacturer's protocol was chosen for the quantification of HCPs in HCD mammalian cell samples. All the HCD mammalian cell samples and the reference standards were tested in triplicate at a range of dilution factors using the dilution buffer provided in the kit. The assay was performed in 96-well microplates (White ½ AreaPlate-96, PerkinElmer, MA, USA) sealed with TopSeal™-A Adhesive Sealing Film (PerkinElmer, MA, USA) to minimise liquid losses through evaporation. Measurements were performed using the EnVision® Multilabel reader (PerkinElmer, MA, USA) by selecting the AlphaScreen for AlphaLISA assays. The standard curve readings were analysed with an online tool (www.myassays.com) using a four parameter logistic curve fit (Equation 2.26) with $1/Y^2$ data weighting to account for the change in variance occurring with an increase in signal. An example of standard curve is plotted in Figure 2.10. The CHO HCP concentration in the HCD mammalian cell samples was determined from the fit. The values falling outside of the 80 - 120 % liner range were not considered for the final analysis. The equation of a four parameter logistic non-linear regression model describes:

$$y = e + \frac{a - e}{1 + \left(\frac{x}{d}\right)^b} \qquad \text{(Equation 2.26)}$$

where x is the independent value (i.e. concentration of the reference standard), y is the dependent value (i.e. response value) and *a*, *b*, *d* and *e* are constants. These constants refer to the following: *a* is the minimum asymptote or response value at 0 reference standard concentration, *b* is the steepness of the curve, *d* is the

inflection point or point on the curve where the curvature changes direction and *e* is the maximum asymptote or the response value for infinite reference standard concentration.

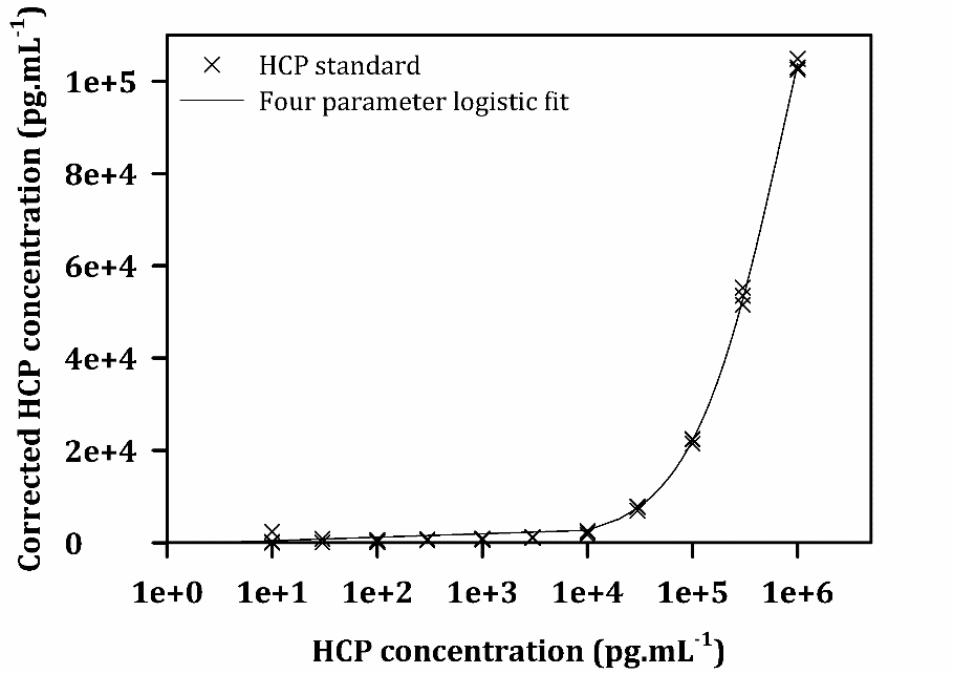

Figure 2.10. Example of standard curve for CHO host cell protein measurements.
Chinese hamster ovary host cell proteins were quantified using a chemiluminescent homogeneous bead-based technology (AlphaLISA® CHO HCP broad reactivity kit). Samples were tested at a range of dilution factors to ensure they were within the assay range. An EnVision® Multilabel reader (PerkinElmer) with AlphaScreen was used for the fluorescence measurements. Unknown concentrations of CHO host cell proteins were interpolated from the standard curve, with all standards and unknown concentration samples measured in triplicate.

2.10.5. Sodium Dodecyl Sulphate-Polyacrylamide Gel Electrophoresis (SDS-PAGE)

Samples were mixed with 4-times concentrated lithium dodecyl sulphate sample buffer (NuPAGE®, Invitrogen, Paisley, UK), then incubated for 10 minutes at 100°C (Thermomixer®, Eppendorf, Hamburg, Germany) and finally centrifuged (Eppendorf 5415R, Eppendorf, Hamburg, Germany) for 1 minute at 216.7 rps before loading them according to manufacturer's protocol into a 4 - 12 % pre-cast Bis-Tris gel (NuPAGE®, 10 or 12 wells format, Invitrogen, Paisley, UK). For SDS-PAGE analysis under reducing conditions, a ten-times concentrated reducing

agent (NuPAGE® Reducing Agent (10x), Invitrogen, Paisley, UK) was added to the lithium dodecyl sulphate sample buffer prior to heat treatment. A MW standard was used for band identification; MarK12™ Unstained Standard (Invitrogen, Paisley, UK) was used in Chapter 3 and PageRuler™ Unstained protein ladder (ThermoFisher Scientific, MA, USA) was used in Chapter 8. Electrophoresis was performed in a gel tank (XCell SureLock® Mini-Cell, Invitrogen, Paisley, UK) at a constant voltage of 200 volts for 45 minutes in the presence of 2-(N-morpholino)ethanesulfonic acid (MES) buffer prepared from a 20-times concentrated NuPAGE® MES SDS running buffer (Invitrogen, Paisley, UK) diluted with deionised water. For gel electrophoresis under reducing conditions NuPAGE® Antioxidant (Invitrogen, Paisley, UK) was added to the running buffer in the upper buffer chamber to maintain reducing conditions and to prevent protein re-oxidation. The post-electrophoresis gels were removed from the cassettes and rinsed three times with deionised water. The rinsed gels were then stained with either a Coomassie based staining solution (InstantBlue™, Expedeon Ltd, Swavesey, UK) or with Silver staining (SilverQuest™ Silver Staining Kit, Invitrogen, Paisley, UK) according to the manufacturer's protocol. After staining, gels were scanned (Gel Doc™ EQ Gel Documentation System, Bio-Rad Laboratories, CA, USA) to acquire images for further analysis.

2.10.6. Liquid Chromatography-Mass Spectrometry/Mass Spectrometry (LC-MS/MS)

Samples were first precipitated with acetone (Fisher Scientific UK, Loughborough, UK) by adding four times the sample volume of cold (-20°C) acetone to the samples before vortexing and incubating for 60 minutes at -20°C. Acetone-compatible 20 mL plastic tubes were used. The samples were then centrifuged (Heraeus™ Megafuge™ 16R, ThermoFisher Scientific Inc., Waltham, USA) for 10 minutes at 253.3 rps and -10°C. The supernatant was discarded, and the remaining acetone in the samples was left to evaporate from the uncapped tubes at room temperature for 30 minutes.

Per every 10 mg of precipitated sample, 2.5 mL of a freshly prepared solution made of 8 M urea (ESA Inc., Chelmsford, MA, USA) and 100 mM ammonium

bicarbonate (Fluka Chemie AG, Buchs, Switzerland) were added. The mixture was then vortexed to resuspend the precipitated proteins in the protein denature-inducing environment. Following this, 0.1 mL of freshly prepared 450 mM DL-dithiothreitol were added after which the mixture was incubated at room temperature for one hour to reduce the disulphide bonds of the proteins. Carboxymethylation was performed by adding 1 mL of a freshly prepared 100 mM iodoacetamide solution and incubating the mixture for 15 minutes at room temperature. The protein mixture was then diluted with 6.4 mL of deionised water. Finally, protein digestion was performed by adding 1 mL of a 0.5 $mg.mL^{-1}$ trypsin solution into the protein mixture and incubating at 37°C for one hour; the trypsin solution was prepared with sequencing-grade modified porcine trypsin (Promega Corporation, Madison, WI, USA) diluted with trypsin resuspension buffer (Promega Corporation, Madison, WI, USA).

A small volume (10 µL) of digested sample was loaded into a Jupiter® 5 µm (particle size) C18 300 Å column (Phenomenex Inc., Cheshire, UK) for reversed phase HPLC separation using an UHPLC+ Focused UltiMate 3000 system (ThermoFisher Scientific Inc., Waltham, USA). Peptides were eluted in an acetonitrile (ACN) multi-step gradient where the two mobile phases were a 0.05 % v/v trifluoroacetic acid (TFA) (ThermoFisher Scientific Inc., Waltham, USA) solution and a 90 % v/v ACN, 0.05 % v/v TFA solution. The peptide fractions separated by reversed phase HPLC were collected with an automatic liquid handling system (PROTEINEER fc II, Bruker Daltoniok GmbH, Leipzig, Germany) on an AnchorChip™ target plate with transporter technology (Bruker Daltoniok GmbH, Leipzig, Germany) as they eluted from the column; every chromatographic peak constituted a spot on the target plate. A peptide calibration mixture was then manually loaded onto the target plate by pipetting 0.5 µL of calibration mixture on every calibration spot. The calibration mixture was prepared by first dissolving the contents of the Peptide Calibration Standard II (Bruker Daltoniok GmbH, Leipzig, Germany) with 125 µL of a solution made of 30 % v/v ACN and 0.1 % v/v TFA; following this, 1.5 µL of the peptide calibration standard solution were mixed with 300 µL of matrix solution, which was made of 280.5 µL of a 85 % v/v ACN, 0.1 % v/v TFA solution, 13.5 µL of Bruker Matrix HCCA (Bruker Daltoniok GmbH, Leipzig, Germany), 3 µL of a 10 % v/v TFA solution and 3 µL of

a 100 mM ammonium phosphate monobasic solution. The target plate was finally loaded into a matrix-assisted laser desorption/ionisation – time of flight/time of flight (MALDI-TOF/TOF) mass spectrometer (ultrafleXtreme, Bruker Daltoniok GmbH, Leipzig, Germany) for mass spectrometry analysis.

The raw data obtained from each of the LC-MS/MS runs was exported as an *mgf* file and searched against all taxonomy entries of the SwissProt/UniProt protein sequence database using the 'MASCOT MS/MS Ions Search' online tool available on the Matrix Science website (www.matrixscience.com). The search parameters used to filter the protein hits during protein identification were: no missed cleavages, carboxymethyl set as fixed modification, oxidation and amidated (C-term) set as variable modifications, 50 ppm peptide mass tolerance, 0.5 Da MS/MS fragment mass tolerance, peptide charge of +1 and monoisotopic mass values.

2.11. Physical Methods

2.11.1. Absorbance and Fluorescence Measurements

Absorbance measurements that did not require a high-throughput approach were performed with 1 cm path length disposable cuvettes (UVette®, Eppendorf, Hamburg, Germany) and a double-beam spectrophotometer (BioMate™ 3S Spectrophotometer, Eppendorf, Hamburg, Germany). Mammalian cell culture samples with absorbance measurements above 1.0 absorbance units (A.U.) were diluted with PBS to ensure the measurements were within the linear range. Absorbance and fluorescence measurements for samples in 96-well microplates were performed using a microplate reader (Safire^{2}™, Tecan Group Ltd., Maännedorf, Switzerland). Measurement specifications varied depending on the microplate used and the measurement wavelength. Measurements were always performed in triplicate.

2.11.2. Turbidity Measurements

Turbidity was measured with a tungsten filament lamp turbidimeter (2100Q Portable Turbidimeter, Hach, Loveland, CO, USA). Measurements required a sample volume of 15 mL and were expressed in nephleometric turbidity

units (NTU). A 10 NTU reference standard was used to verify the turbidimeter calibration curve before each measurement. When required, re-calibration was performed with three reference standards (20, 100 and 800 NTU). The instrument's rapidly settling turbidity measuring mode was used with rapidly settling samples. Measurements were performed in triplicate.

2.11.3. Calculation of Percentage Solids Remaining

Centrifugation performance was assessed in terms of percentage solids remaining in the supernatant, which was calculated as follows:

$$\% \text{ solids remaining} = \left(\frac{OD_s - OD_{ws}}{OD_f - OD_{ws}}\right) \times 100 \quad \text{(Equation 2.27)}$$

where OD_s is the optical density of the centrifuge supernatant (A.U.), OD_{ws} is the optical density of the best possibly clarified centrifuge supernatant, also referred to as well-spun (A.U.), and OD_f is the optical density of the feed material prior to centrifugation (A.U.). To obtain the well-spun supernatant, 2 mL of feed material were centrifuged (Eppendorf 5415R, Eppendorf, Hamburg, Germany) for 30 minutes at 220 rps and 4°C leading to a $V/t\Sigma$ equal to $1.4x10^{-9}$ $m.s^{-1}$. Optical density, which refers to absorbance, was measured at 600 nm wavelength according to Section 2.11.1.

2.11.4. Particle Size Measurements by Laser Light Diffraction

Particle size distribution was measured by blue and red laser light diffraction through a sample flow cell using the Mastersizer 2000 instrument (Malvern Instruments Ltd., Malvern, UK) connected to a Hydro 2000SM wet dispersion unit (Malvern Instruments Ltd., Malvern, UK) set at 16.7 rps. The instrument's particle size detection range was from 0.02 to 2000 µm. The background signal of 60 mL of diluent was subtracted before gradually adding the sample into the dispersion unit until red laser obscuration readings between 13 and 19 % were reached; the instrument's red laser obscuration range was between 10 and 20 %. Different diluents were used depending on the pH of the sample. For mammalian cell samples, PBS was used with pH 7 or untreated samples; 20 mM sodium succinate,

156 mM sodium chloride pH 4.0 was used for pH 4 mammalian cell samples; 20 mM acetic acid, 140 mM sodium chloride pH 5.0 was used for pH 5 mammalian cell samples; and 20 mM N-[Tris(hydroxymethyl)methyl]-3-aminopropanesulfonic acid, 149 mM sodium chloride pH 8.5 was used for pH 8.5 mammalian cell samples. The diluent for clarified yeast homogenate samples was always 100 mM sodium phosphate pH 6.5 buffer. Three measurements per sample were consecutively taken to ensure no particle breakage occurred in the dispersion unit. The wet dispersion unit was emptied at the end of each measurement and flushed with 120 mL of deionised water three consecutive times before the next measurement. To verify the performance of the instrument, polydisperse glass microsphere standards (Malvern Instruments Ltd., Malvern, UK) were used periodically; the performance criteria was set at a relative standard deviation between the glass microsphere d_{50} measurements of ≤ 5 %.

The samples measured were complex and variable biological mixtures of unknown refractive indices, so the sample refractive index was assumed to be that of a 10 $g.L^{-1}$ globulin solution, which is 1.336 (Adair and Robinson, 1930); the total protein concentration values of the samples measured were always above 10 $g.L^{-1}$ (see Section 4.3.1 and Section 5.3.1). Therefore, all the reported PSD results are the equivalent of globulin particle diameters. The same approach in the PSD measurement of complex biological mixtures when using the Mastersizer 2000 instrument has been reported in the literature (Chatel et al., 2014); the authors used the refractive index of latex particles, and they also stated that changes in the values of the refractive index resulted only in small variations in the size distributions.

Particle size distribution was plotted as described by Chatel et al. (2014). The output particle size data obtained by the instrument was percentage volume against the mean size of the particle size interval. The particle size interval was not constant throughout the instrument's particle size detection range (0.02 - 2000 μm) but increased with particle size instead. In order to rationalise the data sets, percentage volume distributions were converted to volume

frequency distributions. For a particle size interval *i*, the volume frequency distribution is calculated as:

$$F_{v,i} = \frac{V_{\%,i}}{W_i} \qquad \text{(Equation 2.28)}$$

where $F_{v,i}$ is the volume frequency distribution, $V_{\%,i}$ is the percentage volume in the size interval and W_i is the width of the particle size interval; the subscripts *i* refer to the particle size interval number.

During PSD analysis the focus was on volume rather than on number distribution. The key performance factor was assessing which process conditions reduced the volume fraction of submicron particles that would negatively impact upon the subsequent solid-liquid separation step.

2.11.5. Viscosity Measurements

A Brookfield cone and plate DV-II+ viscometer (Brookfield Engineering Laboratories Inc., MA, USA) fitted with a spindle (Spindle 40) was used to study the rheological behaviour and measure the viscosity of biological and non-biological materials. A sample volume of 500 μL was exposed to increasing and decreasing shear sweeps performed in six increases and six reductions with 30 seconds hold at each one of them. Shear rates ranged from 37.5 to 1200 s^{-1}. Measurements were taken at 22°C; temperature control was performed via a cooling water circuit. Measurements were done in quadruplicate.

2.11.6. Density Measurements

For every density measurement, three different sample volumes (25, 50 and 200 mL), measured with 25 mL, 50 mL and 200 mL volumetric flasks, were weighted on an analytical balance (Ohaus Pioneer™ PA413, Ohaus Corporation, USA). Triplicate independent measurements were performed for each sample volume. The density value of the sample was the average of the nine independent measurements.

2.12. Optical Microscopy

Phase contrast microscopic images were taken with a Nikon TE2000-PFS inverted microscope (Nikon Instruments Europe B.V, Badhoevedorp, The Netherlands) equipped with a charge-couple device camera. Process image analysis was carried out with 'ImageJ v. 1.47' (http://rsb.info.nih.gov/ij/). Samples were prepared by carefully pipetting 20 μL of sample onto a glass slide and then placing a coverslip on top.

3. Evaluating Flocculation with Centrifuged Mammalian Cell Culture Fluids

3.1. Introduction and Aims

In this thesis flocculation is understood as a particle conditioning step in which insoluble particulates are agglomerated and removed from the liquid phase by the addition of a flocculating agent; the new insoluble particulates formed, called flocs, are then processed via a solid-liquid separation step to recover the clarified fluid. In contrast, precipitation is understood as the formation of insoluble solids from soluble species caused by changes in the physico-chemical conditions of the fluid or by the addition of a precipitating agent.

Flocculation was performed on centrifuged Chinese hamster ovary (CHO) cell culture fluid to remove the cell debris and other process-related impurities present in centrifuge supernatants and that result in the premature clogging of the subsequent depth filter (Iammarino et al., 2007). All the examples of flocculation in mammalian cell processes found in the literature describe the flocculation of cell culture fluids to improve the clearance of cells and cell debris (Aunins and Wang, 1989; Coffman et al., 2006; Kang et al., 2013; Riske et al., 2007; Shpritzer et al., 2006; Singh et al., 2013). Since no evidence is given in the literature of successful flocculation processes using centrifuged mammalian cell culture fluids, the work detailed in this chapter explored the flocculation of centrifuged cell culture fluids from different CHO cell lines using polyethylenimine (PEI) as the flocculating agent. A small set of flocculation variables was also investigated to analyse how they affected flocculation performance, which was described by the size distribution of the flocs, the product yield and impurity removal achieved.

Flocculation with cationic polyelectrolytes, such as that of PEI, has been found to interfere with some analytical assays used to quantify impurity removal (Peram et al., 2010). In order to ensure the results obtained when assessing flocculation performance were accurate, the interference between PEI and the analytical assays employed was studied under different flocculation conditions.

Summary of the chapter's aims and objectives:

1. Evaluate the use of different CHO cell lines and cell culture scales to obtain centrifuged mammalian cell culture fluid for the flocculation experiments.
2. Assess different storage methods for the centrifuged CHO cell culture fluid used in the flocculation experiments.
3. Estimate the interference of PEI with the analytical assays used to quantify flocculation performance and optimise the protocols, if necessary, to reduce or avoid flocculant interference.
4. Study the flocculation of centrifuged CHO cell fluids and the effect that different flocculation variables have on flocculation performance.

3.2. Experimental Set-Up

3.2.1. Mammalian Cell Culture and Centrifugation

Low cell density (LCD) and high cell density (HCD) mammalian cell culture was prepared as described in Section 2.1.1 and Section 2.1.2, respectively. While LCD product titre was measured as described in Section 2.10.2, HCD product titre data was provided by Lonza Biologics (Slough, UK). Total protein concentration was measured according to Section 2.10.1.

3.2.2. Flocculation Experiments

All experiments were performed at laboratory scale using the methodology described in Section 2.7.1. A linear PEI with molecular weigth (MW) between 50,000 and 100,000 Da was used as the flocculating agent. Both the LCD and HCD mammalian cell centrate were used in the flocculation studies. The HCD mammalian cell centrate used had been stored at 5°C during a maximum period of 15 days in the presence of 0.05 % w/v sodium azide. The range of PEI concentrations and pH values chosen for the flocculation experiments were selected based on Lonza Biologics' in-house knowledge of flocculation processes when using their commercial CHO cell lines. Different PEI concentrations, pHs and impeller designs were used to evaluate how these process variables affected

flocculation performance (see Table 3.1). Different PEI stock solutions were used depending on the final PEI concentration and pH. The PEI stock solutions were: 0.20 % w/v (final 0.01 % w/v), 2.0 % w/v (final 0.10 % w/v), 4.0 % w/v (final 0.20 % w/v), 6.0 % w/v (final 0.30 % w/v) and 12 % w/v (final 0.60 % w/v). The flocculant was diluted in the following buffers depending on the pH of the experiment: PBS (pH 7.0); 20 mM sodium succinate, 156 mM NaCl, pH 4.0 (pH 4.0); 20 mM acetic acid, 140 mM sodium chloride, pH 5.0 (pH 5.0); and 20 mM TAPS, 143 mM sodium chloride, pH 8.5 (pH 8.5). These flocculant solutions were prepared the day before the experiment and mixed overnight to ensure PEI was homogeneously distributed. The pH of the mammalian cell centrate was adjusted before flocculant addition with 1 M sodium hydroxide or 1 M citric acid.

Table 3.1. Experimental conditions of the flocculation studies performed with low and high cell density mammalian cell centrate.

Sample	PEI concentration (% w/v)	pH	Impeller design
LCD mammalian cell centrate	0.20	7.0	six-bladed disc turbine
HCD mammalian cell centrate	0.01; 0.10; 0.20; 0.30; 0.60	7.0	six-bladed disc turbine
	0.30	4.0; 5.0; 7.0; 8.5	six-bladed disc turbine
	0.10; 0.60	7.0	three-pitched blade impeller

Flocculation performance was assessed (i) studying the size distribution of the flocs using laser light diffraction measurements (see Section 2.11.4), and (ii) quantifying total protein concentration (see Section 2.10.1), mAb concentration (see Section 2.10.2) and DNA concentration (see Section 2.10.3). The same parameters were also measured on the non-treated HCD mammalian cell centrate used for comparison purposes. Particle size distribution measurements were performed nine times.

3.2.3. Assay-Flocculant Interference Studies

The values of PEI concentration and pH chosen for the assay-PEI interference studies were selected to represent the range of flocculation conditions studied in this thesis.

3.2.3.1. Polyethylenimine Absorbance Spectrum

Polyethylenimine absorbance was measured at 14 different wavelengths ranging from 260 to 750 nm. These wavelengths were: 260, 280, 320, 360, 400, 430, 460, 500, 550, 562, 595, 600, 660 and 750 nm. The effect of PEI concentration and buffer pH on PEI absorbance was studied at 0.10, 0.30 and 0.60 % w/v PEI diluted in pH 7.0 buffer (phosphate buffered saline (PBS)) or in pH 4.0 buffer (20 mM sodium succinate, 156 mM sodium chloride, pH 4.0). The PEI solutions were prepared the day before the experiment and allowed to mix overnight to ensure the flocculant was homogeneously distributed. Absorbance measurements were performed using 1-cm path length disposable cuvettes as described in Section 2.11.1.

3.2.3.2. Quantification of Total Protein Concentration

Total protein concentration was measured as described in Section 2.10.1. The equivalent total protein concentration values obtained with 0.10, 0.30 and 0.60 % w/v PEI diluted in pH 5.0 buffer (20 mM acetic acid, 140 mM sodium chloride, pH 5.0), pH 7.0 buffer (PBS) and pH 8.5 buffer (20 mM TAPS, 143 mM sodium chloride, pH 8.5) were compared to the results obtained with non-treated (i.e. non-flocculated) HCD mammalian cell centrate. The PEI solutions were prepared the day before the experiment and allowed to mix overnight to ensure the flocculant was homogeneously distributed.

3.2.3.3. Quantification of Monoclonal Antibody (mAb) Concentration

Monoclonal antibody concentration in flocculated and non-treated mammalian cell centrate was quantified as described in Section 2.10.2. The chromatograms obtained with 0.10, 0.30 and 0.60 % w/v PEI diluted in PBS buffer were compared to those of non-treated HCD mammalian cell centrate to evaluate flocculant interference. The HPLC protocol referred to as 'LCD mammalian cell centrate

protocol' (see Section 2.10.2) was used to measure the mAb concentration in samples from the CY01 cell line, as well as to evaluate flocculant interference during HPLC analysis. A new HPLC protocol was developed to minimise PEI interference during mAb quantification; this new protocol is referred to as 'HCD mammalian cell centrate protocol' (see Section 2.10.2). The new HPLC protocol was tested with purified IgG_4 (expressed in the Xceed™ cell line) and purified IgG_4 spiked with PEI to a concentration of 0.60 % w/v. The spiked mAb solution was prepared by adding the required amount of pure PEI (i.e. not in solution) into the purified IgG_4 to minimise mAb dilution.

3.2.3.4. Quantification of DNA Concentration

Quantification of DNA was performed as described in Section 2.10.3. The equivalent DNA concentrations of 0.10, 0.20, 0.30 and 0.60 % w/v PEI diluted in PBS were compared to that of non-treated HCD mammalian cell centrate to evaluate PEI interference.

3.3. Results and Discussion

3.3.1. Characterisation of Different Mammalian Cell Lines

Two different mammalian cell lines expressing a human IgG_4 (CY01 and Xceed™) were used; while the CY01 cell line was cultured in a 250 mL orbitally-shake flask and in 5 L STRs, the Xceed™ cell line was cultured in a 15 L STR. Figure 3.1.A shows that very different cell densities were achieved between the two cell lines. The CY01 cell line reached a total cell density at time of harvest of $8.47x10^6$ cells.mL^{-1} with viabilities between 62 and 68 % depending on the cell culture scale (see Figure 3.1.A). The CY01 cell growth curves were similar despite the different scales and systems (250 mL shaked flask *versus* 5 L STR) as well as feeding strategies (batch *versus* fed-batch, respectively) used (see Figure 3.1.A). Maximum total cell density, also referred to as peak cell density, with the CY01 cell line was achieved after 8 days at both scales. The batch mode feeding strategy accounted for the shorter cell culture duration (9 days) at the 250 mL scale, where cell viability rapidly dropped to 62 % after reaching a peak cell density of $9.1x10^6$ cells.mL^{-1} (see Figure 3.1.A). The fed-batch mode used in the 5 L STRs

achieved a lower cell death rate after cell density peaked to $9.7x10^6$ cells.mL^{-1}; harvest occurred on day 12 with a cell viability of 68 % (see Figure 3.1.A). The Xceed™ cell line was cultured in a 15 L STR, which was harvested on day 15 with a total cell density of $19.5x10^6$ cells.mL^{-1} and viability of 65 %. Cell density peaked on day 10 with a value of $29.0x10^6$ cells.mL^{-1} (see Figure 3.1.A). Therefore, with the Xceed™ cell line total cell density at time of harvest was 33 % smaller than peak cell density; with the CY01 cell line the difference was of 6.9 % at the 250 mL scale and of 13 % at the 5 L scale. When comparing the values of peak cell density achieved by each CHO cell line, Xceed™ achieved cell densities 3 times higher than these obtained by the CY01 cell line. With regards to the viable cell density at time of harvest, the increment was between 2.2 and 2.4 fold in favour of the Xceed™ cell line. Feeding strategy (batch *versus* fed-batch) or cell culture scale did not impact upon the cell densities achieved, as observed with the CY01 250 mL shake flask and 5 L STR scales. Instead, the difference in cell density originated in the CHO cell line used. For this reason, in this thesis the CY01 cell line will be referred to as low cell density (LCD) cell line, and the Xceed™ cell line as high cell density (HCD) cell line.

When comparing the product titres achieved by the two CHO cell lines (Figure 3.1.B), final product concentration depended upon both the CHO cell line and the feeding strategy used. Monoclonal antibody concentration in the 5 L STRs was 2.5 fold larger than that in the 250 mL shake flask despite the CY01 cell line was used at both scales (see Figure 3.1.B). The different feeding strategies used at each scale (fed-batch and batch, respectively) could explain the higher cell productivity encountered in the 5 L STR. When compared to the product concentration reached by the Xceed™ cell line in the 15 L STR, the difference was of 5.0 fold (5 L STR) and 12 fold (250 mL shake flask) (see Figure 3.1.B). Total protein concentration also differed depending on the CHO cell line and feeding strategy used (see Figure 3.1.B). Total protein concentration in the LCD centrate was 1.5 fold higher in the 5 L STRs than in the 250 mL shake flask. The difference increased to 7.1 fold (250 mL shake flask) and 4.6 fold (5 L STR) when compared to the HCD mammalian cell centrate (i.e. 15 L STR) (see Figure 3.1.B).

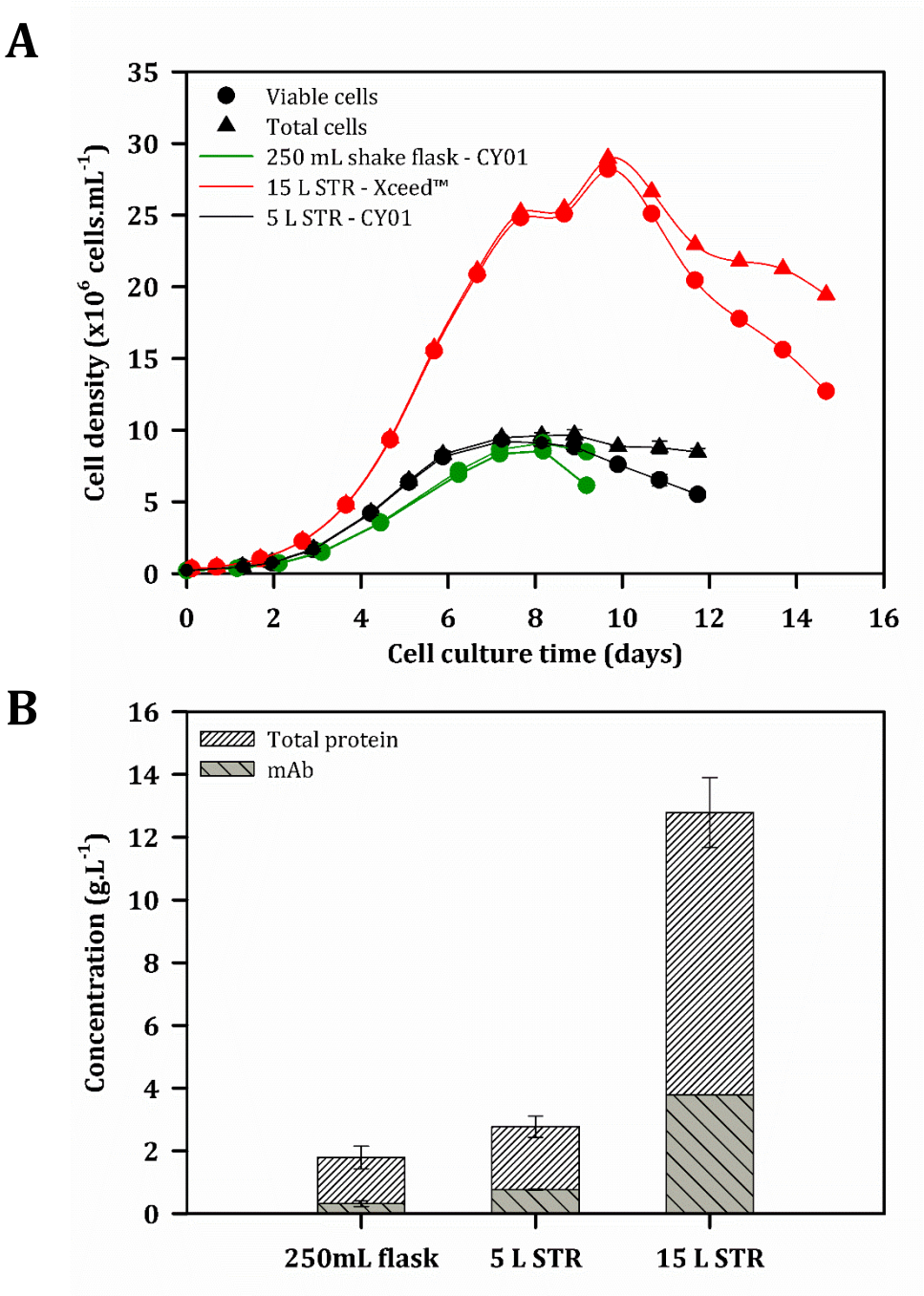

Figure 3.1. Characterisation of CY01 and Xceed™ mammalian cell lines. *Cell culture in the 250 mL shake flask and two 5 L STRs were performed at UCL with the CY01 cell line. Cell culture in the 15 L STR was performed with the Xceed™ cell line at Lonza Biologics' premises (Slough, UK). Cell count and viability (**A**) and product titre (**B**) for the CY01 cell cultures were measured according to Section 2.1.1 and Section 2.10.2, respectively. Cell culture (**A**) and product titre (**B**) data from the Xceed™ cell line were provided by Lonza Biologics. Total protein concentration (**B**) was measured after cell culture clarification via centrifugation as described in Section 2.10.1. In (**A**) error bars indicate one standard deviation where n = 2. In (**B**) error bars indicate one standard deviation from three repeated measurements where n = 1.*

Finally, the ratio of mAb to total protein content varied with both the cell culture scale and the CHO cell line. Antibody represented 18 % of the total protein content in the 250 mL shake flask, 27 % in the 5 L STRs, and 30 % in the 15 L STR. Therefore, the mAb to total protein ratio increased with the cell culture scale. However, it was possibly determined by the feeding strategy used, since the difference between the 5 L and 15 L STRs was only of 3 % despite employing different CHO cell lines.

3.3.2. Effect of Cell Density on Flocculation Performance

Flocculation was performed on cell culture centrate after disc-stack centrifugation. While HCD cell culture was clarified via pilot-scale centrifugation, LCD cell culture was clarified employing the USD centrifugation methodology (see Section 1.4.1) to mimic the HCD cell culture clarification conditions. The PSDs of the centrate obtained from each cell culture system were measured by laser light diffraction and are plotted in Figure 3.2. The centrate was constituted of submicron particles regardless of the CHO cell line and the feeding strategy used (see Figure 3.2). Typically, particles much smaller than 1 μm are difficult to remove using a disc-stack centrifuge at practical operating conditions (Iammarino et al., 2007). The values of percentage volume frequency for the submicron particles ranged between 81 and 214 %, depending upon the feeding strategy used during cell culture (see Figure 3.2). Fed-batch cell cultures (Figure 3.2, middle and Figure 3.2, bottom) resulted in maximum percentage volume frequencies between 191 % (5 L STR) and 214 % (15 L STR), which were 2.5 fold larger than that of the batch cell culture (250 mL shake flask) (Figure 3.2, top).

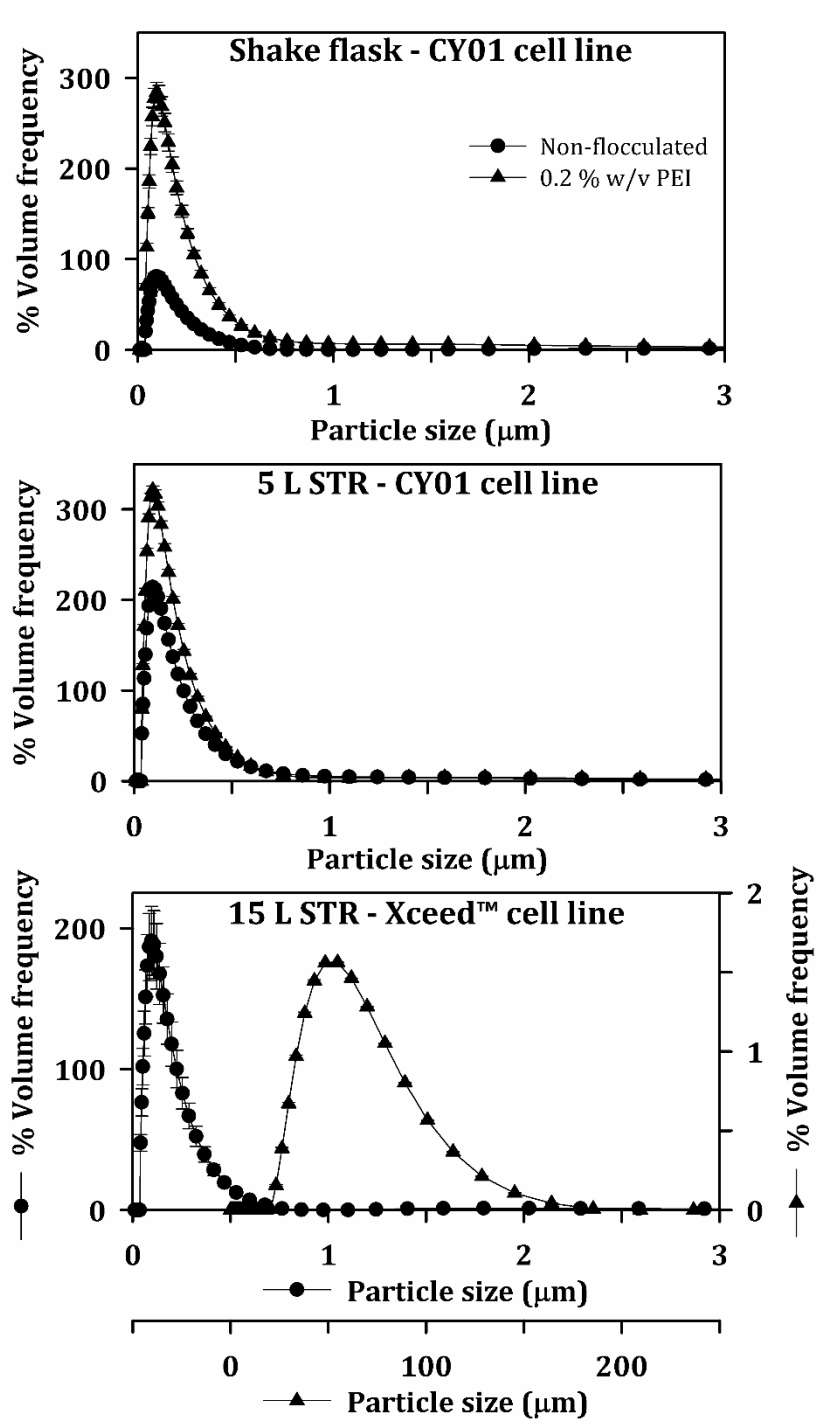

Figure 3.2. Particle size distribution of non-flocculated and flocculated mammalian cell centrate obtained from different CHO cell lines.
Cell culture fluid from the 250 mL shake flask and 5 L STR (both using the CY01 cell line) were clarified via USD centrifugation as described in Section 2.1.1. Cell culture fluid from the 15 L STR (Xceed™ cell line) was provided by Lonza Biologics (Slough, UK) and clarified at UCL via pilot scale disc-stack centrifugation (see Section 2.1.2). Centrate was flocculated at laboratory scale with 0.20 % w/v PEI, pH 7.0 and six-bladed disc turbine as described in Section 2.7.1. Error bars indicate one standard deviation from nine repeated measurements where n = 1.

The difference in the maximum percentage frequency values observed for the submicron particles between the 15 L STR, 5 L STR and 250 mL shake flask (see Figure 3.2) could be due to the longer duration of the fed-batch cell cultures (see Figure 3.1.A); particularly, the difference in the maximum percentage frequency values could have been due to the significant drop in cell viability observed in the fed-batch cell cultures after reaching peak cell density (40 % - 5 L STR and 55 % - 15 L STR) (see Figure 3.1). Literature shows an increase in solids carry over in the centrate of clarified mammalian cell cultures with cell culture age and, in particular, with non-viable cell density (Iammarino et al., 2007; Tait et al., 2009). Higher cell densities and lower cell viabilities result in larger amounts of cell debris and other solid impurities released into the cell culture (Iammarino et al., 2007). In addition to this, Figure 3.1.A also shows that total cell density at time of harvest had dropped by 13 % (5 L STR) and by 33 % (15 L STR) from their corresponding peak cell density values. These data suggest cell death by necrosis where cells break down and release their cellular contents into the media (Arden and Betenbaugh, 2004; Krampe and Al-Rubeai, 2010).

Polyethylenimine, a cationic polyelectrolyte, was the flocculating agent chosen for the flocculation experiments performed in this thesis. This polymer has been extensively characterised with respect to its physico-chemical properties (Horn, 1980; Lindquist and Stratton, 1976; Shepherd and Kitchener, 1956). In addition to this, it has been commonly used to flocculate biological fluids (Barany and Szepesszentgyörgyi, 2004; Cordes et al., 1990; Milburn et al., 1990; Peram et al., 2010; Salt et al., 1995, 1996). Low and high cell density centrate were flocculated with 0.20 % w/v PEI and pH 7 at laboratory scale. Figure 3.2 shows the size distribution of the flocs obtained depended on the CHO cell line used. While flocculation with the LCD centrate (i.e. from the CY01 cell line) resulted in submicron flocs (Figure 3.2, top and Figure 3.2, middle), flocculation with the HCD centrate (i.e. from the Xceed™ cell line) led to flocs ranging between 20 and 185 μm in diameter (Figure 3.2, bottom). Since the aim of the process was to flocculate the submicron particles present in centrifuged mammalian cell cultures to generate feeds easier to process (Riske et al., 2007; Singh et al., 2013; Thömmes and Etzel, 2007), the CY01 cell line proved to be inappropriate for the flocculation studies performed in this thesis.

Flocculation of the submicron particles present in the mammalian cell centrate seemed to be linked to the cell density values achieved during cell culture and not to the cell culture scale or the feeding strategy used (i.e. fed-batch or batch). It is possible that the minimum flocculant dose required with LCD centrate was higher than 0.20 % w/v PEI. However, increasing the flocculant content would have been counter-productive for the subsequent depth filtration stage (see Chapter 6 and Chapter 7) due to electrostatic repulsive forces between the flocculant and the depth filter media, both positively charged. Furthermore, higher PEI concentrations could have resulted in higher amounts of residual flocculant in the feed, thus posing further complications in the capture and polishing chromatography steps (Peram et al., 2010). A flocculant with different physico-chemical characteristics to these of the PEI used could have successfully flocculated the submicron particles of the LCD centrate. Nonetheless, the aim was to mimic the conditions encountered at production scale, where CHO cell lines with cell densities similar to that of the HCD cell line (i.e. > $20x10^6$ cells.mL^{-1}) are employed (Westoby et al., 2011). Therefore, the flocculation studies performed in this thesis were limited to the HCD centrate, that is, to the Xceed™ cell line.

3.3.3. Flocculant Assay Interference

Some polyelectrolytes used as flocculating agents have been reported to interfere with certain analytical assays employed to assess flocculation performance (Peram et al., 2010). The effect of residual PEI on the assays chosen to evaluate flocculation performance was unknown. The interference of PEI on the total protein, mAb and DNA quantification methods chosen was studied at different pHs and PEI concentrations as these were the only two physico-chemical variables adjusted during the flocculation experiments.

3.3.3.1. PEI Absorbance Spectrum

The absorbance of PEI at different wavelengths was measured to study whether the presence of this polyelectrolyte would interfere with the spectrophotometric measurements used for protein and DNA quantification, as well as solids content assessment. The wavelengths studied ranged from 260 to 750 nm, and included DNA and protein quantification measurements at 260 nm and 280 nm,

respectively (Mathews et al., 2000), solids content assessment at 600 nm (Berrill et al., 2008; Chatel et al., 2014; Hogwood et al., 2013b; Kim et al., 2001; Lau et al., 2013; Tait et al., 2009; Tustian et al., 2007) and wavelengths at which protein concentration is measured with commercially available kits (562 nm - BCA protein assay kit from ThermoFisher Scientific; 595 nm - Coomassie-Bradford protein assay kit from ThermoFisher Scientific; 660 nm - protein quantification kit from ThermoFisher Scientific; 750 nm - Lowry protein assay kit from ThermoFisher Scientific).

Figure 3.3 shows that PEI absorbance gradually decreased with increasing wavelengths. The highest absorbance values were obtained at 260 nm, but from 500 nm onwards absorbance did not exceed the 0.009 A.U. (see Figure 3.3). Increasing concentrations of PEI led to higher absorbance readings, but the difference in absorbance values between the different PEI concentrations tested decreased with higher wavelengths (see Figure 3.3). Therefore, the larger the absorbance wavelength, the less sensitive the measurement was to the presence and concentration of PEI. Lower pHs (i.e. pH 4) led to higher absorbance readings than neutral pHs (i.e. pH 7) (see Figure 3.3). Considering that PEI is a weak base where the secondary amines have a pKa of 10.0 (Shepherd and Kitchener, 1956), the lower the pH was, the more secondary amino groups were protonated. Due to the electrostatic repulsive forces between the positively charged groups, it is possible that the molecules of PEI were stretched at low pHs thus exposing more polymer surface and increasing the absorbance values.

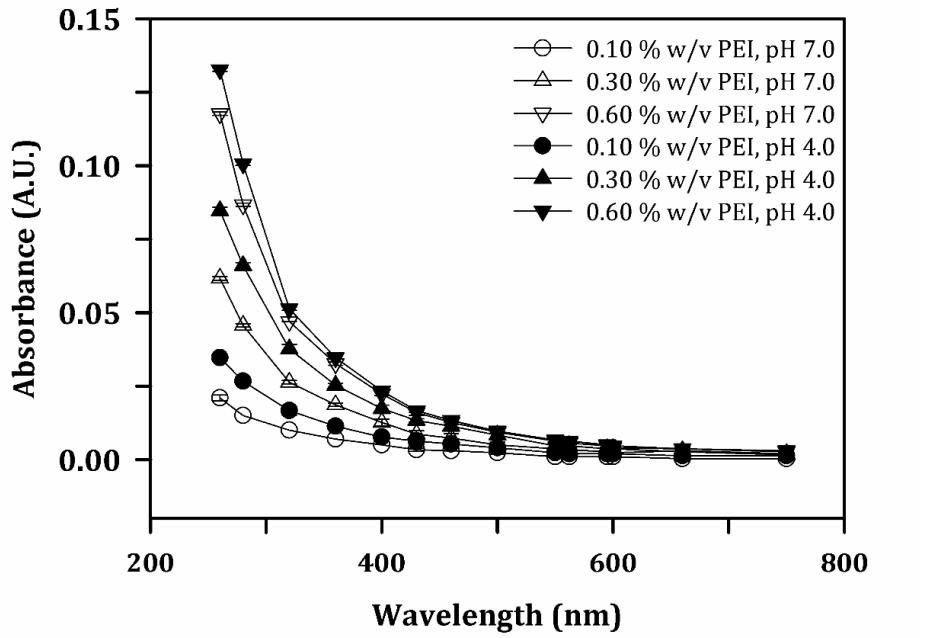

Figure 3.3. Polyethylenimine absorbance spectrum between 260 and 750 nm wavelength.
Absorbance measurements were performed with 1-cm path length disposable cuvettes as described in Section 2.11.1. Samples were prepared by diluting the necessary amount of PEI in PBS buffer (pH 7) or 20 mM sodium succinate, 156 mM sodium chloride, pH 4.0 buffer (pH 4). Absorbance measurements were performed at the following wavelengths: 260 (DNA quantification), 280 (protein quantification), 320, 360, 400, 430, 460, 500, 550, 562 (BCA protein assay kit, ThermoFisher Scientific), 595 (Coomassie-Bradford protein assay kit, ThermoFisher Scientific), 600 (solids content), 660 (protein quantification kit, ThermoFisher Scientific) and 750 nm (Lowry protein assay kit, ThermoFisher Scientific). Error bars indicate one standard deviation where n = 3.

3.3.3.2. Total Protein Quantification

Total protein concentration was quantified with a commercial BCA assay kit (see Section 3.3.3.2). Flocculant interference was studied by comparing the equivalent total protein concentration values obtained with different PEI concentrations and pHs to that of HCD mammalian cell centrate. The results are plotted in Figure 3.4. Higher PEI concentrations led to higher equivalent total protein concentration values; these values ranged from 0.17 $g.L^{-1}$ (0.10 % w/v PEI) to 0.57 $g.L^{-1}$ (0.60 % w/v PEI) (see Figure 3.4). Buffer pH did not impact upon the results (see Figure 3.4). Polyethylenimine interference represented 0.3 % (0.10 % w/v PEI), 3.4 % (0.30 % w/v PEI) and 4.5 % (0.60 % w/v PEI) of the total protein concentration in the HCD mammalian cell centrate used. Nonetheless, PEI interference was expected to be lower than 4.5 % during the flocculation

experiments considering the residual concentration of PEI was going to be lower than 0.6 % w/v after flocculation.

High cell density mammalian cell centrate was considered to be free from any agents interfering with the total protein assay used. The manufacturer of the protein assay kit ensures the assay is compatible with sodium azide at concentrations < 0.2 % w/v; the concentration of sodium azide used to preserve the HCD mammalian cell centrate stored at 5°C was 0.05 % w/v.

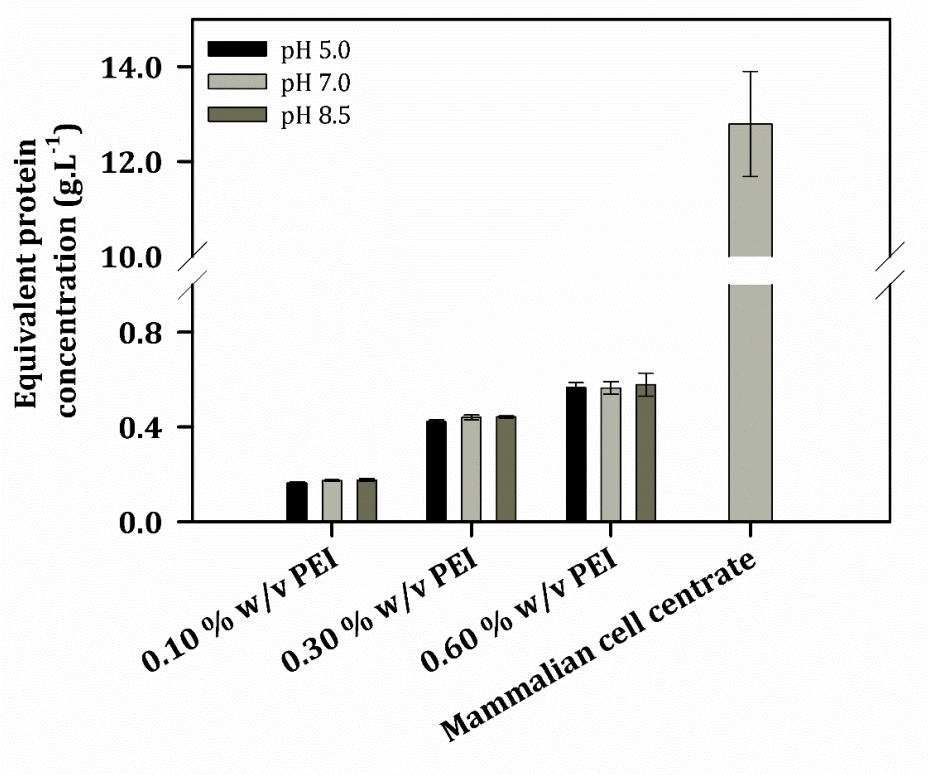

Figure 3.4. Polyethylenimine interference with total protein quantification. *Total protein concentration measurements were performed as described in Section 2.10.1. Samples were prepared by diluting the necessary amount of PEI in 20 mM acetic acid, 140 mM sodium chloride, pH 5.0 buffer (pH 5), PBS buffer (pH 7) or 20 mM TAPS, 143 mM sodium chloride, pH 8.5 buffer (pH 4). Mammalian cell centrate was obtained after the clarification of HCD mammalian cell culture fluid (Xceed™ cell line; peak cell count = 29.0x10^{6} cells.mL^{-1}) with a pilot-scale disc-stack centrifuge (Q/Σ = 2.85x10^{-8} m.s^{-1}) (see Section 2.1.2). Error bars indicate one standard deviation where n = 3.*

3.3.3.3. Monoclonal Antibody Quantification

Monoclonal antibody concentration was quantified via HPLC using a pre-packed protein G chromatography column. Polyethylenimine interference was studied comparing the chromatograms obtained with different concentrations of PEI to that of HCD mammalian cell centrate. The HPLC protocol used consisted of (i) sample loading; (ii) column wash with equilibration buffer (20 mM sodium phosphate, pH 7.0); (iii) elution (20 mM glycine, pH 2.8); (iv) post-elution wash with equilibration buffer; (v) column strip with elution buffer; and (vi) column re-equilibration with equilibration buffer. Figure 3.5 shows the HPLC chromatograms obtained with 0.10, 0.30 and 0.60 % w/v PEI, as well as with HCD mammalian cell centrate. A strong elution peak was obtained in all PEI samples despite the absence of mAb (see Figure 3.5). Furthermore, the signal of the elution peak was proportional to the concentration of PEI in the sample (see Figure 3.5). Other small peaks in the PEI samples were obtained during the post-elution wash and column re-equilibration steps (see Figure 3.5). These data suggested PEI eluted under low pH conditions; the post-elution peaks observed were obtained after a low pH step (elution and column strip). Polyethylenimine could have bound either to the protein G ligand or to the matrix, which has occurred during protein A chromatography when using other polyamines (Peram et al., 2010). The interaction between PEI and the chromatographic resin could displace the bound antibody. In addition to this, the chromatograms showed PEI and mAb eluted at the same time (9.8 and 9.7 minutes, respectively) (Figure 3.5). Due to the high absorbance of PEI at 280 nm wavelength (see Figure 3.3), the co-elution of PEI with the product would have resulted in a higher equivalent mAb concentration.

The HPLC mAb quantification protocol was modified introducing an additional washing step before mAb elution to avoid the co-elution of PEI with the product. A low pH wash was not considered to prevent mAb eluting before the elution step. Instead, a high ionic strength wash was chosen; high amounts of sodium chloride would compete with the PEI molecules for electrostatic interactions with the resin. The addition of a high salt washing step before mAb elution required a new equilibration step in-between. Therefore, the optimised HPLC method consisted

of (i) sample loading; (ii) wash with an equilibration buffer of higher ionic strength (20 mM sodium phosphate, 110 mM sodium chloride, pH 7.0); (iii) high salt wash (20 mM sodium phosphate, 500 mM sodium chloride, pH 7.0); (iv) column re-equilibration wash with equilibration buffer; (v) elution (20 mM glycine, pH 2.8); (vi) post-elution wash with equilibration buffer; (vii) column strip with elution buffer; and (viii) column re-equilibration with equilibration buffer.

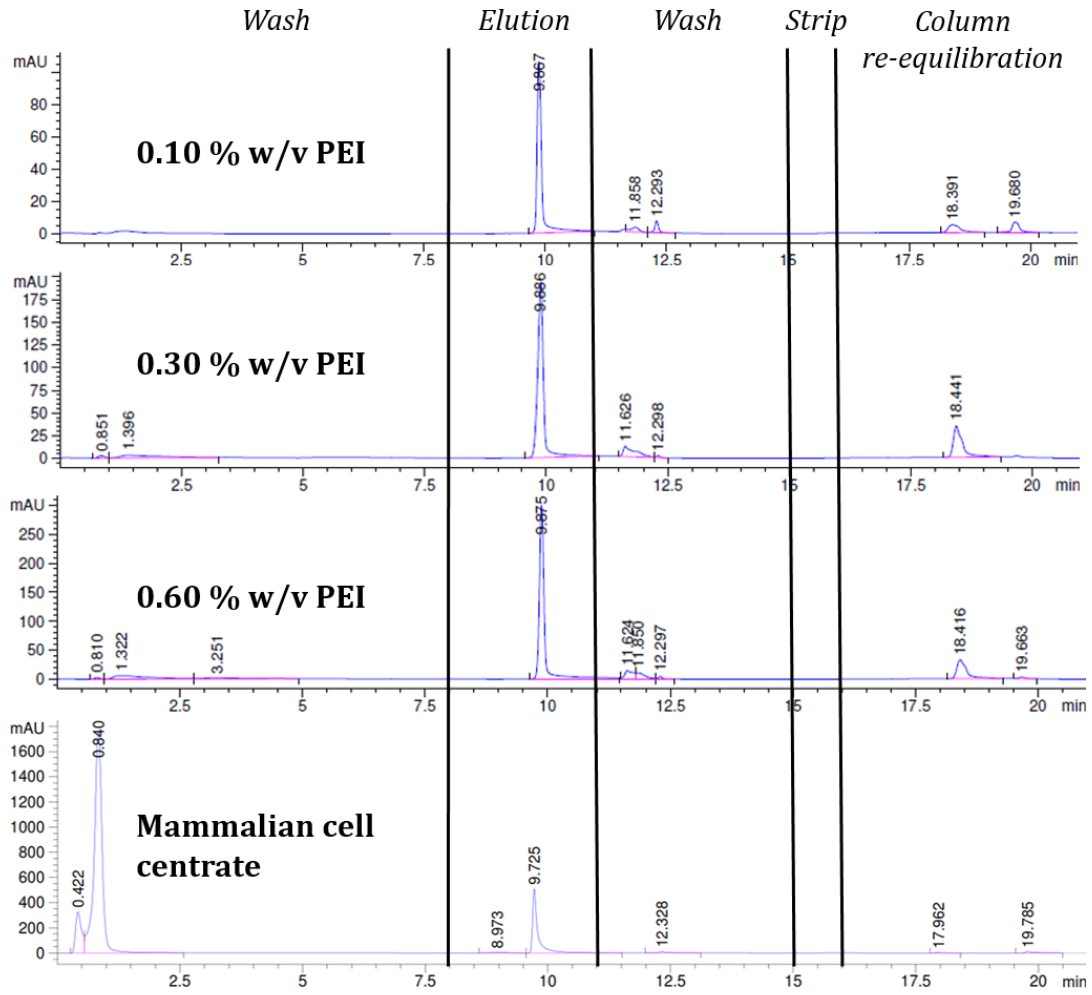

Figure 3.5. Chromatograms displaying polyethylenimine interference during monoclonal antibody quantification.
Monoclonal antibody was quantified via HPLC with a pre-packed protein G column applying the LCD mammalian cell line protocol described in Section 2.10.2. Polyethylenimine samples were prepared by mixing overnight the required amount of flocculant in PBS buffer. Mammalian cell centrate was obtained after the clarification of HCD mammalian cell culture fluid (Xceed™ cell line; peak cell count = 29.0x10^{6} cells.mL^{-1}) with a pilot-scale disc-stack centrifuge (Q/Σ = 2.85x10^{-8} m.s^{-1}) (see Section 2.1.2).

The optimised HPLC method was tested with purified mAb and purified mAb spiked with PEI to a final 0.60 % w/v concentration, which was the maximum PEI concentration used in the flocculation experiments performed in this thesis. The chromatograms obtained are shown in Figure 3.6. Two small chromatographic peaks (20 and 5 mAU) were observed before the elution step when testing the purified mAb (Figure 3.6, top). The 20 mAU peak was obtained during the first wash with equilibration buffer (see Figure 3.6, top); this peak could have been due to process-related impurities still present in the purified sample, or to mAb fragments resulting from the freeze-thawing process (the purified mAb samples were kept at -20°C). The 5 mAU peak was observed during the high salt wash (see Figure 3.6, top); while product elution could not be discarded, the elution of mAb fragments or other impurities should be considered as well. A 185 mAU peak was obtained with purified mAb during the low pH elution step (see Figure 3.6, top), which was attributed to mAb elution; the elution peak area was equal to 4777.6 units. Other smaller peaks (< 5 mAU) were also observed during the post-elution washes (see Figure 3.6, top). The great difference in peak area between the elution step and the high salt wash and post-elution washes suggested that mAb only eluted during the low pH elution step. In the presence of PEI (see Figure 3.6, bottom), the flocculant was observed to elute during both the first equilibration buffer wash (85 mAU) and the high salt wash (170 mAU). In comparison to the non-optimised HPLC mAb quantification protocol (see Figure 3.5), PEI eluted during the first wash due to the higher ionic strength of the equilibration buffer used in the improved HPLC protocol. The intensity of the mAb elution peak (185 mAU) in the presence of PEI (Figure 3.6, bottom) was the same as that of the purified mAb sample (Figure 3.6, top). The elution peak area also remained unchanged in the presence of PEI (4754.4 units), thus indicating the same amount of mAb eluted during the low pH elution step in the presence and absence of PEI.

The improved HPLC mAb quantification method was tested independently three times leading to the same results as the ones discussed here. However, only one chromatogram for the purified mAb sample (Figure 3.6, top) and another one for the mAb sample spiked with PEI (Figure 3.6, bottom) have been shown for exemplification purposes.

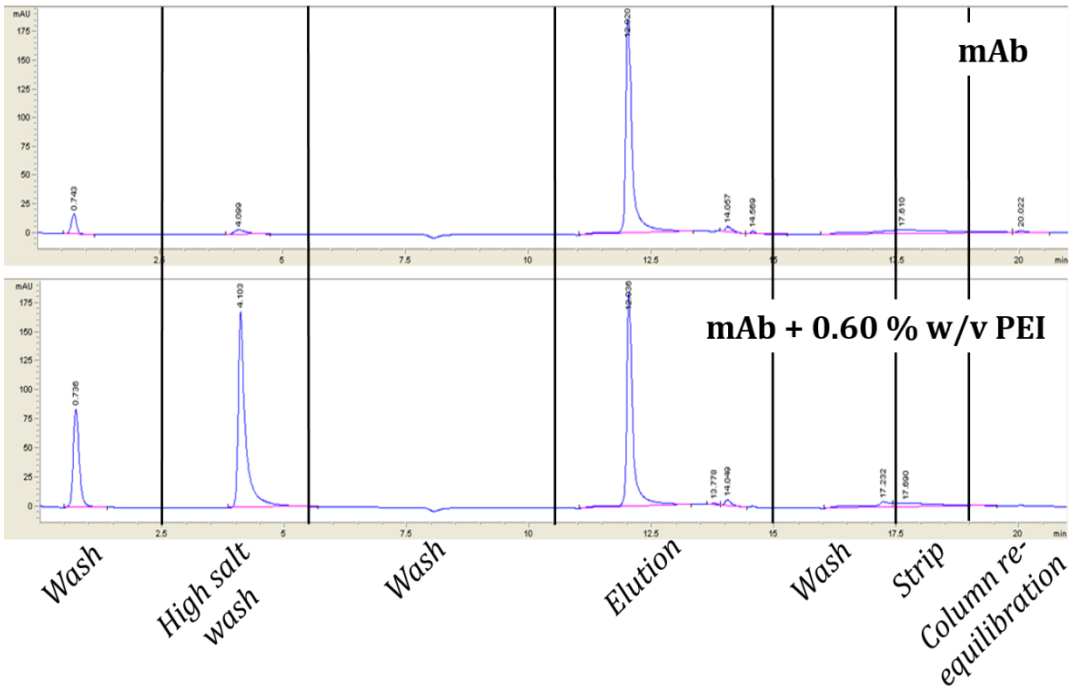

Figure 3.6. Chromatograms of the improved HPLC monoclonal antibody quantification protocol for samples with and without polyethylenimine. *Monoclonal antibody was quantified via HPLC with a pre-packed protein G column applying the HCD mammalian cell line protocol described in Section 2.10.2. The required amount of pure PEI (i.e. not in solution) was spiked into a solution of purified mAb to prepare the 'mAb + 0.60 % w/v PEI' samples. The flocculant was mixed in with a vortex mixer. No flocs were observed upon PEI addition and subsequent mixing. Purified mAb was supplied by Lonza Biologics (Slough, UK).*

3.3.3.4. DNA Quantification

Quantification of DNA in flocculated and non-flocculated samples was performed with a commercially available kit (see Section 3.2.3.4). Polyethylenimine interference was studied comparing the DNA concentration values obtained with different concentrations of PEI to these of HCD mammalian cell centrate. Figure 3.7 shows the PEI samples obtained equivalent DNA concentrations between 1.3 and 1.4 $\mu g.mL^{-1}$. Increasing PEI concentration from 0.10 to 0.60 % w/v resulted in lower equivalent DNA concentration values; the reduction obtained from 0.10 to 0.60 % w/v PEI was of 12 % or the equivalent 0.17 $\mu g.mL^{-1}$. The DNA concentration in HCD mammalian cell centrate was 35 $\mu g.mL^{-1}$, thus it was one order of magnitude larger than these of the PEI samples. The maximum value of equivalent DNA concentration for the PEI samples tested (0.10 % w/v PEI with 1.4 $\mu g.mL^{-1}$) represented 4.1 % that of the HCD mammalian

cell centrate. With an interference below 5 %, optimising this DNA quantification assay was not considered necessary.

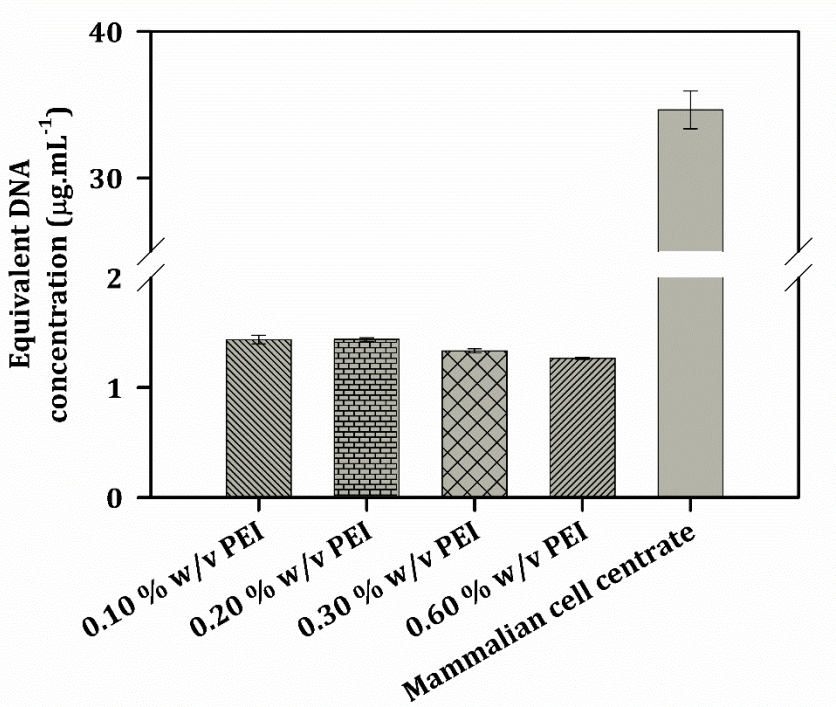

Figure 3.7. Polyethylenimine interference with DNA quantification.
The DNA content in the samples was quantified with a commercially available kit as described in Section 2.10.3. Polyethylenimine samples were prepared adding the required amount of PEI to PBS buffer and mixing overnight. Mammalian cell centrate was obtained after the clarification of HCD mammalian cell culture fluid (Xceed™ cell line; peak cell count = 29.0x10^{6} cells.mL^{-1}) with a pilot-scale disc-stack centrifuge (Q/Σ = 2.85x10^{-8} m.s^{-1}) (see Section 2.1.2). Error bars indicate one standard deviation where n = 3.

3.3.4. Effect of Flocculation Conditions on Flocculation Performance

Three different flocculation variables (flocculant concentration, pH and impeller design) were studied to assess how they affected flocculation performance, which was evaluated via PSD measurements and total protein, mAb and DNA quantification analysis.

3.3.4.1. Particle Size Distribution

The PSDs of the flocs obtained with different PEI concentrations, pHs and impeller designs are plotted in Figure 3.8. Polyethylenimine was manually added into the flocculation vessel, thus no tight control upon flocculant addition rate

was guaranteed. As described in Section 4.3.3 and Section 5.3.2, flocculant addition rate is a critical flocculation variable affecting the size distribution of the flocs. Consequently, the results plotted in Figure 3.8 cannot be taken as a thorough description of the PSDs obtained under the conditions tested, but as an approximation of the impact that these variables have upon flocculation performance.

Figure 3.8, top shows the different PSDs obtained with 0.01, 0.10, 0.30 and 0.60 % w/v PEI. The submicron particles present in the HCD mammalian cell centrate (see Figure 3.2) were not flocculated with 0.01 % w/v PEI (see Figure 3.8, top). However, PEI concentrations larger than or equal to 0.10 % w/v PEI resulted in flocs always larger than 2 μm (see Figure 3.8, top). A narrow monomodal distribution of flocs sized between 2.0 and 33 μm was obtained with 0.10 % w/v PEI (see Figure 3.8, top). Wide bimodal PSDs ranging from 2.30 to 240 μm were achieved with 0.30 and 0.60 % w/v PEI (see Figure 3.8, top). These results showed there was a minimum PEI concentration required to flocculate the submicron particles present in the HCD mammalian cell centrate, and another optimal PEI concentration to obtain a monomodal and narrow distribution of flocs. Pre-treated feeds with narrow and monomodal size distributions are of interest for the subsequent solid-liquid separation steps such as centrifugation (Berrill et al., 2008) or depth filtration (Singh et al., 2013).

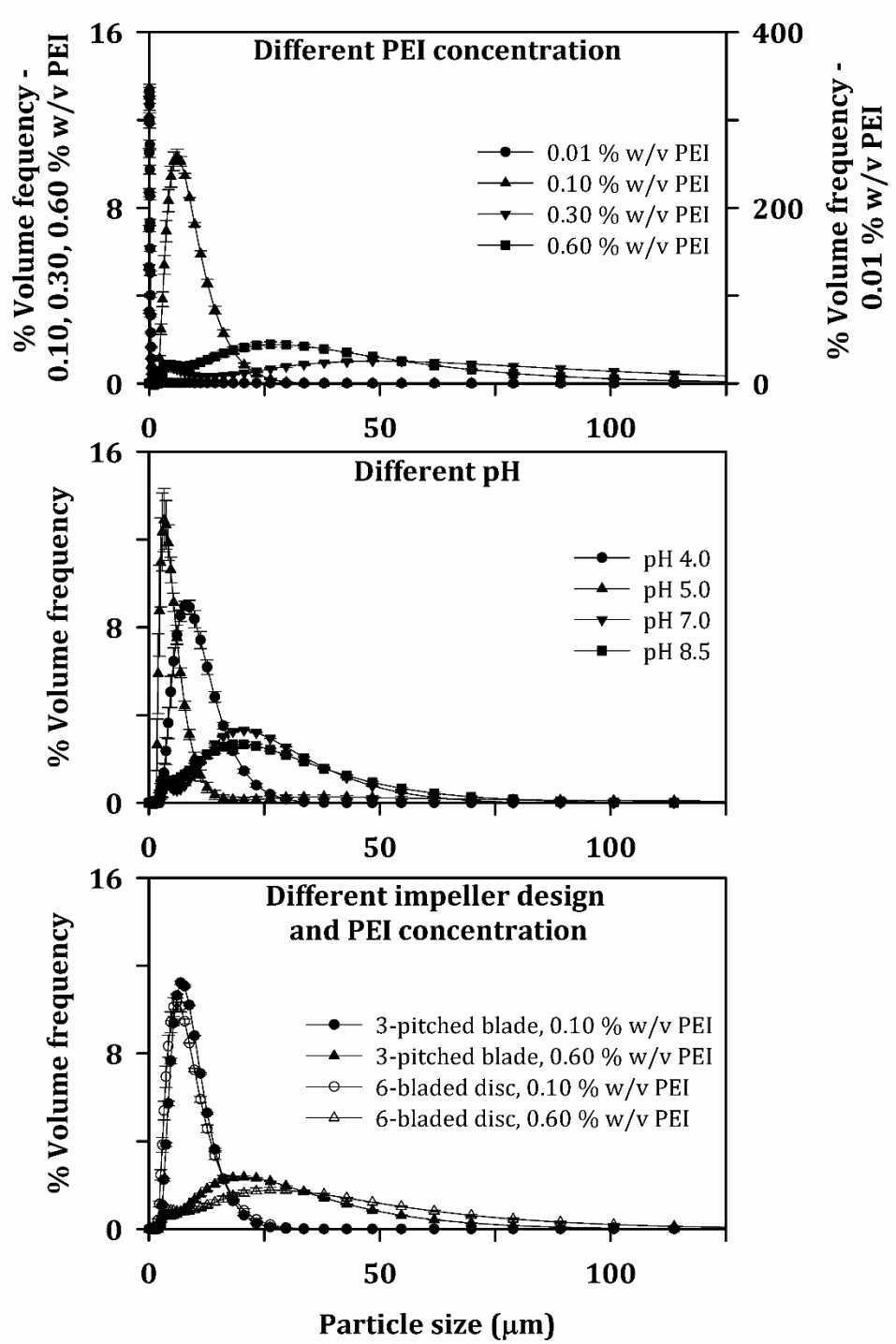

Figure 3.8. Effect of flocculation variables on floc size distribution.
Laboratory-scale (see Section 2.3.2 for vessel details) flocculation with HCD mammalian cell (Xceed™ cell line; peak cell count = 29.0x10^{6} cells.mL^{-1}) centrate (Q/Σ = 2.85x10^{-8} m.s^{-1}) was performed as described in Section 2.7.1. Different PEI concentrations (0.01, 0.10, 0.30, 0.60 % w/v PEI; 6-bladed disc turbine; pH 7.0), pHs (4.0, 5.0, 7.0, 8.5; 6-bladed disc turbine; 0.30 % w/v PEI) and impeller designs (6-bladed disc or 3-pitched blade; 0.10 and 0.60 % w/v PEI; pH 7.0) were studied. Particle size distribution was measured via laser light diffraction as detailed in Section 2.11.4. Error bars represent one standard deviation where n = 9.

The effect of pH on the size and distribution of flocs was studied at four different pH values. Figure 3.8, middle shows pH values ≤ 5 resulted in narrow monomodal distributions with flocs sized between 2.5 and 30 μm. Higher pH values (pH ≥ 7) led to bimodal PSDs with flocs between 2.3 and 90 μm (see Figure 3.8, middle). The difference in the PSDs obtained at pHs 4 - 5 and pHs 7 - 8.5 could have been caused by protein precipitation occurring at the low pHs tested. A sudden change in the turbidity of the centrate was visually observed upon acid addition; the pH of the HCD mammalian cell centrate used was adjusted with a concentrated acid to avoid feed dilution. Acid-induced protein precipitation in mammalian cell culture fluids has been well documented (Chollangi et al., 2015; Lydersen et al., 1994; Senczuk et al., 2016; Singh et al., 2016; Westoby et al., 2011). Protein precipitation would have increased the particulate content in the HCD mammalian cell centrate. Therefore, the narrow PSDs characterised by the high percentage volume frequency values observed at pH 4 and pH 5 (see Figure 3.8, middle) could be explained by the presence of flocs or by the combination of flocs and protein precipitates.

Impeller design was expected to affect the size distribution of the flocs, considering that a six-bladed disc turbine and a three-pitched blade impeller generate different mixing patterns inside a mixing vessel (radial-flow *versus* axial-flow, respectively) (Doran, 1995). However, Figure 3.8, bottom shows the PSDs obtained with the two impeller designs were very similar. The same monomodal size distribution was obtained at 0.10 % w/v PEI with the six-bladed disc and the three-pitched blade impellers used; floc size ranged in both cases between 2.30 and 29.7 μm (see Figure 3.8, bottom). At 0.30 % w/v PEI, the size of the flocs was the same with both impellers (2.30 to 237 μm), but the bimodal PSD curves differed slightly (see Figure 3.8, bottom). The similar PSDs observed with the six-bladed disc and the three-pitched blade impellers used could have resulted from the presence of the same predominant mixing time scale in both vessels (see Section 4.3.8).

3.3.4.2. Total Protein, mAb and DNA Concentration

Flocculation performance with regards to product yield, protein and DNA impurity removal was studied at three different flocculant concentrations (0.10,

0.30 and 0.60 % w/v PEI); lower PEI concentrations were not studied since the results in Figure 3.8, top showed that 0.01 % w/v PEI was unable to successfully flocculate the submicron particles present in the HCD mammalian cell centrate used. In addition to this, the effect of pH on product yield and impurity removal was not studied because of the combined effect of protein precipitation and flocculation at low pH values (see Figure 3.8, middle and Section 3.3.4.1). The results for product yield, protein and DNA impurity removal obtained with the flocculated samples were compared to these of HCD mammalian cell centrate, which was used as a control.

Figure 3.9 shows the total protein, mAb and DNA concentration results obtained for the HCD mammalian cell centrate and for the same HCD centrate flocculated at 0.10, 0.30 and 0.60 % w/v PEI. Protein removal in the flocculated samples could not be concluded due to the large error bars obtained during total protein concentration analysis (see Figure 3.9, top). The mAb quantification results (Figure 3.9, middle) showed no product loss occurred during flocculation with 0.10, 0.30 and 0.60 % w/v PEI. An increase in mAb concentration of 0.02 $g.L^{-1}$ was obtained with the HCD centrate samples flocculated with 0.30 % w/v PEI (see Figure 3.9, middle), although this increment was attributed to experimental error. The error bars in the mAb quantification results increased with flocculant concentration (see Figure 3.9, middle). However, a direct correlation between experimental error and PEI interference could not be established since the error bar for 0.10 % w/v PEI was smaller than that of the HCD mammalian cell centrate (see Figure 3.9, middle). Flocculation with PEI reduced up to 575 times the DNA content in the HCD mammalian cell centrate (see Figure 3.9, bottom). DNA removal depended on the PEI concentration used, with larger flocculant concentrations being less efficient at reducing the DNA content (see Figure 3.9, bottom); a 575 fold reduction was achieved with 0.10 % w/v PEI, 341 fold with 0.30 % w/v PEI and 130 fold with 0.60 % w/v PEI. The DNA quantification results showed that (i) an optimal PEI concentration for DNA removal existed, and (ii) PEI, a positively charged polylectrolyte, was very effective at flocculating DNA at any of the concentrations studied.

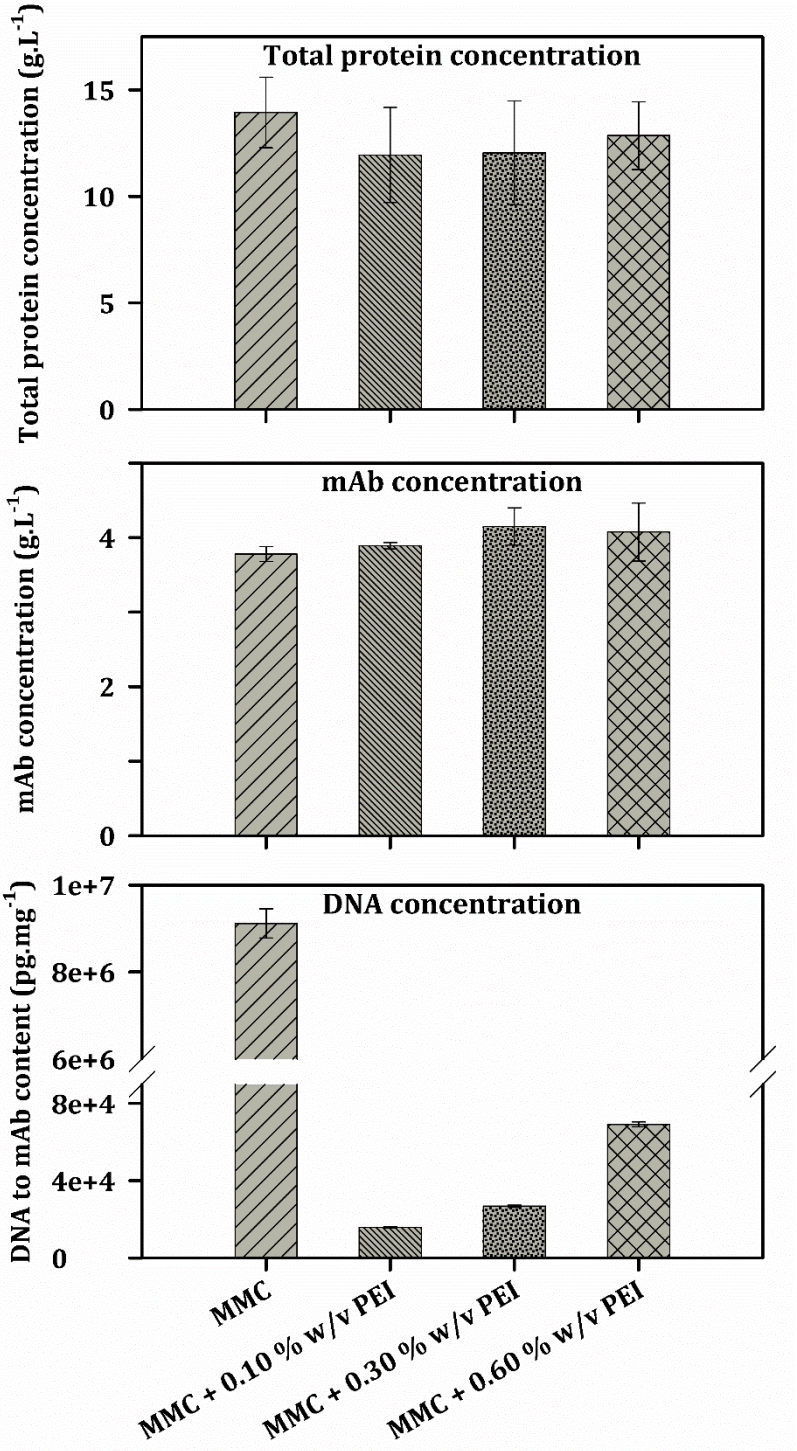

Figure 3.9. Product yield and impurity removal during flocculation with polyethylenimine.

Centrifuged (Q/Σ = 2.85x10^{-8} m.s^{-1}) HCD mammalian cell culture fluid (Xceed™ cell line; peak cell count = 29.0x10^{6} cells.mL^{-1}) was flocculated at laboratory scale as described in Section 2.7.1. Total protein and DNA concentration were measured as described in Section 2.10.1 and Section 2.10.3, respectively. Product content was measured via protein G HPLC and using the HCD mammalian cell protocol (see Section 2.10.2). Error bars represent one standard deviation where n = 3. MMC refers to mammalian cell centrate.

3.4. Conclusions

This chapter has described the evaluation of different mAb-producing CHO cell lines used to generate mammalian cell culture centrate for the flocculation experiments. The analytical techniques and assays chosen to assess flocculation performance were also investigated. A summary of the chapter conclusions, with reference to their aims and objectives, are below.

1. Evaluate the use of different CHO cell lines and cell culture scales to obtain centrifuged mammalian cell culture fluid for the flocculation experiments.

Maximum cell densities larger than $20x10^6$ cells.mL^{-1} achieved during cell culture were necessary for polyethylenimine to successfully flocculate the submicron particles present in the centrifuged mammalian cell fluids evaluated. Such high cell densities were only reached by the Xceed™ CHO cell line studied. A change in the cell culture scale and/or the feeding strategy (i.e. fed-batch or batch) did not improve the flocculation success. Therefore, only centrifuged cell culture fluid obtained from the Xceed™ CHO cell line could be used in the flocculation experiments.

2. Assess different storage methods for the centrifuged CHO cell culture fluid used in the flocculation experiments.

The limited availability of Xceed™ cell centrate (supplied by Lonza Biologics, Slough, UK), and the rapid change in its particulate content when stored at 5°C, made freezing temperatures the best storage option. Freezing also guaranteed the same starting experimental conditions to all the Xceed™ cell centrate samples as long as they were obtained from the same cell culture batch.

3. Estimate the interference of PEI with the analytical assays used to quantify flocculation performance and optimise the protocols, if necessary, to reduce or avoid flocculant interference.

The high absorbance values obtained with polyethylenimine at a wide spectrum of wavelengths limited the use of total protein and DNA quantification methods to colorimetric assays with absorbance readings above 500 nm. The interference

of polyethylenimine with the total protein, DNA and product quantification methods then chosen showed it was necessary to assess flocculant interference based on the sample results and on a case-by-case basis. That is, it is necessary to consider the different flocculation parameters changed during the flocculation studies.

4. Study the flocculation of centrifuged CHO cell fluids and the effect that different flocculation variables have on flocculation performance.

Flocculant concentration and pH, unlike impeller design, determined the size distribution of the particles when flocculating Xceed™ cell centrate with polyethylenimine. Nonetheless, these were preliminary results since flocculant addition time, a critical parameter affecting the size distribution of the flocs (see Section 4.3.3 and Section 5.3.2), was not tightly controlled. The ability to flocculate the submicron particles present in the Xceed™ cell centrate at concentrations as low as 0.10 % w/v, the high affinity for DNA, and the high product yield obtained, suggested polyethylenimine was a good flocculant candidate for the flocculation experiments that follow in this thesis.

4. Development of an Automated Ultra Scale-Down Flocculation Technique

4.1. Introduction and Aims

The results obtained in Chapter 3 show that the success of flocculation processes is determined by a large number of variables and factors, which has also been reported in the literature (Bratby, 1980; Kim et al., 2001; Salt et al., 1995). A large experimental space requires the use of high-throughput, automation and multifactorial design approaches during early process development. However, no attempts have been made to develop a flocculation platform that (i) produces process-relevant material at the microliter scale; and (ii) generates data equivalent to that of production-scale. A platform with these characteristics is also needed to acquire in-depth process understanding during early process development so that time to market, risk of failure and associated costs are reduced (Titchener-Hooker et al., 2008). This chapter describes the development of an ultra scale-down (USD) flocculation technology that will allow the exploration of the large experimental space and the understanding of the key process interactions between this and other subsequent unit operations (e.g. centrifugation, microfiltration and/or depth filtration).

Summary of the chapter's aims and objectives:

1. Investigate the critical parameters controlling the scale-up/scale-down of flocculation unit operations between two geometrically different vessels.
2. Develop an USD flocculation platform based upon the process understanding acquired.
3. Successfully scale-up the flocculation process of pre-clarified cell broths between two non-geometrically similar vessels.

4.2. Experimental Set-Up

4.2.1. Operational Characterisation of the Flocculation Systems

Refer to Section 2.3.1 (pilot scale) and Section 2.3.3 (USD scale) for the detailed methodologies used to achieve a tight control over impeller speed and volume of reagent added.

4.2.2. Preparation and Characterisation of the Clarified Baker's Yeast Homogenate and Polyethylenimine

Clarified Baker's yeast homogenate was prepared as described in Section 2.2 and stored at -20°C. The centrate percentage solid content was calculated as described in Section 2.11.3 as a quality control measure for the different batches of material prepared. The centrate was defrosted at room temperature prior to use. The fresh and thawed centrate were also characterised by their particle size distribution (PSD) measured by laser light diffraction according to Section 2.11.4. The dynamic viscosity and density of the thawed centrate were measured as described in Section 2.11.5 and Section 2.11.6, respectively.

A 4 % w/v polyethylenimine (PEI) stock solution was used to flocculate the clarified yeast homogenate. The PEI stock solution was prepared fresh the day before each flocculation experiment by mixing overnight the required amount of PEI in phosphate buffer (0.1 M NaH_2PO_4, adjusted to pH 6.5 using 3 M NaOH). The dynamic viscosity and density of the PEI stock solution were measured at 22°C as described in Section 2.11.5 and Section 2.11.6, respectively.

4.2.3. Mixing Time Scale Studies

4.2.3.1. Theoretical Calculation

Macromixing, mesomixing and micromixing time constants were theoretically calculated for the pilot-scale flocculation system only. Equation 2.3 to Equation 2.11 were used to calculate the characteristic mixing times. Calculations were performed for an impeller speed of 4.8 rps and for nine different feed addition times (t_f) (12, 18, 24, 45, 71, 102, 143, 200 and 254 s). The value of impeller speed

used was the same as that of the flocculation studies with changing flocculant addition times (see Section 4.2.4). Nine t_f values were chosen to represent a wider range of flocculant addition times than these used in the experimental characterisation of micromixing. The values of flocculant addition volume and kinematic viscosity used in the calculations were 75 mL and $1.92x10^{-6}$ $m^2.s^{-1}$, respectively. These were the actual experimental values; kinematic viscosity was that of the clarified yeast at 22°C.

4.2.3.2. Experimental Calculation

At pilot scale, critical addition time (t_{crit}) was estimated at three different impeller speeds (1.8, 4.8, and 7.9 rps) and eight acid addition times (340, 250, 170, 120, 70.0, 40.0, 20.0 and 3.80 s). At USD scale, t_{crit} was estimated at two different impeller speeds (17 and 27 rps) and eight acid addition times (6.4, 5.5, 4.3, 3.2, 2.0, $9.1x10^{-1}$, $3.2x10^{-1}$ and $7.0x10^{-3}$ s). Refer to Section 2.4.2 for the detailed experimental methodology.

4.2.4. Flocculation Studies

Flocculation conditions were those detailed in Section 2.7.2. Impeller speed and flocculant addition time varied depending upon the flocculation study as follows.

4.2.4.1. Effect of Flocculant Addition Time

The value of impeller speed was kept constant while flocculant addition time changed. Since the volume of flocculant added was constant and equal to 75 mL, addition time was also expressed as addition rate. At pilot scale, impeller speed was set to 4.8 rps and flocculant addition rate to 8.57, 10.7, 15.0, 21.4, 30.0, 47.6, 90.0, 120 and 184 $mL.min^{-1}$. At USD scale, impeller speed was set to 17 rps, or 20 rps during the validation studies, and flocculant addition rate was 1.00, 5.00, 20.0, 100, 250, 400, 550, 700 and 900 $\mu L.s^{-1}$. The impeller speeds chosen were intermediate values within the range of impeller speeds of the motors used at each scale. During the validation studies, impeller speed at USD scale was calculated based on the following scale-up "rule of thumb": constant average turbulent energy dissipation rate per unit mass of fluid (ε_{avg}); that is, impeller speed at USD scale was that translating into an equal ε_{avg} value as that one of pilot

scale. The ranges of flocculant addition rate used were limited by the liquid handling robot (USD scale) and the syringe pump (pilot scale) employed. The PSD of the resultant flocs was measured according to the Section 2.11.4 to evaluate the effect of flocculant addition rate upon flocculation performance.

4.2.4.2. Effect of Impeller Speed

The value of flocculant addition rate was kept constant whilst impeller speed changed. At pilot scale, flocculant addition rate was set to 15 $mL.min^{-1}$ and impeller speed to 1.8, 3.4, 4.8, 6.0, 6.8, 7.5 and 7.9 rps. At USD scale, flocculant addition rate was set to 1 $\mu L.s^{-1}$ and impeller speed to 5.3, 8.4, 12, 15, 17, 20, 23 and 27 rps. The flocculant addition rate values were chosen to guarantee the predominance of a micromixing regime in the flocculation vessel. The ranges of impeller speed studied were determined by the speed limits of the motors used at each scale. Average turbulent energy dissipation rate per unit mass of fluid (ε_{avg}) and impeller tip speed (v_{tip}) were calculated for the same ranges of impeller speed. Calculations were performed as detailed in Section 2.5.

4.3. Results and Discussion

4.3.1. Operational Characterisation of the Flocculation Systems

Impeller speed and reagent addition rate were the two variables changed during the mixing time scale and flocculation studies. The volume of reagent added was kept constant at each scale during the mixing time and flocculation studies. However, this variable also affected flocculation performance. An accurate control over these variables was necessary to successfully scale-up flocculation between the two mixing systems. Consequently, the flocculation systems used at each scale were operationally characterised before performing the mixing time and flocculation experiments. The impeller power number (P_o) of the microwell mixing device used at USD scale was also empirically determined.

4.3.1.1. Pilot Scale

The coupling between the rotational speed displayed on the system's driving unit and the speed of the vessel's impeller shaft was studied to precisely control impeller speed at pilot scale. The results are plotted in Figure 4.1. The correlation,

which showed a strong linear regression (R^2 = 0.999), was used to calculate the rotational speed of the vessel's driving unit during the mixing time and flocculation studies. There was a constant negative offset of 0.18 rps between the displayed and actual rotational speeds. Smaller actual speeds were also described by a slope below the value of 1, although the difference became narrower with faster rotational speeds.

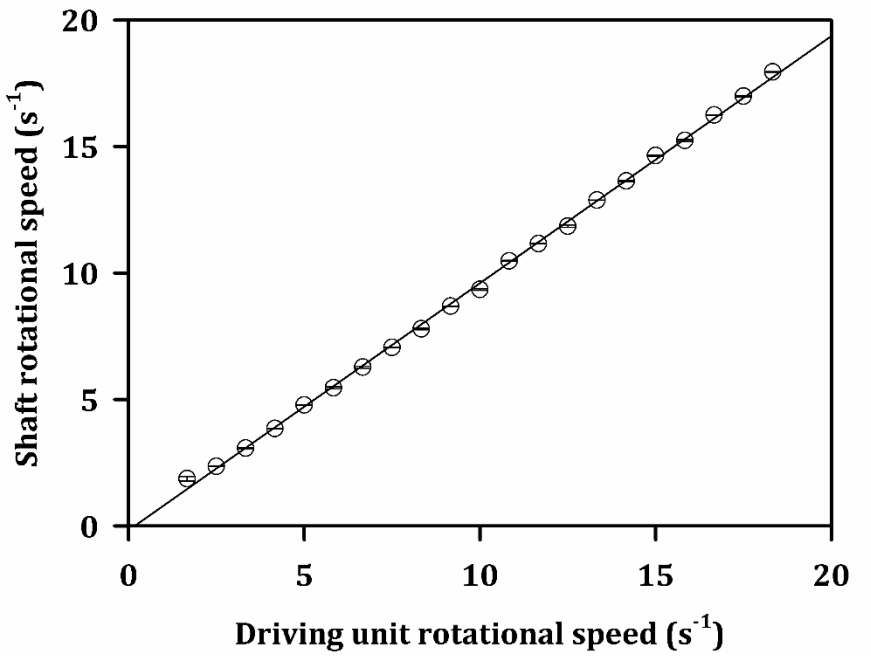

Figure 4.1. Operational characterisation of the impeller speed in the stirred tank reactor used at pilot scale.
A calibrated stroboscope was used to determine the coupling between the rotational speed of the STR driving unit or motor and the vessel's impeller shaft. The linear regression plotted was y = -0.175 + 0.977x with R^2 = 0.999. The error bars represent one standard deviation where n = 4. Refer to Section 2.3.1 for the detailed methodology.

The volume of acid and polyethylenimine (PEI) added into the stirred tank reactor (STR) used at pilot scale was critical for the outcome of the mixing time and flocculation studies. Consequently, the calibration of the syringe pump used at pilot scale for controlled reagent additions was tested. Table 4.1 shows the 0.5 M sulphuric acid solution used in the mixing time studies was delivered with an accuracy of 98.9 %. Table 4.2 shows the accuracy for the PEI stock solution was 99.4 %.

Table 4.1. Calibration of the syringe pump used at pilot-scale flocculation for controlled 0.5 M sulphuric acid addition.
A programmable syringe pump was used. The solution used was 0.5 M sulphuric acid. The total volume of acid added was equal to 6 mL. Calibration was tested by measuring with an analytical balance the weight of the reagent displaced by the syringe pump. Volume was calculated with the 0.5 M sulphuric acid density of 1050 kg.m^{-3}. Refer to Section 2.3.1 for the detailed methodology.

Flow rate (mL.min^{-1})	Weight (g)			Volume (mL)		
184	8.23	8.06	8.25	7.84	7.68	7.86
150	8.29	8.64	8.22	7.90	8.23	7.83
120	8.27	8.47	8.86	7.88	8.07	8.44
90.0	8.16	8.32	8.69	7.77	7.92	8.28
60.0	8.26	8.19	9.15	7.87	7.80	8.71
30.0	8.69	8.22	8.16	8.28	7.83	7.77
15.0	8.43	8.37	8.10	8.03	7.97	7.71
6.00	8.71	8.14	8.28	8.30	7.75	7.89
3.00	8.55	8.34	8.09	8.14	7.94	7.70

Table 4.2. Calibration of the syringe pump used at pilot-scale flocculation for controlled PEI addition.
Calibration methodology was as described in Table 4.1. A 4 % w/v PEI solution was measured. Total volume of PEI added was equal to 75 mL. The density of the PEI stock solution used was 1030 kg.m^{-3}.

Flow rate (mL.min^{-1})	Weight (g)			Volume (mL)		
184	76.37	75.70	77.26	74.15	73.50	75.01
150	77.04	76.36	76.14	74.80	74.14	73.92
120	77.15	77.07	76.89	74.90	74.83	74.65
90.0	75.29	76.13	75.79	73.10	73.91	73.58
60.0	76.41	77.12	76.54	74.18	74.87	74.31
30.0	77.09	76.27	76.29	74.84	74.05	74.07
15.0	76.07	76.09	77.01	73.85	73.87	74.77
6.00	75.18	77.25	76.30	72.99	75.00	74.08
3.00	76.26	75.89	76.89	74.04	73.68	74.65

4.3.1.2. USD Scale

The rotational speed of the magnetic motor used at USD scale was expressed as % speed by the manufacturer. Speed ranged from 0 to 100 %, but its equivalence in revolutions per second needed to be determined before the mixing time scale and flocculation studies. Figure 4.2.A shows that the percentage speed scale followed a strong linear correlation (R^2 = 0.999) with the rotational speed of the motor spindle. The lowest and maximum speeds were 5.2 and 28 rps, respectively. An offset of 4.7 rps in the linear regression equation confirmed that the motor rotated at even 0 % speed.

The coupling between the spindle and the impellers was studied to confirm the magnets were rotating at the same speed as the motor. Nineteen different impellers across the microwell mixing system were evaluated to also ensure there were no differences in rotational speed across the microplate. Figure 4.2.B shows the coupling between the impeller located in well D3 and the magnetic motor. The results described a strong linear correlation (R^2 = 0.999) between the motor and the impeller rotational speed. The speeds were equivalent (i.e. slope = 1), but there was a constant offset of -0.13 rps for the impeller speed. The other eighteen impellers studied showed that the slope equalled to 1 in all cases but the offset ranged from -0.17 to 0.05 rps. The differences in the impeller speed offset could not be correlated to a specific zone on the microplate but were arbitrary instead. The average offset value, which was equal to -0.05 rps, was taken into account in all studies.

Because the viscosity values of the PEI stock solution and 0.5 M sulphuric acid used in the experiments were higher than that of water, a specific liquid class for each solution was created in the software of the liquid handling robot. Specific liquid classes are created to accurately aspirate and dispense fluid. Each liquid class was calibrated with four different liquid volumes. The offsets between the dispensed volume and set volume (i.e. diluter volume) calculated ranged between -1.229 and 0.113 µL. No trend between the solution's density and/or viscosity and the calculated offset was observed.

The magnetically-driven disc impeller power number was empirically estimated from the global best fit of the USD and pilot scale ε_{avg} values. Three power regression equations ($y = ax^b$) were obtained from plotting the pilot scale ε_{avg} values against the particle size characteristic descriptors d_{10}, d_{50} and d_{90} of the flocs generated (see Section 4.3.7); these values correspond, respectively, to the particle diameter below which 10 %, 50 % and 90 % of the sample volume exists. The power regression constants *a* and *b* were used to calculate the P_o of the USD-scale impellers as follows:

$$\varepsilon_{avg,STR,experimental} = \varepsilon_{avg,USD,theoretical} \qquad \text{(Equation 4.1.a)}$$

$$\left(\frac{d_{x,USD}}{a_{y,STR}}\right)^{1/b_{y,STR}} = P_{o,USD}\left(\frac{N^3 D_i^5}{V_l}\right)_{USD} \qquad \text{(Equation 4.1.b)}$$

$$P_{o,USD} = \left(\frac{d_{x,USD}}{a_{y,STR}}\right)^{1/b_{y,STR}}\left(\frac{V_l}{N^3 D_i^5}\right)_{USD} \qquad \text{(Equation 4.1.c)}$$

where ε_{avg} is the average turbulent energy dissipation per unit mass ($W.kg^{-1}$), d_x is the particle size characteristic descriptor (μm) where x is 10, 50 or 90, a_y and b_y are the power regression curve constants where y refers to the d_{10}, d_{50} or d_{90} data sets, P_o is the power number, N is the impeller speed (s^{-1}), D_i is the impeller diameter (m) and V_l is the liquid working volume (m^3). STR and USD subscripts refer to the stirred tank reactor and microwell mixing systems, respectively. The impeller power number was calculated for 24 different conditions. The average value, which was equal to 0.85, was used in all the ε_{avg} calculations at USD scale.

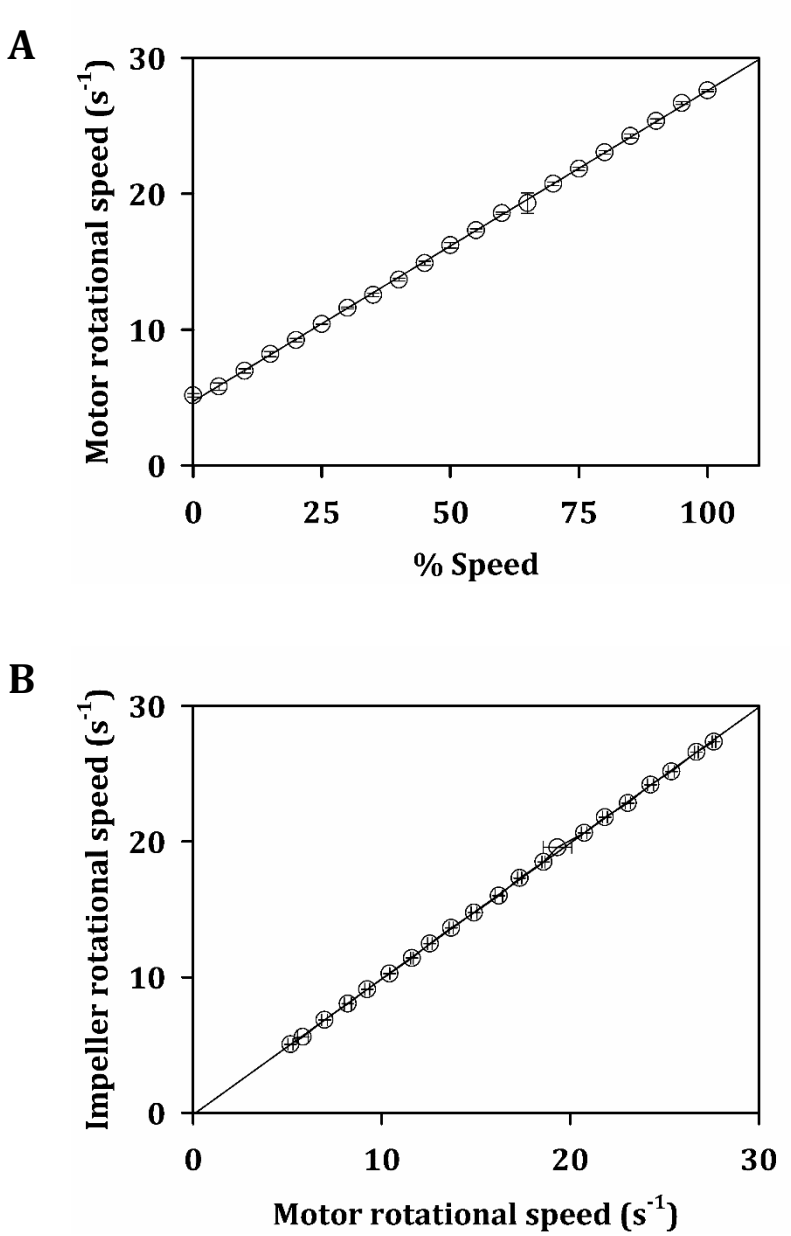

Figure 4.2. Operational characterisation of the impeller speed in the microwell mixing device used at USD scale.
A*. A calibrated stroboscope was used to determine the equivalence of the magnetic motor % speed scale in revolutions per second of the magnetic drive. The linear regression plotted was y = 4.722 + 0.229x with R^2 = 0.999. Error bars indicate one standard deviation where n = 6. Refer to Section 2.3.3 for the detailed methodology.* ***B****. A calibrated stroboscope was used to confirm the coupling between the magnetic discs and the magnetic drive. For the impeller speed measurements the stroboscope was located at a fixed 3 cm from the reference point. The linear regression plotted was y = -0.130 + 1.001x with R^2 = 0.999. Horizontal error bars indicate one standard deviation where n = 6. Vertical error bars indicate one standard deviation where n = 3. Refer to Section 2.3.3 for the detailed methodology.*

4.3.2. Characterisation of the Flocculation Feed Streams

The percentage solid content of the clarified yeast homogenate used in the flocculation studies was 5.6 %. Percentage solids remaining was calculated as detailed in Section 2.11.3. Variability in the solids content up to 32 % was observed possibly due to the inherent batch to batch inconsistency of the fresh Baker's yeast supplied. Table 4.3 shows the OD_{600} values obtained at each step of the preparation of the clarified yeast homogenate. The decrease in OD_{600} between homogenisation and centrifugation described the reduction in particulates present in the feed. Despite the variability in the % solids content, the PSD of the clarified yeast homogenate followed the same bimodal distribution as shown in Figure 4.3. The fresh supernatant was primarily constituted of submicron particles, as represented by the peak between 0 and 0.75 μm with an equivalent 420 % volume frequency. A second peak existed between 1 and 250 μm with a maximum volume frequency of 2.8 % at 2 μm. Particles larger than 250 μm were not detected. Since the clarified yeast supernatant was stored at -20°C, the freeze-thaw effect on the PSD of the clarified yeast homogenate was studied. The PSD continued to be bimodal after freeze-thawing (see Figure 4.3). The population of particles between 0 and 0.75 μm decreased after freeze-thawing, while that between 1 and 250 μm increased on average; however, the large error bars obtained for the particles between 1 and 250 μm, which overlapped the PSD obtained with fresh material, made it impossible to conclude the 1-250 μm population changed after freeze-thawing (see Figure 4.3). The supernatant total protein concentration was equal to 30 ± 3 $g.L^{-1}$ upon freeze-thawing; this result was in accordance with the total protein concentration values reported in the literature for clarified Baker's yeast homogenate (Milburn et al., 1990). The density and dynamic viscosity values measured at 22°C were 1020 $kg.m^{-3}$ and 1.66 mPa.s, respectively. Finally, with regards to the flocculant, the 4 % w/v PEI stock solution used had a density of 1030 $kg.m^{-3}$ and a dynamic viscosity of 1.98 mPa.s at 22°C. Both the clarified Baker's yeast homogenate and the 4 % w/v PEI stock solution used were Newtonian fluids.

Table 4.3. Change in OD_{600} during the different steps of the clarified yeast homogenate preparation.
OD measurements were taken immediately after the preparation of each solution with a double-beam spectrophotometer according to Section 2.11.1. Well-spun samples, which represent the samples with the highest clarification achievable, were the supernatants recovered after centrifuging (Eppendorf 5424R; Eppendorf, Hamburg, Germany) the clarified homogenate for 30 minutes at 220 rps and 4°C. The third column describes one standard deviation where n = 9.

Sample	Average OD_{600}	Standard deviation
Whole yeast cells	109.4	15.2
Homogenate	34.2	2.69
Clarified homogenate	2.54	0.410
Well-spun	0.681	0.151

4.3.3. Effect of Flocculant Addition Time on Particle Size Distribution

The aim was to investigate how flocculant addition time, or addition rate, modulated flocculation performance in the pilot and USD mixing systems. The studies were performed by varying the flocculant addition time (t_f). Flocculation performance was described by the particle size characteristic descriptors d_{10}, d_{50}, and d_{90}.

As observed in Figure 4.4, narrower and smaller PSDs were gradually obtained with longer t_f values at USD and pilot scale. The decrease in particle size was similar in both flocculation systems, with a 60 % reduction in the d_{90} data set. The values of d_{50} decreased by 57 % and these of d_{10} by 30 %. In addition to this, the smallest and largest particles generated at both scales were similarly sized, with size differences only ranging from 0.2 to 13 %. Higher variations in particle size were observed at USD scale when using fast flocculant addition rates. This might have been due to a non-homogeneous, thus non-reproducible, distribution of the flocculant inside the microwell.

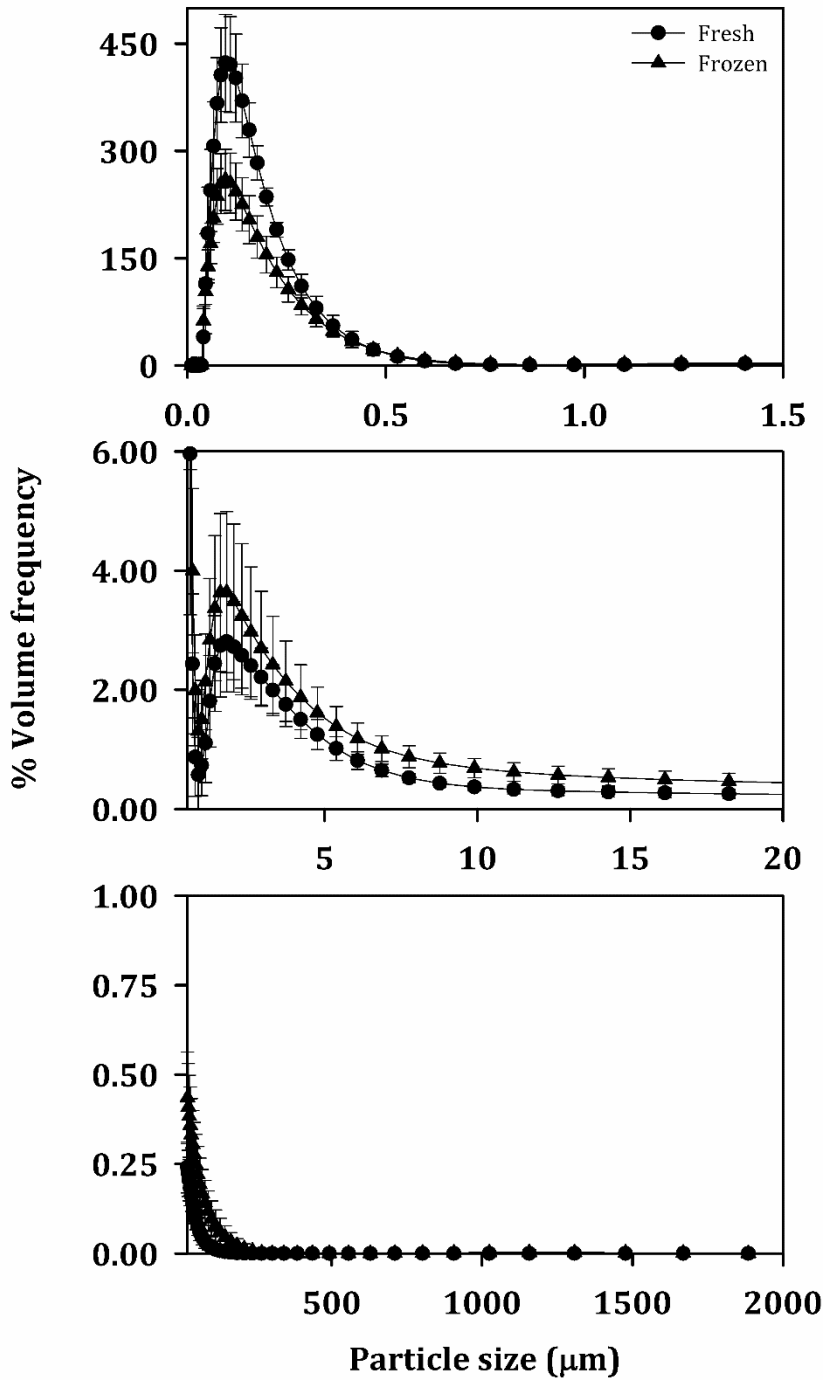

Figure 4.3. Freeze-thawing effect upon the particle size distribution of clarified yeast homogenate.

The PSD curves were divided in 3 graphs with the x and y-axis scales adjusted accordingly. PSD was measured by laser light diffraction as described in Section 2.11.4. Error bars indicate one standard deviation where n = 9 (fresh) and n = 44 (frozen). Frozen material was allowed to reach room temperature before the PSD measurements were taken.

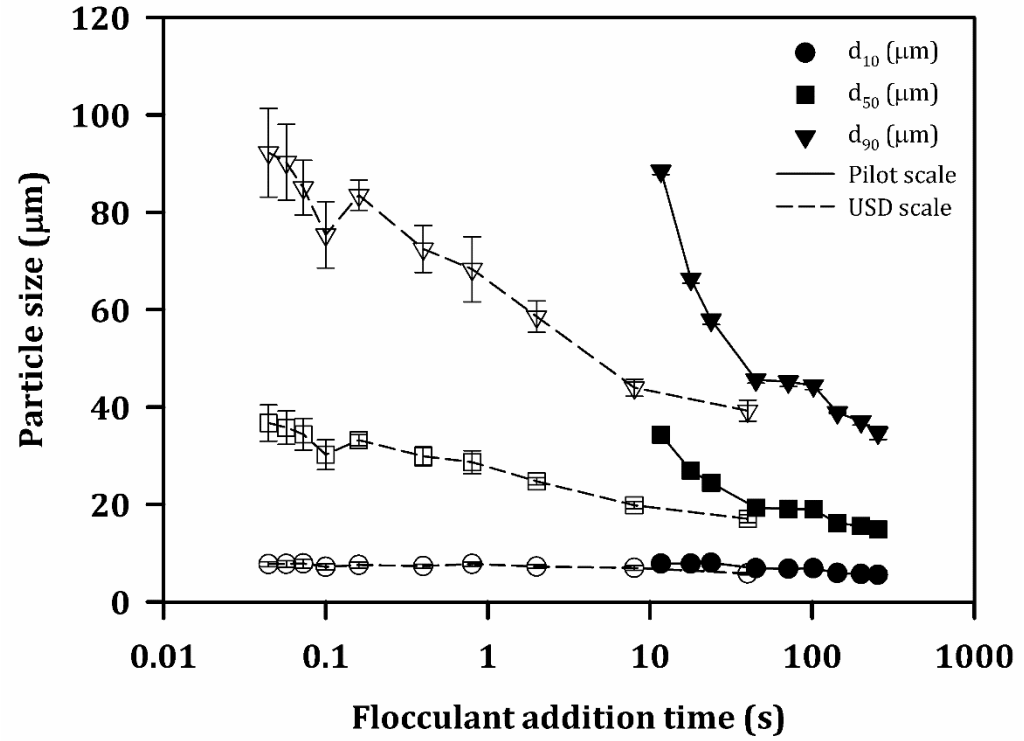

Figure 4.4. Effect of flocculant addition time on PSD in the USD and pilot scale flocculation systems.
The closed data points (●,■,▼) represent the pilot-scale data sets. The open data points (○,□,▽) describe the USD-scale data sets. Freeze-thawed clarified yeast homogenate was flocculated at room temperature with a final PEI concentration of 0.2 % w/v and a impeller speed equal to 17 rps (USD scale) and 4.8 rps (pilot scale). Flocculant was added at different rates with addition time varying from 0.04 to 40 s (USD scale) and from 11.7 to 255 s (pilot scale). After PEI addition the flocs were allowed to mature for 10 minutes (refer to Section 2.7.2 for the detailed flocculation methodology). PSD was measured by laser light diffraction immediately after floc maturation according to Section 2.11.4. Error bars indicate one standard deviation where n = 8 (USD scale) and n = 3 (pilot scale).

The important effect of flocculant addition rate upon PSD was already demonstrated by Berrill and co-authors (2008), who obtained wider and more complex flocculated populations with shorter flocculant addition times. However, this is not an exclusive phenomenon to flocculation, as addition rate has been shown to affect the particle size and its reproducibility, structure and composition of precipitates (Fisher et al., 1986; Franke and Mersmann, 1995; Hofland et al., 2003) and crystals (Torbacke and Rasmuson, 2001).

These results meant that t_f was a key variable affecting flocculation performance and therefore needed to be considered during the scale-up process between the

two geometrically-different flocculation vessels used. The small difference between the largest and smallest particles obtained in the two vessels illustrates that similar physicochemical conditions were obtained at both scales at the fastest and shortest flocculant addition rates studied, and therefore that flocculation could be successfully scaled-up between the two systems. However, the different gradual decrease in floc size observed in Figure 4.4 confirmed the effect of t_f upon particle size was not proportional to its value but was determined by another variable that was at the same time modulated by t_f.

4.3.4. Mixing Time Characterisation of the Flocculation Systems

The effect of reagent addition rate upon PSD in precipitation and crystallisation processes has been described by the influence the predominant mixing time scale (i.e. macromixing, mesomixing or micromixing) has upon the resulting local concentration gradients of the reagent (see Section 1.5.3) (Franke and Mersmann, 1995; Marcant and David, 1991; Pohorecki and Bałdyga, 1988; Torbacke and Rasmuson, 2001; Zauner and Jones, 2002). Before a chemical reaction can occur between two or more reactants, the reactants have to be mixed on a molecular scale. When a reaction is slow in comparison to the mixing process, the reaction will only depend on its chemical kinetics as the solution will be homogeneously distributed before any reaction takes place. However, when the reaction times are of the same order of magnitude as the characteristic mixing times, the mixing process will determine the local reagent concentration gradients thus affecting the yield and selectivity of the reaction (Verschuren et al., 2001).

The rapid polymer adsorption rates of PEI (Birkner and Morgan, 1968) suggested the mixing conditions could also have been responsible for the effect of flocculant addition time upon the PSD of the flocs (see Section 4.3.3). The predominant mixing time scale under each of the addition times studied were theoretically calculated as well as experimentally determined in order to explain the different gradual decrease in floc size observed at both flocculation scales (see Figure 4.4).

4.3.4.1. Theoretical Characterisation

The characteristic mixing time scales were theoretically calculated for the pilot-scale system at nine different feed addition times according to Section 2.4.1. The results obtained are summarised in Table 4.4. The USD-scale mixing system was not characterised due to differences in the vessel and impeller geometries for which the equations applied were developed. Refer to Section 1.5.3 and Figure 1.9 for a description of the different mixing regimes (i.e. macromixing, mesomixing and micromixing time scales).

Macromixing time (t_m) remained constant since it was independent of the feed time (t_f) values and therefore of the experimental flocculant addition times. The results in Table 4.4 show t_m was two orders of magnitude larger than turbulent dispersion mesomixing time (t_d), large eddy disintegration mesomixing time (t_s) and micromixing time (t_e). Additionally, feed addition time was between one to two orders of magnitude larger than circulation time (t_c) and macromixing time. Consequently, at the range of t_f studied the reactor should be assumed to be completely macromixed (Bałdyga and Bourne, 1999; Bałdyga et al., 1993, 1997).

Because macromixing was not the mixing time scale affecting pilot-scale flocculation performance, micromixing and mesomixing time scales were evaluated. The values of t_e, t_d and t_s varied with t_f. At the longest feed addition times ($t_f \geq 143$ s), micromixing time was between four to six times larger than large eddy disintegration mesomixing time and turbulent dispersion mesomixing time (see Table 4.4). Consequently, micromixing time was the limiting mixing time scale at $t_f \geq 143$ s; therefore, it is thought that micromixing governed at long flocculant addition times ($t_f > 140$ s). In contrast, at the shortest feed addition times ($t_f \leq 24$ s) the limiting mixing time scale was turbulent dispersion mesomixing (see Table 4.4); therefore, mesomixing was the predominant mixing time scale at short flocculant addition times ($t_f < 20$ s). For t_f values between 20 and 140 s, it is thought that both micromixing and mesomixing were the controlling mechanisms.

Theoretical characteristic time values cannot be taken as absolute values due to the assumptions used during the calculations regarding vessel geometry and

turbulent mixing conditions. Nonetheless, these theoretical mixing time values can be used as an indication of when the transition between micromixing regimes (i.e. micromixing to mesomixing) occurred in the pilot-scale system.

Table 4.4. Theoretical values of the characteristic mixing time scales for the pilot-scale flocculation system.
Table adapted from Espuny Garcia del Real et al. (2014).
Circulation time (t_c), macromixing time (t_m), turbulent dispersion mesomixing time (t_d), large eddy disintegration mesomixing time (t_s) and micromixing time (t_e) were calculated as described in Section 2.4.1. Calculations were performed for an impeller speed of 4.8 rps and for the nine different feed addition times (t_f) specified in the table. Reagent (i.e. flocculant) volume was equal to 75 mL. The kinematic viscosity of the feed material (i.e. clarified yeast homogenate) was 1.92x10^{-6} m^2.s^{-1}.

	t_f (s)	t_c (s)	t_m (s)	t_d (s)	t_s (s)	t_e (s)
Micromixing	254	1.6	6.4	0.012	0.014	0.081
	200			0.015	0.015	
	143			0.021	0.017	
Micromixing & Mesomixing	102	1.6	6.4	0.030	0.019	0.081
	71			0.042	0.022	
	45			0.067	0.025	
Mesomixing	24	1.6	6.4	0.127	0.031	0.081
	18			0.170	0.034	
	12			0.259	0.040	

4.3.4.2. Experimental Characterisation

The iodide-iodate system of parallel competing reactions developed by Fournier et al. (1996b) was used to study micromixing time in the pilot and USD mixing systems. This experimental method consists in determining the segregation state of the fluid, which is quantified by the segregation index (X_S); the values of X_S lie between 0 and 1, where 0 refers to a perfectly micromixed system and 1 to a completely segregated system. The segregation state of the fluid (i.e. X_S) was studied with increasing addition times to experimentally determine the value of t_f at which the systems transitioned from a micromixing-mesomixing regime to a fully micromixing regime. This transition, which is specific to the vessel and hydrodynamic conditions, is identified as the critical addition time (t_{crit}).

The pilot-scale system was characterised at three different impeller speeds (1.8, 4.8 and 7.9 rps). Figure 4.5.A describes how the value of X_S gradually decreased

at pilot scale with increasing values of acid addition time for the three impeller speeds studied. This trend indicated improved micromixing with longer values of t_f. The transition from a micromixing-mesomixing controlled regime to a fully micromixing regime (Bałdyga and Bourne, 1992) was indicated by the plateauing in the value of X_S at t_f equal to 150 s, approximately. This transition, or t_{crit}, occurred at the three impeller speeds studied. Another trend observed at pilot scale was a decrease in the overall value of X_S, thus improved micromixing, with increasing impeller speeds; the same observation was made by Fournier et al. (1996a). The value of t_{crit} confirmed the theoretical approximation of the time constants shown in Table 4.4.

The results obtained for the USD mixing device (Figure 4.5.B) describe the same trend of decreasing values of X_S with longer addition times and faster impeller speeds observed at pilot scale. Critical addition time was identified to occur at t_f values between 2 and 3 seconds, hence indicating that the system was only micromixing controlled for values of t_f > 3s. However, the influence of macromixing could not be determined in the USD mixing system. Therefore, if the predominance of the micromixing time scale wanted to be guaranteed, a larger value of addition time than the t_{crit} experimentally obtained should be used; Assirelli et al. (2002) and Bałdyga and Bourne (1999) stated the effects of macromixing and mesomixing can be neglected if sufficiently long addition times are used.

Different values of X_S were obtained in each flocculation mixing device (see Figure 4.5) since they are associated with (i) the location of the feed point, (ii) the reaction zone, and (iii) the vessel geometry (Bałdyga and Bourne, 1999). These results confirmed the need to characterise how the segregation state of the fluid changed with increasing feed addition times in each mixing system studied.

No increase in the value of X_S was observed with longer acid addition times (see Figure 4.5), which suggested the absence of backmixing effects at the range of feed addition times used (Bałdyga et al., 1993). The data then confirmed that the feed points were appropriately located and oriented relative to the fluid flow pattern in the USD and pilot-scale mixing vessels.

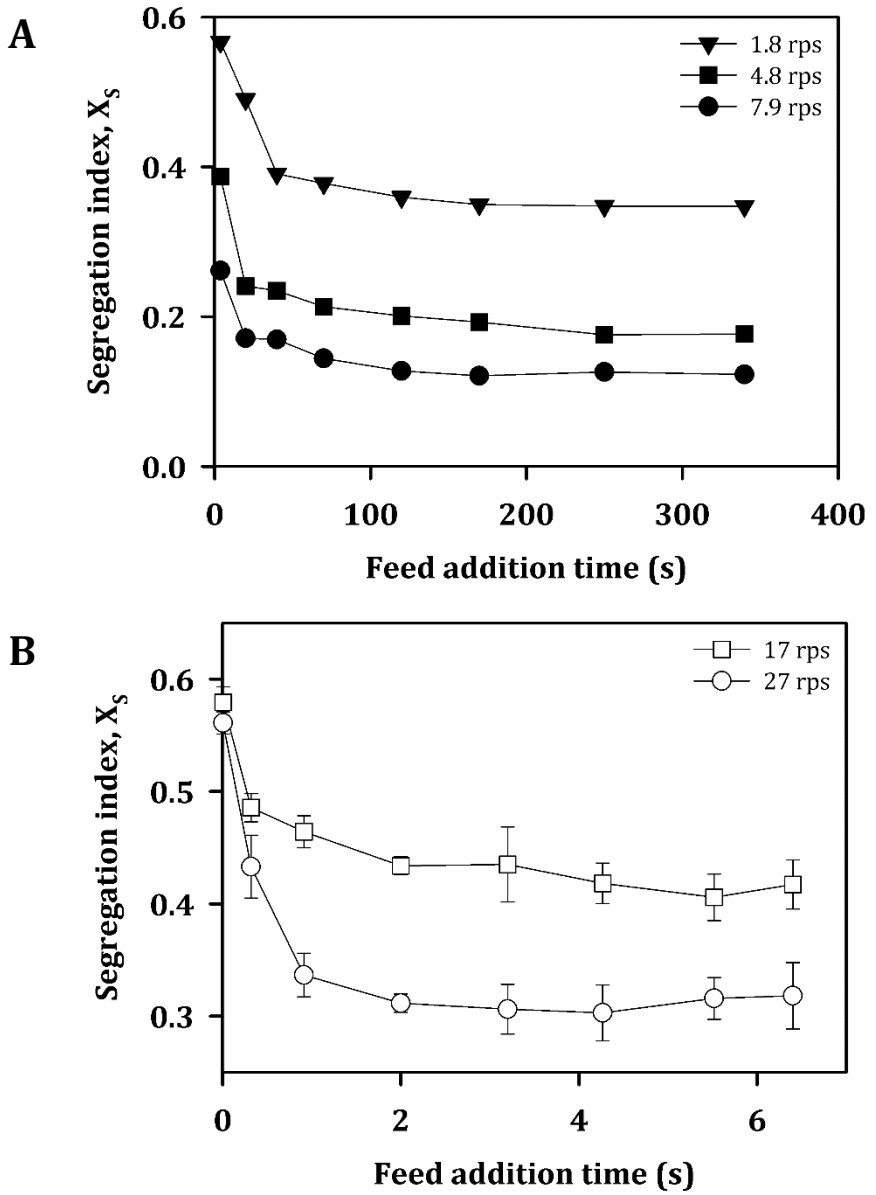

Figure 4.5. Experimental micromixing time studies for the pilot-scale (A) and USD (B) flocculation systems.
Figure adapted from Espuny Garcia del Real et al. (2014).
*Micromixing time was experimentally determined as described in Section 2.4.2. At pilot scale (**A**), micromixing time was studied at three impeller speeds (1.8, 4.8 and 7.9 rps) using eight different acid addition times (340, 250, 170, 120, 70.0, 40.0, 20.0 and 3.80 s). At USD scale (**B**), micromixing time was studied at two impeller speeds (17 and 27 rps) using eight different acid addition times (6.4, 5.5, 4.3, 3.2, 2.0, $9.1x10^{-1}$, $3.2x10^{-1}$ and $7.0x10^{-3}$ s). Error bars indicate one standard deviation where n = 8.*

The viscosity of the two different feed streams employed in the flocculation studies was higher than that of the water-based solutions used in the mixing time

scale experiments, for which a viscosity similar to that of water at 22°C was assumed (i.e. 0.97 mPa.s – (Perry and Green, 2008)). For a given tank and impeller geometry in a fully turbulent flow, viscosity has no effect on the macromixing or mesomixing parameters. However, it does influence the micromixing parameters by increasing molecular segregation and micromixing time, as it can be observed by the larger values of X_S obtained when higher values of viscosity are used when other independent variables are kept constant (Bourne et al., 1989, 1995; Gholap et al., 1994). These effects on the micromixing parameters were observed with a fourfold (Bourne et al., 1989), a seven fold (Gholap et al., 1994) and a six fold (Bourne et al., 1995) increase in viscosity with respect to the control solution. However, the viscosity values of the clarified yeast homogenate and PEI stock solutions used in the flocculation studies were less than double the viscosity of the water-based solutions employed during the micromixing time scale experiments. Therefore, the micromixing parameters obtained during the mixing time studies were assumed to remain unchanged during the flocculation studies.

4.3.5. Effect of Mixing Time Scales on Particle Size Distribution

To understand the effect that mixing time scales had upon the flocculation process in the pilot-scale and USD mixing systems, Figure 4.4 was re-plotted considering the predominant mixing time scale in the vessel at each one of the flocculant addition times studied (see Section 4.3.4 for the results). Figure 4.6 shows the effect of micromixing and mesomixing time scales upon the flocculation performance; flocculation performance was described by the d_{10}, d_{50}, and d_{90} particle size characteristic descriptors, and by the PSD curves with the aim to reveal bimodal or tri-modal distributions.

As described in Section 4.3.3, wider floc distributions were gradually obtained at both scales with decreasing flocculant addition times. However, Figure 4.6.A shows the PSD range differed depending on the predominant mixing regime and the flocculation vessel used. Constant values of d_{10} and d_{50} were found at pilot scale and across the micromixing regime, while the values of d_{90} increased by 8 %. A step increase in the values of d_{50} and d_{90} occurred at pilot scale with flocculant addition times between 102 and 45 s; the step increase was of 4 μm (d_{50}) and of

9 μm (d_{90}). The increase in PSD observed might be explained by both micromixing and mesomixing regimes influencing flocculation despite the theoretical mixing time predictions continued describing the predominance of micromixing within the 102-45 s range (i.e. $t_e > t_d$ and t_s) (see Table 4.4). Faster flocculant addition rates led to wider PSDs at pilot scale (see Figure 4.6.A). When mesomixing was the only mixing mechanism ($t_f < 24$ s) (see Table 4.4), the pilot-scale values of d_{50} and d_{90} increased by 70 % and 90 % in size, respectively; the change in the d_{10} data set was more moderate with a 13 % increase in size. In the USD mixing system, the PSD of the flocs generated decreased in a more gradual manner with longer t_f (see Figure 4.6.A). The largest decrease at USD scale was observed during the transition between a mesomixing to a micromixing-mesomixing controlled regime, where the reductions in size ranged between 35 % and 75 %. The transition to a micromixing controlled regime saw a smaller change in particle size at USD scale, with a 25 % reduction in the size of d_{90} and 20 % for the d_{50} data set. It was also observed that in both flocculation systems the mixing time scales influenced the least upon the size of the smallest particles and the most upon the largest ones, thus significantly impacting upon the width of the PSD.

Figure 4.6.B shows the PSD curves obtained at both scales across the three mixing regimes. Under fully mesomixing conditions, comparable PSD curves (variation < 10 % between 3 and 70 μm) were obtained at USD and pilot scale despite impeller speed and t_f being different at both scales. The fast flocculant addition rates used could have flooded the impeller region with an excess concentration of flocculant. At fast addition rates the flocculant might not uniformly adsorb onto the particles thus resulting in the re-stabilisation of the colloidal suspension; therefore, it is important to ensure the added flocculant is evenly distributed throughout the flocculation vessel (Bolto and Gregory, 2007). While monomodal PSDs were obtained at pilot scale in the micromixing-mesomixing regime, bimodal and wider PSDs were observed at USD scale in the same mixing regime. Finally, the micromixing regime led to narrower monomodal distributions with a maximum difference of 14 % in the values of d_{10}, d_{50}, and d_{90} at both pilot and USD scale.

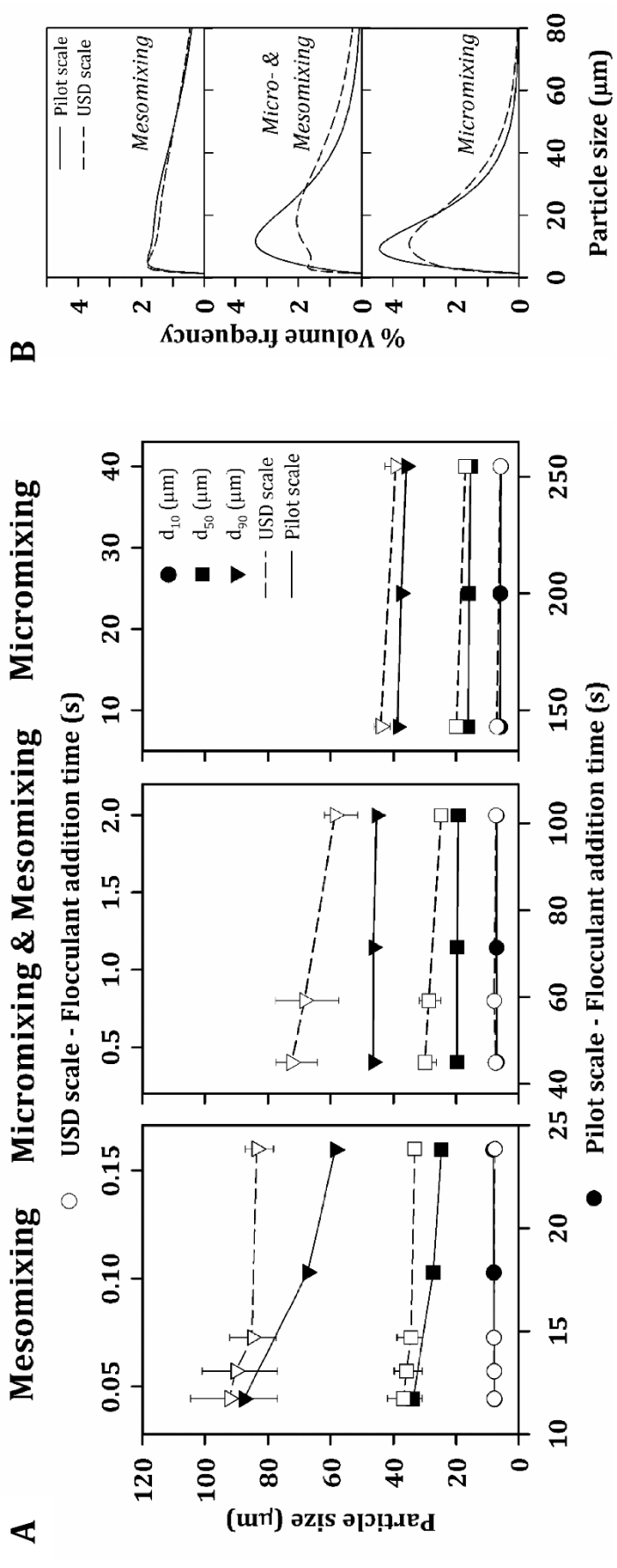

Figure 4.6. Effect of flocculant addition time on the size distribution of the flocs generated in the flocculation systems.

Figure adapted from Espuny Garcia del Real et al. (2014).
Flocculation conditions were: room temperature, 0.2 % v/v PEI concentration, constant impeller speed (17 rps - USD scale and 4.8 rps - pilot scale) and different flocculant addition rates. Refer to Section 2.7.2. for the flocculation methodology. Particle size was measured by laser light diffraction (see Section 2.11.4.). ***A****. The d_{10}, d_{50} and d_{90} data sets were obtained at 1.00, 5.00, 20.0, 100, 250, 400, 550, 700 and 900 µL.s^{-1} (USD scale) and 8.57, 10.7, 15.0, 21.4, 30.0, 47.6, 90.0, 120 and 184 mL.min^{-1} (pilot scale) flocculant addition rates. Error bars describe range of values where n = 8.* ***B****. The PSD curves were obtained at 184, 47.6 and 8.60 mL.min^{-1} (pilot scale) and 900, 50.0 and 1.00 µL.s^{-1} (USD scale) flocculant addition rates. These values represent the different mixing time scales encountered in the flocculation systems.*

Narrow monomodal floc populations are always of interest, particularly if they are clarified by centrifugation (Berrill et al., 2008) or depth filtration (Singh et al., 2013). In addition to the particle size, the complexity of the PSDs obtained at USD and pilot scale was also modulated by the governing mixing regime. Figure 4.7, left, describes that the bimodal and dispersed populations obtained at USD scale with fast flocculant addition rates, shifted to monomodal and narrower distributions with slower flocculant addition rates. This trend, also observed at pilot scale (Figure 4.7, right), might be due to slower flocculant addition rates allowing a more homogeneous distribution of the flocculant inside the mixing vessel. Similar results have been reported by Berrill et al. (2008) on *Escherichia coli* feeds.

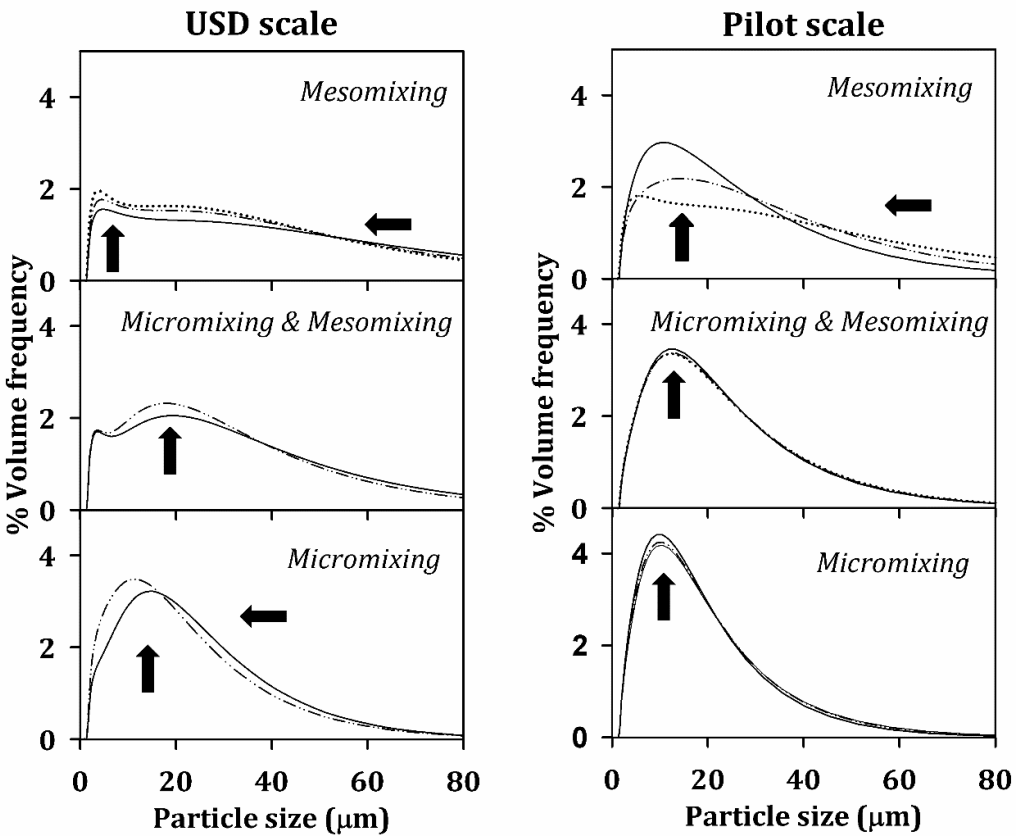

Figure 4.7. Effect of flocculant addition time on the complexity of the population of flocs obtained at USD and pilot scale.
Figure adapted from Espuny Garcia del Real et al. (2014).
Arrows show the shift in PSD with longer flocculant addition times. Flocculation was performed at room temperature with a final 0.2 % v/v PEI concentration and fixed impeller speed (17 rps – USD scale and 4.8 rps – pilot scale). The following flocculant addition rates were used: 1.00, 5.00, 20.0, 50.0, 250, 550, 700 μL.s^{-1} at USD scale and 8.57, 10.7, 15.0, 21.4, 30.0, 47.6, 90.0, 120, 184 mL.min^{-1} at pilot scale. These values represent the different mixing time scales encountered in the flocculation mixing systems. Refer to Section 2.7.2 for the detailed flocculation methodology.

The results described in this subsection have demonstrated that mesomixing regimes resulted in the creation of wide PSDs challenging for the subsequent solid-liquid separation step. In addition to this, they required rapid flocculant addition rates inappropriate for scale-up. Therefore, long flocculant addition times that would guarantee a fully micromixing regime (152 s at pilot scale and 40 s at USD scale) were chosen to study the effect of impeller speed upon flocculation performance (see Section 4.3.6).

4.3.6. Effect of Mixing Intensity on the Particle Size Distribution

Flocculation experiments using the pilot and USD-scale mixing systems at different impeller speeds were performed and their PSDs studied. As observed by Shamlou et al. (1996), the hydrodynamic conditions inside the vessel affected particle growth and particle break-up; nonetheless, these two variables were independent of the source providing the liquid motion. Faster impeller speeds resulted in narrower PSDs both in the USD (Figure 4.8, left) and the pilot-scale (Figure 4.8, right) mixing systems. Particle break-up occurred with faster impeller speeds, as confirmed by the shift of the monomodal PSDs to progressively smaller sizes with increasing impeller speed values. The values of percentage volume frequency also increased with faster impeller speeds as a consequence of particle fragmentation. The rapid decrease in particle size observed between 5.3 and 20 rps at USD scale (Figure 4.8, left) and between 1.8 and 4.8 rps at pilot scale (Figure 4.8, right) suggested that particles formed under low shear environments were more susceptible to break-up than those exposed to fast impeller speeds. These results confirmed that impeller speed is another key process variable affecting flocculation performance and therefore needs to be considered when changes in scale are made.

Particle breakage with increasing impeller speed values was also observed microscopically (Figure 4.9). The images also confirmed that similar particles were obtained at USD and pilot scale under similar values of ε_{avg} or values of v_{tip} that differed two fold.

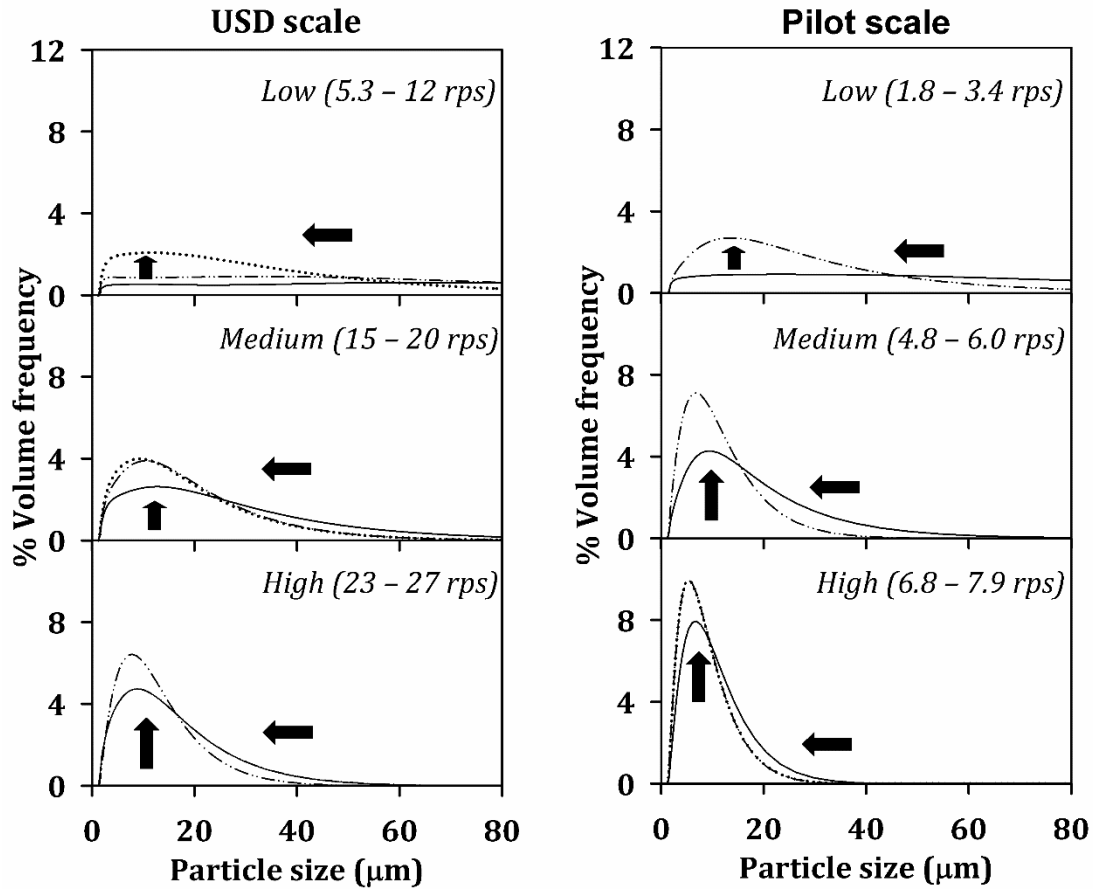

Figure 4.8. Effect of impeller speed on the particle size distribution of the flocs obtained at USD and pilot scale.

Figure adapted from Espuny Garcia del Real et al. (2014).

Arrows show the shift in PSD with faster impeller speeds. Flocculation was performed at room temperature with a final 0.2 % v/v PEI concentration and fixed flocculant addition rate (1.0 μL.s^{-1} – USD scale and 15 mL.min^{-1} – pilot scale). Different impeller speeds were used: 5.3, 8.4, 12, 15, 17, 20, 23, 27 rps at USD scale and 1.8, 3.4, 4.8, 6.0, 6.8, 7.5, 7.9 rps at pilot scale. These values were grouped in low, medium and high impeller speeds as shown in the figure. Refer to Section 2.7.2 for the detailed flocculation methodology.

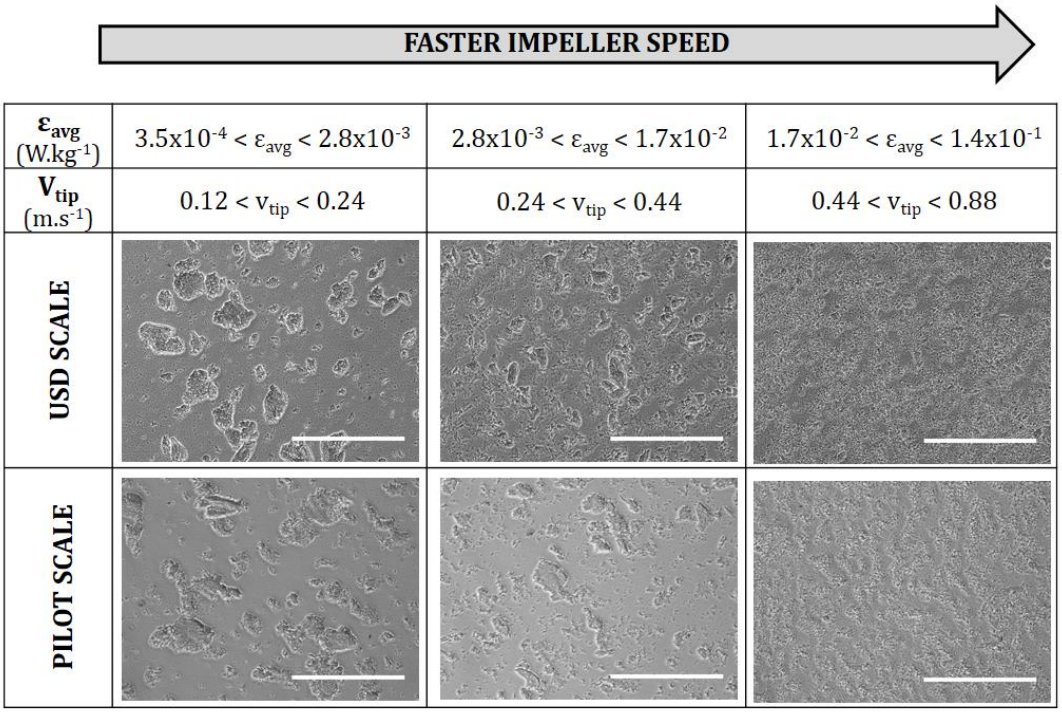

Figure 4.9. Representative images of flocs obtained at increasing values of impeller speed in the USD and pilot-scale flocculation systems.
Figure adapted from Espuny Garcia del Real et al. (2014).
The pictures are arranged in three groups according to the values of ε_{avg} and v_{tip} used to generate the flocs. Flocculation was performed at room temperature with a final 0.2 % v/v PEI concentration, fixed flocculant addition rate (1.0 µL.s^{-1} – USD scale and 15 mL.min^{-1} – pilot scale) and different impeller speeds (8.4, 15, 27 rps – USD scale and 1.8, 3.4, 6.8 rps – pilot scale). Refer to Section 2.7.2 for the flocculation methodology. 20 µL of flocculated sample were carefully pipetted onto a glass slide within 5 minutes of the end of the flocculation experiment and studied under a phase contrast microscope. Refer to Section 2.12 for the microscope details and methodology used to process the images. Bar size on the images indicates 200 µm.

4.3.7. Flocculation Scale-Up Correlations

The effect of increasing values of impeller speed upon floc size was evaluated by two established scale-up correlations found in the literature for impeller-based mixing systems. Impeller tip speed and average turbulent energy dissipation were selected to test if they could predict, under a micromixing-controlled regime, the flocculation performance obtained between non-geometrically similar mixing systems.

The d_{10}, d_{50} and d_{90} data sets obtained in the USD and pilot-scale mixing systems were plotted against the corresponding values of ε_{avg} (Figure 4.10) and v_{tip} (Figure 4.11) at which the flocs were generated. The negative correlation between floc particle size and impeller speed, and therefore ε_{avg} and $v_{tip,}$ was best described by a negative power curve where $R^2 \geq 0.95$ in all cases. Figure 4.10 shows the d_{10}, d_{50} and d_{90} data sets obtained at both scales tightly superimposed each other, thus ε_{avg} was an adequate scale-up correlation to predict the flocculation performance of the pilot-scale vessel from the USD scale data, or vice versa. Impeller tip speed, as shown in Figure 4.11, did not achieve the same results. However, the best fit equations for v_{tip} described that a better correlation could be obtained if the pilot scale-vessel was operated at twice the USD-scale impeller tip speed.

To analyse which scale-up "rule of thumb" best predicted the flocculation performance between the two mixing systems, the ε_{avg} and v_{tip} best fit equations and the different impeller speed values for the two mixing systems were used to generate three parity plots, one for each characteristic particle size descriptor. Figure 4.12 shows the parity plots generated when ε_{avg} was the scale-up correlation applied and Figure 4.13 shows the parity plots obtained when using v_{tip}. The data followed a one to one correlation when using ε_{avg}, but when scaling up based on constant v_{tip} a global best fit was achieved with a two to one correlation for the pilot and USD-scale mixing systems, respectively. The d_{10} data set was predicted within a ± 10 % error margin by ε_{avg} (see Figure 4.12). When scaling based on constant v_{tip}, the error margin increased to ± 25 %; the highest difference was observed under a transitional flow regime ($3x10^3$ < Reynolds number (Re) < 10^4; (Doran, 1995)) (see Figure 4.13). In the d_{50} data sets, the particles formed under a transitional flow regime lay within the ± 10 % error margin line irrespective of the scale-up criteria used; under a turbulent regime (Re > 10^4; (Bates et al., 1966)) they lay between the ± 10 % and ± 25 % error lines. Finally, the d_{90} values were predicted by ε_{avg} with an error margin of ± 25 %, while the v_{tip} error exceeded ± 25 %. Both correlations proved to be successful scale-up bases but ε_{avg} was chosen for further flocculation studies for its ability to more accurately predict the PSD of small flocs. In a polydisperse population the smallest particles determine the filter pore size in depth filtration (Singh et al.,

2013) and microfiltration (Kim et al., 2001) unit operations as well as the supernatant clarification in centrifugation processes (Berrill et al., 2008; Iammarino et al., 2007).

Average turbulent energy dissipation averages the widely different values of local turbulent energy dissipation rate (ε) encountered in the vessel, which can underestimate the impact that the high values of ε existing in the impeller region have upon the flocs (Zhou and Kresta, 1996). However, when micromixing is the limiting mixing time scale and in isotropic turbulent conditions, constant power input per unit volume (P/V_l) is the relevant scale-up criteria (Bourne and Yu, 1994; Zlokarnik, 2002). Micromixing was guaranteed at both flocculation scales using sufficiently long flocculant addition times, yet isotropic turbulence was achieved differently at each scale. In the microwells of the USD-scale mixing system, the oversized impeller guaranteed isotropic turbulence; increasing values of the ratio D_i/D_T decrease the values of maximum energy dissipation rate per unit mass of fluid (ε_{max}) present in the reactor (Henzler, 2000; Hortsch and Weuster-Botz, 2010). At pilot scale, the flocculation experiments were performed at Reynolds values below a fully developed turbulent regime (i.e. $Re \leq 1.3x10^4$); consequently, the ε differences between the impeller area and the bulk of the vessel were reduced. Although this explanation invalidates the assumption of turbulent isotropic regimes required to apply ε_{avg}, it is reinforced by the pilot-scale d_{50} and d_{90} data set deviations observed during turbulent conditions (see Figure 4.12 and Figure 4.13). The tight fit between the d_{10} data sets obtained at pilot and USD scale (Figure 4.13) might be due to the fact that v_{tip} determines maximum fluid shear rate or shear stress (Uhl and Von Essen, 1986). The global best fit between the d_{10}, d_{50} and d_{90} data sets of the pilot and USD flocculation systems needs to be investigated beforehand, thus requires an additional characterisation step during early process development. Consequently, ε_{avg} was the preferred scale-up criteria because (i) it tightly predicted the d_{10} data set, and (ii) it does not require to previously characterise the flocculation systems used.

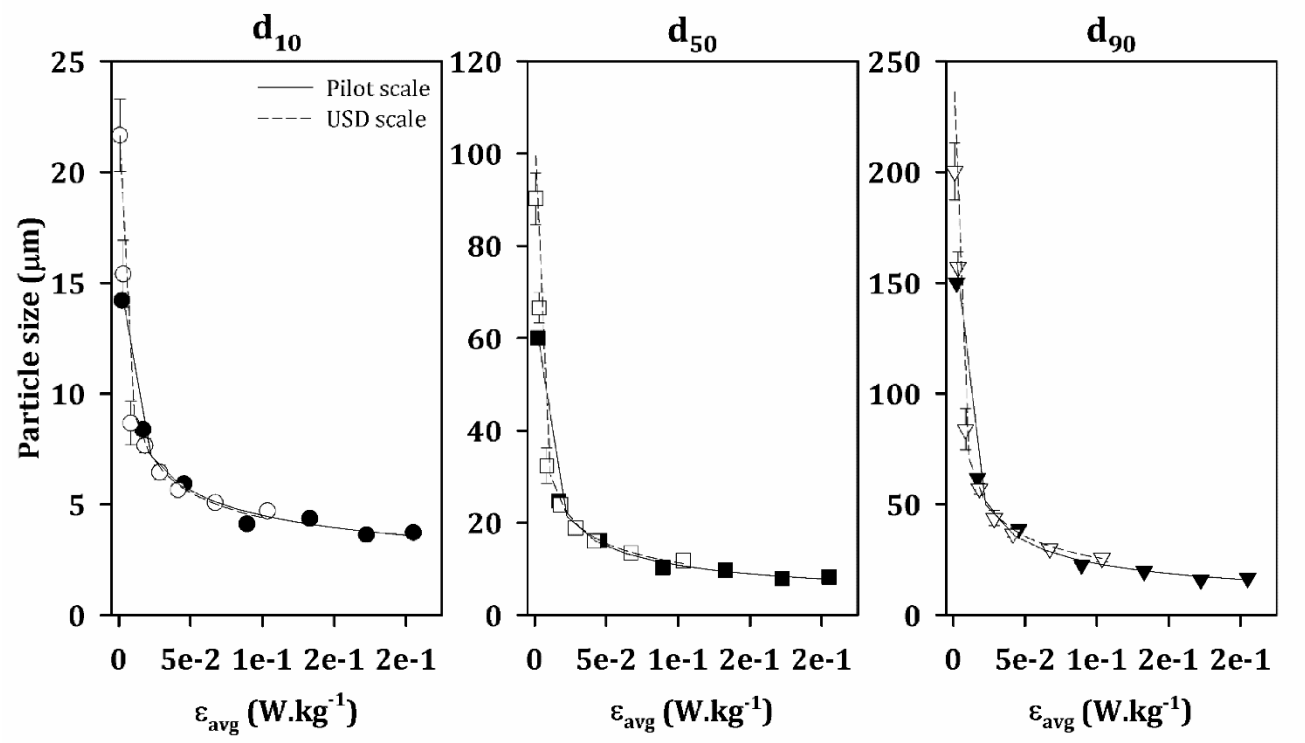

Figure 4.10. Effect of increasing average turbulent energy dissipation values upon floc size for the USD and pilot scale flocculation systems.

Flocculation conditions were: 0.2 % v/v PEI, constant flocculant addition rate (1 µL.s^{-1} – USD; 15 mL.min^{-1} – pilot) and different impeller speeds (5.3, 8.4, 12, 15, 17, 20, 23, 27 rps – USD; 1.8, 3.4, 4.8, 6.0, 6.8, 7.5, 7.9 rps – pilot). See Section 2.7.2. for the detailed flocculation methodology. The flocs PSD was measured according to Section 2.11.4. and described by the d_{10}, d_{50} and d_{90} data sets (●,■,▼- pilot;○,□,▽- USD). Best fit curve equations for each data set are plotted. These were: $d_{10} = 2.01x^{-0.34}$ ($R^2 = 0.98$), $d_{50} = 4.94x^{-0.41}$ ($R^2 = 0.96$), $d_{90} = 12.7x^{-0.40}$ ($R^2 = 0.95$) – USD; $d_{10} = 2.26x^{-0.31}$ ($R^2 = 0.99$), $d_{50} = 3.80x^{-0.46}$ ($R^2 = 0.99$), $d_{90} = 8.08\,x^{-0.48}$ ($R^2 = 0.99$) – pilot.

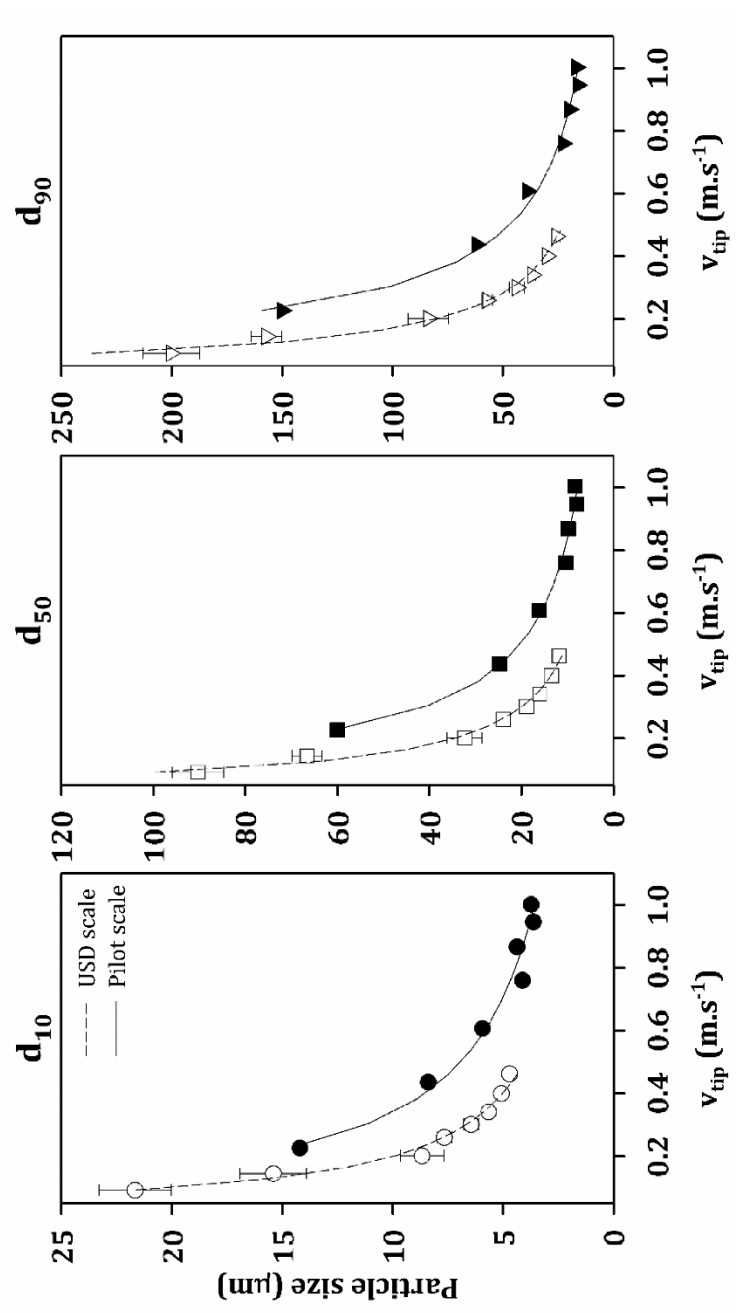

Figure 4.11. Effect of increasing impeller tip speed values upon floc size for the USD and pilot-scale flocculation systems.

Flocculation conditions were: 0.2 % v/v PEI, constant flocculant addition rate (1 μL.s^{-1} – USD; 15 mL.min^{-1} – pilot) and different impeller speeds (5.3, 8.4, 12, 15, 17, 20, 23, 27 rps – USD; 1.8, 3.4, 4.8, 6.0, 6.8, 7.5, 7.9 rps – pilot). See Section 2.7.2. for detailed flocculation methodology. The flocs PSD was measured according to Section 2.11.4. and described by the d_{10}, d_{50} and d_{90} data sets (●,■,▼- pilot;○,□,▽- USD). Best fit curve equations for each data set are plotted. These were: $d_{10} = 1.98x^{1.00}$ ($R^2 = 0.98$), $d_{50} = 4.85x^{1.24}$ ($R^2 = 0.96$), $d_{90} = 12.5x^{1.19}$ ($R^2 = 0.95$) – USD; $d_{10} = 3.68x^{0.92}$ ($R^2 = 0.99$), $d_{50} = 7.85x^{1.37}$ ($R^2 = 0.99$), $d_{90} = 17.5x^{1.45}$ ($R^2 = 0.99$) – pilot.

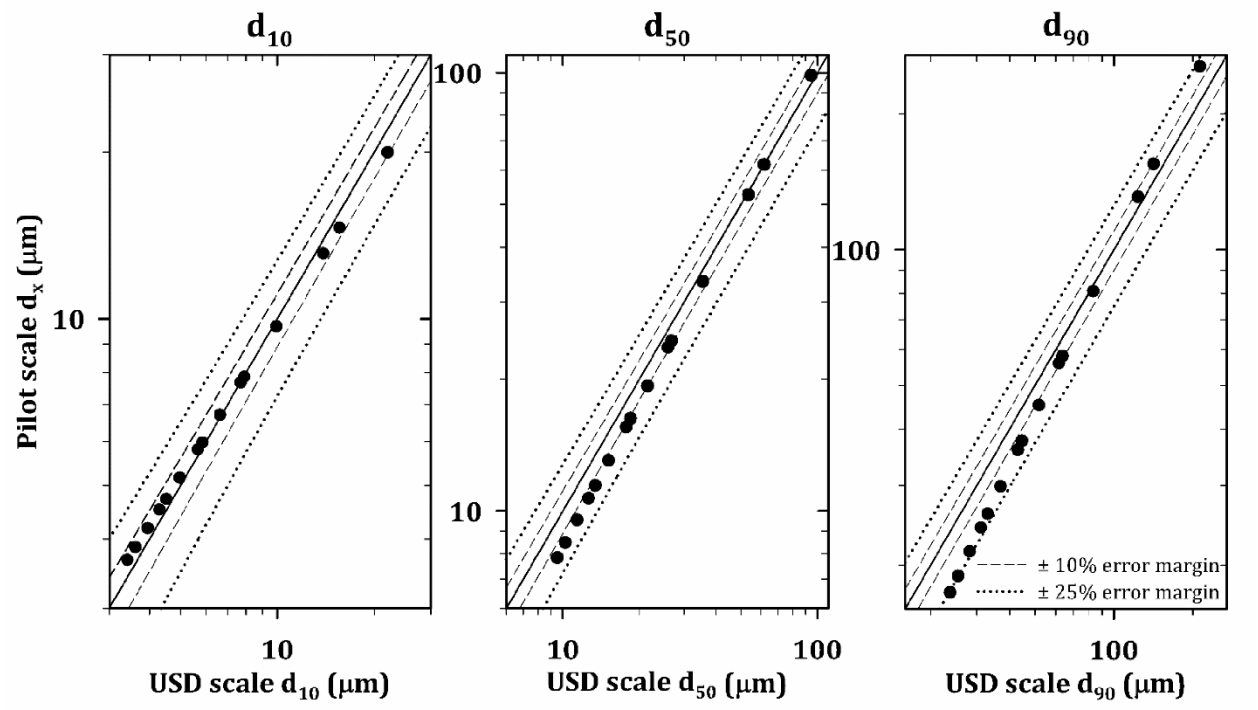

Figure 4.12. Parity plots of the predicted pilot and USD-scale d_{10}, d_{50} and d_{90} data sets when using average turbulent energy dissipation as the scale-up basis.

Figure adapted from Espuny Garcia del Real et al. (2014).
The impeller speed values and power curve equations for the USD and pilot-scale systems described in Figure 4.10. were used to generate the data points plotted. From the USD-scale power curve equations, eight data points were obtained for each d_{10}, d_{50} and d_{90} data set. From the pilot-scale power curve equations, seven data points were obtained for each d_{10}, d_{50} and d_{90} data set. Pilot scale d_x where x is 10, 50 or 90, refers to the pilot-scale d_{10}, d_{50} and d_{90} data sets.

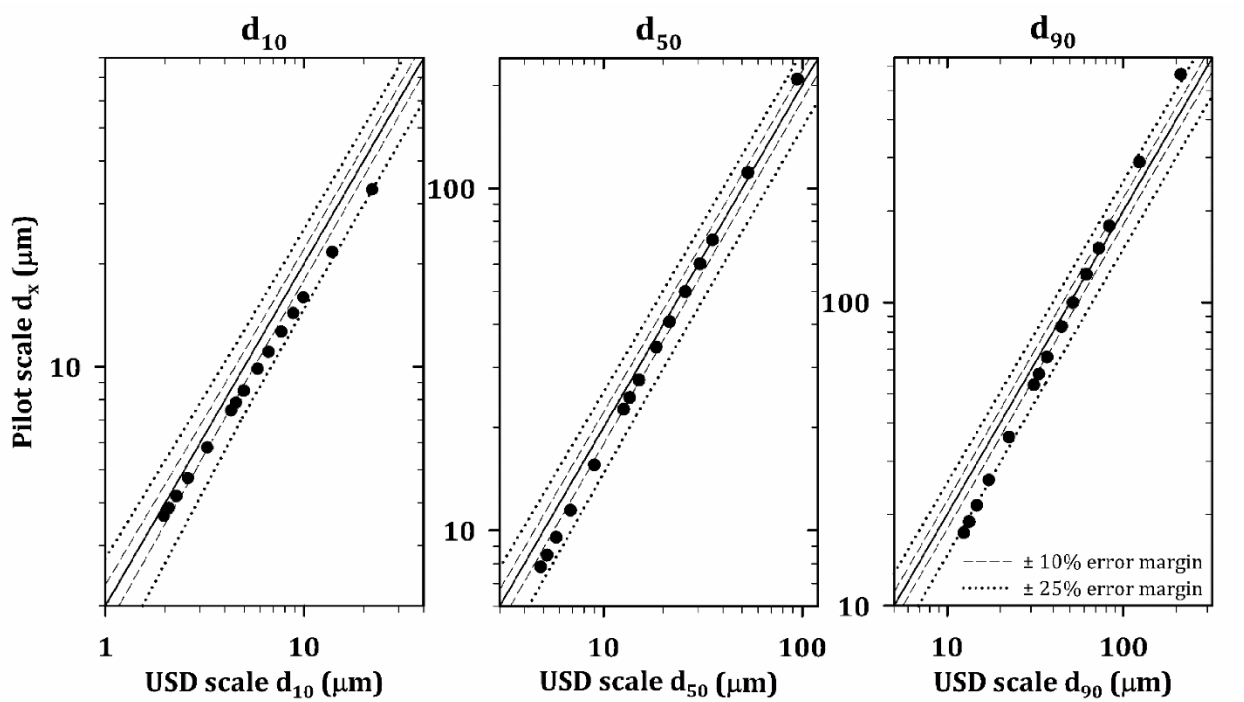

Figure 4.13. Parity plots of the predicted pilot and USD-scale d_{10}, d_{50} and d_{90} data sets when using impeller tip speed as the scale-up basis.

Figure adapted from Espuny Garcia del Real et al (2014).
The impeller speed values and power curve equations for the USD and pilot-scale systems described in Figure 4.11 were used to generate the data points plotted. From the USD-scale power curve equations, eight data points were obtained for each d_{10}, d_{50} and d_{90} data set. From the pilot-scale power curve equations, seven data points were obtained for each d_{10}, d_{50} and d_{90} data set. Pilot scale d_x where x is 10, 50 or 90, refers to the pilot-scale d_{10}, d_{50} and d_{90} data sets. The x-axes were adjusted relative to the y-axes by a factor of 2.

4.3.8. Validation of the Flocculation Scale-Down Methodology

The use of constant ε_{avg} as the scale-up criteria was validated by performing flocculation studies at both scales using the same ε_{avg} value at the USD and pilot-scale mixing systems and over a wide range of flocculant addition times to represent the three mixing time scales.

The USD mixing system predicted the pilot-scale d_{10}, d_{50} and d_{90} particle size characteristic descriptors within a ± 5 % error margin when micromixing was the controlling mixing time scale (see Figure 4.14.A). Furthermore, the PSD curves obtained by the USD and pilot-scale mixing sytems in the micromixing regime overlapped each other with their peak volume frequencies between 9 and 10 µm (see Figure 4.14.B). In the micromixing-mesomixing regime, the USD-scale mixing system predicted the pilot-scale d_{10}, d_{50} and d_{90} data sets within a ± 11 % error margin (see Figure 4.14.A). Additionally, the PSD curves obtained at both scales in the micromixing-mesomixing regime no longer overlapped each other (see Figure 4.14.B). In a fully mesomixing regime the USD-mixing system predicted the pilot-scale d_{10} data set within a ± 5 % error margin, while the d_{50} and d_{90} data sets were underpredicted by up to 50 % in size. The presence of the mesomixing time scale in the vessel resulted in broader PSDs at both scales. The largest particle size increases were observed in the d_{90} data set, with increments between 30 and 170 % at pilot scale and between 5 and 60 % at USD scale (see Figure 4.14.A). The greater sensitivity to mesomixing observed at pilot scale might be due to longer lasting effects of the flocculant flooding the STR impeller region when using fast addition rates when compared to the USD mixing system (see Section 4.3.5).

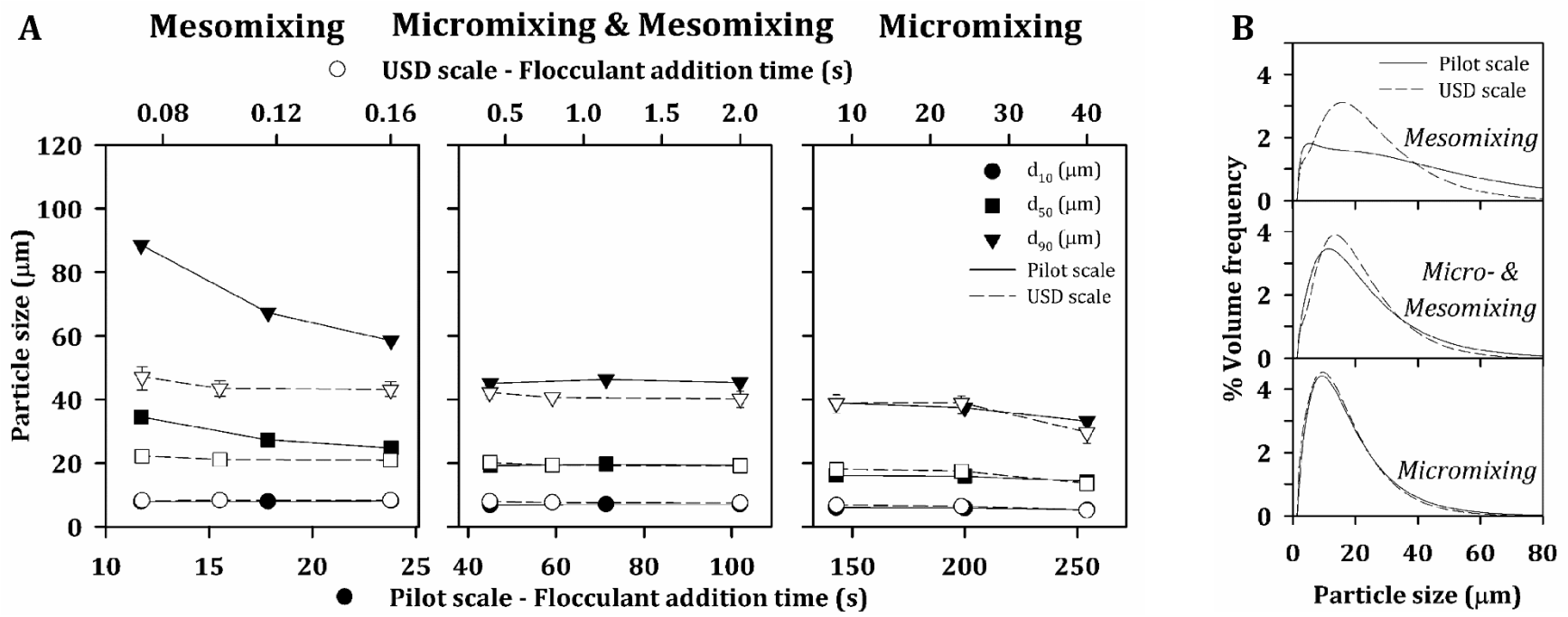

Figure 4.14. Validation of average turbulent energy dissipation as the scale-up basis between the USD and pilot-scale flocculation systems.

Figure adapted from Espuny Garcia del Real et al. (2014).

*Flocculation conditions were: 0.2 % v/v PEI, constant and equal ε_{avg} at both flocculation scales ($4.57x10^{-2}$ $W.kg^{-1}$) and varying flocculant addition times that represented the micromixing and mesomixing time scales in the mixing systems. Refer to Section 2.7.2. for the detailed flocculation methodology. Particle size was measured according to Section 2.11.4. and described either by the d_{10}, d_{50} and d_{90} particle size characteristic descriptors (**A**) or by PSD curves (**B**). The data is split according to the predominant mixing time scale. **A.** The d_{10}, d_{50} and d_{90} data sets were obtained at the following flocculant addition rates: 8.57, 10.7, 15.0, 21.4, 30.0, 47.6, 90.0, 120 and 184 $mL.min^{-1}$ (pilot scale) and 1.00, 5.00, 20.0, 100, 250, 400, 550, 700 and 900 $\mu L.s^{-1}$ (USD scale). Error bars describe range of values where n = 8. **B.** The PSD curves were obtained at the following flocculant addition rates: 184, 47.6 and 8.60 $mL.min^{-1}$ (pilot scale) and 900, 50.0 and 1.00 $\mu L.s^{-1}$ (USD scale).*

4.4. Conclusions

This chapter has described the development and validation of an automated ultra scale-down flocculation technique that is used for the characterisation and optimisation of the flocculation of clarified cell broths. A summary of the chapter conclusions, with reference to their aims and objectives, are below.

1. Investigate the critical parameters controlling the scale-up/scale-down of flocculation unit operations between two geometrically different vessels.

Two key parameters to consider during the flocculation scale-up process between two vessels of different geometry and scale were found. These were: mixing time scales and impeller speed. The governing mixing time scale in the vessel was a critical variable affecting the size and the complexity of the particle size distributions. Impeller speed affected particle growth and breakage hence the final size distribution of the flocs.

2. Develop an USD flocculation platform based upon the process understanding acquired.

The understanding of the mixing fundamentals gained from the study of the flocculation performance of a 1.5 L scale vessel of standard configuration and a 800 µL mixing device resulted in the development of an ultra scale-down methodology to control and mimic the flocculation process between these two mixing systems. This method proposes: (i) maintainance of a micromixing controlled regime by using flocculant addition times larger than the critical addition time; and (ii) the use of constant average turbulent energy dissipation rate to scale up impeller speed between the two mixing systems in order to tightly correlate the distribution of the small particles, which is typically critical for solid-liquid separations. Therefore, this method requires the experimental characterisation of micromixing time in the vessels used with the aim to investigate the values of critical addition time at the conditions used during flocculation.

3. Successfully scale-up the flocculation process of pre-clarified cell broths between two non-geometrically similar vessels.

Using the USD method developed, the particle size distribution of clarified *Saccharomyces cerevisiae* homogenate flocculated in the 1.5 L STR described was mimicked within a ± 5 % error margin by the USD mixing system presented in this chapter. Failing to guarantee micromixing as the predominant mixing regime during scale-up led to particle size distribution predictions that differed by up to 50 % in size.

5. Ultra Scale-Down Flocculation of Clarified Mammalian Cell Culture Broths

5.1. Introduction and Aims

Chapter 4 described an ultra scale-down (USD) flocculation methodology to scale up flocculation processes between two mixing systems of different scale and geometry. The methodology was validated with clarified Baker's yeast homogenate as described in Chapter 4. This method was then used to study flocculation with clarified high cell density (HCD) mammalian cell broths. It was expected that clarified Baker's yeast homogenate and HCD mammalian cell centrate would yield very different feed properties. The impact that these would have upon the USD flocculation methodology was unknown and therefore required its re-validation with clarified mammalian cell broths.

The USD flocculation methodology was developed based on the description of particle size distributions (PSDs) measured by laser light diffraction. Although this approach was suitable for development and validation purposes, analysis by laser light diffraction did not offer the high-throughput (HTP) capabilities that flocculation required during early process development. A HTP methodology that allowed facile identification of the least favourable flocculation conditions in an automated manner was required.

Summary of the chapter's aims and objectives:

1. To validate the USD flocculation methodology described in Chapter 4 with clarified HCD mammalian cell broths.

2. To develop a HTP methodology using the USD mixing device described in Chapter 4 to evaluate flocculation conditions.

5.2. Experimental Set-Up

5.2.1. Mammalian Cell Culture Preparation

High cell density mammalian cell culture was prepared and stored as described in Section 2.1.2. Centrate was defrosted at room temperature prior to use.

5.2.2. Characterisation of the Flocculation Streams

The dynamic viscosity and density values of the thawed HCD mammalian cell centrate were investigated for their effect upon the mixing time scales in the flocculation systems. Measurements were performed according to Section 2.11.5 and Section 2.11.6, respectively. Total protein and monoclonal antibody (mAb) concentration were quantified as described in Section 2.10.1 and Section 2.10.2, respectively.

The dynamic viscosity and density of 4 % w/v polyethylenimine (PEI) were measured as described in Section 2.11.5 and Section 2.11.6, respectively.

5.2.3. Flocculation Experiments

Different PEI stock solutions were used to flocculate HCD mammalian cell centrate. A 4 % w/v PEI stock solution was used during the validation experiments of the USD flocculation methodology, while 4, 6 and 12 % w/v PEI stock solutions were used during the HTP evaluation experiments. Fresh PEI stock solutions were prepared before each flocculation experiment by overnight mixing of the required amount of PEI in phosphate buffered saline (PBS tablets). Refer to Section 2.7.1 for the detailed flocculation methodology. The impeller speed and flocculant addition time were varied depending upon the flocculation study conducted.

5.2.3.1. Validation of the USD Flocculation Methodology

Mammalian cell centrate was flocculated with 0.20 % w/v PEI, constant impeller speed and different flocculant addition rates. At pilot scale, impeller speed was set to 4.6 rps and flocculant addition rate to 8.57, 15.0, 21.4, 47.6, 90.0 and 184 $mL.min^{-1}$. At USD scale, impeller speed was set to 19 rps and flocculant

addition rate to 1.00, 1.67, 5.00, 20.0, 50.0, 100, 250, 400 and 900 μL.s^{-1}. The pilot-scale impeller speed corresponded to the intermediate impeller speed value of the motor used at this scale. Ultra scale-down impeller speed was calculated following the USD flocculation methodology (see Chapter 4), where the values of average turbulent energy dissipation rate per unit mass of fluid (ε_{avg}) are the same at both flocculation scales. The value of ε_{avg} was calculated as described in Section 2.5. Polyethylenimine concentration was chosen based on the results described in Section 3.3.2 for HCD mammalian cell centrate. The ranges of flocculant addition rate used were limited by the liquid handling robot (USD scale) and the syringe pump (pilot scale) employed. The PSD of the flocs was measured by laser light diffraction according to Section 2.11.4.

5.2.3.2. High-Throughput Evaluation

These experiments were performed at USD scale using the microplate-based mixing system described in Chapter 4; refer to Section 2.3.3 for a detailed description of the system's configuration. Impeller speed and flocculant addition rate were kept constant and equal to 17.4 rps and 900 μL.s^{-1}, respectively. Four different PEI concentrations were studied based on Lonza Biologics' in-house knowledge of flocculation processes when using their commercial CHO cell line; these were: 0.05, 0.15, 0.30 and 0.60 % w/v. Flocculation performance was evaluated in two ways: (i) resultant PSD measured by laser light diffraction (see Section 2.11.4), and (ii) supernatant absorbance at 600 nm wavelength at different time points.

Absorbance measurements were performed as follows: after flocculation (see Section 2.7.1 for the detailed methodology), the lid of the microwell mixing system (see Figure 2.3.A) was lifted and the flocs allowed to settle in the microplate for 15, 30, 60, 180 or 360 minutes; then, the liquid handling robot aspirated 200 μL of liquid phase from the liquid surface and dispensed it into a 96-well, flat bottom, transparent microplate (Corning® 96 well plates, UV-transparent; Sigma-Aldrich, Gillingham, UK) suitable for absorbance measurements at 600 nm. A microplate reader was used for the absorbance measurements as described in Section 2.11.1.

5.3. Results and Discussion

5.3.1. Characterisation of the Flocculation Streams

Defrosted HCD mammalian cell centrate was used in the flocculation studies. The effect that freeze-thawing had upon the PSD of clarified HCD mammalian cell culture was studied in Chapter 3. The reader is referred to Section 11.1.2 for a detailed description of the freeze-thawing effect on the PSD of HCD mammalian cell centrate.

The physical properties of the thawed HCD mammalian cell centrate were measured for their effect upon the micromixing parameters of the flocculation vessels under a turbulent flow regime (Bourne et al., 1989, 1995; Gholap et al., 1994). The thawed HCD mammalian cell centrate used was a Newtonian fluid with a dynamic viscosity value at 22°C equal to 1.06 mPa.s and a density value equal to 1010 $kg.m^{-3}$. Total protein concentration was equal to 15.2 ± 0.6 $g.L^{-1}$, while mAb concentration was equal to 4.7 ± 0.2 $g.L^{-1}$ thus representing 31 % of the total protein concentration. The host cell protein (HCP) content in the cell culture centrate is impacted by the cell line, the recombinant protein product, the cell culture media, the feeding strategy, the bioreactor control, the cell culture duration (Jin et al., 2010; Tait et al., 2012) and the harvesting strategy (Hogwood et al., 2013b). Therefore, both total protein concentration and the relative mAb to HCP concentration observed were specific to the HCD mammalian cell centrate used in this chapter.

Finally, with regards to the flocculant, the 4 % w/v PEI stock solution used in the validation experiments was a Newtonian fluid with a density of 1030 $kg.m^{-3}$ and a dynamic viscosity of 1.98 mPa.s at 22°C.

5.3.2. Validation of the Ultra Scale-Down Flocculation Methodology with Mammalian Cell Centrate

The USD flocculation methodology, which is described in Chapter 4, states that flocculation performance can be successfully scaled up between two different mixing systems if (i) slow flocculant addition rates that guarantee a predominant

micromixing regime in the flocculation vessels are used, and (ii) constant ε_{avg} is used to scale up impeller speed. This method was successfully validated with clarified Baker's yeast homogenate (see Section 4.3.8). The differences in the physical and biological properties between the clarified Baker's yeast homogenate and the HCD mammalian cell centrate suggested possible changes in the mixing time scales and hence in the USD flocculation methodology. The validation protocol (see Section 4.3.8) used with HCD mammalian cell centrate was identical to that of Baker's yeast homogenate in order to investigate the possible differences.

The dynamic viscosity values of the flocculation feed streams (i.e. thawed HCD mammalian cell centrate and a 4 % w/v PEI solution) were less than double (see Section 5.3.1) the viscosity of the water-based solutions used to characterise micromixing time in the flocculation vessels (see Section 4.3.4). Changes in the micromixing parameters have been reported with fourfold (Bourne et al., 1989), six fold (Bourne et al., 1995) and seven fold (Gholap et al., 1994) increases in viscosity with respect to the control solution. Therefore, with less than a twofold increase in viscosity, the micromixing values described in Chapter 4 were assumed to remain unchanged during the flocculation studies with HCD mammalian cell centrate. However, the re-validation experiments were still carried out to confirm this hypothesis.

To re-validate the USD flocculation methodology with HCD mammalian cell centrate, ε_{avg} was kept constant at both flocculation scales while a wide range of flocculant addition rates were used. The feed conditions and flocculant concentration were also constant at both scales. The aim was to represent the different mixing time scales in the vessel (i.e. mesomixing and micromixing) and evaluate whether the USD flocculation methodology was successful, independently of the predominant mixing time scale when using HCD mammalian cell centrate. Figure 5.1 describes the particle size characteristic descriptors d_{10}, d_{50} and d_{90}, and the PSD curves resulting from the flocculation studies at USD and pilot scale. Figure 5.1.A shows that wider and larger PSDs were obtained at USD scale with slower flocculant addition rates. The USD d_{10} characteristic descriptor increased, on average, from 13 to 39 μm; the d_{50} from

29 to 78 μm; and the d_{90} from 58 to 152 μm. As observed in Figure 5.1.A, the largest increase in floc size at USD scale occurred when shifting from a micromixing-mesomixing regime to a system where micromixing was the predominant mixing time scale in the vessel; this change represented an increase in particle size between 75 and 110 %. However, the shift from a mesomixing to a micromixing-mesomixing regime resulted in a smaller particle size increase (between 25 and 31 %). With regards to the pilot-scale data set, PSDs became narrower but larger with slower flocculant addition rates (see Figure 5.1.A). The pilot d_{10} characteristic descriptor increased from 31 to 45 μm; the d_{50} from 67 to 82 μm; and the d_{90} remained constant at 148 μm. At pilot scale, particle size only increased when shifting from a mesomixing to a micromixing-mesomixing controlled regime; the pilot d_{10}, d_{50} and d_{90} data sets remained constant, on average, during the shift from a micromixing-mesomixing regime to a micromixing regime (see Figure 5.1.A).

Flocculation, described by the d_{10}, d_{50} and d_{90} data sets, was successfully scaled-up with a ± 7 % error margin in the micromixing regime (see Figure 5.1.A). The PSD curves obtained in this mixing regime overlapped each other with their peak volume frequencies at 55 μm (USD scale) and 62 μm (pilot scale) (see Figure 5.1.B). However, the influence of mesomixing led to the formation of bimodal PSD curves that differed at both scales (see Figure 5.1.B) as well as to d_{10}, d_{50} and d_{90} data sets with particle size differences of up to ± 60 % between the two scales (see Figure 5.1.A). This data confirmed the USD flocculation methodology could be successfully implemented in clarified HCD mammalian cell flocculation processes, but only when a micromixing regime was guaranteed in both flocculation mixing systems.

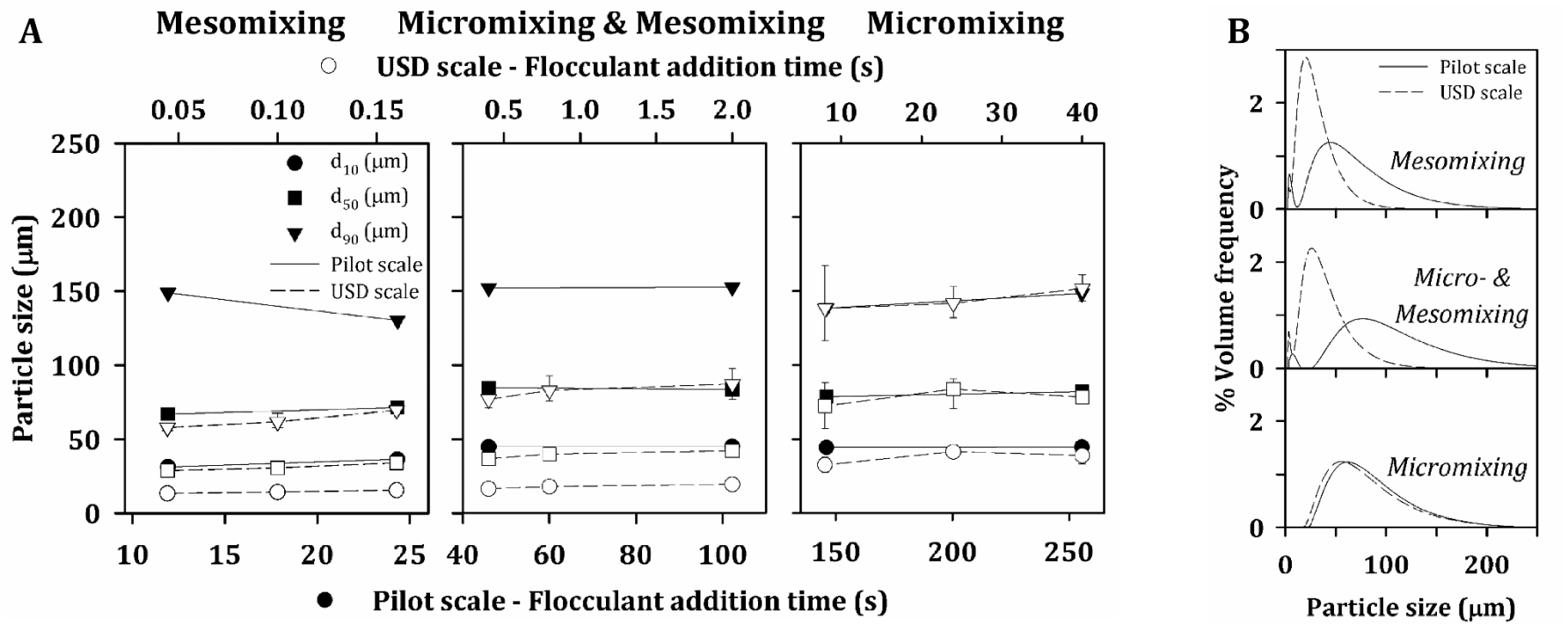

Figure 5.1. Validation of the ultra scale-down flocculation methodology using high cell density mammalian cell centrate.

*High cell density mammalian cell (peak cell count = 28.0x10^6 cells.mL^{-1}) centrate was flocculated with 0.20 % w/v PEI, constant ε_{avg} (3.97x10^{-2} W.kg^{-1}) and varying flocculant addition times. See Section 2.7.1. for the detailed flocculation methodology. Particle size was measured by laser light diffraction (see Section 2.11.4.) and described either by the d_{10}, d_{50} and d_{90} data sets (**A**) or by PSD curves (**B**). **A.** The d_{10}, d_{50} and d_{90} data sets were obtained at the following flocculant addition rates: 8.57, 15.0, 21.4, 47.6, 90.0 and 184 mL.min^{-1} (pilot scale) and 1.00, 1.67, 5.00, 20.0, 50.0, 100, 250, 400 and 900 µL.s^{-1} (USD scale). Error bars describe range of values where n = 8. **B.** The PSD curves were obtained at the following flocculant addition rates: 184, 21.4 and 15.0 mL.min^{-1} (pilot scale) and 900, 20.0 and 1.00 µL.s^{-1} (USD scale).*

The effect of flocculant addition time upon the morphology of the flocculated particles was studied at pilot scale since no significant differences were observed upon particle size as described by the pilot d_{10}, d_{50} and d_{90} data sets (see Figure 5.1.A). Figure 5.2 shows that more consistently shaped and sized particles were obtained with longer flocculant addition times. This observation was validated by Berrill et al. (2008), who visually observed higher variability in floc size when using short flocculant addition times. These results were also corroborated with the pilot-scale PSD curves plotted in Figure 5.1.B. While monomodal PSDs were obtained at long flocculant addition times (i.e. micromixing regime), bimodal PSDs resulted from the influence of mesomixing at shorter flocculant addition times. The formation of complex PSDs might have been due to fast flocculant addition rates not allowing the homogeneous distribution of the flocculant inside the vessel.

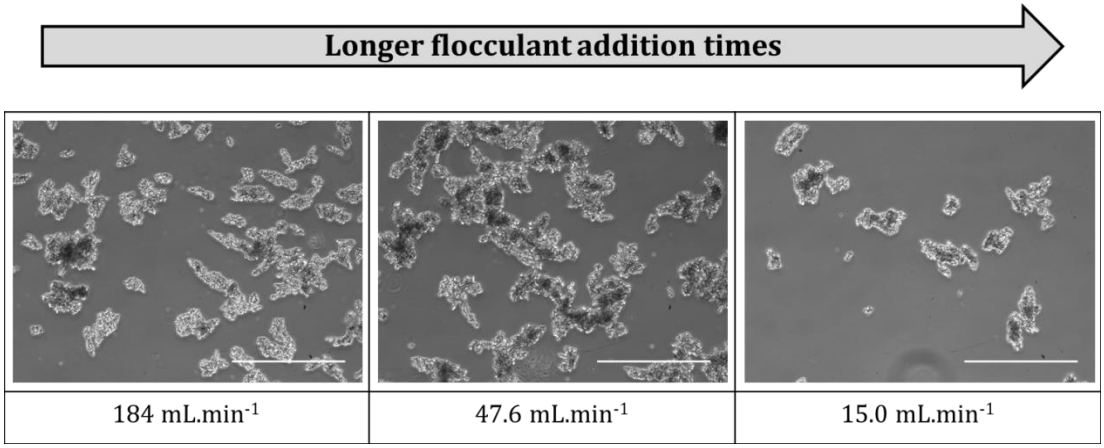

Figure 5.2. Representative images of flocs obtained at pilot scale with high cell density mammalian cell centrate.
High cell density mammalian cell (peak cell count = 28.0x10^6 cells.mL^{-1}) centrate was flocculated with 0.2 % w/v PEI, 4.57 rps impeller speed and 184, 47.6 and 15.0 mL.min^{-1} flocculant addition rates. Refer to Section 2.7.1 for the detailed flocculation methodology. A volume of flocculated sample equal to 20 µL was carefully pipetted onto a glass slide within 5 minutes of finishing the flocculation experiment, and studied under a phase contrast microscope. Refer to Section 2.12 for the microscope details and methodology used to process the images. Bar size indicates 200 µm.

The effect of flocculant addition time upon the size distribution of the resultant flocs differed depending upon the feed material used despite performing flocculation under very similar conditions. Wider and larger PSDs were obtained at both pilot and USD scale with faster addition rates when flocculating clarified

Baker's yeast homogenate (see Figure 4.14 in Section 4.3.8). However, the effect of faster addition rates upon PSD was different depending on the scale when flocculating HCD mammalian cell centrate; while narrower and smaller PSDs were obtained at USD scale, slightly wider floc distributions were observed at pilot scale (see Figure 5.1.A). These data confirm that, although the USD flocculation methodology was successful when using clarified feeds of different characteristics, it might be of interest to study the effect that impeller speed and flocculant addition rate have upon flocculation performance before scaling up. Understanding the effect that process variables have upon process performance allows easier and more accurate troubleshooting, if required.

5.3.3. Automated, High-Throughput Evaluation of Flocculation Conditions

The 96-well microplate-based USD mixing device described in Chapter 4 was developed to obtain a platform that allowed screening flocculation conditions in an automated and HTP manner suitable for early process development studies. Flocculation performance was assessed by means of the resultant PSD measured by laser light diffraction. However, this technique did not offer the automation and HTP capabilities required. Absorbance measurements at 600 nm wavelength (Abs_{600}), also referred to as optical density at 600 nm (OD_{600}), were proposed as an alternative method for the evaluation of optimal flocculation conditions.

Optical density measurements at 600 nm wavelength have been commonly used in bioprocesses to analyse the solid content in samples (Berrill et al., 2008; Chatel et al., 2014; Hogwood et al., 2013b; Kim et al., 2001; Lau et al., 2013; Tait et al., 2009; Tustian et al., 2007). However, the presence of large, non-colloidal particles like flocs would result in highly variable OD_{600} measurements. To avoid this, the flocculated material was allowed to settle under gravity and the OD of the resulting supernatant measured at 600 nm wavelength. After gravitational settling, the flocculated material would be constituted of small colloidal particles that flocculation did not remove. Small particulates determine the performance of the subsequent centrifugation (Berrill et al., 2008; Iammarino et al., 2007) or filtration (Iammarino et al., 2007; Kim et al., 2001; Singh et al., 2013) unit

operations. Therefore, this approach was of interest when scouting for optimal flocculation conditions. In addition to this, this approach offered the opportunity to automate the flocculation experiments and absorbance measurements within the same robotic platform where experiments could be run without supervision. But since the PSD of flocculated particles determines the performance of subsequent solid-liquid separations (Berrill et al., 2008; Singh et al., 2013), it was necessary to study the correlation between the size distribution of the flocs and the OD_{600} values of the settled flocculated material. Furthermore, various settling times were studied to test whether different time points could more accurately identify differences in the PSD.

Four different flocculant concentrations were used to generate an array of PSDs. Figure 5.3 plots the resulting PSDs measured by laser light diffraction. The size and complexity (i.e. monomodal or bimodal distribution) of the population of flocs tightly depended upon the flocculant concentration. An inflection point in the correlation between higher flocculant concentration and larger particle size occurred at PEI concentrations larger than 0.30 % w/v. A concentration of 0.60 % w/v PEI resulted in a narrower and smaller PSD than that achieved with 0.15 and 0.30 % w/v PEI. The smallest PEI concentration studied (0.05 % w/v) was not able to flocculate the submicron particles present in the thawed HCD mammalian cell centrate (see Figure 11.2), possibly due to the fact that flocculant concentration was too low to form any flocs.

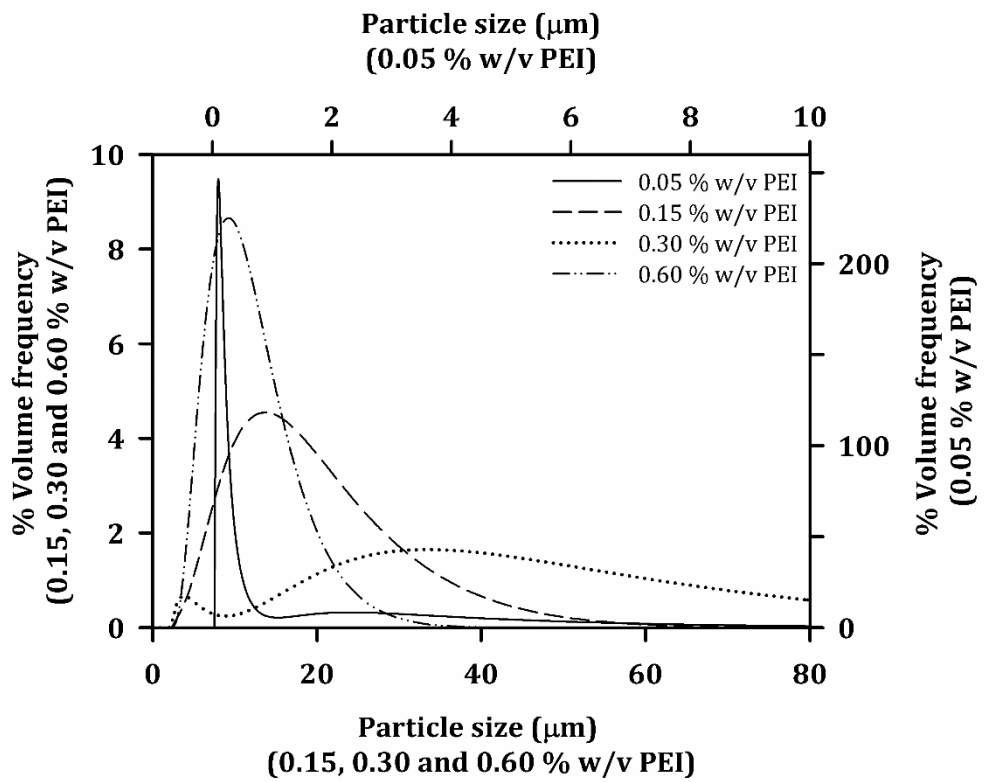

Figure 5.3. Particle size distribution of flocs generated at USD scale with different flocculant concentrations.
High cell density mammalian cell (peak cell count = 28.0x10^6 cells.mL^{-1}) centrate was flocculated at USD scale with 17.3 rps impeller speed, 900 μL.s^{-1} flocculant addition rate and 0.05, 0.15, 0.30 or 0.60 % w/v PEI concentration. Refer to Section 2.7.1 for the detailed flocculation methodology. Particle size was measured by laser light diffraction according to Section 2.11.4. The PSD curves plotted are the average of 10 independent measurements.

The four flocculant concentrations studied also resulted in different gravity settling profiles (see Figure 5.4). Flocculation with 0.05 % w/v PEI led to OD_{600} values around 0.500 A.U. that did not change over the settling period studied. The final OD_{600} value represented an 8 fold increase from the HCD mammalian cell centrate OD. These data suggested flocculation took place at 0.05 % w/v PEI, but the flocs created were so small (see Figure 5.3) that they remained in suspension. As it has been mentioned in this section, small particulates determine the performance of the subsequent centrifugation and filtration unit operations (Berrill et al., 2008; Iammarino et al., 2007; Kim et al., 2001; Singh et al., 2013). Therefore, high OD_{600} values over long settling time periods are indicative of non-optimal flocculation conditions. Flocculant concentrations higher than 0.05 % w/v PEI resulted in particles big enough to settle over time as observed

in Figure 5.4. When flocculating with 0.15 and 0.60 % w/v PEI, OD_{600} increased to 0.110 and 0.650 A.U., respectively, thus representing a 1.6 and 10 fold increment with respect to the HCD mammalian cell centrate OD. After this OD peak at 15 minutes, OD_{600} decreased in the course of a six-hour period to 0.007 A.U. (0.15 % w/v PEI) and 0.014 A.U. (0.60 % w/v PEI). With regards to 0.30 % w/v PEI, the supernatant OD_{600} was never greater than the initial HCD mammalian cell centrate OD and after six hours settling time it was equal to 0.010 A.U. When comparing these OD settling profiles to their corresponding PSDs (Figure 5.3), it was observed that large and wide PSDs like the one obtained with 0.30 % w/v PEI did not result in an initial OD_{600} peak; instead, it gradually decreased from the initial OD_{600} value. In addition to this, the narrower and smaller the PSD of the flocs, the slower particle settling was.

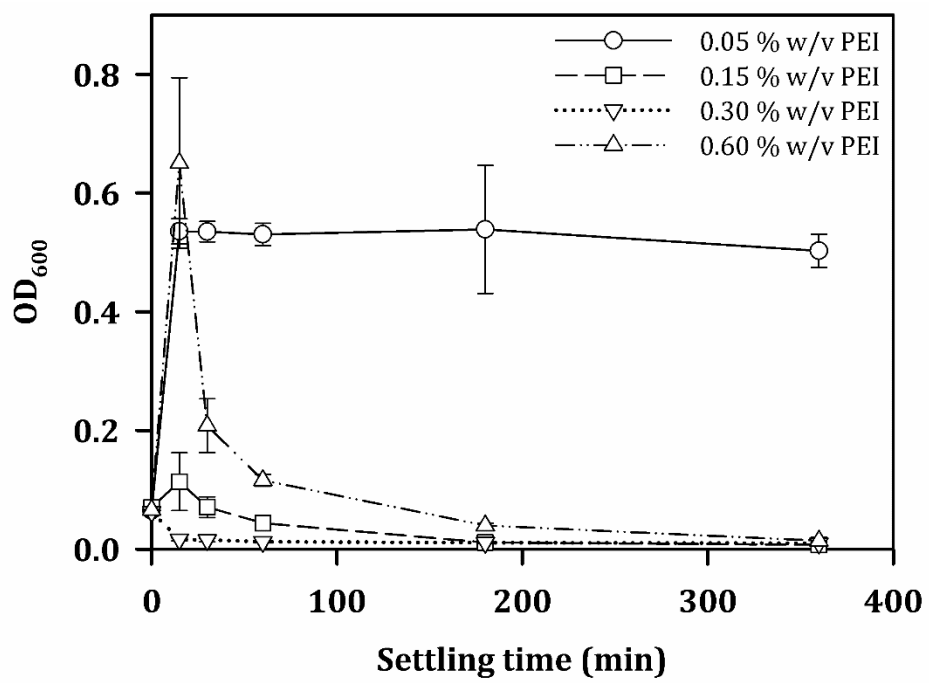

Figure 5.4. OD_{600} of flocculated high cell density mammalian cell centrate after gravity settling.
High cell density mammalian cell (peak cell count = $28.0x10^6$ cells.mL^{-1}) centrate was flocculated at USD scale with 17.3 rps impeller speed, 900 µL.s^{-1} flocculant addition rate and 0.05, 0.15, 0.30 or 0.60 % w/v PEI concentration. Refer to Section 2.7.1 for the detailed flocculation methodology. Optical density measurements were taken with a plate reader according to Section 2.11.1. Error bars describe standard deviation of one where n = 96.

The difference in PSD could be most accurately depicted after 30 minutes of gravity settling (see Figure 5.4). While short experimental times are of interest to speed up process development, longer gravity settling times such as 3 hours allowed the confirmation of non-optimal flocculation conditions (e.g. 0.05 % w/v PEI). Polyethylenimine concentrations equal to 0.15, 0.30 and 0.60 % w/v resulted in distributions with flocculated particles larger than 2.5 μm and changing OD_{600} gravity settling profiles over time. Therefore, the results showed that non-optimal flocculation conditions, defined as those resulting in the formation of submicron particles, could be scouted in an automated and HTP manner by measuring the settled supernatant OD_{600} over a period of 3 hours. The flocculation conditions resulting in rapid settling profiles, hence in flocs bigger than 1 μm, should be considered for the subsequent centrifugation or filtration process development studies where they should be assessed based upon process performance.

5.4. Conclusions

This chapter presented the validation of the USD flocculation methodology with HCD mammalian cell centrate and the implementation of the microplate-based USD mixing device as part of a HTP, automated platform for the analysis of flocculation conditions during early process development studies. A summary of the key findings, based upon the chapter aims and objectives is as follows:

1. To validate the USD flocculation methodology described in Chapter 4 with clarified HCD mammalian cell broths.

The USD flocculation methodology described in Chapter 4 allowed to successfully scale up the flocculation of HCD mammalian cell centrate between two vessels of different scale and geometrical configuration. Scale-up was only successfully achieved when micromixing was the predominant mixing time scale in the flocculation vessels. The influence of mesomixing increased the particle size differences between flocculation scales from ± 7 % to ± 60 %. Mesomixing had a similar effect when flocculating clarified Baker's yeast homogenate since particle size differences increased from ± 5 % to ± 50 % (see Section 4.3.8). Therefore, flocculant addition time was confirmed to be a key flocculation process variable

for the scale-up success between mixing systems of different scale and geometry independently of the biological material being flocculated.

2. To develop a HTP methodology using the USD mixing device described in Chapter 4 to evaluate flocculation conditions.

By letting the flocs settle under gravitational forces and by measuring the absorbance of the resultant supernatant at 600 nm wavelength over a period of 3 hours, (i) non-optimal flocculation conditions, defined as those resulting in submicron flocculated particles, were successfully identified; and, (ii) differences in the size distribution of particles larger than 2 μm were accurately exhibited. This methodology, in combination with the microplate-based USD mixing system, allows automating high-throughput flocculation experiments within the same liquid handling platform making it suitable for early process development activities.

6. Depth Filtration of Flocculated Mammalian Cell Culture Centrate

6.1. Introduction and Aims

The particles generated after flocculation required a subsequent solid-liquid separation step. Charged normal flow depth filtration was chosen for its ability to additionally reduce the impurity content in the feed material (Yigzaw et al., 2006). Examples of its successful implementation with flocculated fluids are reported in the literature (Buyel and Fischer, 2014; Kang et al., 2013, 2013; Singh et al., 2013; Tomic et al., 2015). The introduction of any new unit operation requires a study of how the new process variables will affect the subsequent stages. By investigating unit operations employing ultra scale-down (USD) technologies, a greater understanding of the unit operation and its interaction with other steps can be achieved using only millilitre volumes of process material. Ultra scale-down methodologies allow the evaluation of different operating parameters in an automated and parallel fashion, and can result in relevant process-scale data too. The decision of whether laboratory-scale validation studies are needed before the pilot-plant process development activities can start depends upon a number of factors. One is the experience of past similar USD scale studies (Titchener-Hooker et al., 2008).

The process interaction between flocculation and depth filtration was studied in this chapter. Different flocculation conditions, depth filter media (multi-layer and single-layer filters) and normal flow filtration (NFF) modes were evaluated. Firstly, USD flocculation and USD constant pressure depth filtration (i.e. single-layer filters) were employed to provide an automated, high-throughput technique that integrated both unit operations at USD scale. This allowed the study of several process variables with small volumes of process material. Then, constant flux depth filtration of flocculated feeds was studied at laboratory scale to evaluate the effect of multi-layer depth filtration in the clarification of polydisperse flocculated fluids. These results were used to choose the flocculation and filtration process conditions used in Chapter 7.

Summary of the chapter's aims and objectives:

1. Assess the use of USD flocculation and USD constant pressure depth filtration to investigate how flocculation performance affects depth filtration performance.
2. Assess the suitability of multi-layer depth filters to clarify polydisperse flocculated streams.

6.2. Experimental Set-Up

Figure 6.1 summarises the experimental set-up of this chapter. The experimental details are described below.

6.2.1. Mammalian Cell Culture Preparation

High cell density mammalian cell centrate was prepared and stored as described in Section 2.1.2. Centrate was defrosted at room temperature prior to use.

6.2.2. Ultra Scale-Down Process Integration

Ultra scale-down flocculation and USD constant pressure depth filtration were employed as described in Section 2.7.1 and Section 2.8.1, respectively. A set volume of 800 µL of HCD mammalian cell centrate was flocculated at USD scale with 0.15 % and 0.30 % w/v polyethylenimine (PEI) and fixed impeller speed (17.3 rps). Flocculant was added at 1 and 900 $\mu L.s^{-1}$ to study the effect of mixing time scales (see Chapter 4). The flocs were left to mature for 10 minutes before assessing flocculation performance via particle size distribution (PSD) measurements according to Section 2.11.4.

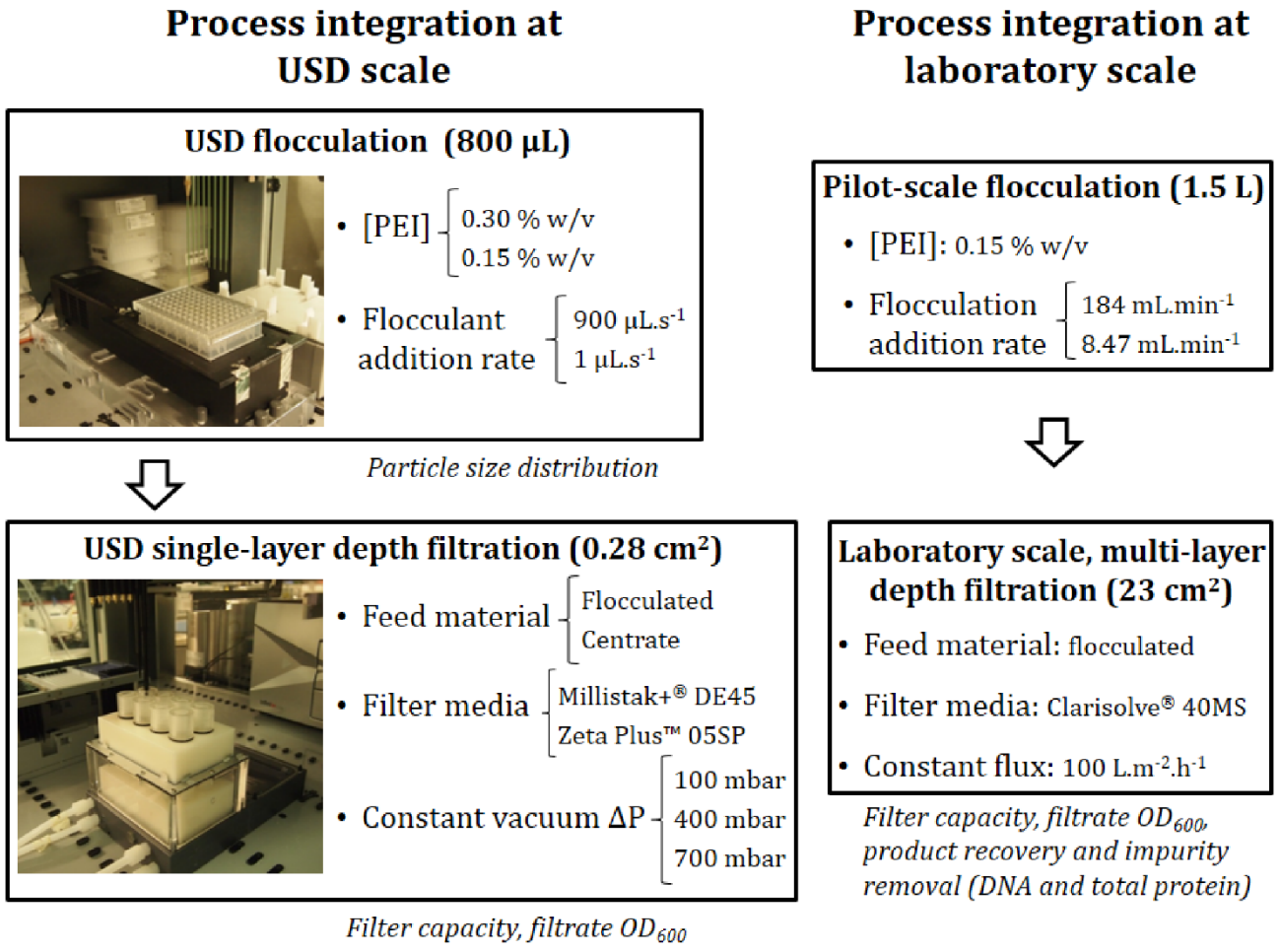

Figure 6.1. Diagram summarising the experimental work performed in Chapter 6.

Less than 3 minutes passed between the completion of USD flocculation and the start of USD filtration; the flocs were kept suspended by gentle inversion during this time. Non-treated centrate was depth filtered using the same conditions as the flocculated material to provide a benchmark comparison for filtration performance. Two different single-layer depth filter media were tested: DE45 grade (Millistak+® DE media series; EMD Millipore Billerica, MA, USA) with a retention rating of 1 – 0.5 µm and 05SP grade (Zeta Plus™ SP series; 3M Purification Inc., St Paul, USA) with a retention rating of 10 – 1.5 µm. Filtration was performed at a constant negative pressure drop (ΔP) of 100, 400 and 700 mbar. A set volume of 4 mL of process material was manually loaded into the filter reservoir per filtration run (equivalent filter loading = 143 $L.m^{-2}$). Four repeats were carried out per filtration condition. Filter specifications and detailed USD methodology are described in Section 2.8.1. At USD scale, filtration performance was assessed based upon filter capacity and filtrate clarification (see Figure 6.1). At USD constant pressure filtration, filter capacity was calculated as the filtration throughput obtained when filter flux equals to 10 % of the value of initial filter flux. Filtrate clarification was expressed in terms of optical density measurements at 600 nm wavelength (OD_{600}). The filtrate samples were stored at -80°C after the OD_{600} measurements.

6.2.3. Laboratory-Scale Process Integration

Flocculation was performed in a 1.5 L vessel (see Section 2.3.1 for the configuration details) following the methodology described in Section 2.7.1. Polyethylenimine was added at 184 and 8.47 $mL.min^{-1}$ to a final concentration of 0.15 % w/v while impeller speed was fixed at 4.8 rps. Flocculation performance was assessed and measured as in Section 6.2.2.

Depth filtration was performed at a constant flux of 100 $L.m^{-2}.h^{-1}$ using a commercially available 23 cm^2 multi-layer depth filter capsule (Clarisolve® 40MS µPod®; EMD Millipore Billerica). Filter specifications and detailed methodology are described in Section 2.8.2. Filtrate was collected in 10 mL fractions. At laboratory scale, filtration performance was assessed based upon filter capacity, filtrate clarification, product recovery and impurity removal

(see Figure 6.1). At constant flux filtration, filter capacity was calculated as the filtration throughput achieved at a pressure differential of 1.4 bar (Kang et al., 2013; Riske et al., 2007; Yavorsky et al., 2003). Filtrate clarification was expressed in terms of OD_{600} measurements. After the OD measurements, the filtrate fractions were pooled together and stored at -80°C for future product recovery and impurity removal analyses. Product recovery was evaluated by measuring the concentration of monoclonal antibody (mAb) before and after depth filtration. Antibody concentration was quantified as described in Section 2.10.2. Impurity removal was evaluated by measuring total protein and DNA concentration before and after depth filtration. Total protein and DNA concentration were quantified as described in Section 2.10.1 and Section 2.10.3, respectively.

6.3. Results and Discussion

Flocculation and depth filtration performance were studied to understand how the PSD of flocculated streams impacts upon depth filtration, and how this can be modulated by the use of different filter media and filtration operating conditions such as pressure drop. The PSD of flocculated streams has been shown to impact upon the performance of subsequent unit operations, such as charged normal flow depth filtration (Singh et al., 2013) and centrifugation (Berrill et al., 2008). Flocculation and depth filtration were studied at USD scale first because (i) flocculation and depth filtration performance depend on many process variables; and (ii) a limited volume of HCD mammalian cell centrate was available. Both USD flocculation (Chapter 4 and Chapter 5) and USD depth filtration (Lau et al., 2013) have been proved to successfully predict the performance of their pilot-scale counterparts. Therefore, the methodology described in this chapter presents the opportunity to be implemented during the early bioprocess development studies when process-relevant materials are often limited, or later in development when process changes might need to be tested (Tait et al., 2009; Titchener-Hooker et al., 2008).

Laboratory-scale experiments were necessary to evaluate how the PSD of flocculated populations impacts upon depth filtration performance when using

multi-layer depth filters; the current USD depth filtration design only allows the fitting of single-layer depth filters. The aim was to investigate if a robust depth filtration process that is not affected by shifts in the size distribution of flocculated particles could be obtained with multi-layer depth filters. The filtration conditions and filter media used at laboratory scale were selected based upon the literature results described for the depth filtration of flocculated HCD mammalian cell feeds (Kang et al., 2013; Singh et al., 2013; Tomic et al., 2015).

6.3.1. Ultra Scale-Down Flocculation

Before any detailed analysis, the aim was to first study whether flocculation affected depth filtration performance in any way. As a result, the USD flocculation parameters and conditions studied were chosen for their ability to generate different PSDs. The two flocculation parameters selected were: flocculant concentration and flocculant addition rate; these two parameters have shown to generate very different PSDs when flocculating HCD mammalian cell feeds (see Figure 3.8 in Section 3.3.4.1 and Figure 5.1 in Section 5.3.2, respectively). Flocculation performance was measured in terms of its ability to generate monomodal and tight PSDs by flocculating the small particles present in the HCD mammalian cell centrate (see Section 3.3.4.1). Flocculated feeds with narrow monomodal PSDs are always of interest, particularly if they are to be processed by depth filtration (Singh et al., 2013) or centrifugation (Berrill et al., 2008).

The different flocculation conditions studied generated a range of PSDs, from wide bimodal distributions to narrow monomodal distributions (see Figure 6.2). Both flocculant concentration and flocculant addition rate determined the complexity of the population of flocculated particles. Flocculant concentrations of 0.30 % w/v led to the formation of small particles with diameters between 2 and 10 μm regardless of the flocculant addition rate used. However, fast addition rates (900 $\mu L.s^{-1}$) formed narrower PSDs. At 0.15 % w/v PEI, small particles were only generated at slow addition rates (1 $\mu L.s^{-1}$) (see Figure 6.2). Nonetheless, it is possible that this small population of particles was produced at any of the flocculation conditions tested, but that at fast addition rates particles of similar

size were also created. These small particles could have been camouflaged under a bigger PSD curve.

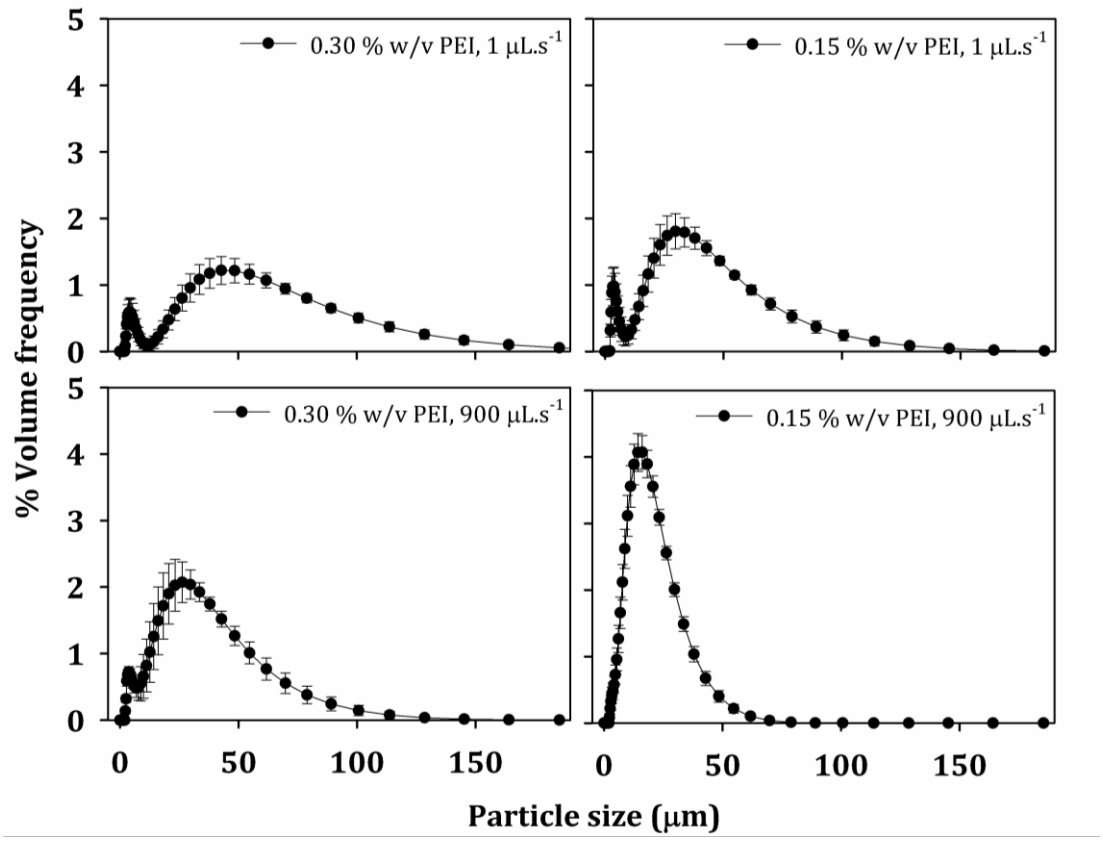

Figure 6.2. Particle size distribution of the flocs generated during the flocculation – depth filtration integration studies at USD scale.
A volume of 800 µL of HCD mammalian cell culture (peak cell count = 29.0x10^{6} cells.mL^{-1}) centrate (Q/Σ = 2.85x10^{-8} m.s^{-1}) was flocculated with PEI (concentration: 0.30 and 0.15 % w/v; addition rate: 1 and 900 µL.s^{-1}). After 10 minutes of floc maturation, the PSD of the flocculated material was measured as described in Section 2.11.4. Error bars represent one standard deviation where n = 12.

6.3.2. Ultra Scale-Down Depth Filtration

Normal flow filtration performance is judged according to filter capacity and retention (Yavorsky et al., 2003). At USD scale, where filtration was performed at constant vacuum pressure, capacity was calculated as the volume of fluid that could be processed at a minimum flow limit. In this chapter all the data was normalised by filter area. Therefore, capacity is redefined as the filtration throughput achieved at a minimum flux limit. Minimum flux was the flux value that was equal to 10 % of the initial flux obtained at the filtration conditions studied. Retention is defined as the filter capacity of the trailing sterile filter

(i.e. 0.22 μm) (Yavorsky et al., 2003). Retention was not studied in this chapter but it is calculated in Chapter 7. Filtrate clarification, measured as the end-point OD_{600}, was also studied to assess filter performance.

Industrially relevant filters with different pore sizes were used. DE45 (1 – 0.5 μm) was chosen for a tighter filter media. 05SP (10 – 1.5 μm) was a looser depth filter. Tight filters (e.g. 0.45 μm) have been successfully used to filter flocculated feeds (Chandler and Zydney, 2004). 05SP media has been repeatedly used to filter crude mammalian cell stocks (Hogwood et al., 2013b; Lau et al., 2013; Singhvi et al., 1996), where large solid volumes similar to those encountered with flocculated feeds were processed. All the filter media used were positively charged. Different pressure drops, which included the maximum and minimum operational pressures with the vacuum system used, were also examined.

To understand the fouling mechanisms that occurred during the filtration runs, the experimental data were fitted to four different linearised constant pressure filtration models (standard pore blockage, intermediate pore blockage, pore constriction and cake filtration) (see Figure 1.6 in Section 1.4.2 for their detailed description). Maximum projected filtration throughput values were calculated where possible to assess filtration performance and not for filter sizing purposes.

6.3.2.1. Filter Resistance Measurements

Filter resistance (R_f) was calculated at the three different pressure drops used during USD filtration. The results are summarised in Table 6.1. The DE45 filter resistance values were higher than those of the 05SP media due to its tighter pore size. Filter resistance increased with ΔP independently of the filter media used. However, the increment was not proportional. While R_f remained constant at 400 and 700 mbar, R_f at 100 mbar was smaller by 39 % and 43 % in the DE45 and 05SP media, respectively. The increment in R_f with ΔP can be attributed to a more compact nature of the sponge-like depth filter material. The physical strength of the filter could have possibly been maintaned at 100 mbar, but not at 400 and 700 mbar. At higher ΔP values, the filter would have compacted thus increasing R_f as a consequence. The effect of ΔP on R_f might be more evident when using filter sheets than with depth filter capsules. In the latter the filter medium is

sealed hence conferring the filter stronger resistance to ΔP (3M Purification Inc, 2011). The R_f values were consistent, as described by the percentage standard deviation calculations (see Table 6.1). However, differences in the R_f of ± 30 % (Yavorsky et al., 2003) or even up to ± 57 % (Chandler and Zydney, 2004) can be expected due to the inherent variability of filter sheets.

Table 6.1. Change in filter resistance with pressure drop during the USD constant pressure filtration studies.
Filter resistance was measured with deionised water, and calculated as described in Section 2.8.1. The dV/dt variable in Equation 2.24 was the first derivative of the linear best fit obtained for the water flux data ($R^2 \geq 0.999$). Viscosity was that of water at 22°C ($9.544x10^{-4}$ Pa.s) and area was the USD effective filter area (0.28 cm^2). Percentage standard deviation was calculated as the ratio between the values of one standard deviation (n = 4) and the average R_f.

	DE45 media		05SP media	
ΔP	**Average R_f (m^{-1})**	**% Standard deviation**	**Average R_f (m^{-1})**	**% Standard deviation**
100	$1.0x10^{10}$	8.0 %	$0.5x10^{10}$	11 %
400	$2.4x10^{10}$	7.6 %	$1.3x10^{10}$	6.1 %
700	$2.3\ x10^{10}$	9.9 %	$1.4x10^{10}$	11 %

6.3.2.2. DE45 Filter Performance: Non-Treated Centrate

The filtration curves obtained from filtering HCD mammalian cell centrate at constant vacuum pressures equal to 100, 400 and 700 mbar are plotted in Figure 6.3. Flux decayed with increasing filtration throughput as the depth filter gradually got clogged with particulates present in the centrate. Flux decreased more rapidly at 100 and 400 mbar than it did at 700 mbar. Consequently, larger filter capacity values were achieved at high pressure drops (40 $L.m^{-2}$ at 100 and 400 mbar *vs*. 55 $L.m^{-2}$ at 700 mbar) (see Figure 6.3). Higher initial fluxes were also obtained with larger ΔP, although the high variability observed at 400 and 700 mbar could only certify differences between 100 mbar and the other two pressure drops (see Figure 6.3).

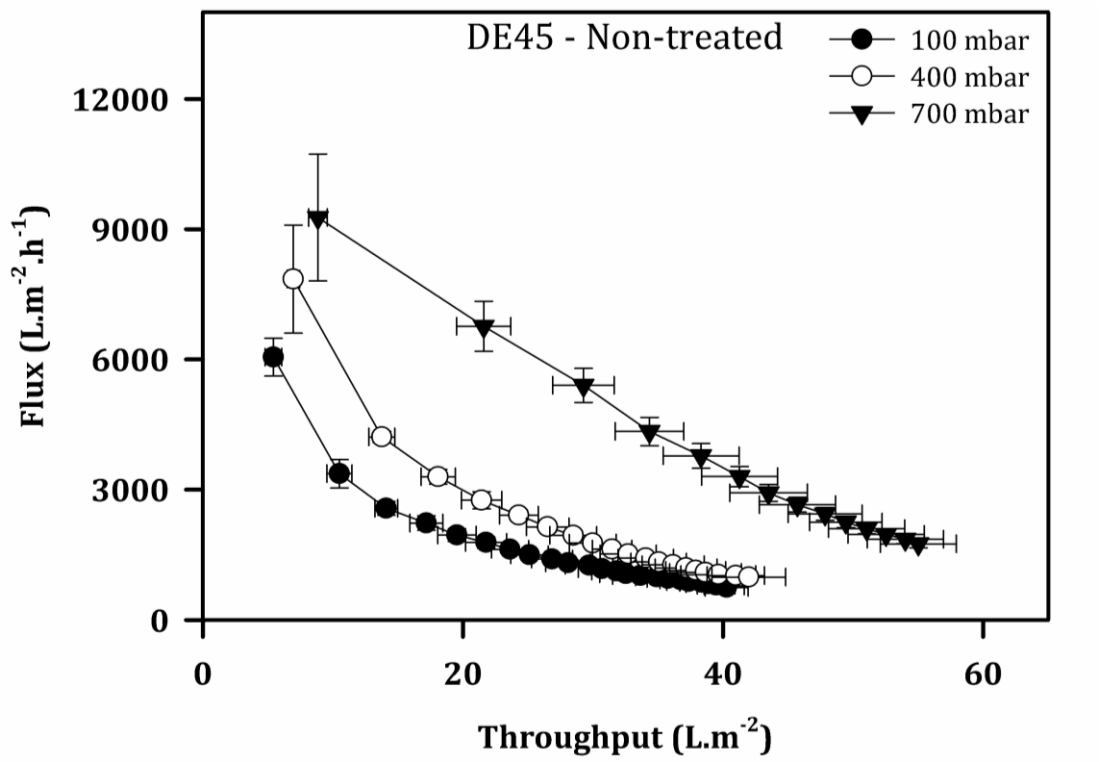

Figure 6.3. Flux decay of the non-treated centrate during USD constant pressure filtration when using DE45 depth filter media.
A set volume of 4 mL of non-treated HCD mammalian cell culture (peak cell count = 28.9x10^{6} cells.mL^{-1}) centrate (Q/Σ = 2.85x10^{-8} m.s^{-1}) was filtered at three different constant vacuum pressures (100, 400 and 700 mbar) employing the USD filtration methodology (see Section 2.8.1). The last data point in the filtration curves is equal to the filter capacity value; filtration stopped when flux decayed by 90 % (see Section 2.8.1). Error bars represent one standard deviation where n = 4.

The raw filtration data obtained experimentally (i.e. cumulative filtrate volume *vs*. time) was transformed and fitted according to the linearised constant pressure filtration fouling models (see Table 2.5 in Section 2.8.1). The linearised forms are convenient for data analysis and model identification (van Reis and Zydney, 2007). The model that best fitted the data was pore constriction ($R^2 \geq 0.981$; $P < 0.01$), meaning that fouling occurred within the depth filter by small particles gradually reducing its effective pore size (van Reis and Zydney, 2007). This is in line with the pore size range of the DE45 filter (1 - 0.5 μm) and the sub-micron particles present in centrifuge supernatants (Iammarino et al., 2007). Nonetheless, none of the other three filtration fouling models could be ruled out since there was no clear difference in the R^2 values obtained ($0.974 \leq R^2 \leq 0.898$). The linearised modified pore constriction model (see Section 2.8.1) was used to calculate the projected maximum volume of fluid per

unit filter area that can be filtered before the filter is completely plugged by fouling, which is referred to as V^*_{max} (L.m^{-2}); this model was developed by Lau et al. (2013) to account for the significant filtration changes occurring in timescales of the order of 1 to 60 seconds when employing the USD constant pressure filtration methodology. The V^*_{max} results are summarised in Table 6.2. As observed in the table, the V^*_{max} values obtained at 100 and 400 mbar were the same (considering the standard deviation of one). However, V^*_{max} increased between 1.5 and 2 fold at 700 mbar.

Higher pressure drops led to higher initial flow rates (see Figure 6.3). Higher initial flow rates are expected to prematurely foul the depth filter resulting in low throughputs (Singhvi et al., 1996; Yavorsky et al., 2003). However, the experimental data showed otherwise. Flux decayed faster at lower initial flow rates (i.e. ΔP = 100 and 400 mbar) resulting in lower filtration throughputs (see Figure 6.3). The more opened filter structure obtained at 100 mbar (i.e. smaller R_f – see Table 6.1) could have drawn big particles into the depth filter that prematurely clogged the filter. Big particles could have been formed upon freeze-thawing the centrate (see Figure 11.2 in Section11.1.2). At 400 mbar the flux declined at a lower rate, probably due to the tighter filter structure (i.e. larger R_f – see Table 6.1), although no difference in filtration throughput was achieved with respect to 100 mbar. The flux decline observed at 700 mbar was almost linear (see Figure 6.3), suggesting that a different filtration fouling mechanism to pore constriction could have occurred. The use of simple fouling models to analyse flux decline data has been shown to be ineffective in describing filtration in some cases. There is experimental evidence showing that a transition in the fouling behaviour from a pore constriction and/or pore blockage fouling behaviour to cake filtration can commonly occur during filtration (van Reis and Zydney, 2007). This could have occurred during filtration at 700 mbar. The formation of a cake layer where large particulates gradually deposited would have prevented the premature clogging of the filter. The cake layer, combined with a larger driving pressure force, led to higher filtration throughput values.

Table 6.2. V^*_{max} values predicted with USD constant pressure filtration when using DE45 and 05SP depth filter media.

		DE45 media		05SP media	
ΔP (mbar)	**Sample**	**Average V^*_{max}† (L.m^{-2})**	**Standard deviation (n = 4)**	**Average V^*_{max}† (L.m^{-2})**	**Standard deviation (n = 4)**
100	Non-treated	54.06	2.746	86.33	7.109
	0.30 % w/v PEI, 1 µL.s^{-1}	18.79	1.040	--	--
	0.30 % w/v PEI, 900 µL.s^{-1}	16.88	0.665	34.66	2.120
	0.15 % w/v PEI, 1 µL.s^{-1}	17.19	1.324	--	--
	0.15 % w/v PEI, 900 µL.s^{-1}	14.68	0.753	--	--
400	Non-treated	49.58	4.815	112.9	6.637
	0.30 % w/v PEI, 1 µL.s^{-1}	20.83	0.551	--	--
	0.30 % w/v PEI, 900 µL.s^{-1}	23.13	1.234	39.32	2.370
	0.15 % w/v PEI, 1 µL.s^{-1}	18.98	1.207	--	--
	0.15 % w/v PEI, 900 µL.s^{-1}	24.74	1.902	--	--
700	Non-treated	72.69	5.836	107.6	11.45
	0.30 % w/v PEI, 1 µL.s^{-1}	34.45	2.372	--	--
	0.30 % w/v PEI, 900 µL.s^{-1}	32.71	2.124	35.54	2.160
	0.15 % w/v PEI, 1 µL.s^{-1}	32.49	2.049	--	--
	0.15 % w/v PEI, 900 µL.s^{-1}	29.11	1.834	--	--

† Values predicted by the modified pore constriction model (see Section 2.8.1).

Finally, Figure 6.4 describes the clarification achieved by depth filtration at any of the flocculation and filtration conditions studied when using the DE45 filter media. The centrate OD_{600} value was reduced by 8 fold after a single depth filtration step with the DE45 filter media. Higher OD_{600} values were achieved at 100 mbar because of the more open filter structure obtained at this ΔP (i.e. lower R_f - see Table 6.1). Nonetheless, the large error bars obtained at 400 and 700 mbar fell within the 100 mbar range of OD_{600} values. Therefore, the dependence between ΔP and filtrate clarification could not be confirmed experimentally at the conditions studied for non-treated HCD mammalian cell culture streams.

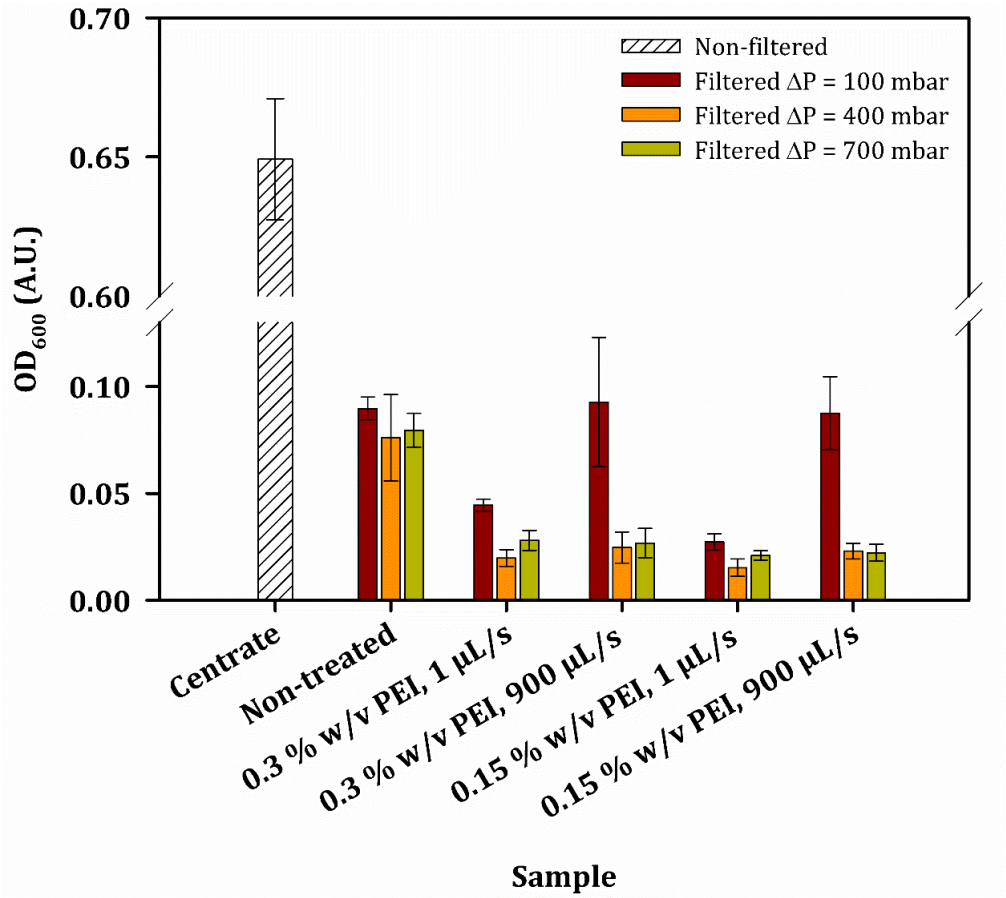

Figure 6.4. Effect of USD-scale flocculation and USD constant pressure depth filtration operations on filtrate clarification when using DE45 filter media. *Filtrate clarification was quantified by optical density measurements at 600 nm wavelength. Centrate was HCD mammalian cell culture (peak cell count = 29.0x10^{6} cells.mL^{-1}) centrifuged at pilot scale (Q/Σ = 2.85x10^{-8} m.s^{-1}). This material was then filtered at USD scale (see Section 2.8.1) at three different constant ΔP (100, 400 and 700 mbar). Prior to filtration, process material was either non-treated (i.e. non-flocculated) or flocculated with PEI at USD scale (see Section 2.7.1) (0.30 % w/v and 0.15 % w/v) using two different flocculant addition rates (1 and 900 µL.s^{-1}). Error bars represent one standard deviation where n = 4.*

6.3.2.3. DE45 Filter Performance: Flocculated Centrate

The filtration curves obtained from filtering centrate flocculated with 0.30 % w/v PEI are plotted in Figure 6.5. Filtration was performed at USD scale using three different constant vacuum pressure drops (100, 400 and 700 mbar). Flocculation was also performed at USD scale using slow (Figure 6.5, top) and fast (Figure 6.5, bottom) flocculant addition rates. Flux rapidly decayed with increasing filtration throughputs for all the ΔP and flocculant addition rates studied. As with the non-treated centrate (Figure 6.3), flux decline was slower at 700 mbar than at 100 and 400 mbar. Consequently, larger filter capacity values were obtained at higher ΔP, possibly due to the tighter filter structure and higher driving force. Flocculant addition rate did not seem to affect filtration at the conditions tested (see Figure 6.5). The same filter capacity values were obtained at the same ΔP independent of flocculant addition rate. The only exception was at 100 mbar, where filter capacity was 2 $L.m^{-2}$ larger when flocculated at 1 $\mu L.s^{-1}$. Figure 6.2 shows similarly sized particles were generated at both flocculant addition rates when flocculating at 0.30 % w/v PEI. Significantly different PSDs might be needed to see any impact upon filter capacity.

The experimental data obtained at USD scale from filtering centrate flocculated at 0.30 % w/v PEI was transformed and fitted into the linearised forms of the constant pressure filtration fouling models (see Table 2.5 in Section 2.8.1). Pore constriction was the best fit ($R^2 \geq 0.983$; $P < 0.01$). Nonetheless, a cake layer build-up could be observed on the filter surface at the end of every filtration run (see Figure 6.6.A). This visual observation contradicted the mathematical predictions from the filtration models. It is possible there was a transition in the fouling behaviour from pore constriction to cake filtration during the filtration run as described in the article published by van Reis and Zydney (2007). Ultra scale-down filtration data was gathered for less than 100 seconds since data acquisition was automatically stopped when flux dropped by 90 %. It is hypothesised that the filtration data points obtained did not include the transition in the fouling behaviour. Assuming the experimental data only contained the initial pore constriction fouling behaviour, the linearised modified pore constriction model (see Section 2.8.1) was used to calculate V_{max}^{*}. The values

summarised in Table 6.2 show V_{max}^{*} increased with ΔP. The increment was not proportional, with the biggest increase in V_{max}^{*} happening between 400 and 700 mbar. The V_{max}^{*} results confirmed flocculant addition rate did not affect USD depth filtration at the conditions tested.

As with the non-treated centrate, filtrate clarification of the centrate flocculated at 0.30 % w/v PEI improved with ΔP (see Figure 6.4) due to the higher R_f values (see Table 6.1). Flocculant addition rate impacted upon filtrate clarification unlike with filter capacity. However, the effect of flocculant addition rate upon clarification performance was subjected to filter resistance. When ΔP was equal to 100 mbar, fast flocculant addition rates (900 μL.s^{-1}) resulted in a 2 fold increase in filtrate OD_{600} when compared to slow addition rates (1 μL.s^{-1}) (see Figure 6.4). In contrast, filtrate OD_{600} was constant at 400 and 700 mbar independently of the flocculation conditions. It is possible that the larger amounts of small particles obtained at 900 μL.s^{-1} (see Figure 6.2), in combination with the lower R_f values of 100 mbar (see Table 6.1), led to more particles passing through the filter thus lowering filtrate clarification.

Figure 6.7 describes the depth filtration curves obtained at USD scale from filtering HCD mammalian cell centrate flocculated at slow (Figure 6.7, top) and fast (Figure 6.7, bottom) flocculant addition rates with PEI concentrations of 0.15 % w/v. Flux rapidly declined with increasing filtration throughputs at pressure drops of 100, 400 and 700 mbar. As observed with the non-flocculated (see Figure 6.3) and 0.30 % w/v PEI-flocculated centrate (see Figure 6.5), flux decayed more slowly at larger ΔP leading to higher filter capacity values. Flocculant addition rate did not impact upon filter capacity despite the different PSDs generated (see Figure 6.2); the exception occurred at 400 mbar, where the fast flocculant addition rate obtained a filter capacity value 5 L.m^{-2} larger than the slow flocculant addition rate (Figure 6.7).

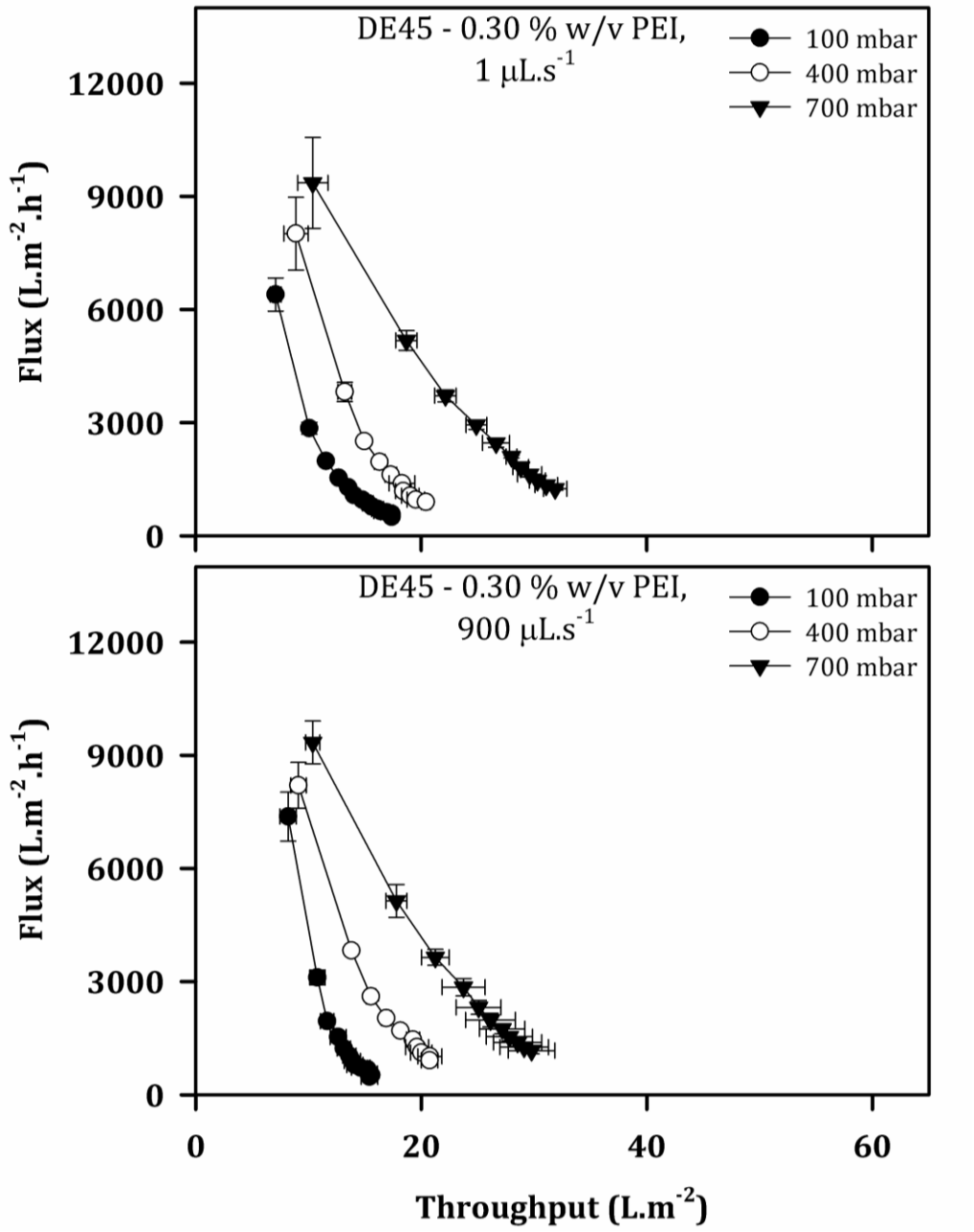

Figure 6.5. Flux decay of 0.30 % w/v PEI-flocculated centrate during USD constant pressure filtration when using DE45 depth filter media.
A set volume of 4 mL of flocculated HCD mammalian cell (peak cell count = 28.9x10^{6} cells.mL^{-1}) centrate (Q/Σ =2.85x10^{-8} m.s^{-1}) was filtered at USD scale (see Section 2.8.1). Depth filtration was performed at three different constant vacuum pressures (100, 400 and 700 mbar). Process material was flocculated at room temperature (0.30 % w/v PEI; flocculant addition rate: 1 μL.s^{-1} and 900 μL.s^{-1}) using the USD flocculation methodology (see Section 2.7.1). The last data point in the filtration curves is equal to the filter capacity value since filtration stopped when flux decayed by 90 % (see Section 2.8.1). Error bars represent one standard deviation where n = 4.

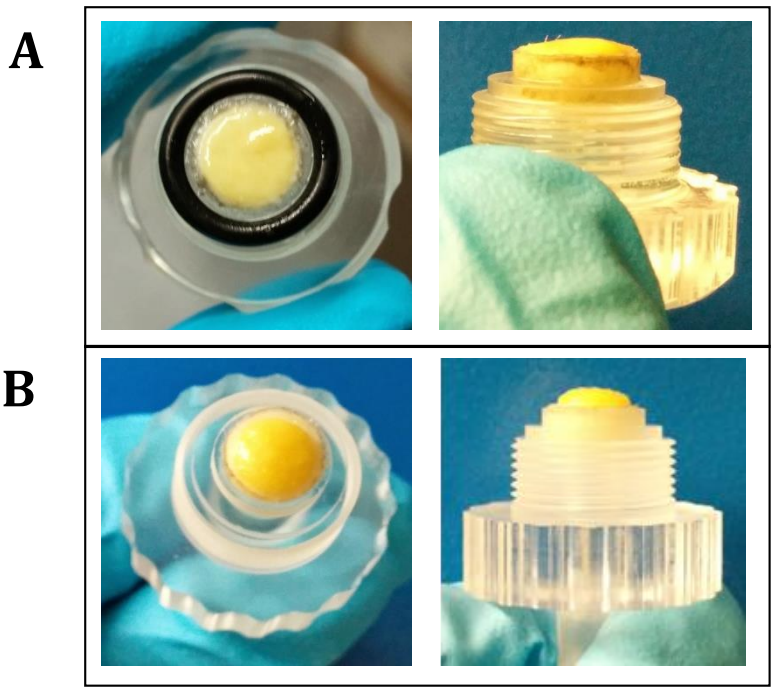

Figure 6.6. Cake layer formation on the filter surface after USD constant pressure filtration with flocculated high cell density mammalian cell centrate.
*Cake layer build-up was observed when filtering flocculated samples using DE45 (**A**) and 05SP (**B**) depth filter media at any of the USD flocculation and USD filtration conditions studied.*

At 0.15 % w/v PEI, the linearised pore constriction model was also the filtration fouling model that best fitted the experimental data ($R^2 \geq 0.989$; $P < 0.01$) despite a cake layer built up on the filter surface (see Figure 6.6.A). As with 0.30 % w/v PEI, a transition in the fouling mechanism from pore constriction to cake filtration could have occurred (van Reis and Zydney, 2007). The linearised modified pore constriction model (see Section 2.8.1) showed V^*_{max} increased with ΔP (see Table 6.2). But while at slow flocculant addition rates the biggest increase in V^*_{max} was observed between 400 and 700 mbar, at fast addition rates the difference was largest between 100 and 400 mbar. Flocculant addition rate did not impact the calculated V^*_{max} value when operating at 100 and 700 mbar; however, a 5.8 $L.m^{-2}$ difference was obtained at 400 mbar between the fast and slow flocculant addition rates (Table 6.2).

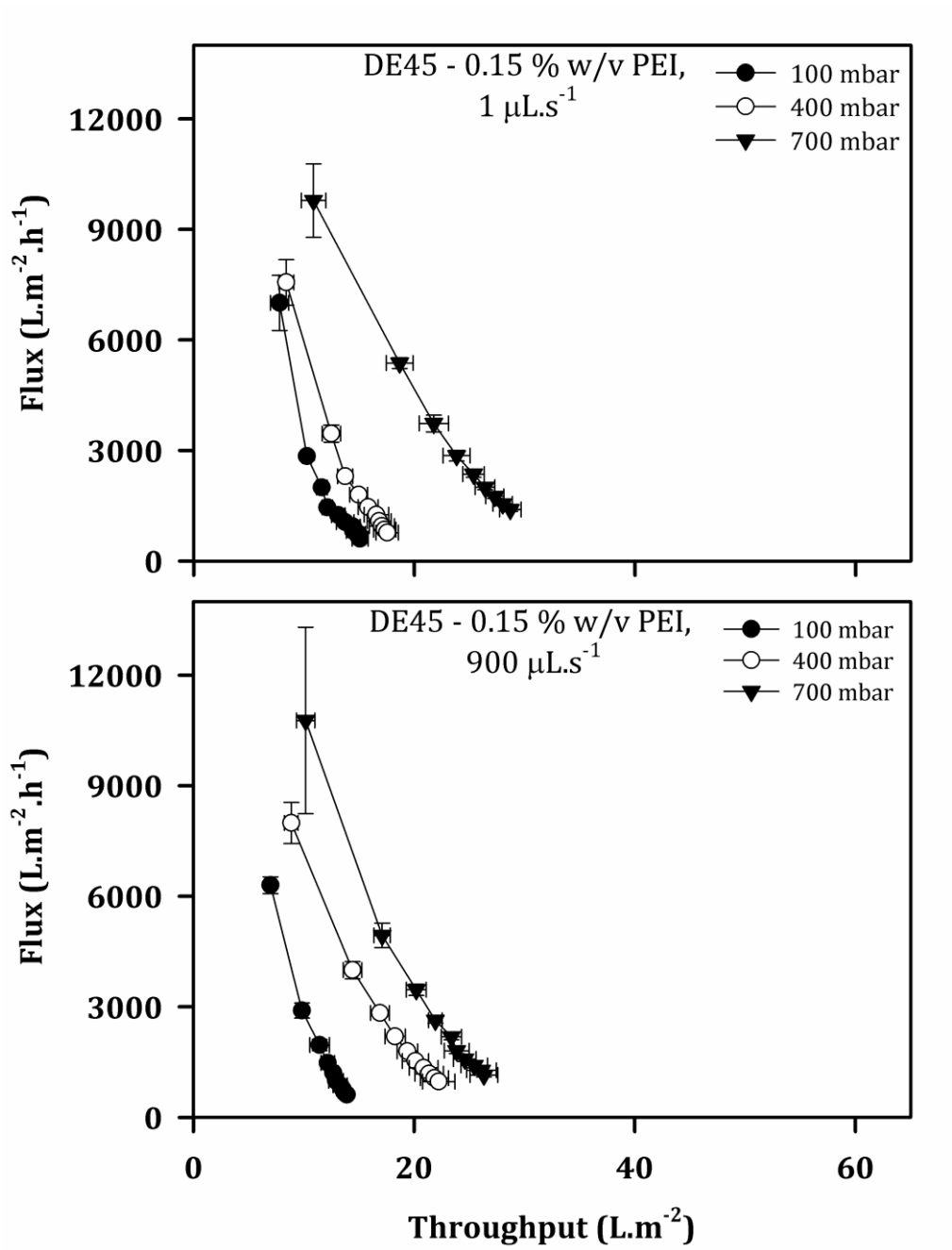

Figure 6.7. Flux decay of 0.15 % w/v PEI-flocculated centrate during USD constant pressure filtration when using DE45 depth filter media.
A set volume of 4 mL of flocculated HCD mammalian cell (peak cell count = 29.0x10^{6} cells.mL^{-1}) centrate (Q/Σ = 2.85x10^{-8} m.s^{-1}) was filtered at USD scale (see Section 2.8.1). Three different constant vacuum pressures were studied (100, 400 and 700 mbar). Process material was flocculated at room temperature (0.15 % w/v PEI; flocculant addition rate: 1 µL.s^{-1} and 900 µL.s^{-1}) using the USD flocculation methodology (see Section 2.7.1). The last data point in the filtration curves is equal to the filter capacity value since filtration stopped when flux decayed by 90 % (see Section 2.8.1). Error bars represent one standard deviation where n = 4.

Finally, flocculant addition rate impacted upon filtrate clarification when flocculating the HCD mammalian cell centrate at 0.15 % w/v PEI, but only at 100 mbar (see Figure 6.4). The same combination of factors as the encountered with the 0.30 % w/v PEI data was assumed. That is, the larger amount of small particles generated at 900 μL.s^{-1} (see Figure 6.2) and the low R_f values when operating at 100 mbar (see Table 6.1) allowed small particles passing through the depth filter thus reducing clarification performance.

6.3.2.4. 05SP Filter Performance: Non-Treated and Flocculated Centrate

A wider pore size range depth filter with 10 - 1.5 μm retention rating was used to evaluate if the rapid flux decay results obtained with the DE45 media were filter specific. Two feed conditions were studied at first to evaluate the 05SP media; these were: non-treated centrate and flocculated centrate (flocculant concentration: 0.30 % w/v PEI; flocculant addition rate: 900 μL.s^{-1}). Filtration was performed at the same three pressure drops used with the DE45 media (100, 400 and 700 mbar). Both flocculation and depth filtration were performed at USD scale. The resultant filtration curves are plotted in Figure 6.8.

When filtering the non-treated centrate (Figure 6.8, top), filter capacity increased by 40 % at 400 and 700 mbar with respect to that obtained at 100 mbar. The trend of larger filter capacity values achieved with larger ΔP was also observed when using the DE45 media. The same hypothesis is given: the tighter filter structure at 400 and 700 mbar (see Table 6.1) prevented large particles present in the centrate from penetrating the filter and prematurely clogging it; big particles could have been generated when freeze-thawing the centrate (see Figure 11.2 in Section 11.1.2). Pore constriction was the filtration fouling model that best fitted the experimental data ($R^2 \geq 0.986$; $P < 0.01$). The value of V^*_{max} was then calculated applying the linearised modified pore constriction model (see Section 2.8.1). The results summarised in Table 6.2 show V^*_{max} increased between 25 and 31 % when operating at 400 and 700 mbar, respectively, with respect to 100 mbar. These values are smaller than the 40 % difference observed with the filter capacity values (i.e. raw experimental data)

(see Figure 6.8, top). Filtration with the 05SP media reduced the centrate OD_{600} by 6 fold, independently of the operating ΔP (see Figure 6.9).

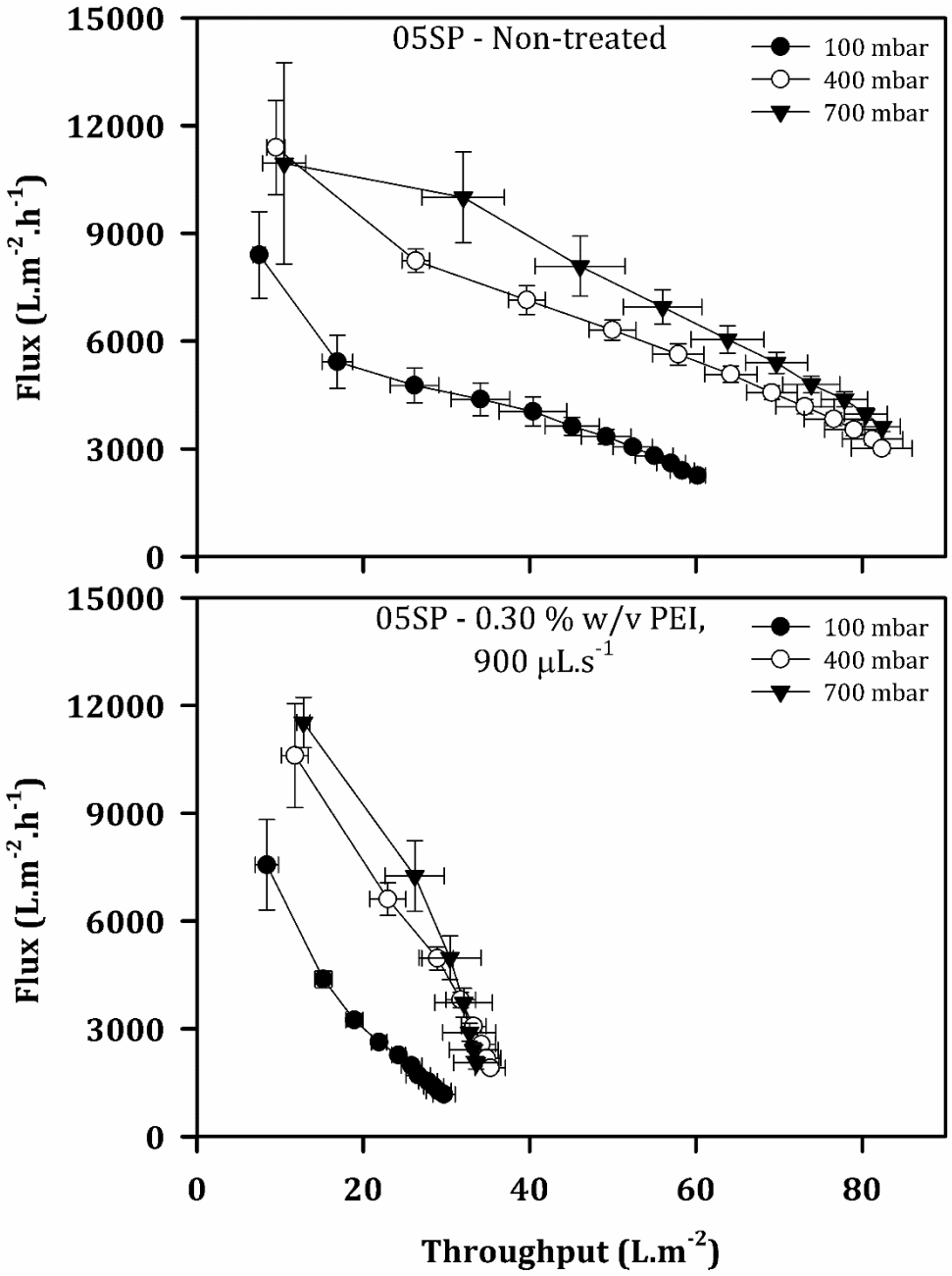

Figure 6.8. Flux decay of non-treated and flocculated centrate during USD constant pressure filtration when using 05SP depth filter media.
A set volume of 4 mL of non-treated and flocculated (0.30 % w/v PEI, flocculant addition rate: 900 µL.s^{-1}) HCD mammalian cell (peak cell count = 29.0x10^{6} cells.mL^{-1}) centrate (Q/Σ = 2.85x10^{-8} m.s^{-1}) was filtered at three different constant vacuum pressures (100, 400 and 700 mbar) employing the USD filtration methodology (see Section 2.8.1). Flocculation was also performed at USD scale (see Section 2.7.1). The last data point in the filtration curves is equal to the filter capacity value since filtration stopped when flux decayed by 90 % (see Section 2.8.1). Error bars represent one standard deviation where n = 4.

The filtration curves resulting from the USD depth filtration of flocculated centrate (0.30 % w/v PEI and 900 µL.s^{-1} flocculant addition rate) are plotted in Figure 6.8, bottom. Flux rapidly decayed at all of the ΔP studied when compared to the non-flocculated curves (Figure 6.8, top). Filter capacity increased by 16 % at 400 and 700 mbar, with respect to that of 100 mbar. The filtration fouling model with the best fit was pore constriction ($R^2 \geq 0.989$; $P < 0.01$) despite the formation of a cake layer on the filter surface in every flocculated run (see Figure 6.6.B). It is thought a transition in the filtration fouling mechanism from pore constriction to cake filtration occurred during the run, as described by van Reis and Zydney (2007). Assuming the filtration run was governed by the pore constriction fouling mechanism, the linearised modified pore constriction model (see Section 2.8.1) was used to calculate V^*_{max}. The value of V^*_{max} did not change with ΔP (see Table 6.2); only a difference of 0.17 L.m^{-2} was calculated between 100 and 400 mbar. Finally, the centrate OD_{600} was reduced by 9 to 14 fold by combining PEI flocculation and the 05SP depth filter media (see Figure 6.9). The best clarification performance was achieved at 400 and 700 mbar due to the tighter filter structure at these ΔP values (i.e. higher R_f – see Table 6.1).

In comparison to the DE45 media results (Figure 6.3 and Figure 6.5), flux decayed more slowly with the 05SP media at all of the ΔP studied. The larger filter capacity values obtained overall were due to the lower filter resistance encountered with the 05SP media (see Table 6.1). However, the lower R_f values were detrimental to filtrate clarification. With the exception of one process condition (0.30 % w/v PEI, 900 µL.s^{-1} addition rate, 100 mbar pressure drop), filtrate OD_{600} increased between 25 and 92 % when compared to the DE45 clarification results (see Figure 6.4 and Figure 6.9).

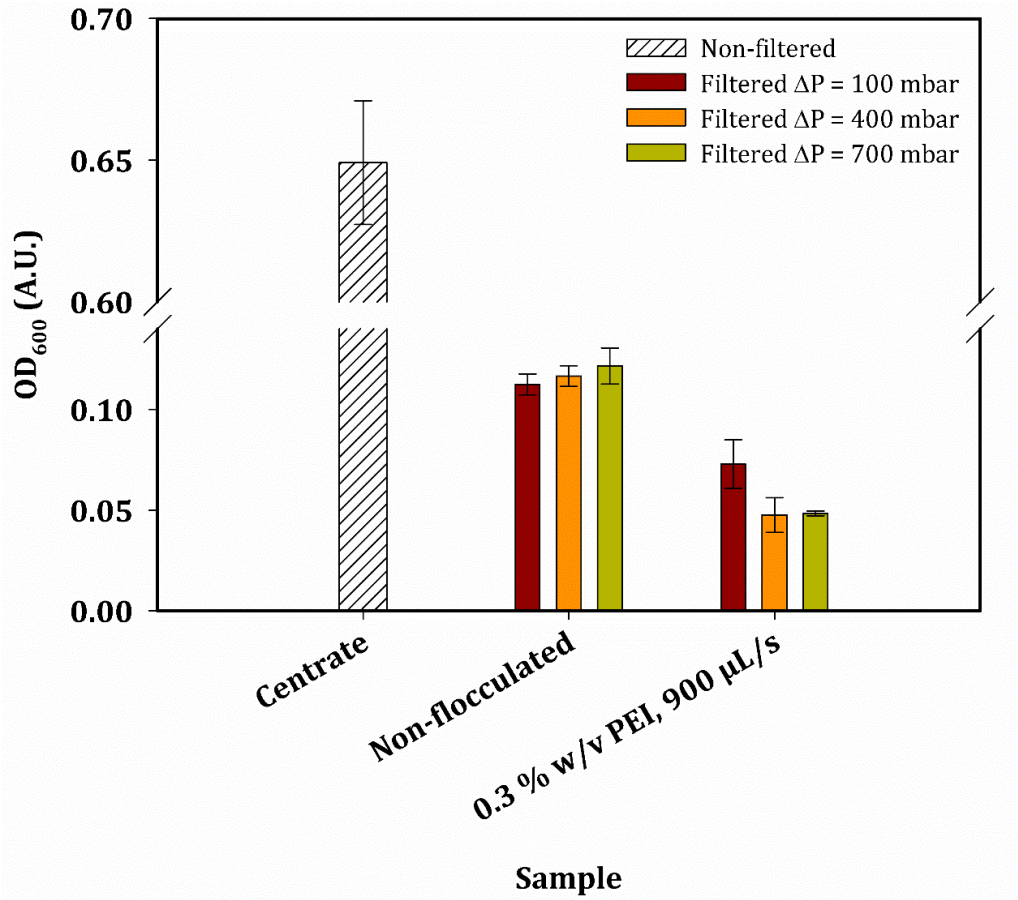

Figure 6.9. Effect of USD flocculation and USD constant pressure depth filtration operations on filtrate clarification when using 05SP filter media. *Filtrate clarification was quantified by optical density measurements at 600 nm wavelength. Centrate was HCD mammalian cell culture (peak cell count = 29.0x10^{6} cells.mL^{-1}) centrifuged at pilot scale (Q/Σ = 2.85x10^{-8} m.s^{-1}). This material was then filtered at USD scale (see Section 2.8.1) at three different ΔP (100, 400 and 700 mbar). Prior to filtration, process material was either non-treated (i.e. non-flocculated) or flocculated at USD scale (see Section 2.7.1) with PEI at 900 µL.s^{-1} to a final concentration of 0.30 % w/v. Error bars represent one standard deviation where n = 4.*

6.3.2.5. Evaluation of the Ultra Scale-Down Method

Flocs rapidly clogged the depth filters studied at USD scale. The filter capacity values achieved when filtering the flocculated centrate ranged between 14 and 32 L.m^{-2} (DE45 media) (see Figure 6.5 and Figure 6.7) and between 30 and 34 L.m^{-2} (05SP media) (see Figure 6.8, bottom) depending upon the flocculation conditions and ΔP. These values represented a throughput reduction between 1.7 and 2.9 fold when compared to the filter capacity values achieved at the same ΔP with the non-treated centrate (see Figure 6.3 – DE45 media and Figure 6.8, top – 05SP media). Furthermore, the filter capacity values obtained with the

flocculated centrate were up to 28 fold smaller than those reported in the literature (110 and 400 $L.m^{-2}$) when depth filtering HCD mammalian cell broths (Singh et al., 2013). Nonetheless, the filter capacity values taken from the literature are considered a reference since the process material, the flocculation conditions and the NFF mode used were different. The filtration fouling models predicted both the DE45 and the 05SP filter media were clogged by a pore constriction mechanism when processing the flocculated centrate. However, there was visual evidence of cake layer formation in all flocculated runs (see Figure 6.6). This indicated that, at the experimental conditions tested, the USD contant pressure filtration methodology was unable to obtain enough data points to appreciate any transition in the fouling mechanism (van Reis and Zydney, 2007). Nonetheless, it is also possible that a very permeable cake layer built up on the filter surface letting small particles through and into the depth filter, which ultimately clogged the filter via the pore constriction fouling mechanism.

When filtering the non-treated centrate at USD scale, the filter capacity values ranged between 40 and 55 $L.m^{-2}$ (DE45 media) (see Figure 6.3) and between 60 and 82 $L.m^{-2}$ (05SP media) (see Figure 6.8, top). The literature reports filter capacity values of ~194 $L.m^{-2}$ when depth filtering non-treated mammalian cell centrate stocks (Riske et al., 2007). However, this is taken as a reference value since the experiments were carried out at a larger scale in the literature, in addition to the fact that the cell culture and centrifugation processes were different, which significantly impacts upon the centrate properties (Liu et al., 2010).

The disparity between the experimental and the reported filter capacity values could be due to the filtration mode employed at USD scale and/or the use of single-layer filters. The implementation of constant flux filtration is advised to obtain an accurate filtration profile and retention performance of a given depth filter media (Liu et al., 2010; Yavorsky et al., 2003). The initial high feed flow rates obtained with constant pressure filtration have been described to inefficiently load the filter and cause premature clogging. However, the experimental data at USD scale showed greater throughputs were achieved with high initial flow rates. Multiple-layer, and not single-layer, depth filters are typically used

post-centrifugation (Liu et al., 2010). Multi-layer depth filters have been developed to improve the particle removal capabilities of the filter, with each layer having a unique pore size, electrical charge, and surface chemistry (van Reis and Zydney, 2007). The stratified retention of different sized particles reduces premature filter fouling and increases filtration capacity. Additionally, multi-layer depth filters have been demonstrated to achieve large filtration capacities when processing flocculated mammalian cell broths (Kang et al., 2013; Singh et al., 2013).

To evaluate the use of multi-layer depth filters, filtration had to be performed at laboratory scale since the USD contant pressure filtration design could only accommodate single-layer filters (see Section 2.8.1). The larger volumes of process-relevant material required limited the number of flocculation and filtration variables that could be studied. Section 6.3.3 explores the use of a selected multi-layer depth filter and studies how flocculant addition rate affects filtration performance.

6.3.3. Laboratory-Scale Depth Filtration

High cell density mammalian cell centrate was flocculated at pilot scale to a final 0.15 % w/v PEI concentration. Flocculant concentration was chosen based upon the flocculation results obtained in Section 3.3.4 and Lonza Biologics' in-house knowledge for flocculation processes when using their high cell density CHO cell line. A slow flocculant addition rate (8.47 $mL.min^{-1}$) that guaranteed the predominance of the micromixing time scale in the pilot-scale vessel (see Chapter 4) was used. The macromixing and mesomixing time scales were studied using a fast flocculant addition rate (184 $mL.min^{-1}$) (see Chapter 4). The flocculant addition rates chosen for the pilot-scale experiments replicated the mixing time scale conditions encountered in the USD flocculation experiments; the aim was to replicate the same flocculation conditions at both scales to isolate the effect that multi-layer depth filters have on filtration performance. Based on the USD flocculation methodology successfully validated at pilot scale with flocculated HCD mammalian cell centrate (see Chapter 5): (i) the PSDs obtained with 8.47 $mL.min^{-1}$ (pilot) and 1 $\mu L.s^{-1}$ (USD) (see Figure 6.2) were assumed to be

identical at both scales at the same PEI concentration; (ii) the PSDs obtained with 184 mL.min^{-1} (pilot) and 900 µL.s^{-1} (USD) (see Figure 6.2) were assumed to be different at both scales at the same PEI concentration; (iii) the PSDs generated at pilot scale with 8.47 mL.min^{-1} and 184 mL.min^{-1} were assumed to be different.

Normal flow depth filtration was performed using a 23 cm^2 positively charged, multi-layer depth filter (refer to Section 6.2.3 for the details) operated at a constant flux of 100 L.m^{-2}.h^{-1}, as recommended by the manufacturer. Filter performance was assessed based on filter capacity, filtrate clarification (measured as filtrate OD_{600}), impurity removal and product recovery (see Figure 6.1). Filter retention, also important to assess depth filtration performance (Yavorsky et al., 2003), was studied in Chapter 7 with flocculation and filtration conditions selected from this section.

6.3.3.1. Multi-Layer Depth Filter Performance

Figure 6.10 shows the evolution of pressure drop, filtrate OD_{600} and absorbance at 280 nm wavelength (Abs_{280}) obtained with filtration throughput. These filtration curves were obtained with centrate flocculated at pilot scale using slow (Figure 6.10, top) and fast (Figure 6.10, bottom) flocculant addition rates. Filter capacity could not be calculated at any of the two flocculant addition rates studied since the pressure drop limit of 1.4 bar was never reached with the volume of flocculated material available. Instead, a constant ΔP around 0.10 bar was maintained during both filtration runs. A throughput value of 490 L.m^{-2} was obtained at the end of both filtration runs. Therefore, flocculant addition rate did not impact upon filtration performance at the conditions tested, although these experiments need to be repeated with larger process volumes to calculate filter capacity.

The filtrate OD_{600} profile changed with flocculant addition rate (see Figure 6.10). Depth filters behave like adsorbent beds where filtrate quality initially is high until the media is saturated with adsorbed material (Yavorsky et al., 2003). After this point, known as breakthrough, the amount of particles in the filtrate increases. At fast flocculant addition rates (Figure 6.10, bottom), filtrate OD_{600} gradually increased to 0.015 A.U. and remained constant around this value until

the end of the filtration run. No breakthrough was observed. The gradual initial increase in OD_{600} was due to filtrate dilution as a consequence of residual phosphate buffer present in the filter capsule (after wetting, flushing and blowing the filter) and the filtration system's dead volume. At slow flocculant addition rates (Figure 6.10, top), filtrate OD_{600} quickly increased up to 0.030 A.U., after which OD_{600} gradually decreased and stabilised around 0.016 A.U.. A similar filtrate OD_{600} profile was obtained in Chapter 7 at identical flocculation and filtration conditions but with a different batch of HCD mammalian cell centrate (see Figure 7.6). It is possible the filter's removal efficiency improved with filtration throughput due to previously retained particles acting as additional collectors for other particles (Zhu et al., 1996). This is known as filter ripening. Clarification improvement with filtration throughput was only encountered at slow flocculant addition rates, where a bimodal PSD with small flocculated particles was expected from the USD flocculation mimic (see Figure 6.2). It is possible the population of small particles initially flowed through the filter before acting as collectors for equally sized or bigger particles. Despite the initial increase in filtrate OD_{600} at slow flocculant addition rates, the pooled filtrate resulted in the same OD_{600} value at both flocculant addition rates when accounting for the standard deviation of one (see Table 6.3). Finally, the combination of flocculation and multi-layer depth filtration reduced the centrate OD_{600} between 40 and 60 times (see Table 6.3).

The filtrate Abs_{280} values obtained at fast flocculant addition rates were 70 % larger than those achieved at slow addition rates (see Figure 6.10). Since Abs_{280} was monitored in-line with un-diluted samples, the large difference observed was not considered to be proportional to the protein content in the filtrate. Analytical measurements confirmed the total protein content was very similar in both filtration runs (see Table 6.3). The table also shows flocculation reduced the total protein content in the centrate between 16 and 23 %, with slightly larger decrements obtained at slow flocculant addition rates. Such decrease in protein content could be attributed to HCP reduction as product concentration remained constant during flocculation (see Table 6.3). Depth filtration further reduced the total protein content by 17 to 25 % thanks to its adsorptive properties. This additional decrease could also be attributed to HCP removal, although some

product loss occurred (see Table 6.3). Finally, flocculation reduced the DNA content present in the centrate by more than 99.9 % (see Table 6.3). Flocculant addition rate did not impact upon DNA removal. The positively charged depth filter also assisted in DNA removal by lowering the DNA content by 4.5 fold (see Table 6.3).

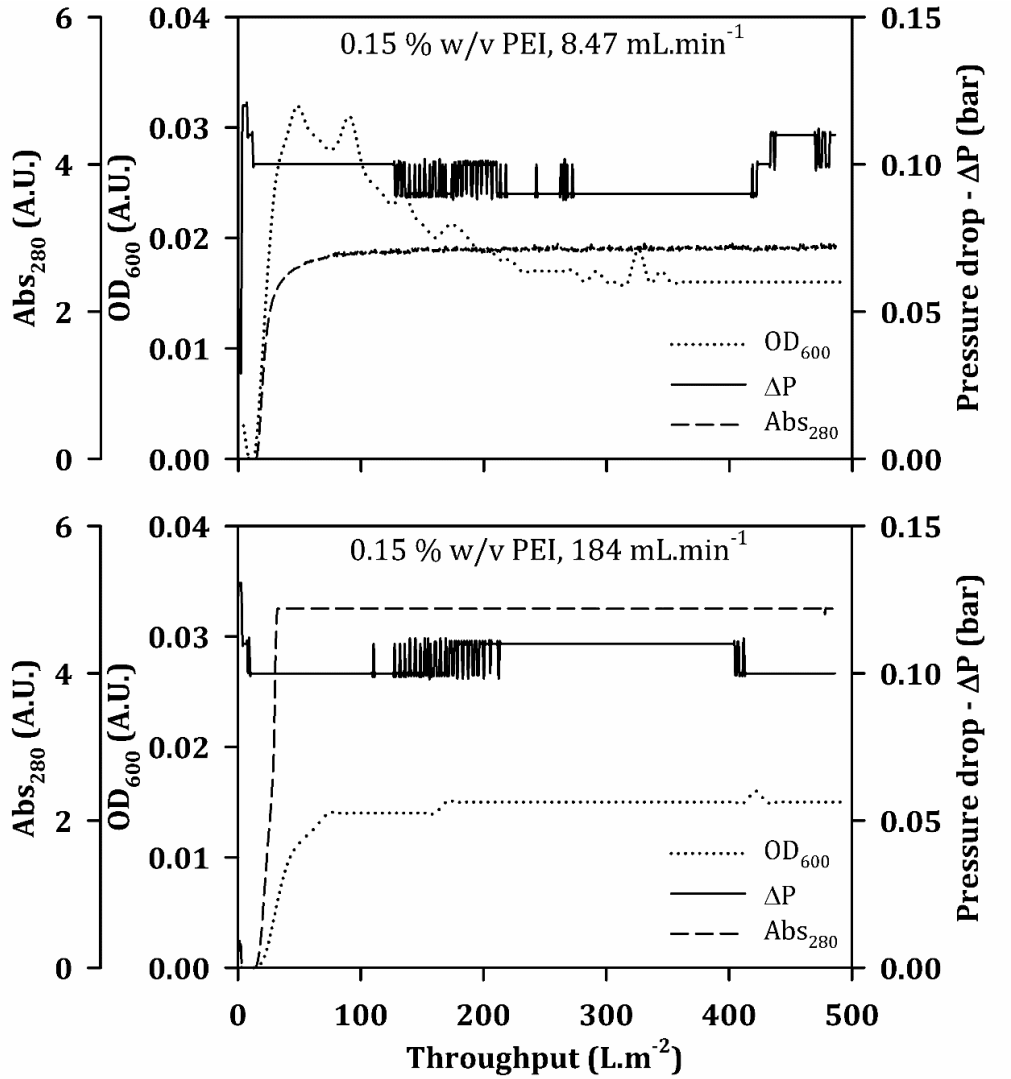

Figure 6.10. Laboratory scale, multi-layer constant flux depth filtration of flocculated mammalian cell centrate.

A set volume of 1.5 L of HCD mammalian cell (peak cell count = 29.0x10⁶ cells.mL⁻¹) centrate (Q/Σ = 2.85x10⁻⁸ m.s⁻¹) were flocculated at pilot scale to a final 0.15 % w/v PEI concentration using slow and fast flocculant addition rates (8.47 mL.min⁻¹ and 184 mL.min⁻¹, respectively) (refer to Section 2.3.1 for the vessel configuration and Section 2.7.1 for the detailed flocculation methodology). After 10 minutes of floc maturation, the flocculated feed was depth filtered at a constant flux of 100 L.m⁻².h⁻¹ using a 23 cm² Clarisolve® 40MS (Millipore) filter capsule. Filtration was performed and monitored with an ÄKTAcrossflow system (GE Healthcare) (see Section 2.8.2 for the detailed filtration methodology). Filtrate was manually collected in 10 mL fractions. Filtrate OD_{600} values were measured every 20 mL of filtrate with a spectrophotometer as described in Section 2.11.1.

Table 6.3. Clarification, impurity removal and product recovery achieved with multi-layer, constant flux depth filtration of flocculated feed at laboratory scale.

Clarification was measured in terms of filtrate OD_{600}. Optical density measurements were taken using a spectrophotometer (see Section 2.11.1) and within 10 minutes of completing the filtration step; centrate values correspond to defrosted supernatant. Impurity removal and product recovery were expressed as percentage yield relative to the HCD mammalian cell centrate. Concentrations for yield calculations were determined as follows: total protein (Pierce™ BCA protein assay, Thermo Scientific) (see Section 2.10.1), DNA (Quant-iT™ PicoGreen®, Thermo Scientific) (see Section 2.10.3) and mAb (protein G HPLC) (see Section 2.10.2). Standard deviations correspond to 3x (OD_{600}) and 6x (total protein, DNA and mAb) measurements where n = 1.

	Sample	OD_{600} (A.U.)	Total protein (%)	DNA (%)	mAb (%)
	Centrate	0.804 ± 0.001	100	100	100
8.47 mL.min^{-1}	*Flocculated*	N/A	77.1 ± 2.63	0.079 ± 0.004	96.0 ± 6.51
	Filtered	0.019 ± 0.005	59.7 ± 2.15	0.018 ± 0.002	90.0 ± 3.90
184 mL.min^{-1}	*Flocculated*	N/A	84.0 ± 1.02	0.082 ± 0.001	95.2 ± 7.19
	Filtered	0.014 ± 0.004	59.5 ± 2.39	0.018 ± 0.001	87.4 ± 4.83

6.3.3.2. Evaluation of Multi-Layer Depth Filters

Depth filtration of HCD mammalian flocculated feeds achieved larger throughput values when performed at laboratory scale using multi-layer depth filters than when carried out at USD scale with single-layer depth filters (as predicted by the V^*_{max} method). The laboratory-scale filtration throughput values were between 4.3 and 33 times larger than those observed at USD scale. Moreover, larger throughput values could be expected at laboratory scale since the maximum filter pressure drop was not achieved during the filtration runs (see Figure 6.10). The superior performance of multi-layer depth filters (laboratory scale), when compared to single-layer depth filters (USD scale), could be attributed to a full utilisation of the depth filter. That is, entrapment and/or adsorption of particles of a wide size range inside the filter thanks to the multiple layers of gradually

tighter media. Furthermore, the filtrate clarification achieved at laboratory scale with multi-layer depth filters was up to 6.3 times higher than those obtained with single-layer USD constant pressure depth filtration; nonetheless, the extent of the clarification improvement depended upon the flocculant addition rate and filtration pressure drop used at USD scale. Notwithstanding, the superior filtration performance observed at laboratory scale could also be attributed to the use of constant flux filtration mode; constant flux filtration has been described to gradually load the filter thus avoiding the high initial feed flow rates characteristic of constant pressure filtration that cause premature clogging (Liu et al., 2010; Yavorsky et al., 2003).

Total protein, DNA and mAb content were not quantified at USD scale, so no comparison was provided for the laboratory-scale experiments. Total protein and DNA measurements showed the filtration conditions chosen at laboratory scale exploited the adsorptive properties of the multi-layer depth filter to assist in the removal of impurities. However, product recovery at laboratory scale was, on average, equal to 89 % due to volumetric losses. The optimisation of the flocculation and filtration conditions could offer greater impurity removal and higher product recovery yields.

6.4. Conclusions

This chapter presented the process interaction between flocculation and depth filtration studied at USD and laboratory scale. A summary of the key findings, based upon the chapter aims and objectives is as follows:

1. Assess the use of USD flocculation and USD constant pressure depth filtration to investigate how flocculation performance affects depth filtration performance.

Ultra scale-down flocculation and ultra scale-down contant pressure depth filtration offered the potential to be integrated in the same robotic liquid handling platform for complete process automation and high-throughput analysis. Process interaction between flocculation and depth filtration unit operations was studied with small volumes of process-relevant material, which was available in limited

quantities. Flocculant concentration, flocculant addition rate and filtration pressure drop impacted upon depth filtration performance, which was assessed via filter capacity and filtrate clarification measurements; the effect on step yield and impurity removal was not assessed at USD scale. Single-layer depth filters showed to be insufficient to cope with the large solid volumes present in the flocculated feeds and the HCD mammalian cell centrate tested. Rapid filter fouling rates were obtained when processing the flocculated HCD mammalian cell centrate, thus limiting data acquisition to few points and consequently hindering the identification of the filter's fouling behaviour. The design of the USD constant pressure filtration device only allowed the use of single-layer filters. Therefore, to investigate if depth filtration performance could be improved with multi-layer depth filters, experiments had to be performed at laboratory scale.

2. Assess the suitability of multi-layer depth filters to clarify polydisperse flocculated streams.

The structure of multi-layer depth filters when operated in constant flux mode offered high filtration throughputs and clarification performance during the flocculation of HCD mammalian cell centrate at laboratory scale. Multi-layer depth filters also provided a robust filtration performance against changes in the flocculant addition rate. However, more studies with larger volumes of flocculated material are necessary before concluding so. Laboratory-scale experiments offered a larger data, set but at the expense of high-throughput capability and sample volume consumption. To characterise process interaction between two or more unit operations many variables need to be evaluated hence demanding high-throughput and low volume requirements. Therefore, the development of a USD filtration methodology to accommodate multi-layer filters is of interest.

7. Laboratory-Scale Comparison of Non-Treated *vs*. Flocculated Mammalian Cell Culture Processes

7.1. Introduction and Aims

Flocculation was introduced as part of the primary recovery step in the production of a monoclonal antibody (mAb) by a high cell density (HCD) mammalian cell line. This unit operation was included after centrifugation to reduce the high impurity levels and particulate content of the centrate. The aim was to enhance the performance of the subsequent depth filtration step and minimise the precipitation of process-related impurities during the low pH elution step of protein A chromatography. The fit of flocculation within the mAb production process had to be assessed before its implementation. In order to investigate this, the newly suggested primary recovery strategy (centrifugation – flocculation – depth filtration) was compared to a platform primary recovery strategy for mAbs (centrifugation – depth filtration – depth filtration). The comparison study extended into the protein A affinity chromatography step. The assessment was made at laboratory scale by comparing filter capacity and filter retention, product recovery and impurity removal achieved after each unit operation. Furthermore, the impact of flocculation upon the purification process was also included in the feasibility assessment.

Summary of the chapter's aims and objectives:

1. Assess at laboratory scale the effect of introducing a flocculation step after centrifugation upon the performance of the primary recovery and capture chromatography processes.

2. Evaluate at laboratory scale the possibility of replacing the mAb platform primary recovery strategy (i.e. centrifugation followed by two depth filtration stages) by the flocculated primary recovery strategy (i.e. centrifugation followed by flocculation and depth filtration).

7.2. Experimental Set-Up

A schematic diagram of the experimental set-up is shown in Figure 7.1. The details of the studies performed are described below.

7.2.1. Mammalian Cell Culture Preparation

High cell density mammalian cell centrate was prepared and stored as described in Section 2.1.2. Centrate was defrosted at room temperature prior to use.

7.2.2. Non-Treated Process Stream

A volume of 1.50 L of HCD mammalian cell culture centrate was filtered at a constant flux of 130 $L.m^{-2}.h^{-1}$. Depth filtration was performed in two stages using a dual-layer ZetaPlus™ BC25 capsule of 25 cm^2 filter area in each stage. In the first depth filtration stage a 60ZA05A (3 - 0.30 μm) filter grade was used. The second filtration stage used a 90ZA05A (3 - 0.20 μm) depth filter grade (see Figure 7.1). After the second filtration stage, the filtrate was stored at +4°C for less than 10 hours. Once room temperature was reached, the material was filtered through a 17.3 cm^2 sterilising grade filter (SartoScale Disposable Sartopore® 2 0.45/0.2 μm) operated at a constant flux of 130 $L.m^{-2}.h^{-1}$ (see Figure 7.1). The filtrate was then stored at -80°C for further affinity chromatography processing. Samples of 10 mL volume from each unit operation were stored at -20°C prior to analysis. The filter grades were chosen based upon Lonza Biologics' manufacturing experience. The flux values were taken from the literature (Riske et al., 2007). Filter specifications and detailed methodology can be found in Section 2.8.2. Filter capacity was calculated as the filtration throughput obtained at a pressure drop (ΔP) of 1.4 bar (Kang et al., 2013; Riske et al., 2007; Yavorsky et al., 2003). Depth filter retention corresponded to the filter capacity of the sterilising grade filter.

7.2.3. Flocculated Process Stream

A volume of 1.50 L of HCD mammalian cell culture centrate was flocculated at pilot scale to a final 0.15 % w/v polyethylenimine (PEI) concentration and neutral pH by adding 75 mL of a 3 % w/v PEI stock solution at a constant addition

rate of 8.47 mL.min^{-1}. See Section 2.3.1 for the detailed configuration of the flocculation system, and Section 2.7.1 for the flocculation methodology. The flocs were left to mature for 10 minutes before filtering 1.38 L through a 23 cm^2, multi-layer depth filter capsule (Clarisolve® 40MS µPod®) at a constant flux of 100 L.m^{-2}.h^{-1}. The resultant filtrate was then stored at +4°C for less than 10 hours to be filtered at room temperature through a 17.3 cm^2 sterilising grade filter (SartoScale Disposable Sartopore® 2 0.45/0.2 µm) at a constant flux of 100 L.m^{-2}.h^{-1} (see Figure 7.1). The resultant filtrate was stored at -80°C for further affinity chromatography studies. Samples of 10 mL volume from each unit operation were stored at -20°C prior to analysis. Depth filter grade was selected based on depth filtration results for flocculated mammalian cell broths published in the literature (Kang et al., 2013; Singh et al., 2013); flux value was chosen based upon the manufacturer's recommendations. Filter specifications and detailed methodology are described in Section 2.8.2. Filter capacity and filter retention were calculated as described in Section 7.2.2.

7.2.4. Affinity Chromatography Using Protein A

The filtrates obtained from sterile filtration in the non-treated and flocculated process streams were defrosted at room temperature prior to use. A volume of 20 mL from the non-treated and flocculated samples was loaded onto an equilibrated 4.7 mL MabSelect SuRe column (10 cm bed height) with a loading capacity of 30 mg.mL^{-1} (see Figure 7.1). At the end of each run, the 2 mL eluate fractions were adjusted to pH 7.0 using 2.0 M Tris base. In the non-treated stream, 2 column volumes (CVs) of pH 2.1 buffer were used to strip the column; six CVs were used in the flocculated stream with the aim to strip any remaining PEI off the column. Flow-through, elution and strip fractions were stored at -20°C for subsequent analysis. Refer to Section 2.9 for details of the column, protocol and equipment used.

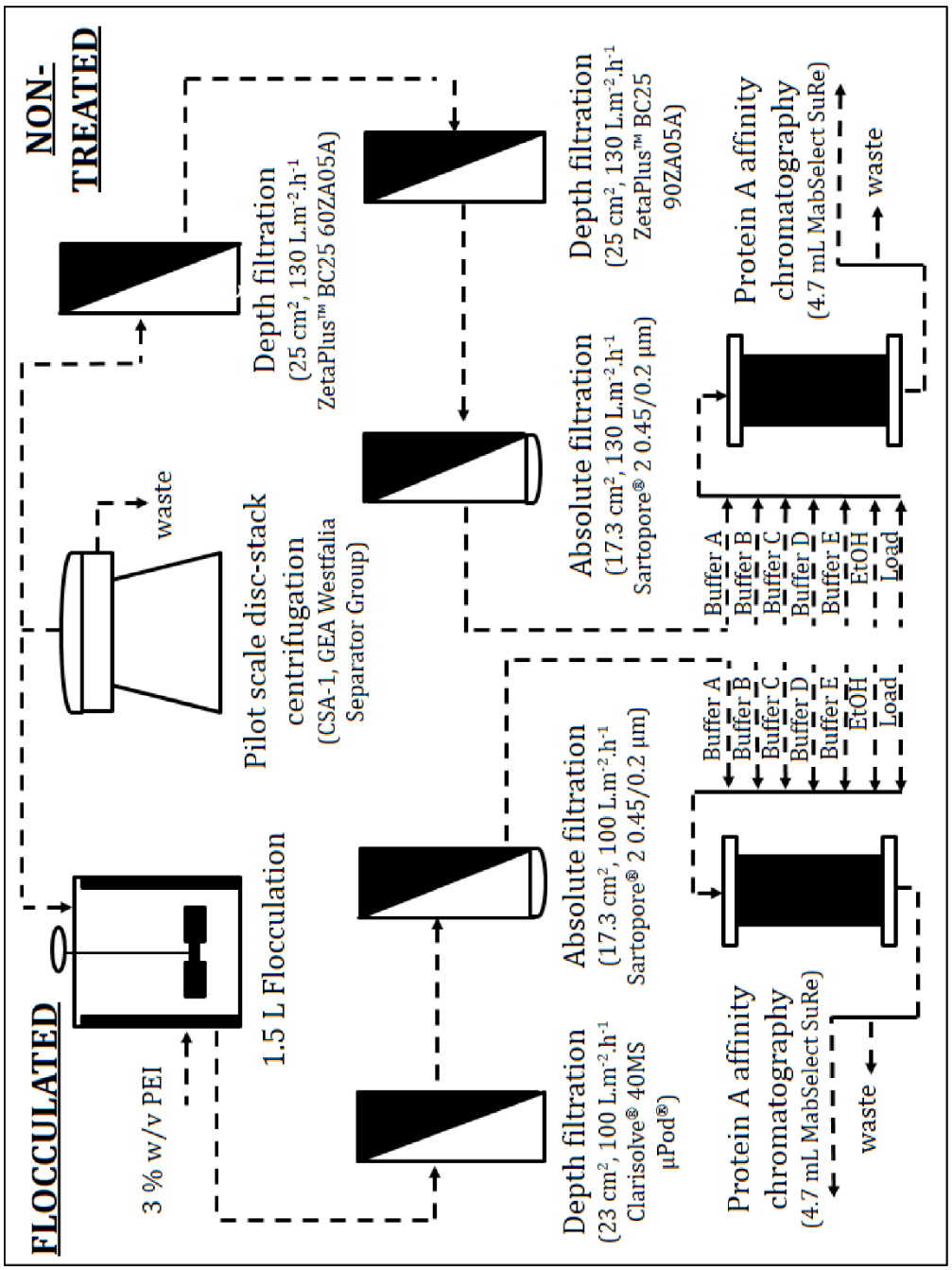

Figure 7.1. Schematic diagram of the flocculated and non-treated mAb production primary recovery strategies.

7.3. Results and Discussion

7.3.1. Filtration of Non-Treated Mammalian Cell Centrate

Centrifugation coupled with depth filtration is the industry's standard for primary recovery, particularly with increasingly high cell density cultures (Roush and Lu, 2008; Shukla et al., 2007). The non-treated primary recovery strategy studied in this chapter consisted of a disc-stack centrifuge (primary clarification) followed by a two-stage depth filtration step (secondary clarification) and a sterilising grade filter; this primary recovery strategy was used as a benchmark for the flocculated process stream (Section 7.3.2). The HCD mammalian cell centrate was provided by Lonza Biologics to obtain a representative production-scale centrate feedstock. Two depth filtration stages were used to remove the significant amounts of debris present in the post-centrifuge centrate (Low et al., 2007; Shukla et al., 2007). One or more depth filters can be used during secondary clarification (Dave et al., 2009; Yavorsky et al., 2003). Multiple depth filtration optimises solid removal with each successive filter progressively removing smaller particles. In the non-treated primary recovery strategy, a loose-grade depth filter was used followed by a tighter-grade media to prevent the premature blockage of the relatively expensive final sterilising grade filter (van Reis and Zydney, 2007; Yavorsky et al., 2003). In turn, the sterilising grade filter was used after depth filtration to remove any residual particulates that may clog the subsequent affinity capture chromatography step, although it is also used to reduce adventitious microbes during production (Shukla and Kandula, 2008).

The study of centrifugation performance was out of the scope of this chapter and was not analysed. Each filtration step was studied individually with the aim to find the limiting step and offer some insight into the filtration fouling mechanisms involved.

7.3.1.1. First Depth Filtration Stage

Figure 7.2 shows the evolution of ΔP, filtrate optical density measured at 600 nm wavelength (OD_{600}) and absorbance at 280 nm (Abs_{280}) with filtration throughput when using the 60ZA05A dual-layer depth filter media. Pressure drop

gradually rose with increasing filtration throughput values. A maximum ΔP of 2.3 bar was reached at filtration throughputs of 540 $L.m^{-2}$. But filter capacity, which was calculated as the filtration throughput obtained at a maximum ΔP of 1.4 bar, was equal to 461 $L.m^{-2}$. A change in the slope of the ΔP curve between 180 and 200 $L.m^{-2}$ was observed, possibly indicating a transition in the fouling mechanism. The experimental data was transformed and fitted with the four different constant flux filtration models (i.e. pore blockage, intermediate blockage, pore constriction and cake filtration) (see Table 2.7 in Section 2.8.2). The entire data set fitted poorly with any of the filtration models studied ($R^2 \leq 0.878$). However, more success was obtained when splitting the data in two sets. Filtration throughputs < 180 $L.m^{-2}$ best fitted the cake filtration model ($R^2 = 0.985$; $P < 0.01$), while pore constriction was the best fit for filtration throughputs > 200 $L.m^{-2}$ ($R^2 = 0.973$; $P < 0.01$). This observation was supported by previous reports in the literature that indicate a single filtration mechanism is unlikely during a filtration run (van Reis and Zydney, 2007). A combination between cake filtration and pore constriction fouling mechanisms might have happened. Freeze-thawing the centrate used in the filtration experiments could have resulted in the formation of large particles formed by the submicron particles present in it, as observed with another batch of HCD mammalian cell centrate (see Figure 11.2 in Section 11.1.2). It is possible that during the freeze-thawing process, particles with diameters bigger than the 3 - 0.30 μm filter retention range were formed. These solids, unable to penetrate deep into the depth filter, would have gradually generated a cake layer on the filter surface. After the formation of this layer, the smaller particles could have clogged the porous cake thus translating into a pore constriction fouling mechanism. Another possibility is that the structure of the cake was very porous and allowed small particulates to flow through the cake and into the depth filter, which was ultimately clogged via pore constriction.

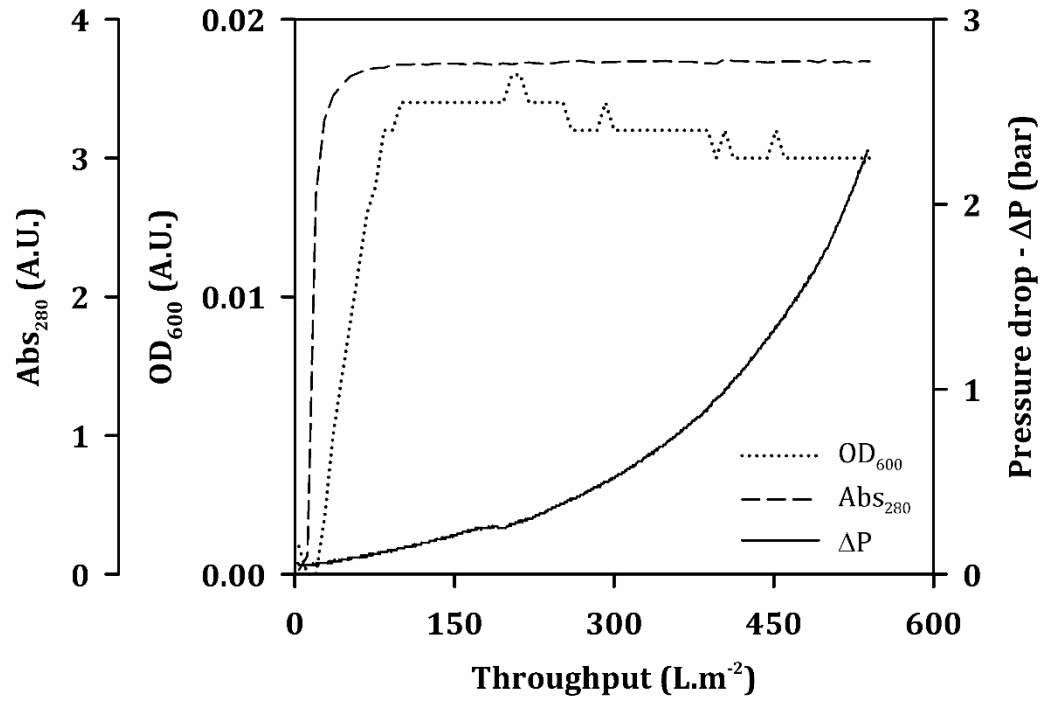

Figure 7.2. Performance of the first constant flux depth filtration stage from the non-treated primary recovery strategy.
A volume of 1.50 L of HCD mammalian cell culture centrate was further clarified using a 25 cm² ZetaPlus™ BC25 capsule with 60ZA05A (3 - 0.30 µm) filter grade (3M Purification Inc.). Filtration was performed at a constant flux of 130 L.m⁻².h⁻¹ and at room temperature. Filtrate was manually collected in 10 mL fractions but the first five fractions were later discarded to avoid filtrate dilution in the subsequent processing steps. Filtration was performed with an ÄKTAcrossflow system (GE Healthcare), which also monitored pressure drop (refer to Section 2.8.2 for the detailed filtration methodology). Filtrate OD_{600} and Abs_{280} were manually measured every 20 mL of filtrate with a spectrophotometer (see Section 2.11.1).

The evolution of clarification performance during the filtration run was monitored off-line with OD_{600} measurements. No solids breakthrough occurred during filtration despite reaching feed pressures close to the maximum specified by the manufacturer (see Figure 7.2). Therefore, either the filter media was not saturated with particulates, or a cake layer formed on the filter surface acted as a pre-filter. After an initial increment in OD_{600} from 0.000 to 0.017 A.U., the OD_{600} gradually decreased to 0.015 A.U. with increasing filtration throughputs. The inherent filtrate dilution caused by the residual phosphate buffer present in the filter capsule (after wetting, flushing and blowing the filter) and the filtration system's dead volume, explained the initial OD_{600} increase. The following reduction in OD_{600} suggested the existence of a cake layer or the occurrence of

filter ripening. If a cake layer was formed, small particles initially penetrated through the filter. As filtration advanced and the cake layer became thicker, the small particles became trapped in it thus acting as a pre-filter. Similar observations are reported in the literature (Sorensen et al., 1995). If filter ripening occurred instead, the particles adsorbed and/or trapped in the filter became additional collectors for other particles hence improving solids retention (Zhu et al., 1996). Finally, Abs_{280} remained constant throughout the filtration run at 3.7 A.U. (see Figure 7.2).

7.3.1.2. Second Depth Filtration Stage

The filtration conditions employed in the second depth filtration stage (90ZA05A dual-layer depth filter media) were the same as those used in the first depth filtration stage (60ZA05A dual-layer depth filter media) (see Figure 7.1). Figure 7.3 shows the ΔP, filtrate OD_{600} and Abs_{280} profiles obtained with increasing filtration throughput values with the 90ZA05A dual-layer depth filter media. Pressure drop had only increased by 0.08 bar when the feed material was totally exhausted at a filtration throughput of 445 $L.m^{-2}$ (see Figure 7.3). Therefore, filter capacity, which was calculated as the filtration throughput obtained at a maximum ΔP of 1.4 bar, could not be determined. In addition to this, the small increase in ΔP indicated that only a reduced amount of solids was retained in the filter media. Also, the filter fouling mechanism could not be identified. Filtrate OD_{600} gradually increased but did not reach a constant value until filtration throughputs of 230 $L.m^{-2}$ were achieved (see Figure 7.3). The filter achieved a reduction in OD_{600} of 0.001 A.U. with respect to the feed material (i.e. filtrate from the first depth filtration stage), hence corroborating the hypothesis of low solids retention drawn from the ΔP results. Filtrate Abs_{280} remained constant across the two depth filtration stages thus implying no protein retention (see Figure 7.2 and Figure 7.3). The data suggested an inefficient utilisation of the filter media chosen. A tighter filter grade should be employed in future studies.

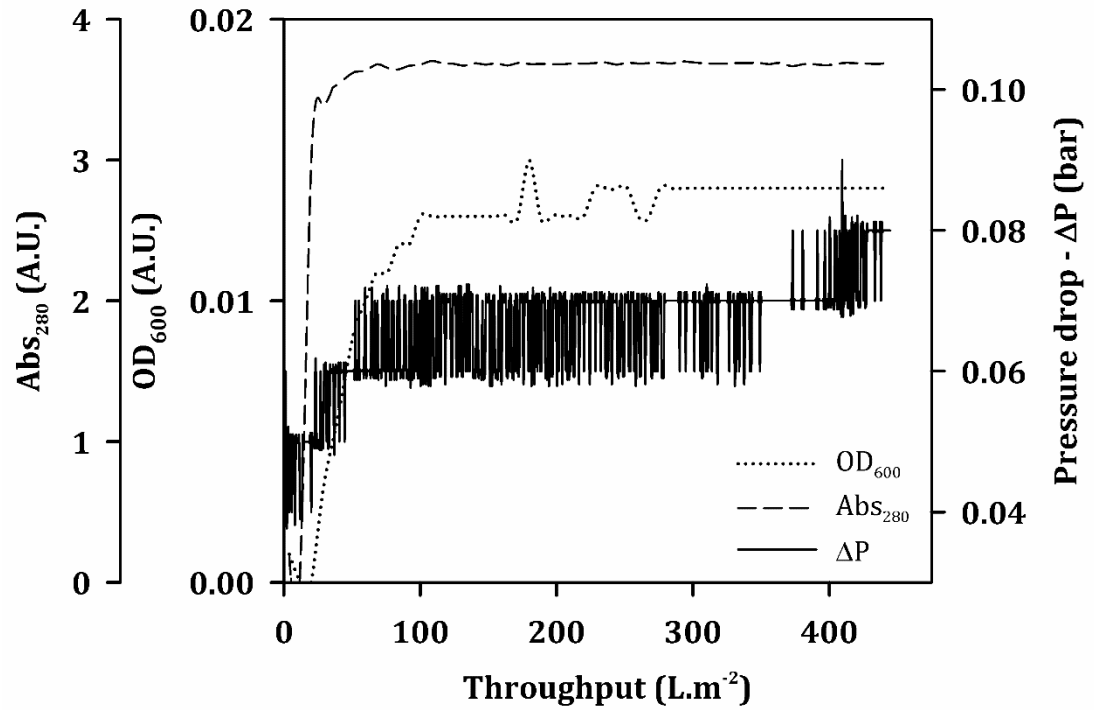

Figure 7.3. Performance of the second constant flux depth filtration stage from the non-treated primary recovery strategy.

The pooled fractions obtained from the first depth filtration stage (Figure 7.2) were immediately filtered at room temperature using a 25 cm² ZetaPlus™ BC25 capsule with 90ZA05A (3 - 0.20 µm) filter grade (3M Purification Inc.). Filtration was performed at a constant flux of 130 L.m^{-2}.h^{-1}. Fractions of 10 mL volume were manually collected to monitor the filtrate OD_{600} and Abs_{280}. The first five filtrate fractions were discarded to avoid feed dilution in the subsequent process steps. The resultant filtrate volume was pooled and stored at +4°C for < 10 hours before the subsequent sterile filtration step. Filtration was performed and monitored as described in Figure 7.2.

7.3.1.3. Sterile Filtration

Sterile filtration was stopped when ΔP reached 3 bar (see Figure 7.4). The resultant filter capacity, which was measured at a maximum ΔP of 1.4 bar, was equal to 527 L.m^{-2}. Pressure drop data was transformed and fitted with the four constant flux filtration models (i.e. pore blockage, intermediate blockage, pore constriction and cake filtration) (see Table 2.7 in Section 2.8.2). The results suggested sterile filtration was governed by a pore constriction fouling mechanism ($R^2 = 0.985$; $P < 0.01$). That is, fouling occurred within the membrane by small particles gradually reducing its effective pore size (van Reis and Zydney, 2007).

Filtrate clarification was maintained constant throughout the filtration run with a filtrate OD_{600} value of 0.013 A.U. (see Figure 7.4). Sterile filtration only achieved a reduction in filtrate OD_{600} of 0.001 A.U.. Therefore, clarification did not improve despite the ΔP data suggesting that there was particle retention. These results confirmed, as it is reported in the literature (Arnold, 2005), that it is very important to measure the evolution of ΔP during the filtration run as well as the difference in turbidity or OD_{600} between the feed material and the filtrate to assess filtration performance. Finally, Abs_{280} was constant (see Figure 7.4) and equal to the two previous depth filtration stages (see Figure 7.2 and Figure 7.3), hence suggesting similar protein content.

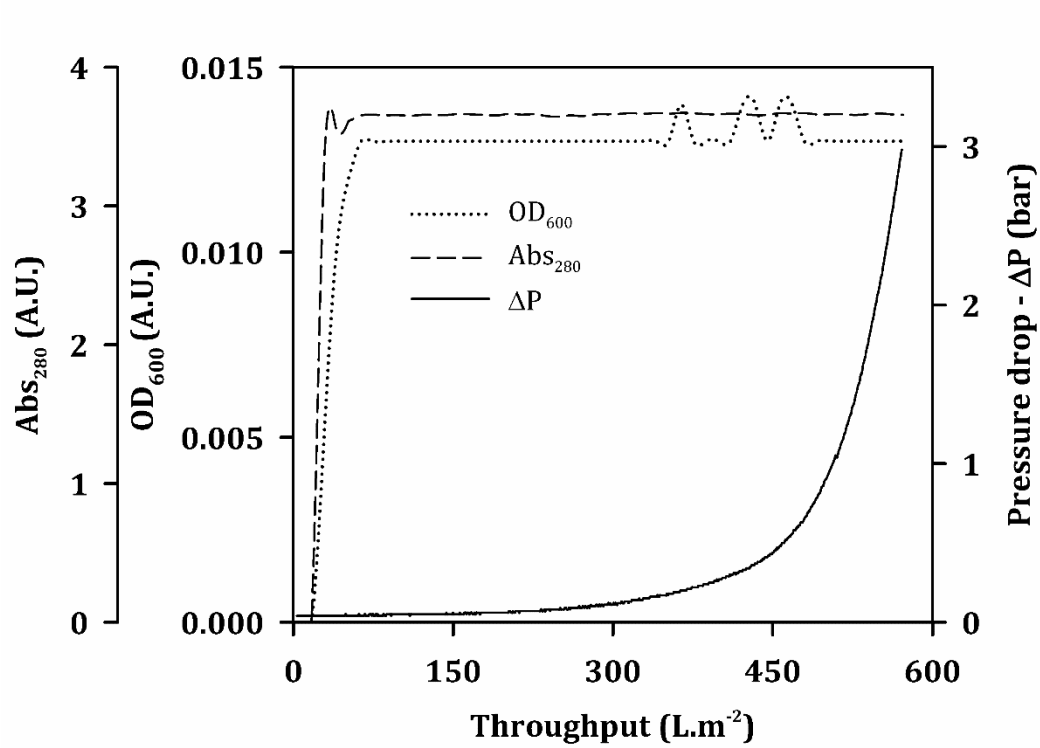

Figure 7.4. Performance of the sterile filtration step from the non-treated primary recovery strategy.

After the two depth filtration stages (Figure 7.2 and Figure 7.3), the resultant material was filtered at room temperature using a sterilising grade filter (17.3 cm^2 SartoScale Disposable Sartopore® 2 0.45/0.2 µm, Sartorius). Filtration was performed at a constant flux of 130 $L.m^{-2}.h^{-1}$. Fractions of 10 mL volume were manually collected to monitor the filtrate OD_{600} and Abs_{280}. The first five filtrate fractions were discarded to avoid feed dilution due to the presence of phosphate buffer in the dead volume of the filtration system used. The resultant filtrate volume was pooled and stored at -80°C for subsequent affinity chromatography processing. Filtration was performed and monitored as described in Figure 7.2.

7.3.2. Filtration of Flocculated Mammalian Cell Centrate

The flocculation of HCD mammalian cell centrate generated a population of particles with a wide range of diameters (see Figure 7.5). The depth filter of choice had to be able to cope with the wide range of particle sizes and the solid content generated during flocculation. Flocculated feeds have traditionally been clarified via centrifugation (Chatel et al., 2014; Habib et al., 1997; Low et al., 2007; Riske et al., 2007) and microfiltration (Aspelund et al., 2008; Karim et al., 2008; Kim et al., 2001; Wickramasinghe et al., 2002, 2004). Nonetheless, the use of normal flow depth filtration has also been reported (Buyel and Fischer, 2014; Kang et al., 2013; Singh et al., 2013).

Centrifugation followed by flocculation and a single depth filtration step was the strategy chosen (see Figure 7.1) because the approach was to develop a clarification process that would fit in the non-treated centrifugation-depth filtration strategy without the addition of any further centrifugation or filtration unit operations. Clarification of the flocculated feed was also chosen to be performed via depth filtration because of the lower investment and more flexible nature of this unit operation when compared to centrifugation (Peram et al., 2010). Furthermore, flocculated solids have been reported to stick to the walls of the centrifuge thus requiring the optimisation of the centrifuge cleaning process (Peram et al., 2010). The selection of filter media, flocculation and filtration operating conditions were explored in Chapter 6. Chapter 7 studies the process performance achieved and its impact upon the subsequent sterile filtration and capture affinity chromatography steps.

7.3.2.1. Flocculation

Flocculation was performed at a slow flocculant addition rate (8.47 $mL.min^{-1}$) to guarantee the predominance of the micromixing time scale in the flocculation vessel, which would allow the successful scale-up and scale-down of the process (see Chapter 4 and Chapter 5). The particle size distribution (PSD) of the flocs generated is shown in Figure 7.5. A monomodal distribution with particle diameters between 26 and 268 μm was obtained; the peak in percentage volume frequency occurred between 40 and 100 μm.

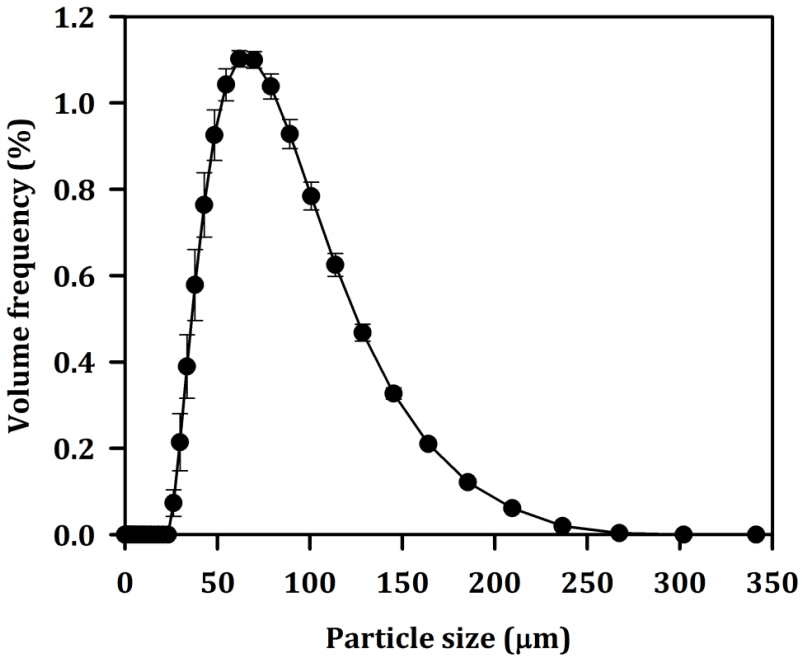

Figure 7.5. Particle size distribution of the flocculated mammalian cell centrate.

A volume of 1.50 L of HCD mammalian cell culture (peak cell count = 46.6x10^{6} cells.mL^{-1}) centrate (Q/Σ = 2.85x10^{-8} m.s^{-1}) was flocculated with PEI added at 8.47 mL.min^{-1} to a final concentration of 0.15 % w/v. Refer to Section 2.3.1 for the vessel configuration and Section 2.7.1 for the detailed flocculation methodology. After 10 minutes of floc maturation, the PSD of the flocculated material was measured as described in Section 2.11.4. Error bars represent standard deviation of six repeated measurements of the same experiment (n = 1).

7.3.2.2. Depth Filtration

A multi-layer depth filter devised for the filtration of flocculated particles with a mean size of 40 μm was used (see Section 7.2.3 for the depth filter details). The resultant ΔP, filtrate OD_{600} and Abs_{280} profiles are plotted in Figure 7.6. Pressure drop gradually increased with filtration throughput, although many fluctuations occurred during the run. Under constant flux conditions, fluctuations in ΔP have been reported to originate from the re-deposit of particle clusters created in the filter media (Burganos et al., 2001; Dave et al., 2009). These particle formations breach after a critical fouling point and re-deposit themselves within the filter. These events cause changes in the filter permeability and measurable flow re-distributions during the filtration run (Burganos et al., 2001).

The ΔP data obtained from the depth filtration run with flocculated material was transformed and fitted with the four different constant flux filtration models

(i.e. pore blockage, intermediate blockage, pore constriction and cake filtration) (see Table 2.7 in Section 2.8.2). The results suggested filtration was governed by a pore constriction fouling mechanism (R^2 = 0.963; P < 0.01), where particles gradually clogged the different media layers by reducing their effective pore size (van Reis and Zydney, 2007). Filter capacity could not be determined since the maximum ΔP of 1.4 bar was not reached during experimentation; the flocculated material was exhausted at a filtration throughput of 596 $L.m^{-2}$ when ΔP was equal to 0.73 bar. Based upon the pore constriction fouling mechanism, filter capacity was projected to be 710 $L.m^{-2}$. Nonetheless, this value can only be considered as an estimation of filter capacity at the conditions tested.

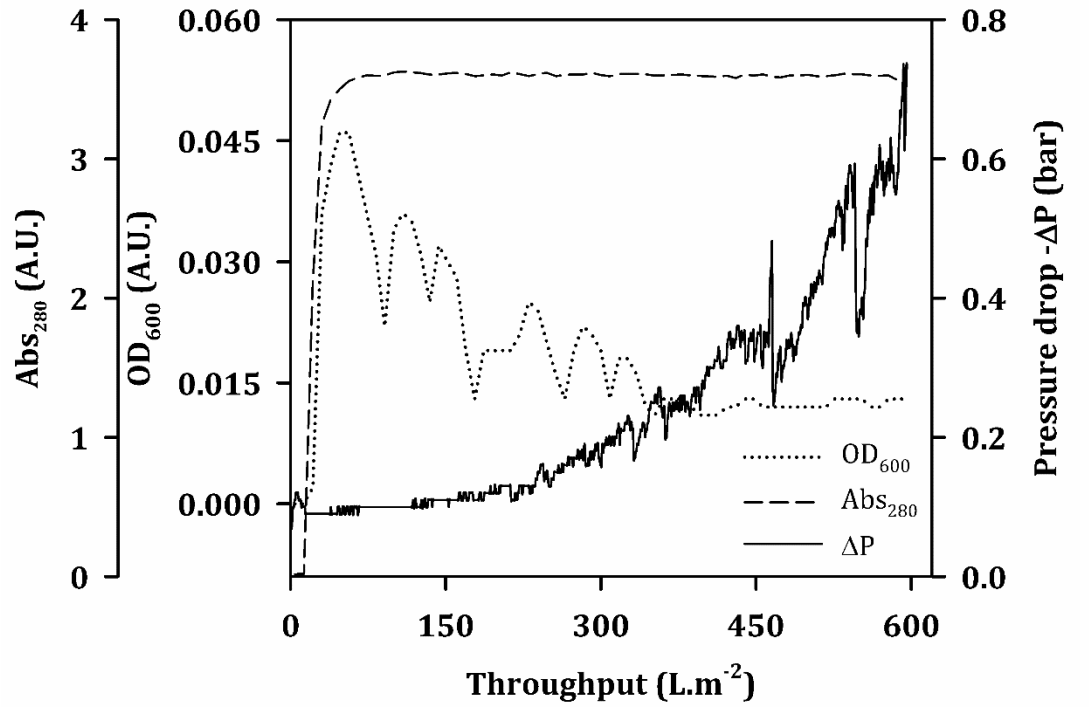

Figure 7.6. Performance of the constant flux depth filtration step from the flocculated primary recovery strategy.
A volume of 1.38 L of flocculated HCD mammalian cell centrate (see Figure 7.5) was filtered via normal flow depth filtration at a constant flux of 100 $L.m^{-2}.h^{-1}$ and at room temperature using a 23 cm^2 Clarisolve® 40MS (Millipore) filter capsule. Filtrate was manually collected in 10 mL fractions but the first five fractions were discarded to avoid feed dilution. The resultant filtrate volume was pooled and stored at +4°C for < 10 hours for subsequent sterile filtration. Filtration was performed and monitored as described in Figure 7.2.

The filtrate clarification achieved with the multi-layer depth filter improved with higher filtration throughputs (see Figure 7.6). Filtrate OD_{600} rapidly increased to 0.046 A.U. at the beginning of the filtration run, but decreased to 0.012 A.U. with higher filtration throughputs (see Figure 7.6). This clarification profile was also observed in Section 6.3.3 when using the same operating conditions with a different batch of flocculated HCD mammalian cell centrate. Filter ripening, where particulates trapped in the filter retain additional particles hence improving clarification (Zhu et al., 1996), could have occurred. Finally, Abs_{280} was maintained constant and equal to 3.6 A.U. throughout the filtration run (see Figure 7.6).

7.3.2.3. Sterile Filtration

The ΔP, filtrate OD_{600} and Abs_{280} profiles obtained with the sterile filtration step from the flocculated primary recovery strategy are plotted in Figure 7.7. Pressure drop rapidly increased to 3 bar during sterile filtration (see Figure 7.7). Filter capacity, which was calculated at a maximum ΔP of 1.4 bar, was determined to be 75.4 $L.m^{-2}$. Pressure drop fluctuations were observed at filtration throughputs exceeding 70 $L.m^{-2}$ (see Figure 7.7). The ΔP data was transformed and fitted with the four different constant flux filtration models (i.e. pore blockage, intermediate blockage, pore constriction and cake filtration) (see Table 2.7 in Section 2.8.2) to elucidate the fouling mechanism governing the filtration run. The best fit was obtained with the cake filtration model ($R^2 = 0.902$; $P < 0.01$). The transformed data showed a change in the slope of the regression line at filtration throughputs around 36 $L.m^{-2}$. This observation suggested the formation of a cake layer on the filter surface with a noticeable change in the permeability of the cake around 36 $L.m^{-2}$. These results indicated the presence of large particles in the feed material.

The OD_{600} measurements showed an initial sudden increase in OD_{600} to 0.058 A.U. followed by a gradual decline and stabilisation around 0.014 A.U. (see Figure 7.7). The gradual clarification improvement with larger filtration throughput values suggested the formation of a cake layer on the filter surface; while some large particles passed initially through the filter, those retained gradually built up a cake layer that acted as a pre-filter. Filtrate Abs_{280} remained constant throughout

the run around values of 3.6 A.U. (see Figure 7.7), hence indicating no change in the protein content with respect to the previous depth filtration step.

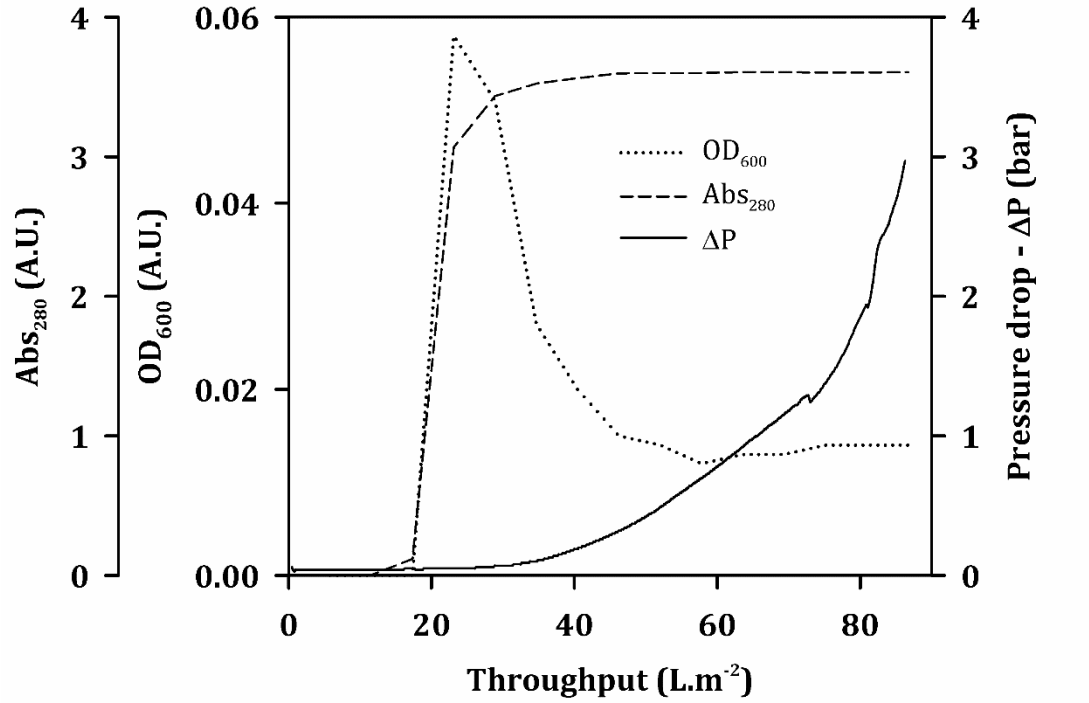

Figure 7.7. Performance of the sterile filtration step from the flocculated primary recovery strategy.
The pooled filtrate obtained from the normal flow depth filtration step (Figure 7.6) was further clarified at room temperature with a sterilising grade filter (17.3 cm² Sartopore® 2 0.45/0.2 µm, Sartorius) operated at a constant flux of 100 L.m⁻².h⁻¹. Filtrate was manually collected in 10 mL fractions. The first five fractions were discarded to avoid filtrate dilution due to the presence of phosphate buffer in the dead volume of the filtration system used. The remaining filtrate was then pooled and stored at -80°C for subsequent chromatography processing. Filtration was performed and monitored as described in Figure 7.2.

Sterile filtration was repeated three times with the same feed material (i.e. filtrate from the previous multi-layer depth filtration step). The ΔP profiles obtained from each run are plotted in Figure 7.8. Filter capacity, which was calculated at a maximum ΔP of 1.4 bar, decreased from 75.4 L.m^{-2} (first run) to 47.7 L.m^{-2} (second run) and 31.7 L.m^{-2} (third run) (see Figure 7.8); therefore, filter capacity was reduced 2.4 fold between the first and the third sterile filtration run. The feed material was filtered at room temperature within a period of < 3 hours, and no more than 90 minutes passed between the completion of two consecutive runs. During this time flocculation could have continued due to the presence of residual

PEI in the feed material. The results shown in Figure 7.8 manifested the need to further optimise flocculant concentration and mixing time during floc maturation if flocculation is to be performed in similar HCD mammalian cell cultures. The development of an analytical assay to quantify the presence of residual PEI in clarified flocculated feeds is also of interest to optimise PEI concentration during flocculation.

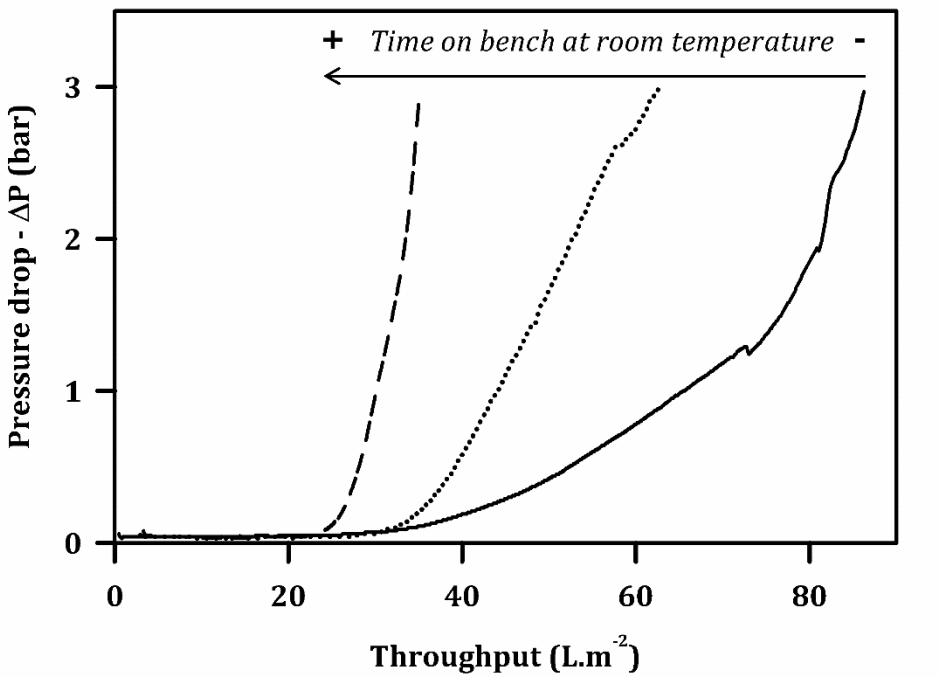

Figure 7.8. Change in the performance of the sterile filtration step from the flocculated primary recovery strategy.
Three different sterile filtration runs (— 1st run, ···· 2nd run, -- -- 3rd run) were performed with the filtrate obtained from the previous depth filtration step (see Figure 7.6). The feed material was filtered at the same conditions described in Figure 7.7 and within a period of < 3 hours. Each run was completed within 90 minutes of completing the previous sterile filtration run. Filtration was performed and monitored as described in Figure 7.2.

7.3.3. Depth and Sterile Filtration Comparison between the Non-Treated and Flocculated Strategies

The depth filters used to process the non-treated centrate were 2 cm^2 larger than the ones used to filter the flocculated centrate. To account for this difference, the ratio of volume loaded to filter area was kept constant. Nonetheless, this was only achieved during the first depth filtration stage of the non-treated stream; filtrate

volume was lost for priming and sampling during the subsequent second depth filtration and sterile filtration stages. The number of layers in the depth filters used during the non-treated strategy (dual-layer filters) were also different to those used in the flocculated strategy (8-layer filters). Since the thickness of each filter layer was not provided by the manufacturers, the volume of feed material loaded onto the filter could not be normalised by the volume of depth filter. Normalising by filter volume instead of by filter area allows the evaluation of filter media utilisation. Examples of this approach can be found in the literature (Singh et al., 2013).

The flocculated stream achieved a depth filter capacity 30 % higher than the non-treated stream (see Table 7.1); the second depth filtration stage of the non-treated stream was not considered in this calculation since pressure drop only increased by 0.08 bar thus suggesting a tighter filter media was necessary for the process studied. Larger differences in depth filter capacity can be expected between both primary clarification strategies since a filter capacity of 710 $L.m^{-2}$ was projected for the flocculated stream by the pore constriction fouling model (see Section 7.3.2). Nonetheless, this projected value must be considered an estimate as filtration throughput should not be predicted from mechanical fouling only; the exhaustion of the filter's adsorptive capacity (i.e. breakthrough), which must be tested explicitly, should be accounted for as well (Dave et al., 2009). Furthermore, more optimisation experiments are needed before a quantitative comparison between both primary recovery strategies can be made.

Sterile filtration indirectly described the capacity of the previous depth filtration steps to retain small particulates and other impurities. That is, filter retention. However, filter retention could not be accurately determined for the flocculated stream; flocculation continued taking place after floc removal by depth filtration possibly due to residual PEI still present in the filtrate (see Section 7.3.2). The flocculation conditions chosen led to a sterile filtration capacity seven times smaller in the flocculated strategy than in the non-treated strategy (see Table 7.1).

Table 7.1. Depth and sterile filter capacities experimentally calculated with the non-treated and flocculated primary recovery strategies.

	Non-treated		Flocculated	
	Throughput‡ ($L.m^{-2}$)	ΔP (bar)	Throughput‡ ($L.m^{-2}$)	ΔP (bar)
Depth filtration†	461	1.4	596	0.73
Sterile filtration	527	1.4	75.4	1.4

† First depth filtration step.
‡ Filtration throughput at the specified ΔP.

7.3.4. Affinity Capture Chromatography

Protein A chromatography was chosen as the first affinity capture step for its high selectivity for mAbs and capacity to extensively remove process-related impurities (e.g. host cell proteins (HCPs), DNA and cell culture media components) (Liu et al., 2010; Shukla and Thömmes, 2010). After the loading step, a neutral pH washing step (50 mM sodium phosphate, 250 mM sodium chloride, pH 7.0), referred to as Wash 1, was used to wash unbound HCPs and other impurities off the column (Shukla et al., 2007). Two more washes were added to improve HCP clearance (Liu et al., 2010; Shukla and Hinckley, 2008). The first one (Wash 2) was a high salt wash (50 mM sodium phosphate, 2.0 M sodium chloride, pH 7.0). The second one (Wash 3) used the same Wash 1 buffer to re-establish the neutral pH and ionic strength conditions before the elution step. Elution was performed at low pH conditions (10 mM sodium formate, pH 3.5). Finally, the column was stripped with an acidic buffer (100 mM citric acid, pH 2.1) and regenerated with 0.1 M sodium hydroxide. Figure 7.9 describes the evolution of Abs_{280} during the different chromatographic steps.

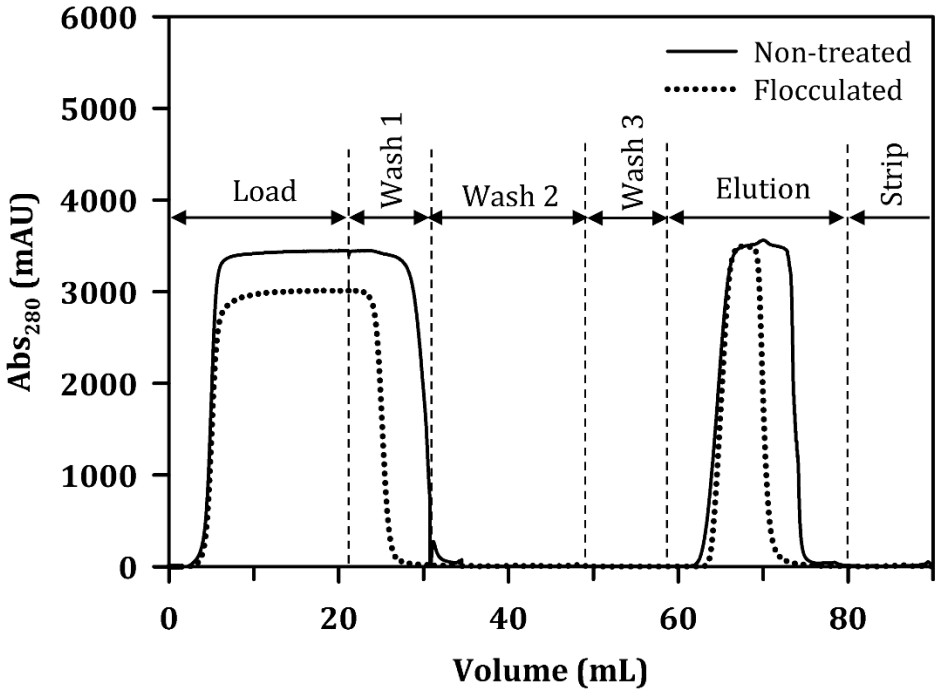

Figure 7.9. Chromatograms obtained with the non-treated and flocculated primary recovery strategies.

A volume of 20 mL of filtrate material obtained after sterile filtration (see Figure 7.4 and Figure 7.7) was loaded at a linear velocity of 200 cm.h^{-1} onto a 4.7 mL MabSelect SuRe pre-packed chromatography column (GE Healthcare). Chromatography steps consisted of (i) 2 CVs of equilibration buffer perfused at a linear velocity of 200 cm.h^{-1} (Wash 1); (ii) 4 CVs of a high salt buffer loaded at a linear velocity of 400 cm.h^{-1} (Wash 2); (iii) 2 CVs of equilibration buffer loaded at a linear velocity of 400 cm.h^{-1} (Wash 3); (iv) 5 CVs of pH 3.5 formate buffer loaded at a linear velocity of 400 cm.h^{-1} (elution); (v) 2 CVs (non-treated run) or 6 CVs (flocculated run) of pH 2.1 citric acid buffer loaded at a linear velocity of 400 cm.h^{-1}(strip). An ÄKTA avant (GE Healthcare) with in-line Abs$_{280}$ measurements and automated 2 mL fraction collection was used. Refer to Section 2.9 for the detailed chromatography methodology.

During the loading step most of the impurities flowed through the column, signalled by the elevated absorbance reading at 280 nm wavelength obtained in both the non-treated and flocculated runs (see Figure 7.9). Wash 1 reduced the absorbance practically to baseline in both chromatography runs. The flow-through signal of the flocculated run during the loading and Wash 1 steps was less intense and shorter than that of the non-treated run. Since Abs_{280} is used to continuously monitor the protein content eluted during chromatography (Noble and Bailey, 2009), the data suggested that a smaller amount of protein impurities were loaded onto the column during the flocculated run; it is also possible that the protein impurities present in the flocculated material eluted faster off the column as well. These results indicated that the flocculation and depth filtration steps from the flocculated strategy were able to remove impurities which may have a higher non-specific affinity for the product and/or the chromatographic resin (Shukla and Hinckley, 2008). This hypothesis was supported by the lower concentration of total protein, HCPs and DNA measured after flocculation (see Table 7.2), as well as the findings reported by Hogwood and co-authors (2013b). In this article, the authors described that the primary recovery strategy significantly impacted upon the HCP profile and the abundance of particular proteins in the material fed into the chromatographic stages. A small increase in Abs_{280} was observed during Wash 2 but only in the non-treated run (see Figure 7.9), possibly due to the lower content in process-related impurities of the flocculated feed. Wash 3 did not result in any noticeable Abs_{280} peak in any of the chromatography runs (see Figure 7.9) as it was only included to remove the high salt content from Wash 2.

Table 7.2. Clarification and purification performance comparison of the flocculated and non-treated primary recovery strategies.

Turbidity measurements were taken within 10 minutes after completion of each unit operation with the exception of centrifugation, which was defrosted supernatant. Yield is expressed as the cumulative yield with respect to the mammalian cell centrate. Total protein, DNA and HCP concentrations were determined with commercially available kits as described in Section 2.10.1, Section 2.10.3 and Section 2.10.4, respectively. Monoclonal antibody concentration was calculated via protein G HPLC (see Section 2.10.2). Standard deviations correspond to 3x (turbidity) and 9x (total protein, HCP, mAb, DNA) measurements where n = 1.

			Yield (%)			
	Clarification / Purification step	**Turbidity (NTU)**	**Total protein**	**HCP**	**mAb**	**DNA**
	Centrifugation	320 ± 2.00	100 (16 $g.L^{-1}$)	100 ($1.5x10^{9}$ $pg.mL^{-1}$)	100 (6.9 $g.L^{-1}$)	100 (38 $\mu g.mL^{-1}$)
Flocculated	***Flocculation (liquid phase)***	7.72 ± 0.110	88.0 ± 3.96	57.9 ± 2.46	105 ± 3.48	0.118 ± 0.005
	Depth filtration	5.13 ± 0.031	85.8 ± 3.99	59.0 ± 2.91	105 ± 1.34	0.118 ± 0.012
	Absolute filtration†	5.07 ± 0.096	81.1 ± 2.73	55.0 ± 2.08	102 ± 2.64	0.106 ± 0.014
	Protein A chromatography	--	40.4 ± 1.87	0.044 ± 0.007 (106 ± 17 ppm)	91.4 ± 3.71	0.080 ± 0.007
Non-treated	***1st Depth filtration***	14.5 ± 0.000	93.4 ± 3.40	103 ± 13.0	104 ± 2.67	36.8 ± 1.42
	2nd Depth filtration	11.2 ± 0.058	95.6 ± 3.97	111 ± 17.1	99.6 ± 1.92	31.7 ± 2.33
	Absolute filtration	7.95 ± 0.000	94.6 ± 3.46	93.0 ± 10.6	101 ± 5.31	30.2 ± 2.32
	Protein A chromatography	--	40.2 ± 1.84	0.066 ± 0.008 (171± 21 ppm)	85.0 ± 9.77	0.085 ± 0.005

†Only the first absolute filtration run is considered.

The elution peaks of the non-treated and flocculated runs (Figure 7.9) differed in width but not in height. It is possible that the maximum signal detectable by the chromatographic system was reached and no differences in signal intensity were measurable. The larger peak width in the non-treated run (see Figure 7.9) described that the product took more CVs to elute than in the flocculated run. Also, the flocculated elution peak was sharper and more symmetrical than that of the non-treated peak (see Figure 7.9). The mAb results summarised in Table 7.2 confirmed there was no difference in product yield between the non-treated and flocculated eluates. However, the HCP content in the non-treated eluate was larger than in the flocculated eluate (see Table 7.2). The greater protein content of the non-treated eluate would have led to differences in peak intensity, which could not be observed (see Figure 7.9) possibly due to the fact that the maximum signal intensity of the chromatographic system was reached.

The low pH conditions used during the elution step often result in the precipitation of the product species and/or process-related impurities (e.g. HCPs) that have persisted protein A purification when followed by pH neutralisation (Gagnon et al., 2014; Kandula et al., 2009; Shpritzer et al., 2006; Shukla and Hinckley, 2008; Shukla and Thömmes, 2010; Shukla et al., 2005, 2007; Yigzaw et al., 2006). The solid particulates formed in consequence result in eluates with elevated turbidity that reduce the lifetime of the chromatographic column and pose filtration challenges post-protein A chromatography (Kandula et al., 2009; Shpritzer et al., 2006; Shukla et al., 2005; Yigzaw et al., 2006). Turbid elution fractions were obtained in the non-treated run (see Figure 7.10.). The mAb step yield values for chromatography were the same for both streams (see Table 7.2), hence suggesting the solid particulates observed in the non-treated eluate could have been HCP impurities; this hypothesis was later confirmed via the mass spectrometry studies discussed in Section 8.3.2. These results proved the use of feed pre-treatment methodologies such as flocculation during primary recovery can have a positive effect on the control of impurities as well as on process economics (e.g. longevity of the protein A chromatography column (Kandula et al., 2009; Shukla et al., 2005) and no need for a depth filtration step after protein A chromatography).

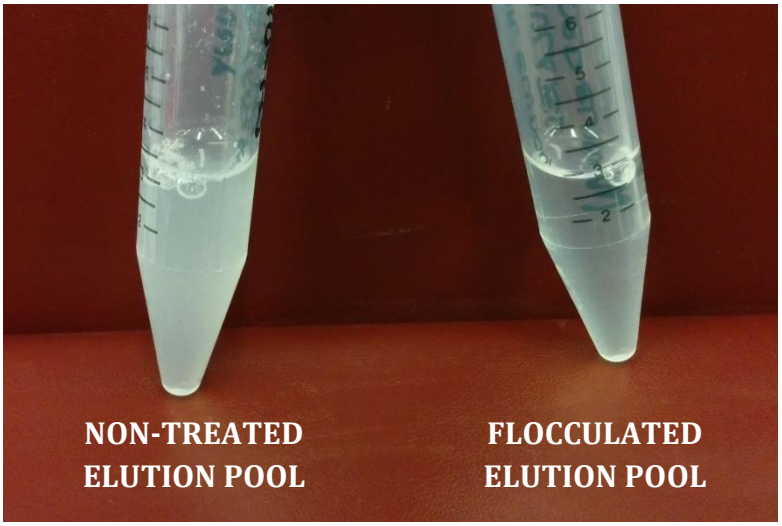

Figure 7.10. Turbidity differences in the chromatographic elution pool of the non-treated and flocculated primary recovery strategies.

7.3.5. Clarification and Purification Performance Comparison between the Non-Treated and Flocculated Strategies

The clarification performance of each unit operation was analysed via turbidity measurements. Purification was assessed in terms of total protein, mAb, HCP and DNA content. Mass balances were calculated to account for differences in the processed volume and were used to determine process yield; a starting yield of 100 % was assumed for the HCD mammalian cell centrate. Results are summarised in Table 7.2.

7.3.5.1. Turbidity

The turbidity of the centrate was 320 ± 2.00 Nephelometric Turbidity Units (NTU) (see Table 7.2). As mentioned in Section 7.3.1, freeze-thawing the centrate could have generated larger solid particles formed by smaller ones coming together that resulted in increased turbidity values. Nonetheless, such high turbidity readings for centrifuged mammalian cell broths have been reported (McNerney et al., 2012). Flocculation reduced the turbidity of the centrate by 41 fold (see Table 7.2). As discussed in Section 7.3.2, flocculation conditions were not optimal hence greater turbidity reductions might be achievable. After multi-layer depth filtration, turbidity had been decreased 62 times from the starting centrate turbidity (see Table 7.2). However, sterile filtration did not have

any effect upon filtrate clarification. With regards to the non-treated process, the first dual-layer depth filter reduced the centrate turbidity by 22 fold (see Table 7.2). After a second dual-layer depth filtration stage and sterile filtration, turbidity was 40 times lower than the centrate turbidity (see Table 7.2). Nonetheless, a greater clarification performance could have been achieved had a tighter filter media being chosen for the second depth filtration stage (see Section 7.3.1).

Both primary recovery strategies greatly improved centrate clarification. But turbidity reduction was mainly achieved by the first step of the primary recovery strategies studied. That is, by flocculation (flocculated strategy) and by the first dual-layer depth filtration stage (non-treated strategy). Depth and sterile filtration contributed to further remove the particulate content. At the end of primary recovery, the clarification performance achieved by both strategies were very similar since turbidity only differed by 2.88 NTU (see Table 7.2). Although this result could change with the optimisation of flocculation and depth filtration unit operations.

7.3.5.2. Total Protein, HCP and mAb Content

The total protein concentration in the centrate was 16 $g.L^{-1}$. Flocculation achieved a reduction in total protein content of 12 % (see Table 7.2). The mAb quantification data suggested there was no product loss during the flocculation step, but the HCP data showed a reduction in the HCP content of 42 % after flocculation (see Table 7.2). These results corroborated the reported ability of PEI to flocculate the HCPs present in centrifuged mammalian cell feedstocks at neutral pH conditions (Peram et al., 2010). With regards to the non-treated stream, the first depth filtration stage reduced the total protein content by 6.6 %, but according to the mAb data no product loss occurred (see Table 7.2). Therefore, protein reduction was attributed to HCP removal by the depth filter adsorptive properties (Yigzaw et al., 2006). Total protein content continued to gradually decrease with depth and sterile filtration in both primary recovery strategies (see Table 7.2). Yet it was affinity chromatography the unit operation that led to the highest reduction in total protein content, with 41 % decrease in

the flocculated process and 54 % in the non-treated process with respect to the previous unit operation (see Table 7.2).

Capture protein A chromatography was the purification workhorse of the non-treated process for reducing the centrate HCP content by 99.9 % (see Table 7.2). The HCP concentration of the non-treated eluate was $2.55x10^6$ pg.mL^{-1}. This value was in accordance with the HCP concentration in the protein A chromatography eluate reported by Hogwood and co-authors (2013b), where the primary recovery strategy chosen for a mAb process was disc-stack centrifugation followed by depth filtration. However, it is possible that the HCP content was higher than the reported by the immunoassay considering there was a large fraction of precipitated proteins (see Figure 7.10. and Section 8.3.2), which might have not been recognised, thus quantified, by the immunoassay antibodies. With regards to the mAb content, HCP concentration in the protein A eluate was 171 ± 21 parts per million (ppm) (i.e. nanograms of HCP per milligrams of mAb). The concentration of HCPs in the protein A eluate of a generic industrial mAb process have been reported to range between 50 and 500 ppm (Müller-Späth and Morbidelli, 2014). Nonetheless, HCP levels between 2,000 and 50,000 ppm have also been encountered (Wang et al., 2009). The HCP data showed that the first and second depth filtration stages of the non-treated process achieved a maximum HCP reduction of 6 % (see Table 7.2). It is possible that HCP removal could be enhanced by optimising the depth filter adsorptive properties (Yigzaw et al., 2006). With regards to the flocculated primary recovery strategy, flocculation decreased the centrate HCP content by 42 %, which continued decreasing during the depth and sterile filtration steps (see Table 7.2). The flocculation primary recovery strategy led to a process where (i) the impurity load passed onto the chromatography column had been significantly reduced; and (ii) the purification performance achieved post-protein A chromatography was higher than that of the non-treated stream since HCP concentration was $1.34x10^6$ pg.mL^{-1} and HCP to mAb content 106 ± 17 ppm (see Table 7.2). Reduced impurity loads have an important positive effect upon the longevity of the protein A column (Hogwood et al., 2013b; Yigzaw et al., 2006) as well as on the post-protein A sterile filtration step by preventing the aggregation and co-elution of HCPs with the product (see Figure 7.10. and Section 8.3.2). Therefore,

flocculation can improve process performance as well as process economics by reducing production costs.

The mAb quantification data showed there was no product loss during the primary clarification steps of the flocculated and non-treated strategies (see Table 7.2). However, mAb yield decreased between 5 and 25 % during affinity chromatography. The column was loaded to the dynamic binding capacity specified by the manufacturer, and the washing steps had been optimised for the capture of the IgG_4 used. Product loss could be explained by excessive mAb being loaded onto the column and, to some extent, due to product aggregation occurring during low pH elution (see Section 7.3.4).

7.3.5.3. DNA Content

In the flocculated primary recovery strategy, flocculation reduced the DNA content in the centrate by 99.88 % (see Table 7.2). The efficacy of PEI to remove DNA from complex biological samples has been reported in the literature (Cordes et al., 1990; Milburn et al., 1990; Salt et al., 1995). The multi-layer depth filter used did not further decrease the DNA content, but sterile filtration did (see Table 7.2). It is thought that flocculation continued taking place after depth filtration thus further flocculating DNA molecules before sterile filtration (see Section 7.3.2). Finally, protein A chromatography achieved an additional 25 % reduction with respect to the pre-column's DNA content, making it a total decrease in the centrate DNA content of 99.92 % (see Table 7.2).

With regards to the non-treated process, the first depth filtration stage decreased the centrate DNA content by 63 % (see Table 7.2). The second depth filter contributed to a further 5 % reduction. A greater decrease in the DNA content was expected since the filter media used was positively charged, thus it was able to trap DNA molecules via electrostatic and hydrophobic interactions (Liu et al., 2010). Sterile filtration did not reduce the DNA content, but protein A affinity chromatography achieved the same DNA purification level as the flocculated stream (see Table 7.2).

7.4. Conclusions

The flocculated primary recovery strategy proposed in Chapter 6, which consisted of a centrifugation step followed by flocculation and depth filtration, was compared in Chapter 7 to a platform primary recovery design constituted of a centrifugation step followed by two depth filtration stages. A summary of the key findings based on the aims and objectives for Chapter 7 is as follows:

1. Assess at laboratory scale the effect of introducing a flocculation step after centrifugation upon the performance of the primary recovery and capture chromatography processes.

The data presented in this chapter provides an insight as to how the choice of primary recovery unit operations can significantly impact upon the purification steps and process economics. The proposed process conditions showed flocculation had great capacity for cell debris, HCP and DNA removal. Multi-layer depth filtration offered larger filter capacities than the ones achieved by the dual-layer depth filters used in the non-treated primary recovery strategy. However, flocculation was the step shown to achieve the greatest clarification and purification improvement pre-protein A chromatography. In conclusion, the results showed that introducing a flocculation step in the primary recovery process can extend the chromatography column lifetime and reduce the post-protein A sterilising grade filter area.

2. Evaluate at laboratory scale the possibility of replacing the mAb platform primary recovery strategy (i.e. centrifugation followed by two depth filtration stages) by the flocculated primary recovery strategy (i.e. centrifugation followed by flocculation and depth filtration).

Further process optimisation studies are necessary both in the flocculated and non-treated primary recovery streams before a decision over one of the two strategies can be made. However, considerations that go beyond process performance need to be included to decide which clarification technologies to use. Cost of goods to manufacture, capital expenditure (e.g. piping reconfiguration, new equipment purchase), scale-up know-how, new equipment

validation and other implementation requirements contribute to the decision of whether to implement a clarification technique besides its clarification performance (Felo et al., 2013).

8. Proteomic Analysis of Protein A Chromatography Eluates

8.1. Introduction and Aims

Host cell proteins (HCPs) are critical process-related impurities encountered in the production of biopharmaceuticals as they pose an immunogenicity risk to patients (Wang et al., 2009). Before the administration of therapeutic monoclonal antibodies (mAbs) to patients, HCPs need to be removed to acceptable levels, typically < 100 parts per million (ppm) (i.e. nanograms of HCP per milligrams of mAb) (Chollangi et al., 2015; Hogwood et al., 2014; Thompson et al., 2014). The quantitative assessment of HCPs investigates the impact that unit operations and process conditions have on the HCP content, but does not allow the identification of specific HCPs (Hogwood et al., 2014; Thompson et al., 2014). Host cell protein identification improves the downstream processing (DSP) knowledge (Hogwood et al., 2013a, 2014), and therefore supports knowledge-based process decisions that can result in reduced DSP costs, which account for ~80 % of the total mAb production costs (Hogwood et al., 2013a).

The choice of depth filter media during secondary clarification has been shown to impact upon the abundance and profile of HCPs post-protein A chromatography (Hogwood et al., 2013b). Chapter 7 showed that the introduction of a flocculation unit operation as part of the primary recovery strategy of a mAb process reduced the abundance of HCPs post-protein A chromatography. The aim of this chapter was to investigate whether the choices of primary recovery studied in Chapter 7 had also changed the HCP profile post-protein A chromatography; this was achieved by comparing the HCP profiles of the protein A eluates from the non-treated and flocculated streams (see Figure 7.1). The mAb content in the protein A eluate samples was first depleted to increase the sensitivity and resolution for HCPs (Thompson et al., 2014), which were in lower abundance. The HCP profiles of the protein A eluate samples were then analysed via sodium dodecyl sulphate polyacrylamide gel electrophoresis (SDS-PAGE), and by combining the liquid chromatography-mass

spectrometry/mass spectrometry (LC-MS/MS) technique with bioinformatic tools.

Summary of the chapter's aims and objectives:

1. Investigate whether flocculation during primary recovery can modify the HCP profile post-protein A chromatography.

8.2. Experimental Set-up

8.2.1. SDS-PAGE

The protein A chromatography eluates from the non-treated (i.e. non-flocculated) and flocculated streams in Chapter 7 (see Figure 7.1) were studied via polyacrylamide gel electrophoresis under reducing conditions as described in Section 2.10.5. The gel was stained using a Coomassie based staining solution.

8.2.2. LC-MS/MS

8.2.2.1. Depletion of mAb Content in Protein A Chromatography Eluate Samples

A schematic diagram of the sample preparation procedure performed before LC-MS/MS analysis is shown in Figure 8.1. The protein A eluates, which were stored at -20°C, were thawed at room temperature. The non-treated protein A eluate was centrifuged (Eppendorf 5180R, Eppendorf, Hamburg, Germany) for 5 minutes at 200 rps using the FA-45-6-30 rotor (45° angle) to separate the soluble fraction from the solid particulates present in the eluate (see Figure 8.1). While the particulates, which constituted the 'solids fraction', were directly analysed via LC-MS/MS, the 'soluble fraction' was further processed to depleat the mAb content in the sample. A 3 mL volume of 'soluble fraction' was pipetted into a Vivaspin®6 centrifugal concentrator (Sartorius Stedim, Göttingen, Germany) with a molecular weight cut-off (MWCO) filter of 100 kDa. The 'soluble fraction' was then centrifuged (Eppendorf 5180R, Eppendorf, Hamburg, Germany) for 10 minutes at 6000 g using a fixed 45° angle rotor (FA-45-6-30 rotor); any molecules with a molecular weight (MW) larger than 100 kDa (i.e. mAb molecules) were retained by the filter, while smaller molecules were

filtered out. The clear protein A chromatography eluate obtained with the flocculated primary recovery strategy (see Figure 8.1) was indicative of no solid particulates present in the sample. Consequently, 3 mL of flocculated protein A eluate were directly pipetted into a Vivaspin®6, 100 kDa MWCO centrifugal concentrator to deplete the sample from the high amounts of mAb present; the centrifugation conditions were these used for the non-treated 'soluble fraction'.

8.2.2.2. Sample Preparation and LC-MS/MS Analysis

The mAb-depleted flow-through fractions obtained from concentrating the non-treated 'solube fraction' and the flocculated protein A eluate (see Figure 8.1 and Section 8.2.2.1) were precipitated with acetone as described in Section 2.10.6 before LC-MS/MS analysis. The 'solids fraction' from the non-treated protein A eluate (see Figure 8.1) did not require acetone precipitation before LC-MS/MS analysis. The three samples were analysed via LC-MS/MS as detailed in Section 2.10.6.

8.2.2.3. Protein Sequence Search

Protein sequence searches were performed against the SwissProt/UniProt data base on the 19th of February 2016 as described in Section 2.10.6; the protein sequence data base contained a total of 60,971,489 entries that date. The results were split in two groups according to the Mascot score obtained. Whilst those above the identity threshold indicated identity or extensive homology (ANOVA $P < 0.05$), those below the threshold denoted tentative identifications. The protein's sequence coverage, MW and calculated pI were obtained from the Mascot search results. The protein's biological and molecular functions were investigated with peer-reviewed publications and by searching in the UniProt website (www.uniprot.org) using the accession number obtained during the protein sequence searches.

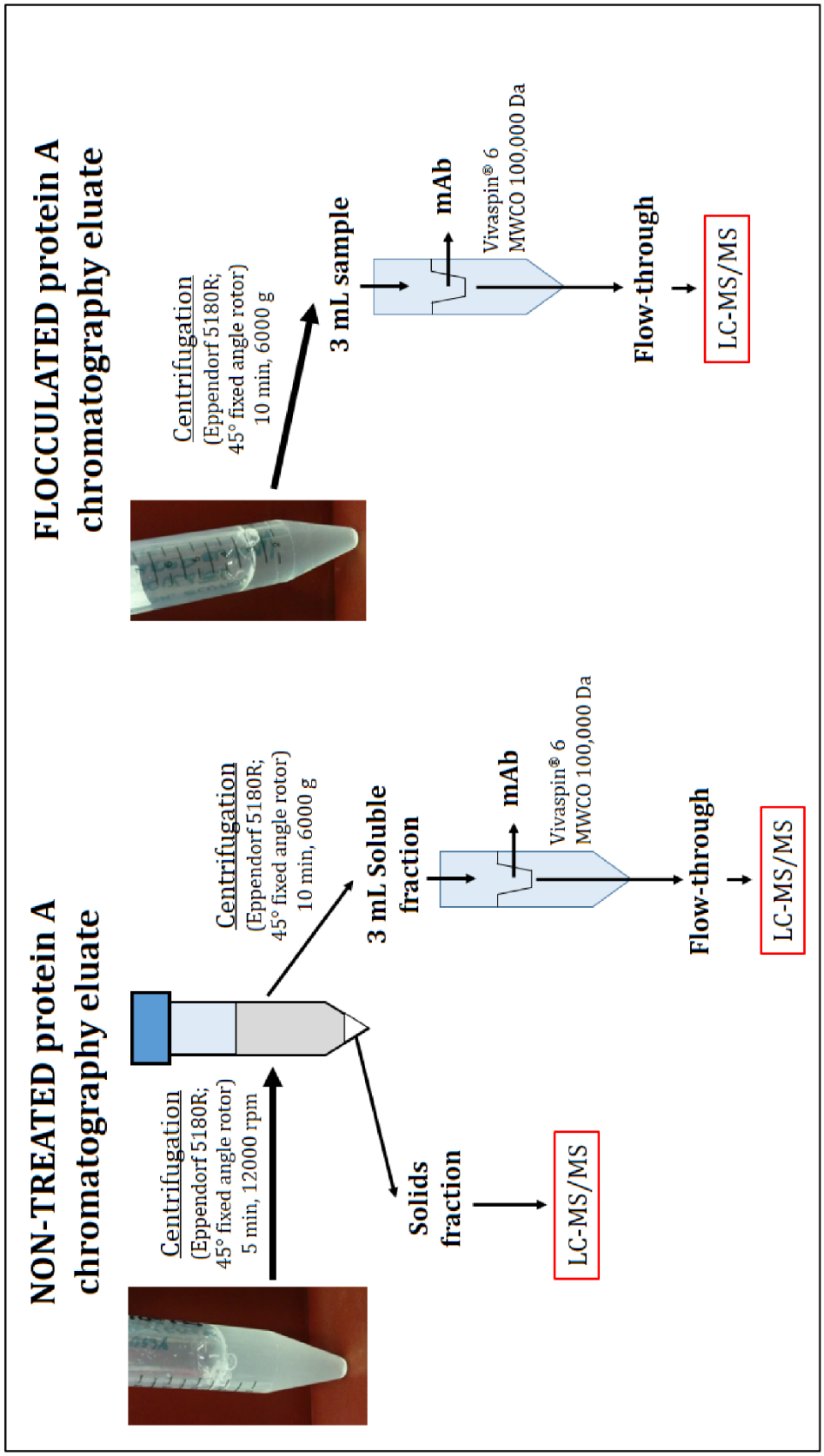

Figure 8.1. Schematic diagram of monoclonal antibody depletion from protein A chromatography eluate samples before LC-MS/MS analysis.

8.3. Results and Discussion

8.3.1. SDS-PAGE Analysis

The protein profiles of the protein A chromatography eluates obtained from the flocculated and non-treated primary recovery strategies studied in Chapter 7 (see Figure 7.1) were first evaluated via polyacrylamide gel electrophoresis. The gel was stained with InstantBlue™ protein stain, a Coomassie based dye of high sensitivity (5 – 25 ng of protein per band), to detect differences in the protein content between the two samples. However, protein quantification of the electrophoretic bands was not intended thus no calibration curves were included.

Figure 8.2 shows the protein bands obtained during gel electrophoresis under reducing conditions. Two overloaded protein bands (number 5 and 9) in both the flocculated and the non-treated protein A eluate samples were observed (see Figure 8.2). These corresponded to the heavy chain (MW = 50 kDa; band number 5) and light chain (MW = 25 kDa; band number 9) of the recombinant mAb, which was present in large amounts (see the initial/centrate mAb concentration in Table 7.2). Other protein bands with higher and lower MWs were observed on the gel (see Figure 8.2), which confirmed the co-elution of protein impurities with the mAb. Protein A chromatography has been reported to remove > 99 % of the impurities present in the feed stream (Follman and Fahrner, 2004). However, HCPs co-elute with the mAb at the low pH elution conditions used due to non-covalent interactions (i.e. electrostatic, hydrophobic and hydrogen bonds) with the mAb (Chollangi et al., 2015; Gagnon et al., 2014; Levy et al., 2014; Nogal et al., 2012; Shukla and Hinckley, 2008; Sisodiya et al., 2012; Tarrant et al., 2012), as well as with the chromatographic resin (Gagnon et al., 2014; Hogwood et al., 2013b; Shukla and Hinckley, 2008; Tarrant et al., 2012). These interactions, which depend upon the chromatographic resin (Sisodiya et al., 2012; Tarrant et al., 2012) and the protein sequence of the mAb (Levy et al., 2014; Nogal et al., 2012; Sisodiya et al., 2012), can be disrupted by the presence of additives in the post-load washing steps (Chollangi et al., 2015; Shukla and Hinckley, 2008; Sisodiya et al., 2012). However, further chromatographic steps are necessary to achieve the purity levels required for the administration of

therapeutic mAbs to patients (Chollangi et al., 2015; Liu et al., 2010; Shukla et al., 2007).

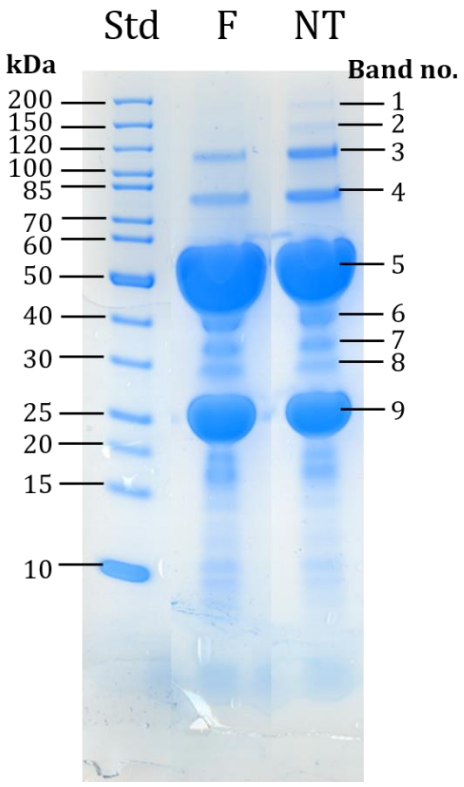

Figure 8.2. SDS-PAGE of the flocculated and non-treated protein A chromatography eluates.
Gel electrophoresis was performed under reducing conditions as described in Section 2.10.5. The gel was stained with InstantBlue™ protein staining solution (see Section 2.10.5). The same total protein concentration of sample (12.9 g.L^{-1}) was loaded in the wells. Sample loading was performed in the same gel but not in consecutive lanes to avoid cross-contamination. A commercial protein standard (see Section 2.10.5), referred to as 'Std' in the figure, was loaded in the first lane; the molecular weight values, expressed in kDa, are detailed in the figure. The samples studied were the protein A chromatography eluates obtained with the flocculated (F) and non-treated (NT) primary recovery strategies described in Figure 7.1. Gel images were obtained as detailed in Section 2.10.5.

Feed conditioning strategies used on mammalian cell culture fluids pre-protein A chromatography have been shown to reduce (i) the impurity load passed onto the chromatographic step; and (ii) the co-elution of process-related impurities with the mAb (Chollangi et al., 2015; Gagnon et al., 2014). In order to evaluate whether the flocculated primary recovery strategy minimised the co-elution of HCPs with the mAb, the intensity of the defined protein bands observed on the gel for the flocculated and non-treated protein A eluates (see Figure 8.2) were compared. Table 8.1 shows the areas (expressed in absolute terms) obtained for

each defined protein band, and the increase or decrease in band intensity achieved with the flocculated strategy. The protein bands 1 to 4 in Figure 8.2 showed the flocculated primary recovery strategy reduced the content of high MW proteins (MW > 70 kDa) by half or completely (i.e. no visual protein band) (see Table 8.1). The protein bands with MWs between 40 and 25 kDa were not always less intense in the flocculated eluate; band number 8 was 34 % more intense in the flocculated than in the non-treated eluate (see Table 8.1). With regards to the mAb, the intensity of the mAb heavy and light chain protein bands (band number 5 and 9, respectively) were higher in the flocculated than in the non-treated eluate; the increase in protein band intensity for the flocculated mAb heavy and light chains were 17 and 5 %, respectively (see Table 8.1). Gel electrophoresis was performed loading the same total protein concentration per sample. Because the initial total protein concentration was larger in the non-treated than in the flocculated protein A eluates (16.21 $g.L^{-1}$ versus 12.91 $g.L^{-1}$, respectively), the non-treated eluate had to be diluted before loading the gel thus explaining the lower mAb content in this sample.

Table 8.1. Protein band intensity comparison between the flocculated and the non-treated protein A chromatography eluates analysed via SDS-PAGE. *Protein band intensity analysis was performed in ImageJ v. 1.47 with the gel image shown in Figure 8.2. First, the intensity profile along the gel lane was obtained for the flocculated and non-treated protein A chromatography eluates. Then, the area of the well-defined intensity peaks, thus well-defined protein bands, was measured using the software; the area under the peak given by the software is an absolute value. Band number is as detailed in Figure 8.2.*

Band number	**Flocculated area** (absolute value)	**Non-treated area** (absolute value)	**Flocculation effect**
1	No band	289.87	-
2	No band	474.60	-
3	1841.3	4704.7	-60.9 %
4	2616.6	4914.8	-46.8 %
5	53742	45769	+17.4 %
6	2049.5	2471.8	-17.1 %
7	1006.4	985.48	+2.12 %
8	945.26	704.36	+34.2 %
9	23224	22133	+4.93 %

Finally, the solid particulates present in the non-treated protein A chromatography eluate (see Figure 8.1) were re-dissolved and migrated through the gel in the reducing conditions used during SDS-PAGE analysis; no band was observed at the top of the gel hence indicating the absence of large insoluble proteins (see Figure 8.2).

8.3.2. LC-MS/MS Analysis

The non-treated and flocculated protein A chromatography eluates were analysed via LC-MS/MS to (i) investigate the nature of the solid particulates contributing to the turbidity of the non-treated protein A eluate (see Figure 8.1); and (ii) compare if the two primary recovery strategies studied in Chapter 7 (i.e. centrifugation-depth filtration *versus* centrifugation-flocculation-depth filtration; see Figure 7.1) resulted in a different HCP profile post-protein A chromatography. To increase the sensitivity of the LC-MS/MS technique for HCPs that might be in low concentration, the mAb content in the protein A chromatography eluates was depleted as shown in Figure 8.1.

The protein searches performed with the mass spectrometry results obtained after LC-MS/MS analysis were not exclusively limited to the Chinese hamster (*Cricetulus griseus*) proteome. Rather, the search was extended to the mouse (*Mus musculus*), rat (*Rattus novergicus*) and human (*Homo sapiens*) proteomes to include homologous proteins in the search. The protein search results (Table 8.2 to Table 8.4) showed the protein sequence coverage values obtained ranged from 1 to 64 %; however, the maximum protein sequence coverage value for an HCP was 11 %. The short protein sequence coverage values obtained for HCPs might have been due to (i) their low concentration in the protein A eluate samples analysed; (ii) protein degradation occurring during sample storage at -20°C as a result of enzymatic and/or non-enzymatic cleavage (Cordoba et al., 2005); and/or (iii) a non-optimal trypsin digestion step used as part of the LC-MS/MS protocol to prepare the samples for analysis. The protein search results were not analysed based on the protein sequence coverage values since the MW and concentration of the protein must be also considered. Instead, the protein search

results were evaluated based upon the proteins' homology to one of the four proteomes searched against.

The protein search results for the 'solids fraction' of the non-treated protein A chromatography eluate (see Figure 8.1) showed the solid particulates were constituted of HCPs and IgG (i.e. mAb) fragments (see Table 8.2). A total of 14 HCPs were identified in the 'solids fraction', although only 7 of these were protein identities or proteins identified with extensive homology. Their theoretical MW values ranged from 177 to 13.9 kDa, with the majority being < 80 kDa (see Table 8.2). With regards to their pI, more than half of the HCPs identified were acidic (i.e. pI < 7.0) (see Table 8.2). The HCPs obtained from harvested Chinese hamster ovary (CHO) cell culture fluids have been reported to tend towards acidic and low to mid-molecular weight proteins (i.e. MW < 75 kDa) (Jin et al., 2010). Published two-dimensional gel electrophoresis images of intracellular proteins obtained from cultured CHO cells also showed some degree of bias towards acidic pI values (Champion et al., 1999). The presence of IgG fragments in the 'solids fraction' could have been triggered by their co-elution with the mAb due to non-specific interactions with HCPs and/or with the resin (Gagnon et al., 2014; Hogwood et al., 2013b; Shukla and Hinckley, 2008; Tarrant et al., 2012). Then, these IgG fragments could have precipitated during the subsequent pH neutralisation step (Kandula et al., 2009; Shukla et al., 2005) or during the low pH elution conditions in protein A chromatography (Shukla et al., 2005).

The numerous HCPs identified in the 'solids fraction' of the non-treated protein A chromatography eluate (Table 8.2) differed from the results obtained in the mAb-depleted non-treated and flocculated protein A eluates (see Table 8.3 and Table 8.4, respectively). The main proteins identified in the mAb-depleted samples were mAb fragments. The mAb fragments could have co-eluted with the product due to non-covalent interactions with the mAb (Chollangi et al., 2015; Gagnon et al., 2014; Levy et al., 2014; Nogal et al., 2012; Shukla and Hinckley, 2008; Sisodiya et al., 2012; Tarrant et al., 2012) and/or with the resin (Gagnon et al., 2014; Hogwood et al., 2013b; Shukla and Hinckley, 2008; Tarrant et al., 2012). Antibody fragments could have also resulted from mAb fragmentation in the IgG's

hinge region during sample storage at -20°C (Cordoba et al., 2005). Only one HCP was identified with extensive homology in the mAb-depleted non-treated and flocculated protein A eluates; this HCP was in both cases ubiquitin carboxyl-terminal hydrolase 30, or USP30 (see Table 8.3 and Table 8.4). This HCP of 59 kDa had a calculated pI value of 8.8 (see Table 8.3 and Table 8.4), and therefore was positively charged at the neutral pH conditions at which flocculation was conducted when using the cationic flocculant polyethylenimine (see Section 7.2.3). USP30 co-eluted with the product possibly as a result of non-covalent interactions with either the protein A resin or the mAb. Finally, one tentative HCP was identified in the mAb-depleted non-treated eluate (see Table 8.3) and none in the mAb-depleted flocculated eluate (see Table 8.4).

The greater number of HCPs identified via LC-MS/MS in the non-treated protein A chromatography eluate when compared to the flocculated eluate was in line with the HCP quantification results reported in Section 7.3.5 and in Table 7.2. The immunoassay results showed the HCP content in the non-treated protein A pooled eluate was higher than in the flocculated protein A pooled eluate; the HCP content was 2.02×10^7 pg and 1.34×10^7 pg, respectively. Nonetheless, it is possible that the HCP content in the non-treated sample was higher than that reported by the immunoassay considering there was a large fraction of precipitated proteins (see Table 8.2); these precipitates might have not been recognised, thus quantified, by the immunoassay antibodies due to the fact that the protein's three-dimensional conformation is lost when precipitation occurs (Mathews et al., 2000). Furthermore, it has been reported that histones, one of the tentative HCPs identified in the solids fraction of the non-treated protein A eluate (see Table 8.2), are not easily detected by the common immunoassay procedures used for HCP quantification (Gagnon et al., 2014). If this was the case for the immunoassay used in this thesis (see Section 2.10.4), the actual HCP content in the non-treated protein A eluate might have been higher than the quantitative value experimentally reported.

Table 8.2. Host cell protein identification in the solids fraction of the non-treated protein A chromatography eluate via LC-MS/MS analysis.

Host cell proteins were identified via LC-MS/MS analysis as detailed in Section 2.10.6. The solids fraction of non-treated protein A chromatography eluate was prepared as shown in Figure 8.1. Protein sequence searches were performed against the SwissProt online protein database; search parameters were as detailed in Section 2.10.6. Protein nominal mass and pI values were given by the Mascot search results. Proteins with Mascot score values above the identity threshold indicate identity or extensive homology (ANOVA $P < 0.05$). Tentative protein identifications, written in italics in the table, were these with Mascot score values below the identity threshold.

Protein identity	Species	SwissProt accession number	Mascot score/ threshold	Matches (duplicates)	Sequences	Nominal mass (Da)/pI	Protein sequence coverage
Cullin-associated NEDD8-dissociated protein 1	*Mus musculus*	CAND1_MOUSE	75/35	2	2	137,985/5.52	1 %
	Rattus norvegicus	CAND1_RAT	75/35	2	2	138,015/5.52	1 %
	Homo sapiens	CAND1_HUMAN	75/35	2	2	138,029/5.52	1 %
Ig kappa chain V-V region K2 (Fragment)	*Mus musculus*	KV5A3_MOUSE	68/35	2 (1)	1	12,747/8.50	11 %
78 kDa glucose-regulated protein	*Mus musculus*	GRP78_MOUSE	61/33	2	2	72,493/5.07	5 %
	Homo sapiens	GRP78_HUMAN	61/33	2	2	72,404/5.07	5 %
	Rattus norvegicus	GRP78_RAT	61/33	2	2	72,476/5.07	5 %
Ig gamma-4 chain C region	*Homo sapiens*	IGHG4_HUMAN	59/33	8 (4)	4	36,440/7.18	14 %
Ig kappa chain C region	*Homo sapiens*	IGKC_HUMAN	59/32	1	1	11,776/5.58	18 %

Continuation from table above.

Protein identity	Species	SwissProt accession number	Mascot score/ threshold	Matches (duplicates)	Sequences	Nominal mass (Da)/pI	Protein sequence coverage
Tubulin alpha-1B/C, -4A/B, -8 chain	*Cricetulus griseus* (Chinese hamster)	TBA1B_CRIGR	55/35	1	1	50,816/4.94	3 %
		TBA1C_CRIGR	55/35	1	1	50,574/4.96	3 %
	Mus musculus	TBA1B_MOUSE	55/35	1	1	50,816/4.94	3 %
		TBA1C_MOUSE	55/35	1	1	50,574/4.96	3 %
		TBA4A_MOUSE	55/35	1	1	50,646/4.95	3 %
		TBA8_MOUSE	55/35	1	1	50,716/4.97	3 %
	Rattus norvegicus	TBA1B_RAT	55/35	1	1	50,816/4.94	3 %
		TBA1C_RAT	55/35	1	1	50,602/4.96	3 %
		TBA4A_RAT	55/35	1	1	50,646/4.95	3 %
		TBA8_RAT	55/35	1	1	50,702/4.97	3 %
	Homo sapiens	TBA1B_HUMAN	55/35	1	1	50,816/4.94	3 %
		TBA1C_HUMAN	55/35	1	1	50,560/4.96	3 %
		TBA4A_HUMAN	55/35	1	1	50,646/4.95	3 %
		TBA4B_HUMAN	55/35	1	1	27,824/7.71	5 %
		TBA8_HUMAN	55/35	1	1	50,758/4.94	3 %
Glyceraldehyde-3-phosphate dehydrogenase	*Cricetulus griseus* (Chinese hamster)	G3P_CRIGR	50/35	3	3	35,957/8.49	15 %
	Homo sapiens	G3P_HUMAN	50/35	3	3	36,204/8.57	15 %

Continuation from table above.

Protein identity	Species	SwissProt accession number	Mascot score/ threshold	Matches (duplicates)	Sequences	Nominal mass (Da)/pI	Protein sequence coverage
Actin-related protein 3-B/C or 3	*Mus musculus*	ARP3B_MOUSE	47/35	2 (1)	1	48,071/5.70	2 %
		ARP3_MOUSE	47/35	2 (1)	1	47,791/5.61	2 %
	Rattus norvegicus	ARP3_RAT	47/35	2 (1)	1	47,791/5.61	2 %
	Homo sapiens	ARP3B_HUMAN	47/35	2 (1)	1	48,099/5.61	2 %
		ARP3C_HUMAN	47/35	2 (1)	1	23,929/5.36	5 %
		ARP3_HUMAN	47/35	2 (1)	1	47,805/5.61	2 %
Putative phospholipase B-like 2	*Mus musculus*	PLBL2_MOUSE	44/35	3 (1)	2	66,653/5.77	3 %
	Rattus norvegicus	PLBL2_RAT	44/35	3 (1)	2	65,762/6.24	3 %
Semaphorin-3E	*Mus musculus*	SEM3E_MOUSE	37/35	1	1	90,704/8.10	1 %
	Homo sapiens	SEM3E_HUMAN	37/35	1	1	90,389/7.20	1 %
Histone H2B type 1-B, -C/E/G, -F/J/L, -H, -K, -M, -P; type 2-B, -E; type 3-A, -B	*Mus musculus*	H2B1B_MOUSE	34/35	1	1	13,944/10.31	11 %
		H2B1C_MOUSE	34/35	1	1	13,898/10.31	11 %
		H2B1F_MOUSE	34/35	1	1	13,928/10.31	11 %
		H2B1H_MOUSE	34/35	1	1	13,912/10.31	11 %
		H2B1K_MOUSE	34/35	1	1	13,912/10.31	11 %
		H2B1M_MOUSE	34/35	1	1	13,928/10.31	11 %
		H2B1P_MOUSE	34/35	1	1	13,984/10.31	11 %
		H2B2B_MOUSE	34/35	1	1	13,912/10.31	11 %
		H2B2E_MOUSE	34/35	1	1	13,985/10.31	11 %
		H2B3A_MOUSE	34/35	1	1	13,986/10.37	11 %
		H2B3B_MOUSE	34/35	1	1	13,900/10.31	11 %

Continuation from table above.

Protein identity	Species	SwissProt accession number	Mascot score/ threshold	Matches (duplicates)	Sequences	Nominal mass (Da)/pI	Protein sequence coverage
Histone H2B type 1-B, -C/E/F/G/I, -D, -H, -J, -K, -L, -M, -N, -O; type 2-E, -F; type 3-B, -F-S	*Rattus norvegicus*	H2B1_RAT	34/35	1	1	13,982/10.36	12 %
	Homo sapiens	H2B1B_HUMAN	34/35	1	1	13,942/10.31	11 %
		H2B1C_HUMAN	34/35	1	1	13,898/10.31	11 %
		H2B1D_HUMAN	34/35	1	1	13,928/10.31	11 %
		H2B1H_HUMAN	34/35	1	1	13,884/10.31	11 %
		H2B1J_HUMAN	34/35	1	1	13,896/10.31	11 %
		H2B1K_HUMAN	34/35	1	1	13,882/10.31	11 %
		H2B1L_HUMAN	34/35	1	1	13,944/10.31	11 %
		H2B1M_HUMAN	34/35	1	1	13,981/10.31	11 %
		H2B1N_HUMAN	34/35	1	1	13,914/10.31	11 %
		H2B1O_HUMAN	34/35	1	1	13,898/10.31	11 %
		H2B2E_HUMAN	34/35	1	1	13,912/10.31	11 %
		H2B2F_HUMAN	34/35	1	1	13,912/10.31	11 %
		H2B3B_HUMAN	34/35	1	1	13,900/10.31	11 %
		H2BFS_HUMAN	34/35	1	1	13,936/10.37	11 %
Protein MMS22-like	*Mus musculus*	MMS22_MOUSE	29/35	1	1	142,580/6.69	1 %
GTP-binding nuclear protein Ran	*Mus musculus*	RAN_MOUSE	29/35	1	1	24,582/7.01	3 %
	Rattus norvegicus	RAN_RAT	29/35	1	1	24,582/7.01	3 %
	Homo sapiens	RAN_HUMAN	29/35	1	1	24,582/7.01	3 %

Continuation from table above.

Protein identity	Species	SwissProt accession number	Mascot score/ threshold	Matches (duplicates)	Sequences	Nominal mass (Da)/pI	Protein sequence coverage
Acyl-coenzyme A thioesterase 4	*Mus musculus*	ACOT4_MOUSE	23/35	1	1	46,799/7.73	2 %
CMP-N-acetylneuraminate-beta-galactosamide-alpha-2,3-sialyltransferase 1	*Mus musculus*	SIA4A_MOUSE	27/33	1	1	39,396/9.32	5 %
	Homo sapiens	SIA4A_HUMAN	27/33	1	1	39,398/9.20	5 %
Glutamine--fructose-6-phosphate aminotransferase	*Rattus norvegicus*	GFPT1_RAT	24/33	1	1	77,590/6.39	2 %
	Homo sapiens	GFPT1_HUMAN	24/33	1	1	79,568/6.66	2 %
Nischarin	*Mus musculus*	NISCH_MOUSE	23/32	1	1	176,527/5.05	1 %

Table 8.3. Host cell protein identification in the mAb-depleted soluble fraction of the non-treated protein A chromatography eluate via LC-MS/MS analysis.

Host cell proteins were identified via LC-MS/MS analysis as detailed in Section 2.10.6. The mAb-depleted soluble fraction of the non-treated protein A chromatography eluate was prepared as shown in Figure 8.1. Protein sequence searches were performed against the SwissProt online protein database; search parameters were as detailed in Section 2.10.6. Protein nominal mass and pI values were given by the Mascot search results. Proteins with Mascot score values above the identity threshold indicate identity or extensive homology (ANOVA $P < 0.05$). Tentative protein identifications, written in italics in the table, were these with Mascot score values below the identity threshold.

Protein identity	Species	SwissProt accession number	Mascot score/ threshold	Matches (duplicates)	Sequences	Nominal mass (Da)/pI	Protein sequence coverage
Ig kappa chain V-V region K2 (Fragment)	*Mus musculus*	KV5A3_MOUSE	95/36	3 (2)	1	12,747/8.50	11 %
Ig gamma-4 chain C region	*Homo sapiens*	IGHG4_HUMAN	86/34	20 (13)	6 (5)	36,440/7.18	22 %
Ig kappa chain C region	*Homo sapiens*	IGKC_HUMAN	76/33	4 (3)	3 (2)	11,776/5.58	49 %
Ubiquitin carboxyl-terminal hydrolase 30	*Mus musculus*	UBP30_MOUSE	36/33	1	1	58,996/8.76	3 %
	Rattus norvegicus	UBP30_RAT	36/33	1	1	58,981/8.84	3 %
	Homo sapiens	UBP30_HUMAN	36/33	1	1	59,278/8.57	3 %
E-selectin	*Homo sapiens*	LYAM2_HUMAN	23/33	1	1	69,395/5.20	3 %

Table 8.4. Host cell protein identification in the mAb-depleted fraction of the flocculated protein A chromatography eluate via LC-MS/MS analysis.

Host cell proteins were identified via LC-MS/MS analysis as detailed in Section 2.10.6. The mAb-depleted fraction of the flocculated protein A chromatography eluate was prepared as shown in Figure 8.1. Protein sequence searches were performed against the SwissProt online protein database; search parameters were as detailed in Section 2.10.6. Protein nominal mass and pI values were given by the Mascot search results. Proteins with Mascot score values above the identity threshold indicate identity or extensive homology (ANOVA $P < 0.05$). Tentative protein identifications, written in italics in the table, were these with Mascot score values below the identity threshold.

Protein identity	Species	SwissProt accession number	Mascot score/ threshold	Matches (duplicates)	Sequences	Nominal mass (Da)/pI	Protein sequence coverage
Ig kappa chain C region	*Homo sapiens*	IGKC_HUMAN	119/34	5 (1)	4 (1)	11,776/5.58	64 %
Ig gamma-4 chain C region	*Homo sapiens*	IGHG4_HUMAN	93/34	19 (13)	6 (4)	36,440/7.18	26 %
Ig kappa chain V-V region K2 (Fragment)	*Mus musculus*	KV5A3_MOUSE	79/34	3 (2)	1	12,747/8.50	11 %
Ubiquitin carboxyl-terminal hydrolase 30	*Mus musculus*	UBP30_MOUSE	50/34	1	1	58,996/8.76	3 %
	Rattus norvegicus	UBP30_RAT	50/34	1	1	58,981/8.84	3 %
	Homo sapiens	UBP30_HUMAN	50/34	2	2	59,278/8.57	5 %

The LC-MS/MS results for the mAb-depleted flocculated fraction (Table 8.4) were not in line with the SDS-PAGE results (Figure 8.2); while only one HCP was identified (i.e. USP30) via LC-MS/MS analysis (see Table 8.4), multiple protein bands that did not correspond to the mAb heavy or light chains were observed on the SDS-PAGE gel (see Figure 8.2). The same observation was made for the mAb-depleted non-treated soluble fraction (see Table 8.3), although the HCP results obtained for the non-treated solids fraction (Table 8.2) could have accounted for the small amount of HCPs identified in the mAb-depleted soluble fraction. Large amounts of IgG fragments in the pooled protein A eluates could have hindered the identification of HCPs present in low quantities during LC-MS/MS analysis (Thompson et al., 2014). The sample preparation protocol (see Section 8.2.2 and Figure 8.1) where the eluates were filtered through a 100 kDa MWCO membrane was not expected to be the reason for the limited number of HCPs identified via LC-MS/MS analysis in the mAb-depleted non-treated and flocculated samples. The MW of the bulk of HCPs present in harvested recombinant CHO cell cultures has been reported to range between 25 and 100 kDa (Jin et al., 2010). Furthermore, most of the protein bands observed on the SDS-PAGE gel attributed to impurities (Figure 8.2) had a MW smaller than 70 kDa. Therefore, the majority of HCPs in the protein A eluate samples were expected to flow through the 100 kDa MWCO filter. The disparity between the LC-MS/MS and SDS-PAGE results showed that (i) the methodology chosen for HCP identification needs to be optimised; and (ii) the effect of the flocculation strategy on the HCP profile post-protein A chromatography could not be concluded with certainty.

All the HCPs identified in the solids fraction of the non-treated protein A chromatography eluate were intracellular proteins with the exception of Semaphorin-3E (see Table 8.5). The abundance of intracellular HCPs in harvested CHO cell culture fluids has been reported by different authors (Hogwood et al., 2013a). Intracellular HCPs are released into the cell culture fluid due to cell lysis or cell breakage after cell death during cell culture, and during primary recovery due to shear stress (Hogwood et al., 2013b; Tait et al., 2012). Table 8.5 also shows the HCPs identified in the solids fraction of the non-treated protein A eluate were involved in, amongst other cellular mechanisms, replication, transcription,

cellular metabolism, protein folding, cell signalling and organisation of the cytoskeleton. One of these HCPs was GRP78 (78 kDa glucose-regulated protein) (see Table 8.2 and Table 8.5), which is also known as chaperone BiP. This HCP has been described as one of the most abundant proteins in the proteome of mAb-producing CHO cells (Champion et al., 1999; Meleady et al., 2011) and murine myeloma NS0 cells (Alete et al., 2005; Smales et al., 2004). GRP78 is a key chaperone involved in the correct assembly of mAbs, as it associates via non-covalent interactions with unfolded antibody chains in the endoplasmic reticulum (Lee et al., 1999; Meunier et al., 2002). Furthermore, GRP78 has been linked to increase mAb productivity in murine myeloma NS0 cells (Alete et al., 2005; Smales et al., 2004). Therefore, the abundance of GRP78 in the high cell density CHO cell culture fluid used in this chapter (see Section 2.1.2) was expected to be high. Glycolytic enzymes, such as the glyceraldehyde-3-phosphate dehydrogenase (G3PDH) encountered in the solids fraction of the non-treated protein A chromatography eluate (see Table 8.2 and Table 8.5), have also been reported to be amongst the most abundant HCPs in high mAb productivity murine myeloma NS0 cells (Smales et al., 2004). Tubulin and actin-related proteins, also identified in the solids fraction of the non-treated protein A eluate (see Table 8.2 and Table 8.5), have been reported to co-elute with the mAb during protein A chromatography in different CHO cell lines (Doneanu et al., 2012). The presence of actin-related protein 3 in the protein A eluate (see Table 8.2) could have been due to attractive interactions between this HCP and the constant region of the mAb (Levy et al., 2014). Moreover, increased levels of cytoskeletal proteins, such as tubulin and actin, are found in high mAb producing mammalian cell lines due to (i) their role in carrying the secretory vesicles containing the mAb to the plasma membrane (Smales et al., 2004); and (ii) to their potential contribution to the cell's translational machinery (Stapulionis et al., 1997).

The tentative HCPs identified in the solids fraction of the non-treated protein A chromatography eluate (see Table 8.2) were integral parts of the cell or proteins involved in various cellular mechanisms such as replication, transcription, cellular metabolism, protein post-translational modifications and cell survival (see Table 8.5). Histone H2, a core component of the nucleosome, was one of the tentative HCPs identified in the solids fraction (see Table 8.2). Histones have been

reported to co-elute with the mAb during protein A chromatography in CHO cell processes, and contribute to the turbidity in neutralised protein A chromatography elution pools (Gagnon et al., 2014). The GTP-binding nuclear protein Ran was another of the tentative HCPs identified in the solids fraction of the non-treated protein A eluate (see Table 8.2). This protein was also identified in proteome studies for different recombinant murine myeloma NS0 cell lines, although it was not present amongst their most abundant HCPs (Smales et al., 2004); nonetheless, these results cannot be directly translated to the CHO cell line or the mAb product used in this chapter since differences in the proteome and interactions HCP-mAb can arise (Sisodiya et al., 2012). Finally, the other two tentative HCPs identified in the solids fraction of the non-treated eluate were glutamine fructose-6-phosphate aminotransferase and CMP-N-acetylneuraminate-beta-galactosamide-alpha-2,3-sialyltransferase 1 (see Table 8.2). These proteins, which are involved in protein glycosylation mechanisms (see Table 8.5), might be more abundant in highly productive recombinant CHO cell lines due their role in the synthesis of functional mAbs.

Ubiquitin carboxyl-terminal hydrolase 30, the HCP identified in both the non-treated and flocculated mAb-depleted protein A eluates (see Table 8.3 and Table 8.4), is involved in the control of mitochondria fusion (Yue et al., 2014). Therefore, this deubiquitinating enzyme is involved in cellular activities related to functional regulation, and not to protein degradation via the ubiquitin-dependent pathway. However, further research is needed to confirm this hypothesis and to elucidate whether USP30 has any role in supporting and maintaining the high mAb productivity of recombinant mammalian cell lines. Finally, E-selectin, the tentative HCP identified in the non-treated mAb-depleted soluble fraction (see Table 8.3), is not directly involved in the synthesis of recombinant mAbs since this is a cell-surface glycoprotein involved in cellular immunoadhesion (Hession et al., 1990). No tentative HCPs were identified in the flocculated mAb-depleted fraction (see Table 8.4).

Table 8.5. Biological function and cellular location of host cell proteins present in the protein A chromatography eluates for the flocculated and non-treated primary recovery strategies.

Host cell proteins were identified via LC-MS/MS analysis and are listed in Table 8.2 to Table 8.4. The samples studied were the non-treated and flocculated protein A chromatography eluates, which were prepared as shown in Figure 8.1. Peer-reviewed publications (refer to the text) and the online UniProt protein database were used to establish the biological function and cellular location of the HCPs identified.

Sample	Protein identity	Biological function
Non-treated protein A chromatography eluate, precipitate fraction	Cullin-associated NEDD8-dissociated protein 1	Negative regulation of catalytic activity. Positive regulation of transcription. Protein ubiquitination. **Location**: cytoplasm
	78 kDa glucose-regulated protein	Involved in the correct folding of proteins and degradation of misfolded proteins. **Location**: endoplasmic reticulum lumen and cytoplasm
	Tubulin alpha -1B/C, -4A or -8 chain	Constituent of the microtubules (cytoskeleton) with functions of cell division, assisting in the correct non-covalent folding of newly formed polypeptides and other processes dependent on the microtubules. **Location**: cytoplasm
	Glyceraldehyde-3-phosphate dehydrogenase	Key enzyme in glycolysis Modulates the organisation and assembly of the cytoskeleton Participates in protein stabilisation, transcription, DNA replication and cell apoptosis. **Location**: cytoplasm and nucleus
	Actin-related protein 3-B/C or 3	Involved in the organisation of the actin cytoskeleton. **Location**: cytoplasm (cytoskeleton)
	Putative phospholipase B-like 2	Lipid degradation in the lipid metabolism. **Location:** lysosome lumen
	Semaphorin-3E	Plays an important role in signalling via a cell surface receptor and mediates reorganisation of the actin cytoskeleton leading to the retraction of cell projections. **Location:** extracellular (secreted)

Continuation from table above.

Sample	Protein identity	Biological function
Non-treated protein A chromatography eluate, precipitate fraction ***Tentative HCPs***	*Histone H2B type 1-B, -C/E/G, -F/J/L, -H, -K, -M, -P; type 2-B, -E; type 3-A, -B*	Core component of the nucleosome, which wraps and compacts DNA into chromatin. Histones are involved in transcription regulation, DNA repair, DNA replication and chromosomal stability. **Location:** nucleus
	Protein MMS22-like	Involved in DNA repair during DNA replication. **Location:** nucleus
	GTP-binding nuclear protein Ran	Involved in the import of proteins into the nucleus and RNA export out of the nucleus. Might be involved in chromatin condensation and control of the cell cycle. **Location:** nucleus and cytoplasm
	Acyl-coenzyme A thioesterase 4	Involved in the catabolism of fatty acids. **Location:** peroxisome
	CMP-N-acetylneuraminate-beta-galactosamide-alpha-2,3-sialyltransferase 1	Involved in protein glycosylation by synthesising the sequence NeuAc-alpha-2,3-Gal-beta-1,3-GalNac found on threonine or serine protein amino acids. **Location:** Golgi apparatus and extracellular (secreted)
	Glutamine-fructose-6-phosphate aminotransferase	Involved in regulating protein glycosylation by controlling the influx of glucose into the pathway. **Location:** cytoplasm
	Nischarin	Induces cell survival and cell growth. Might be involved in pathways preventing cell apoptosis. **Location:** cytoplasm and possibly cell membrane and endosomes
Non-treated & flocculated protein A chromatography eluate, mAb-depleted fraction	Ubiquitin carboxyl-terminal hydrolase 30	Deubiquitinating enzyme acting as a key inhibitor of mitophagy. **Location:** mitochondria

Continuation from table above.

Sample	Protein identity	Biological function
Non-treated protein A chromatography eluate, mAb-depleted fraction ***Tentative HCP***	*E-selectin*	Cell-surface glycoprotein involved in cell adhesion. **Location:** cell membrane

8.4. Conclusions

The non-treated and flocculated protein A chromatography eluates obtained from the experiments performed in Chapter 7 (see Table 7.1) were analysed via SDS-PAGE and LC-MS/MS to compare their protein profiles. A summary of the key findings based on the chapter aims and objectives is as follows:

1. Investigate whether flocculation during primary recovery can modify the HCP profile post-protein A chromatography.

The three pre-elution washes performed during protein A chromatography in Chapter 7 were not effective in disrupting the non-covalent interactions between the HCPs and the mAb and/or the chromatographic resin. Consequently, these bound HCPs co-eluted with the mAb during the low pH elution step in both the non-treated and flocculated primary recovery strategies.

The analysis of the protein A eluates via SDS-PAGE concluded the flocculated primary recovery strategy (i.e. centrifugation – flocculation - multilayer depth filtration) was effective at removing high MW protein impurities (MW > 70 kDa) when compared to the non-treated strategy (i.e. centrifugation – two-stage depth filtration). The LC-MS/MS analysis confirmed the HCP nature of the solid particulates observed in the non-treated protein A chromatography eluate, which were absent in the flocculated eluate. However, SDS-PAGE verified the HCPs identified via LC-MS/MS analysis were an under-representation of the samples' HCP populations. Therefore, the effect of the flocculated primary recovery

strategy on the HCP profile post-protein A chromatography could not be determined with certainty.

The sample preparation protocol used to decrease the mAb content from the protein A eluate samples before LC-MS/MS analysis was not effective at removing the mAb fragments present in the samples. The presence of large quantities of mAb fragments might have hindered the identification of HCPs via LC-MS/MS analysis in both the non-treated and flocculated eluates, particularly those HCPs present in low concentrations. Protein separation via polyacrylamide gel electrophoresis before LC-MS/MS analysis could have enhanced HCP identification by minimising the presence of high quantities of mAb. This and other HCP identification approaches need to be explored.

9. Conclusions and Recommendations for Future Work

The work presented within this thesis has focussed on the implementation of flocculation as a post-centrifugation feed conditioning strategy in a mAb production process using a high cell density (HCD) glutamine synthetase-Chinese hamster ovary (GS-CHO) cell line. This work has been performed using both new and proven ultra scale-down (USD) techniques to explore the impact that flocculation had on subsequent downstream unit operations. The results obtained at USD scale were then validated at laboratory scale and complemented with analytical techniques to evaluate process performance.

The conclusions reached from this thesis research have been summarised in Section 9.1, with reference to the research objectives defined in Section 1.7. Section 9.2 follows with the possible directions for future work. The suggestions made for future work have taken into account the findings obtained in this thesis as well as the results from recent peer-reviewed publications in the field.

9.1. Review of Overall Research Objectives

Objective 1: Assess the possibility to use flocculation as a post-centrifugation feed conditioning strategy, identify a successful flocculant and establish the analytical methods and protocols to characterise flocculation performance.

Chapter 3 described the implementation of cationic polyelectrolyte flocculation as a post-centrifugation unit operation using two different GS-CHO cell lines. This chapter also characterised different analytical methods to evaluate flocculation performance; these methodologies were then used in subsequent chapters.

Polyelectrolyte flocculation in mammalian cell processes had only been reported on cell culture broths (Aunins and Wang, 1989; Kang et al., 2013; Riske et al., 2007; Singh et al., 2013). Therefore, the validation of polyelectrolyte flocculation on centrifuged mammalian cell cultures was required. Maximum cell density was shown to be a critical parameter to successfully flocculate centrifuged GS-CHO

cell cultures with linear polyethylenimine (PEI). Maximum cell densities larger than $20x10^6$ cells.mL^{-1} resulted in a positive flocculation outcome (i.e. PEI successfully flocculated the submicron particles present in that GS-CHO centrate); contrary, values of maximum cell density equal or lower than $10x10^6$ cells.mL^{-1} were insufficient for PEI to successfully flocculate the GS-CHO centrate obtained. These results limited all the flocculation studies included in this thesis to high cell density GS-CHO cell cultures (i.e. maximum cell densities > $20x10^6$ cells.mL^{-1}).

Linear PEI was a successful agent to flocculate the submicron particles present in the centrifuged HCD GS-CHO cell cultures used. The low concentrations of PEI required for flocculation to occur (≥ 0.10 % w/v), in addition to its high affinity for DNA and low binding to the mAb product, made this cationic polyelectrolyte a good candidate. Therefore, linear PEI was used in all the flocculation experiments included in this thesis.

Certain polyelectrolytes have been found to interfere with some analytical assays used to assess flocculation performance (Peram et al., 2010), which in this thesis was characterised according to the size distribution of the flocs, impurity removal and product yield. Polyethylenimine and the flocculation conditions used (i.e. flocculant concentration and pH) determined the analytical methods and protocols chosen to assess impurity removal and product yield. These results showed the need to evaluate, on a case-by-case basis, the interference of the flocculating agent with the analytical assays used and its impact upon the assay results depending upon the flocculation settings chosen.

Objective 2: Develop and validate an ultra scale-down flocculation methodology for the rapid evaluation of flocculation conditions during early process development.

The primary focus of Chapter 4 was to develop a methodology for the scaled-down, automated and high-throughput study of flocculation that mimicked the conditions encountered at production scale. Due to the limited availability of centrifuged HCD GS-CHO cell broth, the methodology was developed and validated using clarified Baker's yeast homogenate. However, the

USD flocculation methodology developed was then validated with centrifuged HCD GS-CHO cell broth in Chapter 5.

Chapter 4 described the development of an automated, high-throughput flocculation methodology based on a 96-well plate with 800 µL working volume in each well. This microplate was equipped with 96 individual magnetic stirrers and could be automated with a robotic liquid handling platform. Clarified Baker's yeast homogenate was then used to develop a methodology to scale-up flocculation between vessels of different geometry and volume capacity. The 96-well plate described (800 µL) and a stirred tank reactor of standard geometrical configuration (1.5 L) were used for this purpose. The fast reaction kinetics of flocculation, when compared to the mixing process after flocculant addition in the vessels used, converted flocculant addition time into a critical variable for the success of the flocculation scale-up process. Impeller speed was another critical flocculation scale-up variable since it determined the growth and breakage of the flocs. The effect of flocculant addition time was described by the influence that the predominant mixing time scale in the vessel (i.e. micromixing, mesomixing or macromixing) had upon the size and the distribution (i.e. monomodal or bimodal) of the flocs. The effect of impeller speed was described by two common scale-up "rules of thumb": average turbulent energy dissipation and impeller tip speed. While only micromixing time scale guaranteed a similar floc size distribution in both flocculation vessels, constant average turbulent energy dissipation offered better particle size predictions than constant impeller tip speed by tightly mimicking the size of the smaller flocs; the tight prediction of small particles is critical for the performance of the subsequent solid-liquid separation step. These results provided the basis for the design of the USD flocculation methodology, which stated the use of (i) flocculant addition times that guarantee the predominance of micromixing (according to the experimental characterisation of micromixing time for the mixing vessel used); and (ii) constant average turbulent energy dissipation to scale up impeller speed. Failing to guarantee a predominant micromixing time scale in both flocculation vessels resulted in yeast flocs that differed up to 50 % in size.

The findings obtained with the clarified Baker's yeast homogenate (Chapter 4) were applied to clarified HCD GS-CHO cell broths (Chapter 5). However, slight differences in the scale-up error margins were observed depending on the characteristics of the fluid being flocculated; while clarified Baker's yeast homogenate was scaled up within a ± 5 % error margin, clarified GS-CHO cell fluid was scaled up within a ± 7 % error margin. Failing to guarantee the established USD flocculation methodology also led to higher floc size deviations when using clarified GS-CHO cell fluid (Chapter 5).

The automated, 96-well mixing system described in Chapter 4 required an equally automated, high-throughput platform to achieve a first evaluation of different flocculation conditions when using GS-CHO HCD mammalian cell centrate. Chapter 5 describes that absorbance measurements at 600 nm wavelength over a period of 3 hours were a good approach to assess different flocculation conditions since they allowed (i) the identification of non-optimal flocculation conditions (i.e. these resulting in submicron flocculated particles); and (ii) the differentiation of floc populations of different sizes. Automated absorbance measurements can be combined with automated analytical assays for the study of protein and DNA removal, as well as for product yield studies if a high performance liquid chromatography instrument is integrated in the robotic platform. All together, these methods offer the capability to fully automate the evaluation of flocculation conditions early in process development.

Objective 3: Evaluate the capacity of post-centrifuge flocculation to assist depth filtration in the removal of solids and process-related impurities during mAb production with GS-CHO cell lines.

The downstream impact of a post-centrifuge flocculation step was studied in Chapter 6 to Chapter 8 to assess the fit of this new unit operation in the current Lonza Biologics monoclonal antibody (mAb) production process. To accommodate flocculation in the current primary recovery strategy of centrifugation followed by two depth filtration steps, a single depth filtration step was chosen for floc removal. This strategy reduces the capital investment necessary (in comparison to a centrifugation step) and offers the ability to reduce the impurity content of the post-flocculated fluid (Yigzaw et al., 2006).

Chapter 6 described the integrated study of flocculation and constant pressure depth filtration using USD methodologies, which were chosen to gain process understanding of larger scale operations using millilitre volumes of process material (4 mL). Flocculant concentration, flocculant addition rate, depth filter media and filtration pressure drop impacted differently upon filtration throughput and clarification performance. However, the USD depth filtration study was limited by the need to use single layer filters when employing the USD constant pressure filtration methodology due to the design limitations of the filter housings used. Single layer filters (0.28 cm^2) were shown to be insufficient to cope with the large solid volumes present in both the non-treated (i.e. centrifuged) and flocculated feeds since they resulted in rapid filter clogging and low filtration throughput values thereof (< 85 and < 35 $L.m^{-2}$, respectively). As a consequence, only small data sets were acquired, which hindered the identification of the filter's fouling behaviour.

Multi-layer depth filters have been shown to be capable of obtaining favourable throughput values for pilot and manufacturing scale production when filtering flocculated CHO cell feeds (Kang et al., 2013; Singh et al., 2013). Multi-layer depth filters were then used at laboratory scale to process the flocculated clarified HCD GS-CHO cell material (Chapter 6). The multi-layer depth filter capsules chosen (23 cm^2) offered high filtration throughput values (> 490 $L.m^{-2}$) and high clarification performance independently of the size distribution of the flocs filtered. Nonetheless, the large volumes of feed material consumed limited the number of flocculation and depth filtration variables studied to two and one, respectively. The constraints of the USD constant pressure filtration methodology with flocculated feeds shown in Chapter 6 provides scope for future work into the modification of this technology to use multi-layer depth filters. Such improvement would allow to integrate USD flocculation and depth filtration studies in the same automated platform.

Chapter 7 extended the downstream evaluation of post-centrifuge flocculation to protein A chromatography and compared the process performance achieved by this new strategy to that of the current mAb production process (i.e. centrifugation – two-step depth filtration – protein A chromatography). All

the settings for the process variables were determined by the flocculation and filtration results obtained in Chapter 6 or by the recommendations from the manufacturer and Lonza Biologics. At these conditions, the flocculated strategy achieved larger depth filter capacities and greater clarification performance pre-protein A chromatography. No differences were observed in the DNA and mAb content post-protein A chromatography between the flocculated and non-treated processes. However, a smaller host cell protein (HCP) content post-protein A chromatography was obtained with the flocculated strategy. Furthermore, the impurity load (i.e. HCP and DNA content) pre-protein A chromatography was considerably lower in the flocculated stream, mainly due to the polyelectrolyte flocculation step. Different examples describing the positive impacts upon the purification process of reduced impurity loads pre-protein A chromatography can be found in the literature (Kandula et al., 2009; Thömmes and Etzel, 2007; Yigzaw et al., 2006). Nonetheless, studying such effects upon the chromatographic purification train, both from the process performance and process economics points of view, constitutes future work. Notwithstanding, further flocculation and depth filtration optimisation studies are also required in both the flocculated and non-treated process streams before a final decision over the suitability of a post-centrifuge flocculation step can be made.

Precipitated particles were observed in the neutralised non-treated protein A chromatography elution pool, but not in that of the flocculated stream (Chapter 7). Studies employing the liquid chromatography – mass spectrometry/mass spectrometry (LC-MS/MS) technique combined with bioinformatic tools showed these precipitates were mainly constituted of HCPs negatively charged at neutral pH (Chapter 8). This technique, however, under-represented the population of HCPs in the soluble fractions of the non-treated and flocculated protein A chromatography eluates, as corroborated by the multiple non-mAb protein bands observed on a polyacrylamide gel (Chapter 8). Gel electrophoresis also confirmed that PEI removed high molecular weight (MW) proteins (MW > 70 kDa), albeit the identity of these HCPs could not be determined by LC-MS/MS analysis (Chapter 8). The poor sensitivity for HCPs in the protein A elutes showed by the LC-MS/MS technique could have been related to faults in the sample preparation protocol. The mAb content in the

eluate samples was depleted by filtering out the intact mAb molecules taking advantage of the differences in MW between the mAb and the HCPs. Contrary, the fragments of mAb, probably also present in large amounts, could not be removed by this strategy. Future work will therefore need to include the depletion of mAb molecules and mAb fragments from the protein A elutes for increased sensitivity to characterise their HCP profiles.

9.2. Future Work

This thesis has demonstrated the challenges posed and opportunities offered by the implementation of a polyelectrolyte flocculation step in the primary recovery of a mAb production process when using a GS-CHO cell line. Although the work presented in this thesis has addressed the objectives defined for this project, questions that were out of the scope of the investigation presented have arisen. This section discusses the opportunity for future investigations, either directly related to the research described in this thesis or in other areas of potential interest.

9.2.1. Validation of the USD Flocculation Methodology with Whole Cell Broths

The flocculation of whole cell broths has been commonly reported in the literature for its ability to improve the removal of cells and cell debris (Aunins and Wang, 1989; Coffman et al., 2006; Kang et al., 2013; Riske et al., 2007; Shpritzer et al., 2006; Singh et al., 2013). Flocculating whole cell broths also offers the advantage of adding the flocculating agent into the fermenter thus not requiring the modification of the process flow with an additional flocculation vessel (or in-line flocculant addition) and a solid-liquid separation step. Predicting the flocculation performance that will be obtained at pilot and manufacturing scale when flocculating whole cell broths during early process development is important. For example, the size distribution of the flocs will determine the performance of the subsequent centrifugation (Berrill et al., 2008; Milburn et al., 1990) or filtration (Aspelund et al., 2008; Kang et al., 2013; Singh et al., 2013) steps. Consequently, the size distribution of the flocs will establish

which the subsequent downstream unit operations and their operating conditions will be. It is therefore of interest for the biopharmaceutical industry to investigate how the presence of solids and the change to non-Newtonian fluids of higher viscosity and density values will affect the USD flocculation methodology described in Chapter 4 and Chapter 5. Viscosity-raising polymers have been used in the literature to study how mixing time scales, and product distribution in fast chemical reactions thereof, are affected by the values of fluid viscosity (Bourne et al., 1989, 1995; Gholap et al., 1994). Model fluids and latex particles of different diameters, for instance, could be used to evaluate how the rheological behaviour and the presence of solid particles in the fluid being flocculated affect the mixing time scales and, ultimately, the USD filtration methodology.

9.2.2. Ultra Scale-Down Filtration with Multi-Layer Depth Filters

Multi-layer depth filters are being commonly used either as a primary clarification step (Roush and Lu, 2008; Singh et al., 2013) or as a secondary clarification step (i.e. following centrifugation or tangential flow microfiltration) (Roush and Lu, 2008). In order to improve depth filtration capacity, different depth filter media need to be screened to identify the optimal filter for the intended feed stream (Roush and Lu, 2008). These studies are performed before the pilot scale trials due to their cost and high process volume requirements. Ultra scale-down techniques offer the possibility to obtain process design information during early process development (Titchener-Hooker et al., 2008). As demonstrated in Chapter 6 by the USD constant pressure filtration data obtained, it is of interest for the biopharmaceutical industry to modify the current USD filtration technique (see Section 1.4.2) to accommodate multi-layer filters. Noyes and co-workers (2015) developed a proprietary technology that scaled down a double-layer filter from 23 cm^2 to 0.22 cm^2 cross-sectional area. However, further work is needed in this field since the authors could not explain the basis for the hydrodynamic scaling differences they observed between the single and double-layer filters tested. Furthermore, a USD filtration methodology that is not limited to dual-layer filters is necessary considering that commercially available depth filters used for pre-treated feeds are constituted by up to eight filter layers. The development of USD multi-layer depth filters might require the input of filter

manufacturers, not only to acquire the individual depth filter media a multi-layer depth filter is constituted of, but to also cut the different filters in small discs with ultimate precision and seal them together without damaging the structure of the filter.

9.2.3. Protein A Resin Lifetime Studies

Protein A chromatography has become the workhorse of mAb and Fc fusion protein purification processes despite the high cost of the protein A resin, reusability and concerns over the clearance of leached ligand (Kelley, 2007; Liu et al., 2010; Low et al., 2007; Shukla et al., 2007). Protein A chromatography performance has been reported to decrease with chromatographic cycles thus resin usage (Jiang et al., 2009; Kelley et al., 2008). The consequences of a decrease in protein A chromatography performance are such that health authority guidance for mAb production requires to specify the number of times a chromatography resin can be used in manufacturing based upon validation studies specific to the process under review (U.S. Department of Health and Human Services, Food and Drug Administration, 1997). Process impurities can remain on the resin and either block pores and/or block the access to surface ligands thus reducing the useful lifetime of the chromatography resin over repeated uses (Jiang et al., 2009). Chapter 7 and Chapter 8 showed that the impurity load passed onto the protein A chromatography step was lower for the flocculated feed stream than for the non-treated stream. Consequently, it is of interest to study the effect that a flocculation feed conditioning step during primary recovery would have upon the protein A resin lifetime. The same studies should be performed with the non-treated stream for direct comparison purposes. Evaluating the effect of residual amounts of flocculant present in the feed stream upon the protein A resin lifetime is also necessary. Finally, these studies should be complemented with an assessment of the impact that extended or reduced protein A resin lifetime has upon the overall process costs.

9.2.4. Identification of HCPs in the Presence of High Amounts of mAb

The identification of HCPs and the study of how the HCP profile changes over the clarification and purification steps will improve the process knowledge of its downstream unit operations (Hogwood et al., 2013a, 2014). The characterisation of individual HCPs is a critical step forward in (i) process development for its potential to reduce the downstream processing costs through knowledge-based process decisions (Hogwood et al., 2013a); (ii) ensuring patient safety since certain HCPs have been referred to as of particular concern for the risk they pose to patient safety (Tscheliessnig et al., 2013); and (iii) formulation design studies since certain HCPs have been shown to compromise the integrity of highly purified mAb products (Gao et al., 2011).

The LC-MS/MS results for protein A chromatography eluates described in Chapter 8 suggested large amounts of fragmented mAb might have interfered with the detection of HCPs present in small amounts. The depletion of intact mAb molecules by pre-filtering the samples was not efficient at removing the smaller mAb fragments. Filtering out the mAb fragments is not a possibility due to the similar molecular weight between mAb fragments and HCPs. Future work developing a technique where mAb fragments can be isolated from the HCPs present in the sample could resolve this issue. Such problem could be approached by separating the protein via gel electrophoresis first, and then analysing the protein bands obtained on the electrophoretic gel via LC-MS/MS. These changes would increase the content of HCPs available for LC-MS/MS analysis and improve the technique's sensitivity to identify them even when their content in the sample is low.

9.2.5. Microscale Whole Bioprocessing

The work presented in this thesis and the review article published by Titchener-Hooker et al. (2008) have described the opportunities offered by the USD approach in the race for biopharmaceutical drug launch to market. The ultimate goal would be to scale-down and integrate all the process unit operations to gain in-depth knowledge of the key process interactions between

each step. With regards to upstream operations, systems for the automated study of different cell lines and cell culture conditions are commercially available (e.g. ambr® cell culture systems from Sartorius Stedim). With regards to downstream operations, USD centrifugation (Tait et al., 2009) and USD normal flow filtration (Jackson et al., 2006; Kong et al., 2010; Lau et al., 2013), which have been demonstrated to mimic the conditions of their laboratory and pilot-scale counterparts, can be partially integrated in automated platforms. Commercial systems for the automated study of chromatography are also available (e.g. MediaScout® MiniColumns from Atoll GmbH and PhyTip® from PhyNexus). The integration of all these unit operations in a single automated platform would require to adapt current liquid handling platforms to incorporate, amongst others, bench-top centrifuges and vacuum pressure manifolds. Such approach would allow the optimisation of the overall process with limited feed volume. This, in combination with high-throughput analytical techniques, would generate a deeper understanding of the production process. Consequently, process development would be accelerated and the overall production costs would be reduced by minimising risk of failure during the pilot plant trials and subsequent GMP production for clinical trials and in-market supply. Furthermore, the data generated could be used to create models for process development and process control and, ultimately, increase process robustness by applying the quality by design (QbD) approach (Rathore and Winkle, 2009).

10. Process Validation Concerns during Early Phase Product Development

This chapter has been included in this thesis to satisfy the requirements of the Validation module of the Engineering Doctorate programme.

10.1. Introduction

Monoclonal antibodies (mAbs) are complex high molecular weigth molecules difficult to manufacture because deviations from their final product quality attributes can detrimentally impact upon patient safety. Consequently, regulation of biologics includes final product characterisation, characterisation and control of raw materials and manufacturing process validation (Lutz, 2005). Process validation needs to meet the regulations set by the Food and Drug Administration (FDA), European Medicines Agency (EMA) and any other regulatory agencies required in the country where the drug is intended to be commerciliased.

This chapter provides an overview of specific process validation issues arising for this project. That is, from the introduction of a post-centrifuge flocculation step in the mAb production process of a contract manufacturing organisation (CMO) such as Lonza Biologics.

10.2. Validation Concerns for a Contract Manufacturing Organisation

10.2.1. Technology Transfer between Manufacturing Sites

Lonza Biologics is a CMO with production and research and development centres worldwide. While in some cases these two departments will be based at the same location, in others the facilities will be exclusively dedicated to one of them. Therefore, technology transfer, one of the major challenges in process validation, will have to take place at some point during the process development phase.

The output of this research project has been obtained at small (process volumes < 1 mL) and laboratory (process volumes < 2 L) scale. The ultimate goal

was to translate these findings to production scale (process volumes of 20,000 L). As a consequence, the CMO will face difficulties when translating the flocculation and depth filtration unit operations investigated in this thesis to a different scale and location while ensuring that an equivalent flocculation performance is achieved.

10.2.2. Flocculation: an Alternative, Non-Established Primary Recovery Strategy

This project relies on the use of a novel downstream technology for the biopharmaceutical industry. Although some research in the area has been published and previous studies have been performed within the CMO, no historical data and manufacturing knowledge has been built for this specific unit operation. Consequently, validation using historical data is not possible. This means process data has to be generated to achieve in-depth knowledge of the variables affecting flocculation performance and how this step affects subsequent unit operations.

10.2.3. Process Monitor and Control

Flocculation is a technology that depends on a myriad number of variables that affect the output of the process. Therefore, a strategy for process control and monitoring needs to be in place at manufacturing scale to maintain the critical process parameters within their acceptable range, as identified during process development. Such critical variables include the different flocculation parameters (e.g. stirrer speed, flocculant concentration, flocculant addition rate) and the characteristics of the fluid being flocculated. In that regard, all the cell culture variables and the levels of solid content and process-related impurities will need to be monitored as they determine the properties of the cell culture broth.

A control or action plan is required in addition to a monitoring strategy. In the case physico-chemical variables such as pH and ionic strength are beyond the pre-determined thresholds, strategies like feed dilution, salt addition or pH adjustment must be in place and take place before flocculation is carried out. These action points may be performed in the same flocculation vessel or in-line

between the centrifuge and the flocculation vessel. Nonetheless, planning before the implementation of flocculation at manufacturing scale is necessary in order to perform any required minor changes in the process design, which will have to be re-validated. With regards to cell debris and other process-related impurities, these will vary depending upon (i) cell culture performance (e.g. peak cell density and/or viability at harvest); (ii) the effect of centrifugation shear forces on the cells; and (iii) centrifugation performance. The quantification and control of these process-related impurites is not as straight forward as with pH, for instance, and might not be performed within the specified time frame (i.e. from harvesting to centrifugation). As a consequence, other strategies such as empirical correlations between cell density or viability at harvest and process-related impurity content in the centrifuge supernatant might be useful in planning how to maintain the critical flocculation variables within their thresholds.

Finally, the flocculation output and its effect upon the performance of the subsequent depth filtration step must be taken into account as well. Process control in this case might be carried out by empirical correlations between flocculation conditions and filter capacity, filtration throughput, impurity removal or/and process yield; quality control of the flocs such as particle size distribution or floc density may not be possible in the time frame required since these are off-line and time-consuming measurements.

To sum up, process control and monitoring relies on the knowledge the manufacturer has of its process. In the case of new technologies, such as flocculation, this knowledge needs to be generated since no historical data is currently available for the CMO at production scale.

10.2.4. Project-Specific Validation Concerns

10.2.4.1. Flocculation

One of the main validation concerns of adding a flocculation step in the primary recovery or purification steps of a bioprocess is the ability of the subsequent downstream unit operations to remove any residual flocculant present in the feed. First of all, it is necessary to determine whether the flocculation agent has any toxicity effects upon the patients, which can be humans or animals, if for

veterinary purposes. Toxicity may be defined differently depending upon the flocculant used. For example, the nature of the substance, the polymeric form (i.e. monomer *versus* polymer), final concentration, or the origin of the raw materials in the case of natural flocculants. Validated clinical studies must be carried out before the final Validation Master Plan so that patient safety is ensured and the toxicity thresholds of the flocculating agent used are defined.

Following the toxicity concern, efforts must be concentrated in validating an assay to quantify the flocculating agent. This assay might vary depending on the flocculant used. However, this assay must be straightforward and robust so that flocculant removal (either total or below critical levels) can be proved during the validation and production runs.

In addition to the above, the effect that the residual flocculating agent has upon the lifetime, stability and performance of the depth filter and chromatography resins used has to be considered within the validation scenario. Potential detrimental effects are: (i) filtration media and chromatography resin blockage by the flocculant, particularly by high molecular weight polymeric flocculants; and (ii) charge interaction between the flocculant and the charged depth filter and/or chromatographic resin.

10.2.4.2. Depth Filtration

The most relevant filtration concerns for this unit operation are: (i) the nature of the interaction between the flocculant and the depth filter; and (ii) how flocculant-filter media interaction translates into filtration robustness.

The removal of flocs and process-related impurities such as cell debris, host cell proteins and DNA by the depth filter chosen needs to be characterised and validated. However, enough historical data must be generated before process validation since similar processes might not be available for comparison purposes.

Next, data for filter media extractables should be obtained from water and model solvent extraction studies performed by the filter supplier. If applicable, testing

for leachables will need to be carried out on-site by the CMO, although it could be performed by the filter supplier it they have a service in place.

It is to be noted that, in the case the ultra scale-down (USD) depth filtration technology was validated, filtration studies could be performed at USD scale using process-relevant flocculated feed for the final Validation Master Plan.

10.2.4.3. Assays for Process Performance Analysis

The content of mAb, process-related impurities and residual flocculant need to be quantified after the flocculation and depth filtration steps. The presence of residual flocculant in the samples has been proved to interfere with assays used for process performance analysis such as enzyme-linked immunosorbent assays used during host cell protein quantification (Peram et al., 2010). Therefore, in the event of flocculant interference these assays will have to be modified or substituted by others depending on the flocculant used. This implies that the quantification methods for product and/or process-related impurities might have to be validated on a case-by-case basis in addition to the flocculant quantification assay developed.

Furthermore, the reproducibility of the above assays must be ensured since the output of this research project was initially planned to be implemented into a different manufacturing location, hence they will eventually be performed by different operators.

11. Appendix

11.1. Effect of Storage Conditions on the Characteristics of Mammalian Cell Centrate

The effect of storage conditions (5°C vs. -80°C) on high cell density (HCD) mammalian cell centrate was evaluated measuring the centrate's particle size distribution (PSD) and the optical density at 600 nm wavelength (OD_{600}); measurements were performed according to Section 2.11.4 and Section 2.11.1, respectively. Protein degradation during storage at 5°C was also studied for a period of 95 days; protein degradation was studied via polyacrylamide gel electrophoresis in non-reducing conditions and with silver staining as described in Section 2.10.5.

11.1.1. Storage at 5°C

High cell density centrate was stored at 5°C in the presence of 0.05 % w/v sodium azide to prevent bacterial growth (Lichstein and Soule, 1944) for a period of up to 95 days. However, the HCD centrate used in the flocculation studies was stored at 5°C for a period of up to 15 days. In order to evaluate the effect that storage at 5°C had upon the centrate's protein profile, HCD centrate samples were taken over a period of 3 months and analysed via SDS-PAGE. The electrophoresis gel was stained with silver ions to achieve higher protein sensitivity (i.e. in the nanogram range) than with the Coomassie blue dye (Merril et al., 1981a, 1981b). A visual inspection of the gel (see Figure 11.1) concluded that the number of bands per sample did not change over the time period studied. Protein quantification of the bands could not be performed due to the limitations of silver staining with regards to quantification purposes (Grove et al., 2009). Nonetheless, protein degradation reactions such as peptide bond hydrolysis and/or aspartic acid isomerisation are expected to have taken place (Rathore and Rajan, 2008).

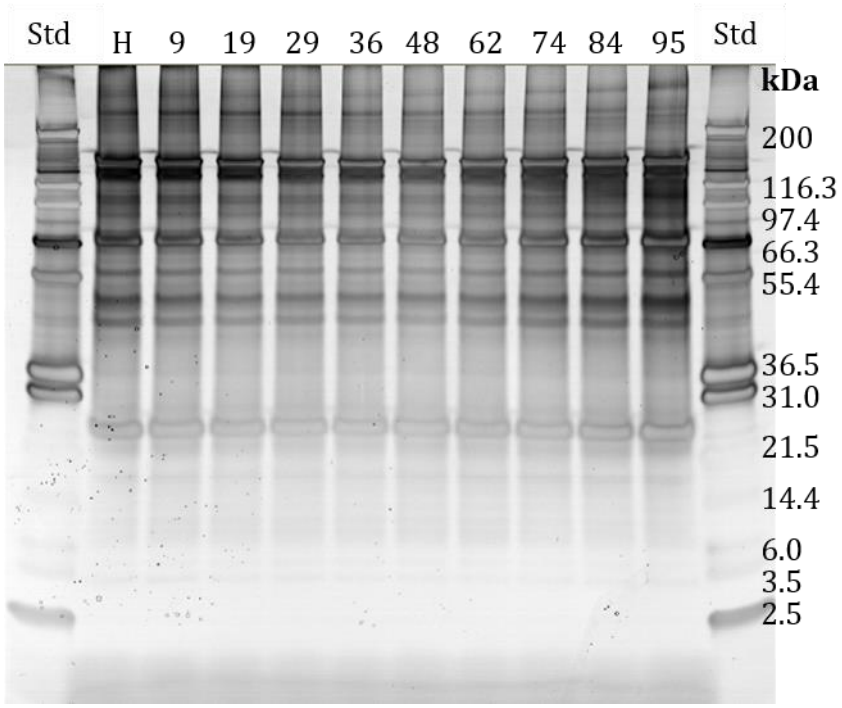

Figure 11.1. Effect of storage at 5°C on the protein profile of high cell density mammalian cell centrate.
Gel electrophoresis was performed in non-reducing conditions and stained with a commercial silver staining kit as described in Section 2.10.5. Samples were diluted 1 in 200 before gel loading. A commercial protein standard (see Section 2.10.5), referred to as Std in the figure, was loaded in the first and last lanes; the molecular weight values, expressed in kDa, are detailed in the figure. From left to right, HCD mammalian cell centrate samples were: H (centrate sampled on harvest day) and 9, 19, 29, 36, 48, 62, 74, 84 and 95 (days in storage at 5°C from cell culture harvest). All samples contained 0.05 % w/v sodium azide.

The OD_{600} of the HCD centrate was also measured over a period of 3 months to evaluate any change in the solids content (Berrill et al., 2008; Chatel et al., 2014; Hogwood et al., 2013b; Kim et al., 2001; Lau et al., 2013; Tait et al., 2009; Tustian et al., 2007). Table 11.1 shows OD_{600} increased 1.7 fold after a three-month storage period at 5°C. This data suggested the formation of larger solid particles (Roush and Lu, 2008) as a result of particle aggregation and/or protein degradation during long-term storage (Rathore and Rajan, 2008). The values of OD_{600} were maintained around 0.090 A.U. during the first 11 days of storage, when the HCD centrate was used in the flocculation studies.

Due to the limited availability of HCD cell culture material, which was supplied by Lonza Biologics (Slough, UK), HCD centrate was required to be stored for long

periods of time. The results obtained when storing the HCD centrate at 5°C suggested that other storage methods were needed.

Table 11.1. Change in optical density at 600 nm wavelength of the high cell density mammalian cell centrate stored at 5°C.
Optical density measurements at 600 nm were taken with a spectrophotometer as described in Section 2.11.1. Cell culture (Xceed™ cell line; peak cell count = 29.0x10^{6} cells.mL^{-1}) was obtained from Lonza Biologics (Slough, UK), and clarified at UCL using a pilot scale disc-stack centrifuge ($Q/\sum$ = 2.85x10^{-8} m.s^{-1}). Centrate was stored at 5°C in the presence of 0.05 % w/v sodium azide. One standard deviation of triplicate measurements where n = 1 is indicated.

Days stored at 5°C	OD_{600} (A.U.)
0	0.087 ± 0.003
6	0.092 ± 0.002
8	0.096 ± 0.003
11	0.093 ± 0.009
90	0.152 ± 0.012
91	0.130 ± 0.015
92	0.148 ± 0.011

11.1.2. Storage at -80°C

A 200 mL aliquot of HCD mammalian cell centrate was stored at -80°C to study the effect of freeze-thawing on the particle content of the centrate, and by doing so, assess whether freezing was a viable storage option for the HCD centrate. The PSD and the OD_{600} of the HCD centrate were measured before and after freezing at -80°C; the measurements were performed in less than 1 hour after centrifugation (i.e. fresh centrate) and after thawing at room temperature the HCD centrate stored at -80°C (i.e. thawed centrate). Figure 11.2 shows the HCD centrate was always constituted of a bimodal population of particles. In the fresh centrate the particles ranged from 0.041 to 0.974 μm and from 1.24 to 128 μm (see Figure 11.2). In the thawed material the solid particulates ranged from 0.041 to 0.862 μm and from 1.24 to 100 μm (see Figure 11.2). Therefore, freeze-thawing did not significantly change the size of the solid particulates since particle size decreased by 0.112 μm (submicron particles) and by 28.0 μm (larger sized particles). Nonetheless, the percentage volume frequency values changed during the freeze-thawing process (see Figure 11.2). The maximum percentage volume frequency value for the submicron particles decreased from 372 to 152 % after freeze-thawing (see Figure 11.2), thus representing a 2.5 fold reduction.

Contrary, the percentage volume frequency of the larger sized particles increased from 4.4 to 6.6 % after freeze-thawing (see Figure 11.2), which was equal to a 1.5 fold increase. These data suggested the submicron particles (allegedly cell debris) formed larger particles sized between 1.24 and 100 μm during the freeze-thawing process.

When comparing the values of OD_{600} before and after freezing, freeze-thawing led to a 2.3 fold increase (0.094 ± 0.002 A.U. – fresh centrate and 0.220 ± 0.005 A.U. – thawed centrate). The increase in the percentage volume frequency of particles sized between 1.24 and 100 μm (see Figure 11.2) could have led to the rise in OD_{600} observed. However, proteins in solution and other impurities could have also precipitated upon freeze-thawing (Rathore and Rajan, 2008) and resulted in particles out of the detection size range of the laser light diffraction technique used (0.02 to 2000 μm).

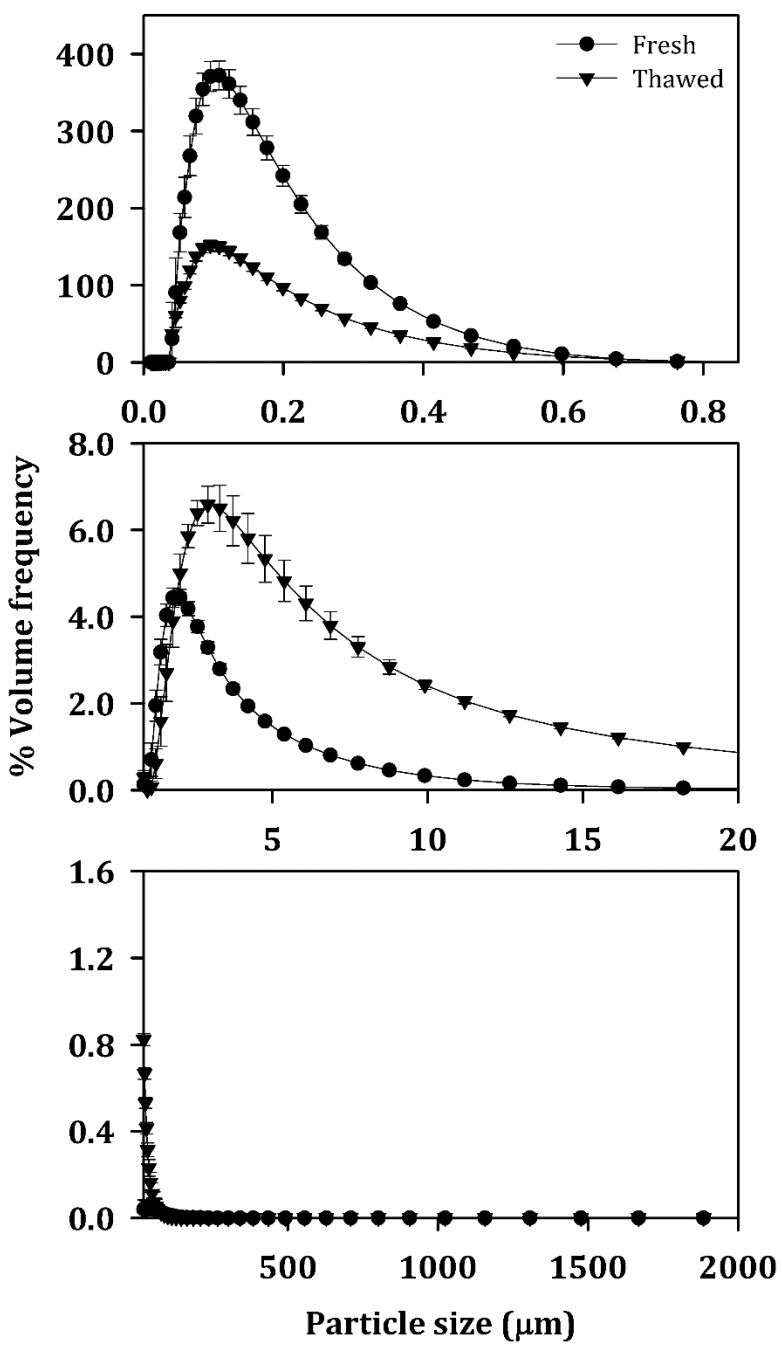

Figure 11.2. Effect of freeze-thawing on the particle size distribution of high cell density mammalian cell centrate.

The PSDs of fresh and thawed HCD mammalian cell (Xceed™ cell line; peak cell count = 29.0x10^{6} cells.mL^{-1}) centrate (Q/Σ = 2.85x10^{-8} m.s^{-1}) were measured via laser light diffraction (see Section 2.11.4). The fresh PSD curves were obtained within an hour of centrifuging the HCD mammalian cell culture fluid. The thawed PSD curves were obtained after a 200 mL aliquot of HCD centrate stored at -80°C was defrosted at room temperature. The PSD results are divided in 3 graphs with the x and y-axis adjusted accordingly. Error bars indicate one standard deviation where n = 6 (fresh) and n = 12 (thawed).

Publications by the Author

American Chemical Society Spring 2015 249th National Meeting and Exposition (Denver, Colorado, USA); 22th March to 26th March 2015; **Session Speaker**. Title: *Integrated Flocculation and Depth Filtration High-throughput Process Development for CHO Supernatants*.

Recovery of Biological Products XVI (Rostock, Germany); 27th June to 31st June 2014; **Poster session**. Title: *Characterisation of Post-Centrifugation, CHO Cell Flocculation Using and Ultra Scale-Down Mixing Methodology*.

Espuny Garcia del Real, G., Davies, J., Bracewell, D.G. (2014), *Scale-Down Characterization of Post-Centrifuge Floculation Processes for High-Throughput Process Development*. Biotechnol Bioeng, 111: 2486-2498

American Chemical Society Spring 2014 247th National Meeting and Exposition (Dallas, Texas, USA); 16th March to 20th March 2014; **Session Speaker**. Title: *An Automated Ultra Scale-Down Methodology for the Characterisation of Post-Centrifuge Flocculation Processes and its Verification*.

References

3M Purification Inc (2011). Zeta PlusTM EXT ZA Series lenticular depth filter cartridges.

Adair, G., and Robinson, M. (1930). The specific refraction increments of serum-albumin and serum-globulin. Biochem J *24*, 993–1011.

Adin, A., and Rebhun, M. (1974). High-rate contact flocculation—filtration with cationic polyelectrolytes. J Am Water Works Ass *66*, 109–117.

Albertsson, P., Edsall, J., and Richards, F. (1970). Partition of cell particles and macromolecules in polymer two-phase systems. In Advances in Protein Chemistry, C. Anfinsen, ed. (Academic Press), pp. 309–341.

Alete, D., Racher, A., Birch, J., Stansfield, S., James, D., and Smales, C. (2005). Proteomic analysis of enriched microsomal fractions from GS-NS0 murine myeloma cells with varying secreted recombinant monoclonal antibody productivities. Proteomics *5*, 4689–4704.

Ambler, C. (1959). The theory of scaling up laboratory data for the sedimentation type centrifuge. Biotechnol Bioeng *1*, 185–205.

Anspach, F., Curbelo, D., Hartmann, R., Garke, G., and Deckwer, W. (1999). Expanded-bed chromatography in primary protein purification. J Chromatogr A *865*, 129–144.

Arden, N., and Betenbaugh, M. (2004). Life and death in mammalian cell culture: strategies for apoptosis inhibition. Trends Biotechnol *22*, 174–180.

Arnold, T. (2005). Fluid purification using charge-modified depth filtration media. Bioprocess Int *3*, 44–49.

Aspelund, M., Rozeboom, G., Heng, M., and Glatz, C. (2008). Improving permeate flux and product transmission in the microfiltration of a bacterial cell suspension by flocculation with cationic polyelectrolytes. J Membr Sci *324*, 198–208.

Assirelli, M., Bujalski, W., Eaglesham, A., and Nienow, A. (2002). Study of micromixing in a stirred tank using a rushton turbine: comparison of feed positions and other mixing devices. Chem Eng Res Des *80*, 855–863.

Aunins, J., and Wang, D. (1989). Induced flocculation of animal cells in suspension culture. Biotechnol Bioeng *34*, 629–638.

Bałdyga, J., and Bourne, J. (1990). The effect of micromixing on parallel reactions. Chem Eng Sci *45*, 907–916.

Bałdyga, J., and Bourne, J. (1992). Interactions between mixing on various scales in stirred tank reactors. Chem Eng Sci *47*, 1839–1848.

Bałdyga, J., and Bourne, J. (1999). Turbulent mixing and chemical reactions (Chichester: Wiley).

Bałdyga, J., and Pohorecki, R. (1995). Turbulent micromixing in chemical reactors — a review. Chem Eng J & Biochem Eng J *58*, 183–195.

Bałdyga, J., Bourne, J., and Yang, Y. (1993). Influence of feed pipe diameter on mesomixing in stirred tank reactors. Chem Eng Sci *48*, 3383–3390.

Bałdyga, J., Bourne, J., and Hearn, S. (1997). Interaction between chemical reactions and mixing on various scales. Chem Eng Sci *52*, 457–466.

Barany, S., and Szepesszentgyörgyi, A. (2004). Flocculation of cellular suspensions by polyelectrolytes. Adv Colloid Interface Sci *111*, 117–129.

Barrett, T., Wu, A., Zhang, H., Levy, M., and Lye, G. (2010). Microwell engineering characterization for mammalian cell culture process development. Biotechnol Bioeng *105*, 260–275.

Bates, R., Fondy, P., and Corpstein, R. (1963). Examination of some geometric parameters of impeller power. Ind Eng Chem Process Des Develop *2*, 310–314.

Bates, R., Fondy, P., and Fenic, J. (1966). Impeller characteristics and power. In Mixing: Theory and Practice, (New York: Academic Press),.

Bell, D., and Dunnill, P. (1982a). Shear disruption of soya protein precipitate particles and the effect of aging in a stirred tank. Biotechnol Bioeng *24*, 1271–1285.

Bell, D., and Dunnill, P. (1982b). The influence of precipitation reactor configuration on the centrifugal recovery of isoelectric soya protein precipitate. Biotechnol Bioeng *24*, 2319–2336.

Benavides, J., Mena, J., Cisneros-Ruiz, M., Ramírez, O., Palomares, L., and Rito-Palomares, M. (2006). Rotavirus-like particles primary recovery from insect cells in aqueous two-phase systems. J Chromatogr B *842*, 48–57.

Berrill, A., Ho, S., and Bracewell, D. (2008). Ultra scale-down to define and improve the relationship between flocculation and disc-stack centrifugation. Biotechnol Prog *24*, 426–431.

Bilanovic, D., and Shelef, G. (1988). Flocculation of microalgae with cationic polymers - Effects of medium salinity. Biomass *17*, 65–76.

Birkner, F., and Morgan, J. (1968). Polymer flocculation kinetics of dilute colloidal suspensions. J – Am Water Works Assoc *60*, 175–191.

Bolto, B., and Gregory, J. (2007). Organic polyelectrolytes in water treatment. Water Res *41*, 2301–2324.

Bonnerjea, J., Jackson, J., Hoare, M., and Dunnill, P. (1988). Affinity flocculation of yeast cell debris by carbohydrate-specific compounds. Enzyme Microb Technol *10*, 357–360.

Bourne, J., and Yu, S. (1994). Investigation of micromixing in stirred tank reactors using parallel reactions. Ind Eng Chem Res *33*, 41–55.

Bourne, J., Hilber, C., and Petrozzi, S. (1989). The influence of viscosity on micromixing in turbulent flows. Chem Eng Process *25*, 133–139.

Bourne, J., Gholap, R., and Rewatkar, V. (1995). The influence of viscosity on the product distribution of fast parallel reactions. Chem Eng J *58*, 15–20.

Boychyn, M., Doyle, W., Bulmer, M., More, J., and Hoare, M. (2000). Laboratory scaledown of protein purification processes involving fractional precipitation and centrifugal recovery. Biotech Bioeng *69*, 1–10.

Boychyn, M., Yim, S., Ayazi Shamlou, P., Bulmer, M., More, J., and Hoare, M. (2001). Characterization of flow intensity in continuous centrifuges for the development of laboratory mimics. Chem Eng Sci *56*, 4759–4770.

Boychyn, M., Yim, S., Bulmer, M., More, J., Bracewell, D., and Hoare, M. (2003). Performance prediction of industrial centrifuges using scale-down models. Bioprocess Biosyst Eng *26*, 385–391.

Bradley, A., and Scott, M. (2004). Separation and purification of methoxypoly(ethylene glycol) grafted red blood cells via two-phase partitioning. J Chromatogr B *807*, 163–168.

Bratby, J. (1980). Coagulation and flocculation : with an emphasis on water and wastewater treatment (Croydon, Eng: Uplands Press).

Brekke, O., and Sandlie, I. (2003). Therapeutic antibodies for human diseases at the dawn of the twenty-first century. Nat Rev Drug Discov *2*, 52–62.

Brodsky, Y., Zhang, C., Yigzaw, Y., and Vedantham, G. (2012). Caprylic acid precipitation method for impurity reduction: an alternative to conventional chromatography for monoclonal antibody purification. Biotechnol Bioeng *109*, 2589–2598.

Büchs, J., Lotter, S., and Milbradt, C. (2001). Out-of-phase operating conditions, a hitherto unknown phenomenon in shaking bioreactors. Biochem Eng J *7*, 135–141.

Burganos, V., Skouras, E., Paraskeva, C., and Payatakes, A. (2001). Simulation of the dynamics of depth filtration of non-Brownian particles. AIChE J *47*, 880–894.

Busch, P., and Stumm, W. (1968). Chemical interactions in the aggregation of bacteria bioflocculation in waste treatment. Environ Sci Technol *2*, 49–53.

Buyel, J., and Fischer, R. (2014). Flocculation increases the efficacy of depth filtration during the downstream processing of recombinant pharmaceutical proteins produced in tobacco. Plant Biotechnol J *12*, 240–252.

Camp, T., and Stein, P. (1943). Velocity gradients in internal work in fluid motion. J Boston Soc Civil Eng *30*, 219–237.

Carter, P. (2011). Introduction to current and future protein therapeutics: a protein engineering perspective. Exp Cell Res *317*, 1261–1269.

Chadd, H., and Chamow, S. (2001). Therapeutic antibody expression technology. Curr Opin Biotech *12*, 188–194.

Chames, P., Van Regenmortel, M., Weiss, E., and Baty, D. (2009). Therapeutic antibodies: successes, limitations and hopes for the future. Br J Pharmacol *157*, 220–233.

Champion, K., Arnott, D., Henzel, W., Hermes, S., Weikert, S., Stults, J., Vanderlaan, M., and Krummen, L. (1999). A two-dimensional protein map of Chinese hamster ovary cells. Electrophoresis *20*, 994–1000.

Chan, A., and Carter, P. (2010). Therapeutic antibodies for autoimmunity and inflammation. Nat Rev Immunol *10*, 301–316.

Chandler, M., and Zydney, A. (2004). High throughput screening for membrane process development. J Membr Sci *237*, 181–188.

Chatel, A., Kumpalume, P., and Hoare, M. (2014). Ultra scale-down characterization of the impact of conditioning methods for harvested cell broths on clarification by continuous centrifugation—Recovery of domain antibodies from rec E. coli. Biotechnol Bioeng *111*, 913–924.

Chollangi, S., Parker, R., Singh, N., Li, Y., Borys, M., and Li, Z. (2015). Development of robust antibody purification by optimizing protein-A chromatography in combination with precipitation methodologies. Biotechnol. Bioeng. *112*, 2292–2304.

Coffman, J., Shpritzer, R., and Vicik, S. (2006). Flocculation of antibody-producing mammalian cells with precipitating solutions of soluble cations and anions. (Litchfield, AZ),.

Cordes, R., Sims, W., and Glatz, C. (1990). Precipitation of nucleic acids with poly(ethyleneimine). Biotechnol Progr *6*, 283–285.

Cordoba, A., Shyong, B., Breen, D., and Harris, R. (2005). Non-enzymatic hinge region fragmentation of antibodies in solution. J Chromatogr B *818*, 115–121.

Dave, P., Dizon-Maspat, J., and Cano, T. (2009). Evaluation and implementation of a single-stage multimedia harvest depth filter for a large-scale antibody process. Bioprocess Int *7*, 8–17.

Doig, S., Pickering, S., Lye, G.J., and Baganz, F. (2005). Modelling surface aeration rates in shaken microtitre plates using dimensionless groups. Chem Eng Sci *60*, 2741–2750.

Doneanu, C., Xenopoulos, A., Fadgen, K., Murphy, J., Skilton, S.J., Prentice, H., Stapels, M., and Chen, W. (2012). Analysis of host-cell proteins in biotherapeutic proteins by comprehensive online two-dimensional liquid chromatography/mass spectrometry. mAbs *4*, 24–44.

Doran, P. (1995). Bioprocess Engineering Principles (United Kingdom: Academic Press).

Duetz, W., and Witholt, B. (2001). Effectiveness of orbital shaking for the aeration of suspended bacterial cultures in square-deepwell microtiter plates. Biochem Eng J *7*, 113–115.

Ecker, D., Jones, S., and Levine, H. (2015). The therapeutic monoclonal antibody market. mAbs *7*, 9–14.

Elvin, J., Couston, R., and van der Walle, C. (2013). Therapeutic antibodies: market considerations, disease targets and bioprocessing. Int J Pharm *440*, 83–98.

Espuny Garcia del Real, G., Davies, J., and Bracewell, D. (2014). Scale-down characterization of post-centrifuge flocculation processes for high-throughput process development. Biotech Bioeng 111, 2486–2498.

Fane, A., Fell, C., and Suki, A. (1983). The effect of ph and ionic environment on the ultrafiltration of protein solutions with retentive membranes. J Membr Sci *16*, 195–210.

Felo, M., Christensen, B., and Higgins, J. (2013). Process cost and facility considerations in the selection of primary cell culture clarification technology. Biotechnol Progr *29*, 1239–1245.

Felo, M., Kang, Y., Hamzik, J., Balderes, P., and Ludwig, D. (2015). Industrial application of impurity flocculation to streamline antibody purification processes. Pharm Bioprocess *3*, 115–125.

Fisher, R., Glatz, C., and Murphy, P. (1986). Effects of mixing during acid addition on fractionally precipitated protein. Biotech Bioeng *28*, 1056–1063.

Follman, D., and Fahrner, R. (2004). Factorial screening of antibody purification processes using three chromatography steps without protein A. J Chromatogr A *1024*, 79–85.

Fournier, M., Falk, L., and Villermaux, J. (1996a). A new parallel competing reaction system for assessing micromixing efficiency—Determination of micromixing time by a simple mixing model. Chem Eng Sci *51*, 5187–5192.

Fournier, M., Falk, L., and Villermaux, J. (1996b). A new parallel competing reaction system for assessing micromixing efficiency—Experimental approach. Chem Eng Sci *51*, 5053–5064.

Franke, J., and Mersmann, A. (1995). The influence of the operational conditions on the precipitation process. Chem Eng Sci *50*, 1737–1753.

Frerix, A., Müller, M., Kula, M., and Hubbuch, J. (2005). Scalable recovery of plasmid DNA based on aqueous two-phase separation. Biotechnol Appl Biochem *42*, 57–66.

Gagnon, P., Nian, R., Lee, J., Tan, L., Latiff, S., Lim, C., Chuah, C., Bi, X., Yang, Y., Zhang, W., et al. (2014). Nonspecific interactions of chromatin with immunoglobulin G and protein A, and their impact on purification performance. J Chromatogr A *1340*, 68–78.

Gao, S., Zhang, Y., Stansberry-Perkins, K., Buko, A., Bai, S., Nguyen, V., and Brader, M. (2011). Fragmentation of a highly purified monoclonal antibody attributed to residual CHO cell protease activity. Biotechnol Bioeng *108*, 977–982.

Gasner, L.L., and Wang, D.I.C. (1970). Microbial cell recovery enhancement through flocculation. Biotech Bioeng *12*, 873–887.

Gholap, R., Petrozzi, S., and Bourne, J. (1994). Influence of viscosity on product distribution of fast competitive chemical reactions. Chem Eng Technol *17*, 102–107.

Gregory, J. (1986). Kinetic aspects of polymer adsorption and flocculation. In Process Technology Proceedings, Y. Attia, ed. (Amsterdam: Elsevier), pp. 31–44.

Grove, H., Færgestad, E., Hollung, K., and Martens, H. (2009). Improved dynamic range of protein quantification in silver-stained gels by modelling gel images over time. Electrophoresis *30*, 1856–1862.

Guibal, E., and Roussy, J. (2007). Coagulation and flocculation of dye-containing solutions using a biopolymer (Chitosan). React Funct Polym *67*, 33–42.

Guichardon, P., and Falk, L. (2000). Characterisation of micromixing efficiency by the iodide–iodate reaction system. Part I: experimental procedure. Chem Eng Sci *55*, 4233–4243.

Habib, G., Holwill, I., and Hoare, M. (1997). Rapid piloting of a selective flocculation process for product purification. J Biotechnol *59*, 91–101.

Hamilton, G. (2015). Antibody-drug conjugates for cancer therapy: The technological and regulatory challenges of developing drug-biologic hybrids. Biologicals *43*, 318–332.

Hebel, D., Huber, S., Stanislawski, B., and Hekmat, D. (2013). Stirred batch crystallization of a therapeutic antibody fragment. J Biotechnol *166*, 206–211.

Hekmat, D. (2015). Large-scale crystallization of proteins for purification and formulation. Bioprocess Biosyst Eng *38*, 1209–1231.

Henzler, H. (2000). Particle stress in bioreactors. In Influence of Stress on Cell Growth and Product Formation, K. Schügerl, G. Kretzmer, H. Henzler, P. Kieran, G.

Hughes, J., Ramsden, D., and Symes, K. (1990). The flocculation of bacteria using cationic synthetic flocculants and chitosan. Biotechnol Tech *4*, 55–60.

Kretzmer, P. MacLoughlin, D. Malone, W. Schumann, P. Shamlou, and S. Yim, eds. (Berlin Heidelberg: Springer), pp. 35–82.

Hermann, R., Lehmann, M., and Büchs, J. (2003). Characterization of gas–liquid mass transfer phenomena in microtiter plates. Biotechnol Bioeng *81*, 178–186.

Hession, C., Osborn, L., Goff, D., Chi-Rosso, G., Vassallo, C., Pasek, M., Pittack, C., Tizard, R., Goelz, S., McCarthy, K., et al. (1990). Endothelial leukocyte adhesion molecule 1: Direct expression cloning and functional interactions. Proc Natl Acad Sci USA *87*, 1673–1677.

Ho, C.S., Oldshue, J.Y., and American Institute of Chemical Engineers (1987). Biotechnology processes : scale-up and mixing / edited by Chester S. Ho, James Y. Oldshue (New York, NY: American Institute of Chemical Engineers).

Hofland, G., Berkhoff, M., Witkamp, G., and van der Wielen, L. (2003). Dynamics of isoelectric precipitation of casein using sulfuric acid. AIChE J *49*, 2211–2223.

Hogwood, C., Bracewell, D., and Smales, C. (2013a). Host cell protein dynamics in recombinant CHO cells. Bioengineered *4*, 288–291.

Hogwood, C., Tait, A., Koloteva-Levine, N., Bracewell, D., and Smales, C. (2013b). The dynamics of the CHO host cell protein profile during clarification and protein A capture in a platform antibody purification process. Biotechnol Bioeng *110*, 240–251.

Hogwood, C., Bracewell, D., and Smales, C. (2014). Measurement and control of host cell proteins (HCPs) in CHO cell bioprocesses. Curr Opin Biotech *30*, 153–160.

Hollas, J. (2004). Modern spectroscopy (Chichester: John Wiley & Sons).

Hoogenboom, H., and Chames, P. (2000). Natural and designer binding sites made by phage display technology. Immunol Today *21*, 371–378.

Horn, D. (1980). PEI physico-chemical properties and applications. In Polymeric Amines and Ammonium Salts, (Oxford/New York/Toronto/Sydney/Paris/Frankfurt: Pergamon Press), pp. 333–355.

Hortsch, R., and Weuster-Botz, D. (2010). Power consumption and maximum energy dissipation in a milliliter-scale bioreactor. Biotechnol Prog *26*, 595–599.

Huang, C. (2009). Receptor-Fc fusion therapeutics, traps, and MIMETIBODY™ technology. Curr Opin Biotech *20*, 692–699.

Huang, Y., Hu, W., Rustandi, E., Chang, K., Yusuf-Makagiansar, H., and Ryll, T. (2010). Maximizing productivity of CHO cell-based fed-batch culture using chemically defined media conditions and typical manufacturing equipment. Biotechnol Progr *26*, 1400–1410.

Hutchinson, N., Bingham, N., Murrell, N., Farid, S., and Hoare, M. (2006). Shear stress analysis of mammalian cell suspensions for prediction of industrial centrifugation and its verification. Biotechnol. Bioeng. *95*, 483–491.

Iammarino, M., Nti-Gyabaah, J., Chandler, M., Roush, D., and Göklen, K. (2007). Impact of cell density and viability on primary clarification of mammalian cell broth: an analysis using disc-stack centrifugation and charged depth filtration. BioProcess International *5*, 38–50.

Iritani, E. (2013). A review on modeling of pore-blocking behaviors of membranes during pressurized membrane filtration. Drying Technol *31*, 146–162.

Jackson, N., Liddell, J., and Lye, G. (2006). An automated microscale technique for the quantitative and parallel analysis of microfiltration operations. J Membr Sci *276*, 31–41.

Jain, E., and Kumar, A. (2008). Upstream processes in antibody production: evaluation of critical parameters. Biotechnol Adv *26*, 46–72.

Jarvis, P., Jefferson, B., Gregory, J., and Parsons, S. (2005). A review of floc strength and breakage. Water Res *39*, 3121–3137.

Jiang, C., Liu, J., Rubacha, M., and Shukla, A. (2009). A mechanistic study of Protein A chromatography resin lifetime. J Chromatogr A *1216*, 5849–5855.

Jin, M., Szapiel, N., Zhang, J., Hickey, J., and Ghose, S. (2010). Profiling of host cell proteins by two-dimensional difference gel electrophoresis (2D-DIGE): implications for downstream process development. Biotechnol Bioeng *105*, 306–316.

Kandula, S., Babu, S., Jin, M., and Shukla, A. (2009). Design of a filter train for precipitate removal in monoclonal antibody downstream processing. Biotechnol Appl Biochem *54*, 149–155.

Kang, Y., Hamzik, J., Felo, M., Qi, B., Lee, J., Ng, S., Liebisch, G., Shanehsaz, B., Singh, N., Persaud, K., et al. (2013). Development of a novel and efficient cell culture flocculation process using a stimulus responsive polymer to streamline antibody purification processes. Biotechnol Bioeng *110*, 2928–2937.

Karim, M., Graham, H., Han, B., and Cibulskas, A. (2008). Flocculation enhanced microfiltration of Escherichia coli lysate. Biochem Eng J *40*, 512–519.

Kawase, Y., and Moo-Young, M. (1990). Mathematical models for design of bioreactors: applications of Kolmogoroff's theory of isotropic turbulence. Chem Eng J *43*, B19–B41.

Kelley, B. (2007). Very large scale monoclonal antibody purification: the case for conventional unit operations. Biotechnol Progr *23*, 995–1008.

Kelley, B. (2009). Industrialization of mAb production technology: the bioprocessing industry at a crossroads. mAbs *1*, 443–452.

Kelley, B., Jakubik, J., and Vicik, S. (2008). Viral clearance studies on new and used chromatography resins: critical review of a large dataset. Biologicals *36*, 88–98.

Kim, J., Akeprathumchai, S., and Wickramasinghe, S. (2001). Flocculation to enhance microfiltration. J Membr Sci *182*, 161–172.

Koh, P., Andrews, J., and Uhlherr, P. (1984). Flocculation in stired tanks. Chem Eng Sci *39*, 975–985.

Kong, S., Aucamp, J., and Titchener-Hooker, N. (2010). Studies on membrane sterile filtration of plasmid DNA using an automated multiwell technique. J Membr Sci *353*, 144–150.

Krampe, B., and Al-Rubeai, M. (2010). Cell death in mammalian cell culture: molecular mechanisms and cell line engineering strategies. Cytotechnology *62*, 175–188.

Kresta, S. (1998). Turbulence in stirred tanks: anisotropic, approximate, and applied. Can J Chem Eng *76*, 563–576.

Kumar, A., Kamihira, M., Galaev, I., Mattiasson, B., and Iijima, S. (2001). Type-specific separation of animal cells in aqueous two-phase systems using antibody conjugates with temperature-sensitive polymers. Biotechnol Bioeng *75*, 570–580.

Lau, E., Kong, S., McNulty, S., Entwisle, C., Mcilgorm, A., Dalton, K., and Hoare, M. (2013). An ultra scale-down characterization of low shear stress primary recovery stages to enhance selectivity of fusion protein recovery from its molecular variants. Biotechnol Bioeng *110*, 1973–1983.

Lee, Y., Brewer, J., Hellman, R., and Hendershot, L. (1999). BiP and immunoglobulin light chain cooperate to control the folding of heavy chain and ensure the fidelity of immunoglobulin assembly. Mol Biol Cell *10*, 2209–2219.

Lee, K., Teng, T., Morad, N., Poh, B., and Mahalingam, M. (2011). Flocculation activity of novel ferric chloride–polyacrylamide (FeCl3-PAM) hybrid polymer. Desalination *266*, 108–113.

Levy, M., Ciccolini, L., Yim, S., Tsai, J., Titchener-Hooker, N., Ayazi Shamlou, P., and Dunnill, P. (1999). The effects of material properties and fluid flow intensity on plasmid DNA recovery during cell lysis. Chem Eng Sci *54*, 3171–3178.

Levy, N., Valente, K., Choe, L., Lee, K., and Lenhoff, A. (2014). Identification and characterization of host cell protein product-associated impurities in monoclonal antibody bioprocessing. Biotechnol Bioeng *111*, 904–912.

Li, F., Vijayasankaran, N., Shen, A., Kiss, R., and Amanullah, A. (2010). Cell culture processes for monoclonal antibody production. mAbs *2*, 466–479.

Lichstein, H., and Soule, M. (1944). Studies of the effect of sodium azide on microbic growth and respiration. J Bacteriol *47*, 221–230.

Lindquist, G., and Stratton, R. (1976). The role of polyelectrolyte charge density and molecular weight on the adsorption and flocculation of colloidal silica with polyethylenimine. J Colloid Interface Sci *55*, 45–59.

Liu, H., Ma, J., Winter, C., and Bayer, R. (2010). Recovery and purification process development for monoclonal antibody production. mAbs *2*, 480–499.

Low, D., O'Leary, R., and Pujar, N. (2007). Future of antibody purification. J Chromatogr B *848*, 48–63.

Lutz, H. (2005). Introduction to validation of biopharmaceuticals.

Lydersen, B., Brehm-Gibson, T., and Murel, A. (1994). Acid precipitation of mammalian cell fermentation broth. Ann N Y Acad Sci *745*, 222–231.

Lye, G., Ayazi-Shamlou, P., Baganz, F., Dalby, P., and Woodley, J. (2003). Accelerated design of bioconversion processes using automated microscale processing techniques. Trends Biotechnol *21*, 29–37.

Ma, J., Hoang, H., Myint, T., Peram, T., Fahrner, R., and Chou, J. (2010). Using precipitation by polyamines as an alternative to chromatographic separation in antibody purification processes. J Chromatogr B *878*, 798–806.

Mannweiler, K., and Hoare, M. (1992). The scale-down of an industrial disc stack centrifuge. Bioprocess Eng *8*, 19–25.

Marcant, B., and David, R. (1991). Experimental evidence for and prediction of micromixing effects in precipitation. AIChE J *37*, 1698–1710.

Mathews, C., Ahern, K., and Van Holde, K. (2000). Biochemistry (San Francisco, Calif; Harlow: Benjamin Cummings).

Maybury, J., Mannweiler, K., Titchener-Hooker, N., Hoare, M., and Dunnill, P. (1998). The performance of a scaled down industrial disc stack centrifuge with a reduced feed material requirement. Bioprocess Eng *18*, 191–199.

Maybury, J., Hoare, M., and Dunnill, P. (2000). The use of laboratory centrifugation studies to predict performance of industrial machines: studies of shear-insensitive and shear-sensitive materials. Biotechnol Bioeng *67*, 265–273.

McCabe, W., Smith, J., and Harriott, P. (2001). Unit operations of chemical engineering (Boston ; London: McGraw-Hill).

McCabe, W., Smith, J., and Harriott, P. (2005). Unit operations of chemical engineering (New York: McGraw-Hill).

McDonald, P., Victa, C., Carter-Franklin, J., and Fahrner, R. (2009). Selective antibody precipitation using polyelectrolytes: a novel approach to the purification of monoclonal antibodies. Biotechnol Bioeng *102*, 1141–1151.

McNerney, T., Thomas, A., Petty, P., Zhao, X., Piper, R., Carvalho, J., Hammond, M., Goss, M., and Bussiere, J. (2012). PDADMAC flocculation of CHO cells with non-ionic polymers and surfactants. (Stowe, Vermont, USA),.

McNerney, T., Thomas, A., Senczuk, A., Petty, K., Zhao, X., Piper, R., Carvalho, J., Hammond, M., Sawant, S., and Bussiere, J. (2015). PDADMAC flocculation of Chinese hamster ovary cells: enabling a centrifuge-less harvest process for monoclonal antibodies. mAbs *7*, 413–427.

Meleady, P., Doolan, P., Henry, M., Barron, N., Keenan, J., O'Sullivan, F., Clarke, C., Gammell, P., Melville, M., Leonard, M., et al. (2011). Sustained productivity in recombinant Chinese Hamster Ovary (CHO) cell lines: proteome analysis of the molecular basis for a process-related phenotype. BMC Biotechnology *11*, 78.

Merril, C., Dunau, M., and Goldman, D. (1981a). A rapid sensitive silver stain for polypeptides in polyacrylamide gels. Anal Biochem *110*, 201–207.

Merril, C., Goldman, D., Sedman, S., and Ebert, M. (1981b). Ultrasensitive stain for proteins in polyacrylamide gels shows regional variation in cerebrospinal fluid proteins. Science *211*, 1437–1438.

Meunier, L., Usherwood, Y., Chung, K., and Hendershot, L. (2002). A subset of chaperones and folding enzymes form multiprotein complexes in endoplasmic reticulum to bind nascent proteins. Mol Biol Cell *13*, 4456–4469.

Micheletti, M., and Lye, G. (2006). Microscale bioprocess optimisation. Curr Opin Biotech *17*, 611–618.

Milburn, P., Bonnerjea, J., Hoare, M., and Dunnill, P. (1990). Selective flocculation of nucleic acids, lipids, and colloidal particles from a yeast cell homogenate by polyethyleneimine, and its scale-up. Enzyme Microb Technol *12*, 527–532.

Müller-Späth, T., and Morbidelli, M. (2014). Purification of human monoclonal antibodies and their fragments. In Human Monoclonal Antibodies, M. Steinitz, ed. (Humana Press), pp. 331–351.

Narkis, N., and Rebhun, M. (1983). Inhibition of flocculation processes in systems containing organic matter. J Water Pollut Con F *55*, 947–955.

Nealon, A., O'Kennedy, R., Titchener-Hooker, N., and Lye, G. (2006). Quantification and prediction of jet macro-mixing times in static microwell plates. Chem Eng Sci *61*, 4860–4870.

Ng, K., and Yianneskis, M. (2000). Observations on the distribution of energy dissipation in stirred vessels. Chem Eng Res Des *78*, 334–341.

Noble, J., and Bailey, M. (2009). Chapter 8 Quantitation of Protein. In Methods in Enzymology, R. Burgess, and M. Deutscher, eds. (Academic Press), pp. 73–95.

Nogal, B., Chhiba, K., and Emery, J. (2012). Select host cell proteins coelute with monoclonal antibodies in protein a chromatography. Biotechnol Progr *28*, 454–458.

Norwood, K., and Metzner, A. (1960). Flow patterns and mixing rates in agitated vessels. AIChE J *6*, 432–437.

Noyes, A., Basha, J., Frostad, J., Cook, S., Millard, D., Mullin, J., LaCasse, D., Wright, R., Huffman, B., Fahrner, R., et al. (2015). A modular approach for the ultra-scale-down of depth filtration. J Membr Sci *496*, 199–210.

Owen, A.T., Fawell, P.D., Swift, J.D., and Farrow, J.B. (2002). The impact of polyacrylamide flocculant solution age on flocculation performance. Int J Miner Process *67*, 123 – 144.

Palmer, D., Ramette, R., and Mesmer, R. (1984). Triiodide ion formation equilibrium and activity coefficients in aqueous solution. J Solution Chem *13*, 673–683.

Peram, T., McDonald, P., Carter-Franklin, J., and Fahrner, R. (2010). Monoclonal antibody purification using cationic polyelectrolytes: an alternative to column chromatography. Biotechnol Progr *26*, 1322–1331.

Perry, R., and Green, D. (2008). Perry's chemical engineers' handbook (New York: McGraw-Hill).

Pohorecki, R., and Bałdyga, J. (1988). The effects of micromixing and the manner of reactor feeding on precipitation in stirred tank reactors. Chem Eng Sci *43*, 1949–1954.

Porter, M. (1972). Concentration polarization with membrane ultrafiltration. Ind Eng Chem Prod RD *11*, 234–248.

Qian, J.W., Xiang, X.J., Yang, W.Y., Wang, M., and Zheng, B.Q. (2004). Flocculation performance of different polyacrylamide and the relation between optimal dose and critical concentration. Eur Polym J *40*, 1699–1704.

Rathore, A., and Winkle, H. (2009). Quality by design for biopharmaceuticals. Nat Biotech *27*, 26–34.

Rathore, N., and Rajan, R. (2008). Current Perspectives on Stability of Protein Drug Products during Formulation, Fill and Finish Operations. Biotechnol Progr *24*, 504–514.

Reichert, J. (2012). Marketed therapeutic antibodies compendium. mAbs *4*, 413–415.

Roussy, J., Van Vooren, M., Dempsey, B., and Guibal, E. (2005). Influence of chitosan characteristics on the coagulation and the flocculation of bentonite suspensions. Water Research *39*, 3247–3258.

van Reis, R., and Zydney, A. (2001). Membrane separations in biotechnology. Curr Opin in Biotechnol *12*, 208–211.

van Reis, R., and Zydney, A. (2007). Bioprocess membrane technology. J Membr Sci *297*, 16–50.

van Reis, R., Leonard, L., Hsu, C., and Builder, S. (1991). Industrial scale harvest of proteins from mammalian cell culture by tangential flow filtration. Biotechnol Bioeng *38*, 413–422.

Reynolds, T., Boychyn, M., Sanderson, T., Bulmer, M., More, J., and Hoare, M. (2003). Scale-down of continuous filtration for rapid bioprocess design: recovery and dewatering of protein precipitate suspensions. Biotechnol Bioeng *83*, 454–464.

Rice, R., and Baud, R. (1990). The role of micromixing in the scale-up of geometrically similar batch reactors. AIChE J *36*, 293–298.

Riske, F., Schroeder, J., Belliveau, J., Kang, X., Kutzko, J., and Menon, M. (2007). The use of chitosan as a flocculant in mammalian cell culture dramatically improves clarification throughput without adversely impacting monoclonal antibody recovery. J Biotechnol *128*, 813–823.

Roush, D., and Lu, Y. (2008). Advances in primary recovery: centrifugation and membrane technology. Biotechnol Prog *24*, 488–495.

Rousseaux, J., Falk, L., Muhr, H., and Plasari, E. (1999). Micromixing efficiency of a novel sliding-surface mixing device. AIChE J *45*, 2203–2213.

Saerens, D., Ghassabeh, G., and Muyldermans, S. (2008). Single-domain antibodies as building blocks for novel therapeutics. Curr Opin Pharmacol *8*, 600–608.

Salemi, S., Markovic, M., Martini, G., and D'Amelio, R. (2015). The expanding role of therapeutic antibodies. Int Rev Immunol *34*, 202–264.

Salt, D., Hay, S., Thomas, O., Hoare, M., and Dunnill, P. (1995). Selective flocculation of cellular contaminants from soluble proteins using polyethyleneimine: a study of several organisms and polymer molecular weights. Enzyme Microb Technol *17*, 107–113.

Salt, D., Bentham, A., Hay, S., Idris, A., Gregory, J., Hoare, M., and Dunnill, P. (1996). The mechanism of flocculation of a Saccharomyces cerevisiae cell homogenate using polyethyleneimine. Bioprocess Eng *15*, 71–76.

Schaer, E., Guichardon, P., Falk, L., and Plasari, E. (1999). Determination of local energy dissipation rates in impinging jets by a chemical reaction method. Chem Eng J *72*, 125–138.

Seiler, F., Gronski, P., Kurrle, R., Lüben, G., Harthus, H., Ax, W., Bosslet, K., and Schwick, H. (1985). Monoclonal antibodies: their chemistry, functions, and possible uses. Angew Chem Int Ed Engl *24*, 139–160.

Senczuk, A., Petty, K., Thomas, A., McNerney, T., Moscariello, J., and Yigzaw, Y. (2016). Evaluation of predictive tools for cell culture clarification performance. Biotechnol Bioeng *113*, 568–575.

Shamlou, P., Gierczycki, A., and Titchener-Hooker, N. (1996). Breakage of flocs in liquid suspensions agitated by vibrating and rotating mixers. Chem Eng J *62*, 23–34.

Shepherd, E., and Kitchener, J. (1956). The ionization of ethyleneimine and polyethyleneimine. J Chem Soc 2448–2452.

Shpritzer, R., Vicik, S., Orlando, S., Acharya, H., and Coffman, J. (2006). Calcium phosphate flocculation of antibody-producing mammalian cells at pilot scale. (San Francisco, CA),.

Shukla, A., and Hinckley, P. (2008). Host cell protein clearance during protein a chromatography: development of an improved column wash step. Biotechnol Progr *24*, 1115–1121.

Shukla, A., and Kandula, J. (2008). Harvest and recovery of monoclonal antibodies from large-scale mammalian cell culture. Biopharm Int *21*, 34–45.

Shukla, A., and Kandula, J. (2009). Harvest and recovery of monoclonal antibodies: cell removal and clarification. In Process Scale Purification of Antibodies, U. Gottschalk, ed. (John Wiley & Sons, Inc.), pp. 53–78.

Shukla, A., and Thömmes, J. (2010). Recent advances in large-scale production of monoclonal antibodies and related proteins. Trends Biotechnol *28*, 253–261.

Shukla, A., Hinckley, P., Gupta, P., Yigzaw, Y., and Hubbard, B. (2005). Strategies to address aggregation during protein A chromatography. Bioprocess Int *3*, 36–44.

Shukla, A., Hubbard, B., Tressel, T., Guhan, S., and Low, D. (2007). Downstream processing of monoclonal antibodies—Application of platform approaches. J Chromatogr B *848*, 28–39.

Singh, N., Pizzelli, K., Romero, J., Chrostowski, J., Evangelist, G., Hamzik, J., Soice, N., and Cheng, K. (2013). Clarification of recombinant proteins from high cell

density mammalian cell culture systems using new improved depth filters. Biotechnol Bioeng *110*, 1964–1972.

Singh, N., Arunkumar, A., Chollangi, S., Tan, Z., Borys, M., and Li, Z. (2016). Clarification technologies for monoclonal antibody manufacturing processes: current state and future perspectives. Biotechnol Bioeng *113*, 698–716.

Singhvi, R., Schorr, C., O'Hara, C., Xie, L., and Wang, D. (1996). Clarification of animal cell culture process fluids using depth microfiltration. BioPharm *9*, 2–8.

Sisodiya, V., Lequieu, J., Rodriguez, M., McDonald, P., and Lazzareschi, K. (2012). Studying host cell protein interactions with monoclonal antibodies using high throughput protein A chromatography. Biotechnol J *7*, 1233–1241.

Slater, R.W., and Kitchener, J.A. (1966). Characteristics of flocculation of mineral suspensions by polymers. Discuss Faraday Soc *42*, 267–275.

Smales, C., Dinnis, D., Stansfield, S., Alete, D., Sage, E., Birch, J., Racher, A., Marshall, C., and James, D. (2004). Comparative proteomic analysis of GS-NS0 murine myeloma cell lines with varying recombinant monoclonal antibody production rate. Biotechnol Bioeng *88*, 474–488.

Sommerfeld, S., and Strube, J. (2005). Challenges in biotechnology production—generic processes and process optimization for monoclonal antibodies. Chem Eng Process *44*, 1123–1137.

Sorensen, P., Christensen, J., and Bruus, J. (1995). Effect of small scale solids migration in filter cakes during filtration of wastewater solids suspensions. Water Environ Res *67*, 25–32.

Stapulionis, R., Kolli, S., and Deutscher, M. (1997). Efficient mammalian protein synthesis requires an intact F-actin system. J Biol Chem *272*, 24980–24986.

Strand, S., Vårum, K., and Østgaard, K. (2003). Interactions between chitosans and bacterial suspensions: adsorption and flocculation. Colloids Surf B *27*, 71–81.

Strand, S., Vandvik, M., Vårum, K., and Østgaard, K. (2001). Screening of chitosans and conditions for bacterial flocculation. Biomacromolecules *2*, 126–133.

Strober, W. (2001). Trypan blue exclusion test of cell viability. In Current Protocols in Immunology A3.B.1-A3.B.3, (John Wiley & Sons, Inc.),.

Sukenik, A., Bilanovic, D., and Shelef, G. (1988). Flocculation of microalgae in brackish and sea waters. Biomass *15*, 187–199.

Tait, A., Aucamp, J., Bugeon, A., and Hoare, M. (2009). Ultra scale-down prediction using microwell technology of the industrial scale clarification characteristics by centrifugation of mammalian cell broths. Biotechnol Bioeng *104*, 321–331.

Tait, A., Hogwood, C., Smales, C., and Bracewell, D. (2012). Host cell protein dynamics in the supernatant of a mAb producing CHO cell line. Biotechnol Bioeng *109*, 971–982.

Tarrant, R., Velez-Suberbie, M., Tait, A., Smales, C., and Bracewell, D. (2012). Host cell protein adsorption characteristics during protein a chromatography. Biotechnol Prog *28*, 1037–1044.

Tenney, M., and Stumm, W. (1965). Chemical flocculation of microorganisms in biological waste treatment. J Water Pollut Con F *37*, 1370–1388.

Tenney, M., Echelberger, W., Schuessler, R., and Pavoni, J. (1969). Algal flocculation with synthetic organic polyelectrolytes. Appl Microbiol *18*, 965–971.

Thömmes, J., and Etzel, M. (2007). Alternatives to Chromatographic Separations. Biotechnol Prog *23*, 42–45.

Thompson, J., Chung, W., Zhu, M., Tie, L., Lu, Y., Aboulaich, N., Strouse, R., and Mo, W. (2014). Improved detection of host cell proteins (HCPs) in a mammalian cell-derived antibody drug using liquid chromatography/mass spectrometry in conjunction with an HCP-enrichment strategy. Rapid Commun Mass Spectrom *28*, 855–860.

Titchener-Hooker, N., Dunnill, P., and Hoare, M. (2008). Micro biochemical engineering to accelerate the design of industrial-scale downstream processes for biopharmaceutical proteins. Biotechnol Bioeng *100*, 473–487.

Tomic, S., Besnard, L., Fürst, B., Reithmeier, R., Wichmann, R., Schelling, P., and Hakemeyer, C. (2015). Complete clarification solution for processing high density cell culture harvests. Sep Purif Technol *141*, 269–275.

Torbacke, M., and Rasmuson, A. (2001). Influence of different scales of mixing in reaction crystallization. Chem Eng Sci *56*, 2459–2473.

Treweek, G., Montgomery, J., and Morgan, J. (1979). Determination of flocculant effectiveness in aggregating suspended particulate matter. J Water Pollut Control Fed *51*, 1859–1877.

Tscheliessnig, A., Konrath, J., Bates, R., and Jungbauer, A. (2013). Host cell protein analysis in therapeutic protein bioprocessing – methods and applications. Biotechnol J *8*, 655–670.

Tustian, A., Salte, H., Willoughby, N., Hassan, I., Rose, M., Baganz, F., Hoare, M., and Titchener-Hooker, N. (2007). Adapted ultra scale-down approach for predicting the centrifugal separation behavior of high cell density cultures. Biotechnol Progress *23*, 1404–1410.

Uhl, V., and Von Essen, J. (1986). Scale-up of equipment for agitating liquids. In Mixing: Theory and Practice, (Orlando ; London: Academic Press),.

U.S. Department of Health and Human Services, Food and Drug Administration (1997). Points to consider in the manufacture and testing of monoclonal antibody products for human use.

U.S. Department of Health and Human Services, Food and Drug Administration (1998). Q5A viral safety evaluation of biotechnology products derived from cell lines of human or animal origin.

Vandezande, P., Gevers, L., Paul, J., Vankelecom, I., and Jacobs, P. (2005). High throughput screening for rapid development of membranes and membrane processes. J Membr Sci *250*, 305–310.

Verschuren, I., Wijers, J., and Keurentjes, J. (2001). Effect of mixing on product quality in semibatch stirred tank reactors. AIChE J *47*, 1731–1739.

Vicum, L., Ottiger, S., Mazzotti, M., Makowski, Ł., and Bałdyga, J. (2004). Multi-scale modeling of a reactive mixing process in a semibatch stirred tank. Chem Eng Sci *59*, 1767–1781.

Villermaux, J., and Falk, L. (1994). A generalized mixing model for initial contacting of reactive fluids. Chem Eng Sci *49*, 5127–5140.

Wang, X., Hunter, A., and Mozier, N. (2009). Host cell proteins in biologics development: identification, quantitation and risk assessment. Biotechnol Bioeng *103*, 446–458.

Weiss, S., John, G., Klimant, I., and Heinzle, E. (2002). Modeling of mixing in 96-well microplates observed with fluorescence indicators. Biotechnol Progr *18*, 821–830.

Westoby, M., Chrostowski, J., de Vilmorin, P., Smelko, J., and Romero, J. (2011). Effects of solution environment on mammalian cell fermentation broth properties: enhanced impurity removal and clarification performance. Biotechnol Bioeng *108*, 50–58.

Wickramasinghe, S., Wu, Y., and Han, B. (2002). Enhanced microfiltration of yeast by flocculation. Desalination *147*, 25–30.

Wickramasinghe, S., Han, B., Akeprathumchai, S., Chen, V., Neal, P., and Qian, X. (2004). Improved permeate flux by flocculation of biological feeds: comparison between theory and experiment. J Membr Sci *242*, 57–71.

Wu, H., and Patterson, G. (1989). Laser-Doppler measurements of turbulent-flow parameters in a stirred mixer. Chem Eng Sci *44*, 2207–2221.

Xu, X., Hirpara, J., Epting, K., Jin, M., Ghose, S., Rieble, S., and Li, Z. (2014). Clarification and capture of high-concentration refold pools for E. coli-based therapeutics using expanded bed adsorption chromatography. Biotechnol Progr *30*, 113–123.

Yavorsky, D., Blanck, R., Lambalot, C., and Brunkow, R. (2003). The clarification of bioreactor cell cultures for biopharmaceuticals. Pharm Technol 62–76.

Yigzaw, Y., Piper, R., Tran, M., and Shukla, A. (2006). Exploitation of the adsorptive properties of depth filters for host cell protein removal during monoclonal antibody purification. Biotechnol Prog *22*, 288–296.

Yue, W., Chen, Z., Liu, H., Yan, C., Chen, M., Feng, D., Yan, C., Wu, H., Du, L., Wang, Y., et al. (2014). A small natural molecule promotes mitochondrial fusion through inhibition of the deubiquitinase USP30. Cell Res *24*, 482–496.

Zauner, R., and Jones, A. (2002). On the influence of mixing on crystal precipitation processes—application of the segregated feed model. Chem Eng Sci *57*, 821–831.

Zhang, H., Lamping, S., Pickering, S., Lye, G., and Shamlou, P. (2008). Engineering characterisation of a single well from 24-well and 96-well microtitre plates. Biochem Eng J *40*, 138–149.

Zhou, G., and Kresta, S. (1996). Impact of tank geometry on the maximum turbulence energy dissipation rate for impellers. AIChE J *42*, 2476–2490.

Zhu, H., Smith, D., Zhou, H., and Stanley, S. (1996). Improving removal of turbidity causing materials by using polymers as a filter aid. Water Res *30*, 103–114.

Zlokarnik, M. (2002). Scale-up in chemical engineering (Weinheim: Wiley-VCH).